Single-particle modelling of X-ray Absorption and X-ray Raman Scattering spectra : from the impact of vibrations on multipole transition channels to the implementation of L2,3 edges

Steven Delhommaye

To cite this version:

Steven Delhommaye. Single-particle modelling of X-ray Absorption and X-ray Raman Scattering spectra : from the impact of vibrations on multipole transition channels to the implementation of L2,3 edges. Geochemistry. Sorbonne Université, 2022. English. NNT : 2022SORUS076 . tel-03715388

HAL Id: tel-03715388
https://theses.hal.science/tel-03715388v1

Submitted on 6 Jul 2022

SORBONNE UNIVERSITÉ

ÉCOLE DOCTORALE 397 : PHYSIQUE ET CHIMIE DES MATÉRIAUX - ED397

Institut de Minéralogie, de Physique des Matériaux et de Cosmochimie - UMR 7590

Single-particle modelling of X-ray Absorption and X-ray Raman Scattering spectra : from the impact of vibrations on multipole transition channels to the implementation of $L_{2,3}$ edges

THÈSE DE DOCTORAT EN PHYSIQUE ET CHIMIE DES MATÉRIAUX

par

Steven DELHOMMAYE

Sous la direction de Delphine CABARET et Guillaume RADTKE

Présentée et soutenue publiquement le 3 février 2022 devant un jury composé de:

Mme. Emilie GAUDRY	Professeur des Universités	Rapportrice
M. Francesco SOTTILE	Ingénieur de recherche	Rapporteur
Mme. Christel GERVAIS	Professeur des Universités	Examinatrice
M. James ABLETT	Chercheur scientifique de ligne	Examinateur
Mme. Delphine CABARET	Professeur des Universités	Directrice de thèse
M. Guillaume RADTKE	Directeur de recherche CNRS	Co-encadrant de thèse

Table of Contents

List of Tables

List of Figures

Acknowledgments

This thesis manuscript is the culmination of three years of work, very interesting and stimulating but also very demanding, with problems sometimes piling up along the way. As such, I would like to thank all the people who kindly offered their help and support. First, I would like to thank my thesis supervisor and co-supervisor, Delphine Cabaret and Guillaume Radtke, who were always there, from offering important insight and answering questions, to offering emotional support in the most difficult times. I would also like to thank all the colleagues of IMPMC, for the war welcome I was offered during these three years, and useful discussions with several of these colleagues. I would especially like to thank the two other (at the time) PhD students who I shared an office with during these three years, Alexis Amouretti and Weibin Li, who contributed in no small part to making these three years truly special to me. I would also like to thank Simo Huotari from the university of Helsinki and Steven Collins from the Diamond light source for providing the data used in this work, as well as Cristoph Sahle and Emmanuelle de Clermont Gallerande from the ID20 beamline at ESRF for measuring and providing data also used in this work. Finally, and maybe most importantly, I would like to thank my family, especially my mother and my twin brother. I probably would have handled these three years much more poorly without their constant support.

Abstract

This thesis work focuses on core level spectroscopies, their use to study the electronic and structural properties of materials and their modelling by Quantum ESPRESSO, based on DFT, the use of pseudopotentials and periodic boundary conditions. Indeed, combination of theory (calculations) and experiment is very important to analyse the spectrum measured using those techniques, given the rich amount of information they contain. The two core level spectroscopies used in this work are the well established X-ray Absorption Spectroscopy (XAS) and X-ray Raman Scattering (XRS), which has been rising in popularity, and can be used as an alternative to XAS for measurement on light elements, or under harsh experimental conditions (high pressure, high temperature). The first objective of this thesis was the assessment of the effect of thermal vibrations of the nuclei on the multipole contributions to XAS and XRS spectra. To that end, comparison was made between experimental data obtained via collaborations and calculations for two well known materials, α-Al_2O_3 and rutile TiO_2. The method used to account for thermal vibrations effects, referred to as the QHA model, consists in calculating the spectrum as the average of spectra calculated for out of equilibrium configurations of the material. Though this method was previously used to study XAS spectrum of light oxides, it was never used to study the effect of thermal vibrations on the secondary contributions in XAS and XRS. In the case of TiO_2, a flaw of the QHA model was brought to light when trying to reproduce subtle angular dependence signals, and corrected by a method based on group theory. The second objective was to implement calculation of XRS $L_{2,3}$ edges in the XSpectra module of Quantum ESPRESSO. Implementation was inspired by previous implementations of XAS $L_{2,3}$ edges and XRS K edges calculations in XSpectra. The monopole and dipole contributions, up to the 1^{st} order of the expansion of the XRS transition operator, are implemented. Implementation was tested on a Cu test case, as well as by comparison between calculation and measured data on

various sulphur compounds. Good agreement with data could be produced, but was found very sensitive to the presence or absence of a core hole on the excited atom. The origin of the variations of $L_{2,3}$ edges spectra of the sulphur compounds, as well as the sensitivity to the different core hole approximations available to XSpectra, were studied.

Résumé

Tout le travail présenté dans cette thèse est ici résumé en français, le reste du manuscrit étant rédigé en anglais. Bien entendu, il ne s'agit que d'un résumé qui souligne la trame générale du manuscrit. Plus de détails, ainsi que les références, se trouvent dans le reste du manuscrit.

Ce travail de thèse porte sur les spectroscopies de niveau de cœur, leur utilisation pour sonder les propriétés structurales et électroniques de la matière ainsi que leur modélisation, en particulier par la suite de code open source Quantum ESPRESSO et du module XSpectra. Quantum ESPRESSO est une suite de code open source, basée sur la théorie de la fonctionnelle de la densité (ou Density Functional Theory, DFT, en aglais), l'utilisation de peudopotentiels, et des conditions aux bords périodiques. XSpectra est le module de Quantum ESPRESSO qui permet le calcul des spectres XAS et XRS. Les deux spectroscopies sur lesquelles se concentre ce travail, en particulier, sont l'absorption des rayons x (ou X-ray Absorption Spectroscopy, XAS, en anglais) et la spectroscopie Raman des rayons X, aussi connue sous le nom de diffusion inélastique des rayons x (X-ray Raman Scattering, XRS, an anglais). L'absorption des rayons X est déjà établie comme une technique de référence pour étudier les propriétés électroniques et structurales de la matière, permettant par exemple de remonter à des informations telles que la coordinence d'éléments spécifiques, leur état d'oxydation, ou encore dans le cas du seuil K d'éléments de transition $3d$ d'obtenir des informations sur les états $3d$ vides, en analysant la zone du préseuil du spectre. La spectroscopie Raman des rayons x, quant à elle, se présente comme une alternative de plus en plus populaire à l'absorption des rayons x, par exemple pour l'étude d'éléments légers ou de mesure en température et préssion élevées, le fait d'utiliser des rayons x durs (très énergétiques, environ 10 keV) la rendant plus pratique dans ces cas. La grande quantité d'informations contenues dans ces spectres (par exemple, les différentes contributions multipolaires, toutes mélangées dans le spectre experimental) rend la modélisation de ces spectres par la théorie désirable pour pouvoir les interpréter faiblement. Outre le cadre théorique dans lequel se situe cette thèse, et développé en grandes partie dans le premier chapitre, puis quand cela est nécessaire, ce manuscrit présente les deux objectifs principaux de ce travail de thèse.

Le premier objectif, présenté dans le chapitre 3, consiste en l'étude de l'impact des fluctuations quantiques des noyaux sur les composantes multipolaires des spectres de seuils K en XAS et en XRS. Ces contributions sont les contributions monopolaire, dipolaire et quandripolaire, mais la contribution monopolaire est formellement interdite en XAS. Elles ont pour origine, respectivement, des transitions électroniques de l'électron de cœur ($1s$ pour un seuil K) vers les états vides s, p et d. Pour les seuils K, la contribution majoritaire aux spectres XAS et XRS est la contribution dipolaire. Cette étude se base sur la comparaison entre données expérimentales, acquises par diverses collaborations, et spectres calculés au seuil K de deux composés de référence bien connus.

Dans le cas de l'étude de l'étude des vibrations sur les seuils K en XRS, le seuil K de Al dans le corindon α-Al_2O_3 est étudié. La mesure de ce seuil a été effectué en XRS sur la ligne ID20 de l'ESRF (European Synchrotron Radiation Facility), à température ambiante, sur un échantillon de poudre, et pour une valeur de la norme q du vecteur de diffusion $\boldsymbol{q}$ élevé. Cela permet à la contribution monopolaire de gagner en intensité et ainsi de participer de manière visible au seuil, ce qui n'est pas le cas pour les petites valeurs de q. Ainsi, l'étude de ce cas permet d'apporter des conclusions quant à l'effet des vibrations thermiques des noyaux sur les spectres XRS, et en particulier sur les composantes monopolaires et dipolaires.

Pour l'étude portant sur l'effet des vibrations quantiques des noyaux sur les seuils K en XAS, le seuil K de Ti dans la phase rutile de TiO_2 est étudié. Les mesures expérimentales de ce seuil ont étés fournies par S. Collins, et mesurées sur la ligne I16 de la Diamond Light Source, aux Royaume-Uni. La mesure a été réalisée sur un cristal synthétique, et suivant un protocole expérimental particulier, pour des températures allant de 6 à 698 K. Ce dernier a permis de mesurer à la fois la dépendance en température de la du préseuil et du seuil de Ti, mais aussi celle d'un signal plus subtil, lié à la dépendance angulaire de la région du spectre signature des états $3d$ vides de Ti. En effet, la zone du pré-seuil de seuils K d'éléments de transition $3d$ étant une zone où les états $3d$ vides créent des signatures spectrales, l'étude de ce cas pourra fournir de précieuses informations sur l'impact des vibrations thermiques des noyaux sur les composantes dipolaire et quadripolaire du seuil K de Ti dans la phase rutile de TiO2.

La méthode utilisée pour prendre en compte les effets de vibrations thermiques des noyaux, à température donnée, sur les spectres aux seuils K en XAS et en XRS a été développé par R. Nemausat lors de son travail de thèse. Elle a notamment fait l'objet de deux articles portant sur l'étude des vibrations thermiques des noyaux sur la Résonnance Magnétique Nucléaire et le XAS, par exemple au sein d'oxides d'éléments légers (Mg, Al, ...). Bien que cette techniques (et d'autres techniques ayant le même but, développées précédemment) ait été utilisé pour sonder l'effet des vibrations thermiques sur la contribution dipolaire en XAS, cette méthode n'a encore jamais utilisé pour sonder l'effet de ces vibrations sur la contribution quadripolaire en XAS, ou en XRS. La méthode, que l'on désigne par méthode QHA, consiste à calculer le spectre comme la moyenne de spectres calculés pour des configurations hors-équilibre du matériau étudié. Dans ces différentes configurations, les atomes sont déplacés de leurs positions d'équilibre d'après les propriétés vibrationnelles du matériau (phonon) ainsi que la statistique quantique à température donnée.

Cette étude permet de montrer que les vibrations quantiques des noyaux affectent majoritairement la contribution dipolaire des spectres de seuil K en XAS et en XRS. Ces effets se traduisent par deux mécanismes différents sur les spectres calculés. Le premier est un changement d'intensité relative de certaines structures, notamment celle de la montée du seuil, parfois important avec le changement de température, ou en comparaison avec le spectre calculé pour la structure avec les noyaux à leur position d'équilibre. Le deuxième effet est l'apparition d'une contribution quadripolaire à des structures spectrales pourtant signatures des états vide s ou d. Cela s'explique par une hybridation, activée par la température, des états p vides de l'atome excité, avec ses états s et d vides. Dans le cas de $\mathrm{TiO_2}$, cette hybridation est le fruit de la brisure de symétrie du site de Ti par le déplacement hors de leur positions d'équilibre des différents atomes. Par ailleurs, dans le cas de l'étude de la phase rutile de $\mathrm{TiO_2}$, la reproduction du subtil signal lié à la dépendance angulaire des états $3d$ vides de Ti échoue. Cela est dû à l'apparition d'une contribution dipolaire non attendue théoriquement d'après la symétrie de la phase rutile de TiO_2 , et non mesurée non plus, à ce signal. Cela est expliqué par un défaut de la méthode utilisée, non observé auparavant, et lié à l'utilisation de configuration hors-équilibre du matériau, pour lesquelles la symétrie d'origine est perdue. Cela empêche dans notre cas, en tout cas en utilisant un nombre raisonnable de configurations, de reproduire simultanément, et en bon accord avec l'expérience, la variation en température de ce subtil signal, et le signal lui-même. Une méthode, justifiée dans le cadre théorique sur lequel est développée la méthode QHA, et basée sur la théorie des groupes, permet de retrouver la bonne dépendance angulaire de ce signal sans perdre les résultats précédents.

Le deuxième objectif de cette thèse, présenté dans le chapitre 4, concerne l'implémentation du calcul de spectres $L_{2,3}$ en XRS au sein de Quantum ESPRESSO. Ce travail fait suite à une partie du travail de thèse d'E. de Clermont Gallerande qui a implémenté, dans une version modifiée du module XSpectra de Quantum ESPRESSO, le calcul de seuils K en XRS. Le calcul des seuils $L_{2,3}$ en XAS a par ailleurs déjà été implémenté au sein de Quantum ESPRESSO, et utilisé pour modéliser avec succès le spectre $L_{2,3}$ du cuivre dans le cuivre mettalique, par exemple. Il est donc tout à fait intéressant de disposer, au sein de Quantum ESPRESSO et pour l'XRS aussi, d'un outil théorique permettant de modéliser les seuils $L_{2,3}$. Après l'implémentation, le but était notamment d'étudier sa capacité à reproduire des données expérimentales, obtenues en collaboration avec a la ligne ID20 de l'ESRF. Ces données ont été mesurés sur divers composés du soufre et pour plusieurs valeurs de q, permettant ainsi la reproduction de spectres $L_{2,3}$ au delà de la limite des petites valeurs de q, pour lesquelles le XAS et l'XRS sont équivalents.

Dans un premier temps, des éléments théoriques indispensables à une implémentation correcte du calcul de seuils $L_{2,3}$ au sein du module XSpectra sont présentés. Cela concerne par exemple l'expression du facteur de structure dynamique, utilisé pour calculer l'intensité du spectre, dans notre cadre théorique spécifique à Quantum ESPRESSO. Cela concerne également l'origine des seuils L_2 et L_3 (dont la somme forme le seuil $L_{2,3}$), qui est la levée de dégénérescence partielle des états $2p$ par le couplage spin-orbite. Cette partie permet notamment d'introduire par la suite des détails sur la manière dont est implémenté le calcul des seuils $L_{2,3}$ dans XSpectra. Par exemple, il est précisé, après avoir explicité la formulation mathématique de l'expression permettant de calculer les seuils $L_{2,3}$ en XRS, quels termes sont ou ne sont pas (pour l'instant !) implémentés dans XSpectra. A l'heure actuelle, seules les contributions dipolaire et monopolaire, provenant des termes du développement de l'opérateur de transition de l'XRS jusqu'à l'ordre 1 en qr. Par ailleurs, l'implémentation étant inspiré des implémentations précédentes, dans XSpectra, des calculs des seuils K en XRS et $L_{2,3}$ en XRS, les calcul des composantes monopolaires, ainsi que des contributions provenant du seuil L_2 et L_3, sont effectués séparément. Cela veut notamment dire, par exemple, que les cross-terms entre les contributions monooplaires et dipolaires sont négligés à l'heure actuelle, mais s'annulent de tout manière dans le cas de calculs sur des échantillons de poudre, ce qui est le cas des calculs présentés ici.

Après avoir rappelé certains résultats attendus d'après notre cadre mono-électronique, l'implémentation est d'abord testé sur un cas test proposé par Quantum ESPRESSO pour tester le calcul de seuil $L_{2,3}$ en XAS. Ce cas test n'est pas optimisé pour donner des résultats fiables, étant à la place optimisé pour être rapide, et pouvoir réaliser un calcul simple permettant une certains prise en main du code. Dans notre cas, ce cas test est un excellent premier test, car en plus d'être très rapide, il permet de vérifier certaines propriétés attendues des spectres calculés, comme la relation entre les spectres individuels des seuils L_3 et L_2, qui doivent être calculés comme égaux par XSpectra vu le cadre théorique mono-électronique sur lequel est basé Quantum ESPRESSO. Par ailleurs, l'équivalence de la composante dipolaire du spectre XAS avec le spectre XRS de seuils $L_{2,3}$ est aussi vérifiée.

Par la suite, des calculs sont réalisés et comparés à des données expérimentales disponibles, pour plusieurs valeurs de q, pour étudier la capacité du code à reproduire ces données expérimentales. Ces données sont la mesure des seuils $L_{2,3}$ du soufre dans Li_2SO_4 ainsi que le soufre pur (structure α). Cela permet notamment d'étudier l'origine de la différence, parfois très marquée, entre les spectres mesurés pour des basses et hautes valeurs de q, via la décomposition du spectre calculé dans ses composantes monopolaires et dipolaires. La décomposition du spectre calculé dans les contributions individuelles des spectres L_2 et L_3 est aussi évalué, et peut être comparé dans le cas du soufre à l'interprétation qui est faite dans la littérature des structures à basses énergies du seuil XAS $L_{2,3}$ de S comme signatures des seuils L_2 et L_3. Par ailleurs, des calculs sont aussi réalisés sur d'autres composés du soufre (orpiment, realgar, arsenopyrite et pyrite) mais ne sont pas comparés à des données expérimentales. Cela s'explique par un problème survenu lors de la préparation des échantillons devant servir à la mesure du seuil $L_{2,3}$ du soufre en XRS sur la ligne ID20 de l'ESRF. Cependant, les résultats obtenus sont discutés d'après les résultats obtenues sur les autres composés, et via comparaison avec des données en XAS trouvées dans la littérature.

Bien qu'un accord avec l'expérience satisfaisant avec l'expérience soit obtenu pour les composés mesurés sur l'ensemble du spectre, la forme des structures spectrales dans les basses energies du spectre est très dépendante de la présence, ou non, d'un trou de cœur sur l'atome excité. La présence ou absence de ce trou de cœur est en effet le facteur qui permet d'obtenir, ou non, un bon accord avec l'expérience au niveau de cette partie du seuil $L_{2,3}$. Par exemple, l'accord entre calcul et expérience est très bon pour le soufre pur en n'incluant pas de trou de cœur sur l'atome S excité. Par ailleurs, il est parfois difficile de reproduire les variations du spectre avec la valeur croissante de q en ne considérant qu'une approximation de trou de cœur pour le calcul. Par exemple, l'accord avec l'expérience au niveau de ces structures spectrales à basses énergies du seuil est bon dans le cas du seuil $L_{2,3}$ du soufre dans Li_2SO_4 pour les petites valeurs de q, mais se dégrade avec des valeurs de q croissante. Cette sensibilité du spectre basse énergies est interprété comme provenant de l'effet du trou de cœur sur les états p vides, en particulier.

Enfin, le manuscrit se termine sur une conclusion qui rappelle les résultats obtenus pour ces différents objectifs, ainsi que sur quelques perspectives sur une courte et moyenne échelles de temps.

1 General Introduction

This thesis work focuses on the use of core level spectroscopies to study electronic and structural properties of materials as well as on the reproduction of data measured using such spectroscopies. Core level spectroscopies rely on the excitation of core level electrons to be able to extract precise information related to the structural environment, or the electronic structure, related to a specific element in the studied material. The two core level spectroscopies which will be focused on in this thesis are X-ray Absorption Spectroscopy and X-ray Raman Scattering. Calculations used to model those spectroscopies were performed using the Quantum ESPRESSO (55; 56; 57) open source suit of codes and more specifically the XSpectra (58; 59; 60) module, used to calculated the different spectra presented in this thesis. Quantum ESPRESSO based on Density Functional Theory, the use of a plane wave basis set to expand the wave functions describing the studied system an pseudopotentials, as well as periodic boundary conditions. This thesis work focused on two main objectives.

The first was to assess the effects of quantum thermal vibrations of the nuclei in the studied material on the multipole contributions to K edge spectra (i.e relying on the excitation of a $1s$ core electron) measured using those spectroscopies. Indeed, temperature-dependent measurements are widely employed in X-ray Absorption Spectroscopy (XAS) to monitor the evolution of the local atomic and electronic structure of materials undergoing phase transitions, such as superconductors,(1; 2; 3; 4) colossally magnetoresistive manganites,(5; 6; 7) ferroelectrics (8; 9; 10) or thermochromics (11; 12). While XAS still appears as a technique of reference, X-ray Raman Scattering spectroscopy (XRS) is becoming increasingly popular in materials and earth sciences for conducting *in-situ* experiments. This is mostly due to its bulk sensitivity, its ability to probe low-energy edges and thus, light elements, and to its high flexibility in terms of sample environments.(16; 17) Indeed, this non-resonant spectroscopy is based on the inelastic scattering of hard X-rays and therefore permits the use of highly absorbing experimental cells for pressure (18; 19; 20; 21) and temperature (22; 23; 24) dependent measurements, which are often hindered by the use of soft X-rays in XAS. Temperature appears therefore as a key parameter in many studies based on core-level spectroscopies. Understanding how atomic thermal fluctuations can influence the shape of XAS or XRS spectra is, consequently, of fundamental importance to interpret these data accurately. To this end, strategies have been developed to account theoretically for atomic vibrations when modelling the spectra. Methods that do not require the explicit calculation of phonon modes have been implemented first, either based on displacing the core-state orbital only while treating final states within the *crude* Born-Oppenheimer approximation,(30; 31) displacing the entire absorbing atom around its equilibrium position (32; 33) or convoluting the spectrum with an approximate phonon spectral function (34; 32). However, heavier numerical approaches based on averaging spectra calculated for series of vibrationally distorted structures generated either from snapshots of molecular dynamics simulations (23; 35; 36) (where the nuclear dynamics is always classic) or from the phonon quantum dynamics (37; 41; 42) were later preferred and proved to be necessary for capturing the subtle effects of temperature on the spectral shape. In this context, it would be interesting to evaluate the impact of atomic quantum thermal fluctuations on the different transition channels observed at K edges in X-ray Absorption and X-ray Raman spectroscopies. K pre-edge XAS spectra of $3d$ transition metal ions are indeed built from a sum of electric dipole and quadrupole transitions(43). Whereas the former give access to the absorber unoccupied p states and thus, to the $3d$ states only indirectly through off-site and, possibly, on-site hybridization, the latter provide a direct channel for probing the absorber $3d$ final states(45). Along the same line, under certain scattering conditions where large momenta are transferred to the specimen, electronic transitions observed in K pre-edge XRS spectra of light elements can strongly deviate from the standard electric dipole channel (46) to include monopole transitions and therefore probe selectively final states with s or p character(47; 48). Although the impact of nuclear quantum fluctuations on electric dipole transitions has been investigated in a number of studies(31; 32; 41; 42), little is known about their influence on these secondary transition channels. Here, we present an in-depth experimental and theoretical investigation of the Ti-K pre-edge temperature dependence in rutile $\mathrm{TiO_2}$. In particular, we extend the numerical approach developed in previous works to account for lattice quantum fluctuations (41; 42) to the calculation of a weak dichroic signal on the basis of group-theoretical arguments. We also consider the case of the Al-K edge in corundum α-$\mathrm{Al_2O_3}$ measured in XRS at 300 K and for a norm of the scattering vector close to 10 $\mathrm{\AA}^{-1}$ to assess the effect of temperature on both electric monopole and dipole transitions with this spectroscopy.

The second main objective of the thesis was the implementation of XRS $L_{2,3}$ edges (excitation of a $2p$ core level electron) calculation in the XSpectra module of Quantum ESPRESSO. Indeed, study at the $L_{2,3}$ edges of diverse materials is as useful as the study of K edges to obtain information on specific elements in the studied materials. Given that the $L_{2,3}$ edges stem from the excitation of a $2p$ electron, the multipole contributions channels to the spectrum give access to information on different empty states than they do for a K edge. For example, the dipole contribution to $L_{2,3}$ edges gives access to information on both empty s and d states, rather than the p states (for a K edge). Though at low values of the norm q of the scattering vector $\boldsymbol{q}$ XRS and XAS provide the same information, with increasing values of q the monopole transition channel, forbidden in XAS, rises in intensity and may substantially change the shape of the spectrum. Moreover, these edges can still be used to obtain the same kind of information as the K edge. For example, the XAS $L_{2,3}$ edges of sulphur in diverse sulphur compounds have been shown to shift towards higher energies, according to the oxidation state of the sulphur atom (80; 79). $L_{2,3}$ calculation of XAS spectra was already implemented in XSPectra by Bunau et al. (60), whereas the calculation of K edge XRS spectra was implemented in a modified XSpectra module by E. de Clermont Gallerande during her thesis work, the implementation being detailed in a dedicated article (47). Quantum ESPRESSO is a DFT-based suit of codes and by definition relies on a single-particle theoretical scheme. The $L_{2,3}$ edges refer to the separate L_2 and L_3 edges, stemming respectively from the $2p_{1/2}$ and $2p_{3/2}$ states, in which the $2p$ state split due to spin-orbit coupling. Unlike the case of K edges mentioned earlier, many-electrons effects can occur at $L_{2,3}$ edges. For instance, it has been well known for some time that these effects can be dominant in $L_{2,3}$ edges of $3d$ transition metals (see for example ref. (44)). Thus, DFT cannot properly treat the case of the transition metals at the $L_{2,3}$

edges (60; 62) because in these cases the single-electron scheme breaks down. Indeed, these many-electrons effects can couple the core level state and the possible final states involved in the electronic transition of the core electron, which can strongly change the $L_{2,3}$ edges from the expected picture in a single electron framework. An example of this failure is the inability for DFT-only based approach to reproduce the observed branching ratio (i.e the ratio between the intensity of the L_3 and L_2 edges) for early transition metals. Indeed, while single-particle scheme based calculations lead to the 2:1 branching ratio expected from the multiplicity of the split $2p$ states, the observed branching ratio for the Ca $L_{2,3}$ edges of Ca in pure Ca (fcc) or in CaF_2, and even for the Ti $L_{2,3}$ edges of rutile and anatase TiO_2, is closer to 1:1 (62; 63). In the cases where pure DFT is not sufficient to accurately describe spectra at the $L_{2,3}$ edges, other methods based on many-body schemes can be used. For instance, methods based on solving the Bethe Salpeter Equation (or BSE based methods for short) have been used to properly reproduce XAS spectra at the $L_{2,3}$ edges of early transition metals (63). BSE based methods were also used to model the XRS Si and Na $L_{2,3}$ edges spectra (64) of powder Si and a polycrystalline Na sample, respectively, for different values of q, and with good accuracy according to comparison with experimental data measured on ID16 at the European Synchrotron Radiation Facility. These specific calculations also allowed to highlight the evolution of the different multipole contributions to the spectra with an increasing value of q, quite stronger in than what was observed in general for K edges in ref (47) as well as the first part of this work, and evaluate its origin in terms of relative multipole contribution weight. Hybrid approaches, making use of both the many-electrons and single-electron schemes, also exist. For example, such an hybrid approach in the form of the OCEAN code has been able to properly reproduce the XAS Ti $L_{2,3}$ edge of $SrTiO_3$ (61). However, many-particle approaches often are limited in the size of the material cell that can be treated. On the other hand, DFT nevertheless has been used to successfully model measured spectra at the $L_{2,3}$ edges. Indeed, for instance Bunau et al.(60) accurately reproduced the measured Cu $L_{2,3}$ edges XAS spectrum of metallic Cu, as well as of other Cu compounds. All of this, coupled with the already mentioned increasing popularity of the XRS spectroscopy, justified completing the work of E. de Clermont Gallerande and implement XRS $L_{2,3}$ edges calculations in XSpectra. The implementation is first tested on a simple test case on metallic Cu. The modified XSpectra module is then used to calculate S $L_{2,3}$ edges spectra of various compounds and compared with available experimental data, obtained at different values of q. The capacity of the modified XSpectra module to accurately reproduce measured XRS $L_{2,3}$ edges spectra is thus tested, as well as the evolution of the calculated spectra with the increasing value of q. More over, the effect of the core hole approximations available in DFT on the calculated spectra are investigated.

The rest of the thesis is structured as follows. In the second chapter (chapter one being this introduction), theoretical elements regarding the framework on which all calculations are performed is given, as well as basic theoretical elements regarding the XAS and XRS techniques. This second chapter describes all common elements needed to understand the other chapters. The following two chapters are dedicated to the two objectives detailed earlier. The third chapter is dedicated to the assessment of the quantum thermal fluctuations of the nuclei on the multipole contributions, stemming from different transition channels, available to both XAS and XRS. The fourth chapter is dedicated to the implementation of XRS $L_{2,3}$ edges calculation in XSpectra, as well as the presentation, and analysis, of the obtained results. Finally, the final chapter concludes this work and offers some perspectives to the work that could follow, in more or less short time frames, this work.

2 Core-level spectroscopies and Theory

In this section, we start by describing the two core-level spectroscopies that were studied during this thesis. X-ray absorption spectroscopie (XAS) and X-ray Raman scattering (XRS), are briefly presented, introducing the expression of the XAS cross section and the XRS dynamic structure factor, which the intensity of a XAS or XRS spectrum, respectively, are proportional to. This thesis focused on the modelling of those spectroscopies, using the open source suite of code Quantum ESPRESSO.Quantum ESRPRESSO is based on Density Functional Theory (DFT), and uses a plane wave basis set to expand wave functions. It also relies on the use of periodic boundary conditions, and pseudopotentials. Calculations are made in two steps. First, a charge density calculation is performed, which is the foundation of a second calculation, which evaluates the spectrum intensity as a continued fraction. Given how this brief summary cannot help to understand precisely how the XAS or XRS spectra are calculated, the second part of this chapter is dedicated to explaining the theoretical framework used to perform calculations in more detail, starting from the foundation Quantum ESPRESSO relies on (DFT), up to how the spectrum intensity is calculated as a continued fraction, in a pseudopotential framework.

2.1 Core-level Spectroscopy to study materials

2.1.1 X-ray Absorption Spectroscopy and its principles

One of the two core-level spectroscopies mainly used during this PhD thesis is the X-ray Absorption Spectroscopy (XAS). This spectroscopy is first presented from a practical point of view. To obtain an x-ray absorption spectrum, the absorption of x-ray photons by a studied material is measured, as a function of said x-ray photons energy. The absorption coefficient, dependent on this energy $E = \hbar\omega$ and often noted $\mu(E)$, is defined by the Beer-Lambert law

$$I = I_0 e^{-\mu l}. \tag{2.1}$$

In eq.2.1, I_0 and I are respectively the intensity of the incident x-ray beam and the transmitted x-ray beam, and l is the thickness of the material sample.

The energy of the x-ray photons, E, is not chosen randomly. For XAS, the spectrum is measured for energies around the binding energy of a core level of one of the atom species in the sample. Indeed, XAS involves on the well-known photoelectric effect: an x-ray photon is absorbed and its energy is transferred to an electron, leading to its promotion to the continuum. This excitation creates an excited electron and a hole on the core level of the absorbing atom (or core hole). The excited electron is also called the photoelectron. To be able to excite the core level electron, the energy of the x-ray thus must be related to the electron's binding energy. It is important to note that XAS is consequently an element-selective spectroscopy. Indeed, because each atom has specific energies for its different core levels, it is possible to chose precisely which element is probed. All is needed is to tune the x-ray photon energy to the core level binding energy of a specific element in the material. In the same way, since each core level is defined by a specific binding energy, it is possible to chose which core level electron is excited ($1s$, $2s$, $2p$, ...). This double selectivity is part of what makes XAS such a powerful tool to study materials.

When the x-ray photons have the necessary energy to excite a core level electron, there is a sharp rise of the absorption coefficient, called an absorption edge. The absorption edge is named according to which core level electron was excited. For example, a K edge corresponds to the excitation of a $1s$ electron, and an $L_{2,3}$ edge to the excitation of a $2p$ electron. In this thesis, K edge and $L_{2,3}$ edge were focused on. When the x-ray photon energy E is higher than the absorption edge energy, noted E_0, the photoelectron is given kinetic energy E_k equal to $E_k = E - E_0$. The photoelectron can then interact with the excited atom's neighbours. The photoelectron's mean free path is determined by its kinetic energy (13). It is common to separate the XAS spectrum in two parts, according to this kinetic energy. Within approximately 30 to 50 eV of the absorption edge energy, as well as just before the absorption edge, is the XANES (X-ray Absorption Near Edge Structure) region of the spectrum. There, the photoelectron's low kinetic energy means a high mean free path, and this region is dominated by multiple scattering effects. The region just before the absorption edge, called the pre-edge region, can in some cases be interpreted by considering transitions to empty available states. For example, the pre-edge region of the K edge of $3d$ transition metals can be interpreted as features arising from transitions to empty $3d$ states (43).While is it hard to get any quantitative information out of the XANES region, it can be used to obtain qualitative information regarding structural or electronic properties such as coordination and oxidation states (38; 39; 40) (for example, by comparing a measured XAS spectrum with reference spectra of well known materials). Indeed, the absorption edge can greatly vary in shape and energy position according to those properties. After the XANES region, at higher photo-electron energy, which leads to a smaller mean free path, the EXAFS (Extended X-ray Absorption Fine Structure) portion of the spectrum can be found. This portion of the XAS spectrum is dominated by the scattering of the photoelectron by the close neighbours of the absorbing atom, which causes the well known EXAFS oscillations. From this EXAFS region, much more quantitative information can be obtained, such as number of first neighbours and distance to these neighbours. Fig. 2.1 shows an example of the separation of a K edge spectrum (Sc K edge of scandia, published in (95)) into the XANES and EXAFS regions.

From a more theoretical point of view, XAS is best understood by first describing the interaction of the X-ray electromagnetic wave with the electrons in the material. X-rays are defined by an electromagnetic field using a scalar and vector potential, respectively $\phi(\boldsymbol{r},t)$ and $\boldsymbol{A}(\boldsymbol{r},t)$. The Hamiltonian of an electron of charge q, mass m, gyromagnetic factor g and spin $\boldsymbol{s}$, submitted to this electromagnetic field, in an external potential $V(r)$ is written as (53)

$$H = \frac{1}{2m}[-i\hbar\nabla - q\boldsymbol{A}(\boldsymbol{r},t)]^2 + V(\boldsymbol{r}) + q\phi(\boldsymbol{r},t) - \frac{gq}{2m}\boldsymbol{s}\cdot\nabla\times\boldsymbol{A}(\boldsymbol{r},t), \tag{2.2}$$

where $\hbar$ is the reduced Planck constant. From there, in (53), C. Brouder manages to derive the expression of the absorption cross section, to which the intensity of the XAS spectrum is

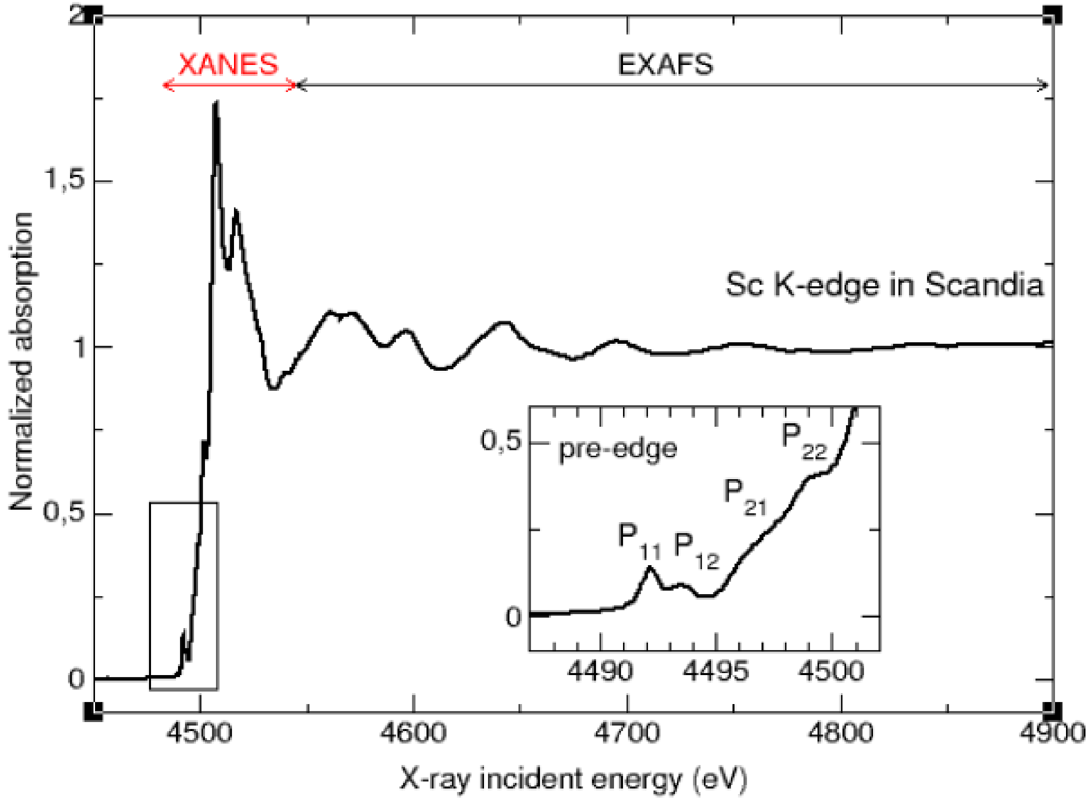

Figure 2.1: Example of the separation of the Sc XAS K edge of scandia (Sc_2O_3) into the XANES and EXAFS regions.

proportional. First, the exciting electromagnetic wave is expressed as a plane wave of wave vector $\boldsymbol{k}$ in the Coulomb gauge so that $\phi(r,t) = 0$ and $\nabla \cdot \boldsymbol{A}(\boldsymbol{r},t) = 0$. The A^2 term is shown to be negligible. By applying Fermi's golden rule (which governs the transition probability from an initial state to a final state), stemming from a time-dependent perturbation theory framework, the expression of the absorption cross section is finally obtained. It is defined by the rate at which energy is removed from the photon beam by the photoelectric effect divided by the rate at which energy in the photon beam crosses a unit area perpendicular to $\boldsymbol{k}$. The final expression for the absorption cross section reads

$$\sigma(\hbar\omega) = 4\pi^2\alpha_0\,\hbar\omega \sum_f \left|\langle f|\mathcal{O}^{XAS}(\hat{\boldsymbol{\varepsilon}},\boldsymbol{k})|i\rangle\right|^2\ \delta(E_f - E_i - \hbar\omega), \tag{2.3}$$

where $\mathcal{O}_{XAS}$ is the XAS transition operator, and $\hbar\omega$, $\hat{\boldsymbol{\varepsilon}}$ and $\boldsymbol{k}$ are respectively the incident X-ray beam's energy, polarisation unit vector, and wave vector. The Dirac function ensures the energy conservation when the electron is promoted from the initial state $|i\rangle$ of energy E_i to an excited state $|f\rangle$ of energy E_f. The final state $|f\rangle$ includes a core hole where the core level electron was excited. The calculation of the final state and its energy, as well as spectrum calculations, are possible in many different theoretical frameworks. The theoretical framework used to perform calculations in this thesis, the Density Functional Theory (DFT), is detailed later in this section (2.2). Moreover, the XAS transition operator is described more explicitly in section 3.1.1.1, which allows to consider the different transition channels contributing to the absorption cross section.

2.1.2 X-ray Raman Scattering and its principles

The second core level spectroscopy focused on in this thesis is X-ray Raman Scattering (XRS), also known as Non-Resonant Inelastic X-ray Scattering or NRIXS. Whereas XAS relies on a simple absorption process which involves one X-ray photon at a time, XRS relies on a scattering process which involves two X-ray photons, the incident photon of energy $E_{in} = \hbar\omega_{in}$ and wave vector $\boldsymbol{k}_{in}$ and the scattered photon of energy $E_{out} = \hbar\omega_{out}$ and wave vector $\boldsymbol{k}_{out}$. Indeed, similarly to XAS, the incident X-ray photon can cause the excitation of a core-level electron, but ends up scattered instead of being absorbed by the sample. Because both XAS and XRS rely on core level excitations, they can yield similar information. However, since the core level excitation is caused by different light-matter interactions (absorption *vs.* scattering), XRS can also yield information unavailable to XAS. Moreover, the use of hard X-rays allows to study low-Z elements in harsher experimental conditions than XAS, which requires the use of soft X-rays to study these low-Z elements. These facts, and the relatively recent development of experimental tools designed for XRS measurements, make XRS an increasingly popular alternative option to XAS to study low-Z elements.

This scattering process is referred to as inelastic because there is a momentum and energy transfer to the sample when the X-ray photon is scattered, and non-resonant because the incident X-ray photon energy is far higher than the binding energy of the excited core electron. The non-resonant inelastic scattering of X-rays is part of the broader Inelastic X-ray Scattering (IXS). Thus, whereas in XAS the X-ray photon energy simply had to be tuned to measure a specific absorption edge, in the case of XRS tuning the measured energy loss to the energy of a specific absorption edge allows both to measure the XRS spectrum at the desired edge, and to avoid measuring the other IXS processes, when possible. Indeed, for example, core level excitations for low-Z elements can be in the same range as the Compton scattering energy range.

From a more theoretical point of view, XRS can also be understood by first considering the interaction between the X-ray electromagnetic field and the electrons in the material. In eq. 2.2 from the previous section, the Hamiltonian for this interaction was expressed. The A^2 term that was shown to be negligible when studying XAS, is in fact the term describing all the interactions involving two photons. The $i\hbar\nabla \cdot \boldsymbol{A}(\boldsymbol{r}, t)$ term on the other hand, is responsible for the single photon processes such as X-ray absorption. The two photon interactions include the scattering of X-rays, and more specifically, the non-resonant inelastic scattering of X-rays which XRS relies on. Thus, for an electron with charge q, mass m and an X-ray electromagnetic wave described by its vector potential $\boldsymbol{A}(\boldsymbol{r}, t)$, the Hamiltonian describing the scattering interactions can be written as follows (15)

$$H = \frac{q^2}{2m} A^2(\boldsymbol{r}, t). \tag{2.4}$$

Using Fermi's golden rule (time dependent perturbation theory), and focusing on the terms

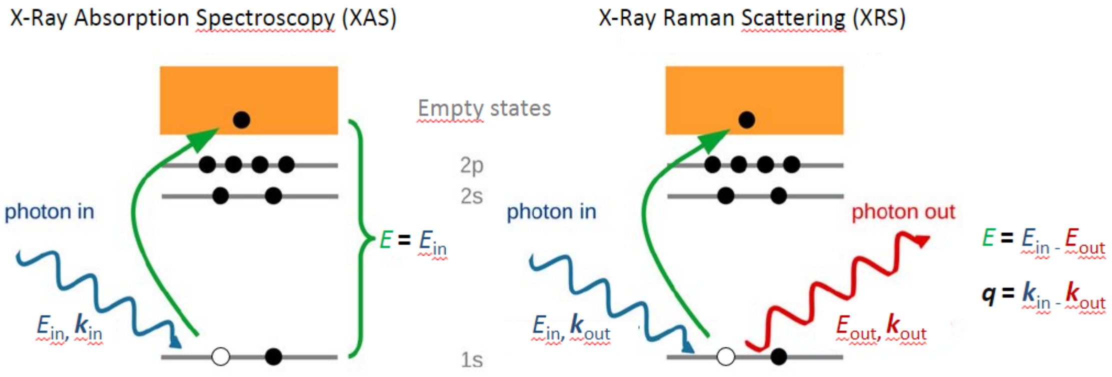

Figure 2.2: Summary illustration of the XAS and XRS spectroscopies, in the case of a K edge. In this illustration, ”photon in” refers to the incident X-ray photon used to excite a $1s$ core level of the probed atom, and ”photon out” refers to the scattered electron in the case of XRS.

describing only the non resonant inelastic X-ray scattering then allows to express the dynamic structure factor $S(\boldsymbol{q}, \omega)$, which the XRS spectrum intensity is proportional to, as (15; 14)

$$S(\boldsymbol{q}, \omega) = \sum_f \left|\langle f|\mathcal{O}^{XRS}(\boldsymbol{q})|i\rangle\right|^2 \delta(E_f - E_i - \hbar\omega). \tag{2.5}$$

This equation involves the scattering vector $\boldsymbol{q} = \boldsymbol{k}_{in} - \boldsymbol{k}_{out}$ in the XRS transition operator $\mathcal{O}_{XRS}$, which will be detailed more explicitly in section 3.1.1.2 and 4.1.2. Just like for XAS, the XRS transition operator can written to highlight the different transition channels contributions to the XRS spectrum. It should be noted that in eq. 2.5 contrarily to XAS (in eq. 3.3), $\hbar\omega = \hbar(\omega_{in} - \omega_{out})$ represents the energy loss of the X-ray photon occurring during the scattering process, and not the incident X-ray beam energy. More details regarding the calculation of the initial and final states $|i\rangle$ and $|f\rangle$ and their energies will be given in section 2.2. Additionally, the implementation, in the XSpectra module of Quantum ESPRESSO, of $L_{2,3}$ edges calculation in XRS is presented in chapter four (4.1 and 4.2). More details on the dynamic structure factor can be found there.

Fig.2.2 shows an illustrated summary of the XAS and XRS spectroscopes, and Fig.2.3 shows an example illustration of the XRS geometry, that is to say the relation between $\boldsymbol{k}_{in}$, $\boldsymbol{k}_{out}$ and $\boldsymbol{q}$. As is shown in fig.2.3, in the case of XRS, the placement of the detectors to mea-

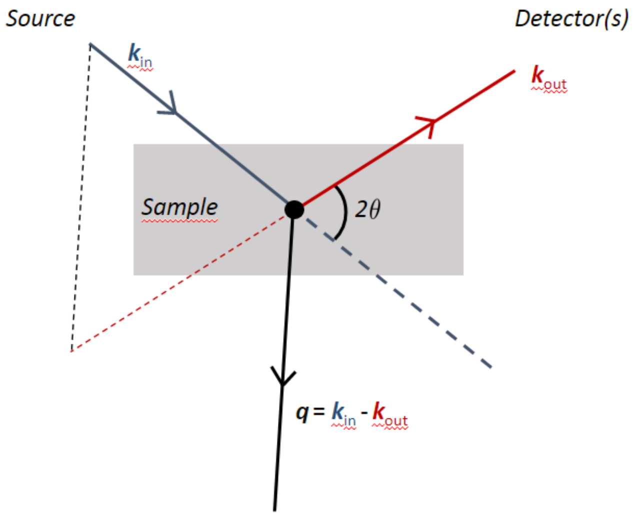

Figure 2.3: Simplified and fictitious XRS experiment to illustrate the relations between $\boldsymbol{k}_{in}$, $\boldsymbol{k}_{out}$ and $\boldsymbol{q}$. 2θ is often referred to as the scattering angle. The scattering vector $\boldsymbol{q}$ represents the fact that during the scattering process, the incident x-ray photon transfers a part of its momentum to the sample, quantified as $\hbar k$, along the orientation of $\boldsymbol{q}$.

sure the signal at specific $\boldsymbol{k}_{out}$ orientation given a constant $\boldsymbol{k}_{in}$ allows to measure the XRS signal for different orientations of $\boldsymbol{q}$. It should be kept in mind that higher or lower values of $\boldsymbol{q}$ are chosen by setting up the correct scattering angle, as using $\boldsymbol{q} = \boldsymbol{k}_{in} - \boldsymbol{k}_{out}$ and the relation between the speed of light c, k and the pulsation ω for the incident and scattered photons, the value of $\boldsymbol{q}$ can be expressed as:

$$q^2 = |\boldsymbol{q}|^2 = \frac{1}{c^2}[\omega_{in}^2 + \omega_{out}^2 - 2\omega_{in}\omega_{out}\cos(2\theta)]. \tag{2.6}$$

For example, a scattering angle close to 0 corresponds to a very low value of the norm of $\boldsymbol{q}$ while a scattering angle close to $\pi/2$ corresponds to a higher value of the norm of $\boldsymbol{q}$.

2.2 Modelling core-level spectroscopies

2.2.1 Density Functional Theory

The studied crystal can be considered as a system of N atom nuclei and N_e electrons, with electrons interacting with each other as well as with all the nuclei in the system. To describe this quantum system's properties, and calculate its evolution, the Schrödinger equation (non-relativistic) has to be solved

$$H\Psi(\boldsymbol{R}, \bar{\boldsymbol{r}}, t) = i\frac{\partial\Psi(\bar{\boldsymbol{R}}, \bar{\boldsymbol{r}}, t)}{\partial t}. \tag{2.7}$$

$\Psi(\bar{\boldsymbol{R}}, \boldsymbol{r}, t)$ is the wave function describing the system of N nuclei and N_e electrons, $\bar{\boldsymbol{R}} = \{\boldsymbol{R}_I\}$ ($I = 1..N$) being the collective coordinates of the nuclei and $\bar{\boldsymbol{r}} = \{\boldsymbol{r}_i\}$ ($i = 1..N_e$) the collective coordinates of the electrons, and H is the Hamiltonian of the system. Some approximations can be adopted to begin simplifying this very complex problem (and very unsolvable, as N and N_e are very large !). First, only the stationary cases are considered, so that we can instead solve the time-independent version of Schrödinger's equation

$$H\Psi(\bar{\boldsymbol{R}}, \bar{\boldsymbol{r}}) = E\Psi(\bar{\boldsymbol{R}}, \bar{\boldsymbol{r}}), \tag{2.8}$$

with $\Psi(\boldsymbol{R}, \boldsymbol{r})$ and E the eigenstates and eigenvalues of the time-independent Schrödinger's equation. At this point, the Hamiltonian of the system include the kinetic energy terms for the nuclei and electrons, as well as the terms describing the nucleus-nucleus, electron electron and electron-nucleus Coulombian interactions potentials. The Hamiltonian of the system can thus be written, taking these terms in that order, as

$$H = T_N + T_e + V_N + V_e + V_{eN}. \tag{2.9}$$

The kinetic energy terms read, for nuclei and electrons respectively

$$T_N = \sum_{I=1}^{N} \frac{P_I^2}{2M_I} \tag{2.10}$$

and

$$T_e = \sum_{i=1}^{Ne} \frac{p_i^2}{2m}, \tag{2.11}$$

where P_I and p_i are the norms of the momentum of the I^{th} nucleus and i^{th} electron and M_I and m the mass of the I^{th} nucleus and of the electron. The nucleus-nucleus, electron-electron and electron-nucleus Coulombian interaction potentials are expressed respectively as

$$V_N = \frac{1}{2} \sum_{I \neq J} \frac{e^2 Z_I Z_J}{|\boldsymbol{R}_J - \boldsymbol{R}_I|}, \tag{2.12}$$

$$V_e = \frac{1}{2} \sum_{i \neq j} \frac{e^2}{|\boldsymbol{r}_j - \boldsymbol{r}_i|}, \tag{2.13}$$

and finally

$$V_{eN} = \frac{1}{2} \sum_{I=1}^{N} \sum_{i=1}^{N_e} \frac{e^2 Z_I}{|\boldsymbol{R}_I - \boldsymbol{r}_i|}, \tag{2.14}$$

where $e = |q|/\sqrt{4\pi\varepsilon_0}$. As before (section 2.1.1), q is the electron charge and ε_0 is the vacuum permittivity.

Another approximation, called the Born-Oppenheimer approximation, also greatly simplifies the problem. This approximation is named after the two physicists M. Born and J. R. Oppenheimer that presented it in their famous article (52), and yields the starting point from which DFT can be built. The approximation is based on taking into consideration the vast difference between the mass of an electron and the mass of the atom's nucleus. Because the mass of a proton (and of a neutron) is approximately 1837 times that of an electron, the speed of the electron is in return far greater than the speed of any atom nucleus. That is to say, the response of an electron following the movement of the nucleus can be considered as instantaneous. This allows to consider a configuration of the material where the atom nuclei are immobile, and focusing on the electrons instead. In other words, instead of being a variable of the problem, $\bar{\boldsymbol{R}}$ becomes a parameter of the problem. From a more practical point of view, this approximation allows to separate the electronic and nuclear parts of the Hamiltonian H and the wave function $\Psi(\bar{\boldsymbol{R}}, \bar{\boldsymbol{r}})$. On the one hand, the wave function can now be factored as

$$\Psi^i_m(\bar{\boldsymbol{R}}, \bar{\boldsymbol{r}}) = \chi^i_m(\bar{\boldsymbol{R}})\psi_m(\bar{\boldsymbol{r}}; \bar{\boldsymbol{R}}). \tag{2.15}$$

In eq. 2.15, $\chi^i_m(\bar{\boldsymbol{R}})$ is the wave function describing the nuclei, with the i exponent defining the vibrational level and the index m is the electronic quantum number. $\psi_m(\bar{\boldsymbol{r}}; \bar{\boldsymbol{R}})$ is the electronic part of the wave function, describing the electrons, and for which $\bar{\boldsymbol{R}}$ is now a parameter, meaning that $\psi_m(\bar{\boldsymbol{r}}; \bar{\boldsymbol{R}})$ is a function of $\bar{\boldsymbol{r}}$ and defined for a specific configuration $\bar{\boldsymbol{R}}$. On the other hand, the Hamiltonian can now be written as

$$H = T_N + H_e, \tag{2.16}$$

where

$$H_e = T_e + V_N + V_e + V_{eN}. \tag{2.17}$$

In eq. 2.17, V_N depends only on $\bar{\boldsymbol{R}}$ which has become a parameter. This means that V_N is now a constant, defined for a specific $\bar{\boldsymbol{R}}$; This in turn makes He dependent only on $\bar{\boldsymbol{r}}$, and built for a specific configuration $\bar{\boldsymbol{R}}$. Thus, the V_N term can safely be ignored from now on. The electronic wave function is a solution of the following Schrödinger equation

$$H_e\psi_m(\bar{\boldsymbol{r}}; \bar{\boldsymbol{R}}) = \varepsilon_m\psi_m(\bar{\boldsymbol{r}}; \bar{\boldsymbol{R}}), \tag{2.18}$$

where ε_m is the energy of the N_e electron system, subjected to the Coulomb potential created by the N nuclei clamped at their position defined by $\bar{\boldsymbol{R}}$.

The Born-Oppenheimer approximation allows to reduce the number of variables from $3(N+N_e)$ to $3N_e$ by separating the electronic and nuclear parts of the total system wave function $\Psi^i_m(\bar{\boldsymbol{R}}, \bar{\boldsymbol{r}})$, but even the electronic problem alone (eq. 2.17) is hardly solvable in practice. It is however a very good start to develop DFT, which allows to find a fictitious but equivalent system to our real system, but for which we know the exact solutions. As mentioned just now, the electronic problem we arrived at after the Born-Oppenheimer approximation is still unsolvable in practice. However, if we consider a system of N_e independent electrons, which are not interacting together, the problem is simpler. Indeed, if we consider that the electrons do not interact together, the term V_e disappears, and we are left with the V_{eN} and T_e terms. The V_{eN} term, since $\bar{\boldsymbol{R}}$ is now a parameter, can be expressed as

$$V_{eN} = \sum_{i}^{N_e} \sum_{I}^{N} -\frac{e^2 Z_I}{|\boldsymbol{R}_I - \boldsymbol{r}_i|} = \sum_{i}^{N_e} V^{ext}(\boldsymbol{r}_i). \tag{2.19}$$

V_{eN} is thus the sum of the same external potential, created by all the nuclei in a specific configuration $\bar{\boldsymbol{R}}$, applied individually to each electron of the system. In the same way, T_e is expressed (see eq. 2.11) as the sum of the kinetic energy of each electron in the system. Thus, a specific Hamiltonian can be written for each electron of the system, as

$$H_e^i = T_e^i + V^{ext}(\boldsymbol{r}_i), \tag{2.20}$$

and the electronic Hamiltonian, in the case electrons are not interacting with each other, can be written as

$$H_e = \sum_{i}^{N_e} H_e^i. \tag{2.21}$$

In this case, the exact solution of eq.2.18 is well known. The electronic wave function $\psi_m(\bar{\boldsymbol{r}}; \bar{\boldsymbol{R}})$ can be factorised as a Slater determinant using the single electron wave functions $\phi_i(\boldsymbol{r}_i; \bar{\boldsymbol{R}})$, defined as the eigenstates of the single electron Hamiltonian H_e^i:

$$H_e^i \phi_i(\boldsymbol{r}_i; \bar{\boldsymbol{R}}) = \varepsilon_i \phi_i(\boldsymbol{r}_i; \bar{\boldsymbol{R}}) \tag{2.22}$$

The Slater determinant formalism comes from both the decomposition of the Hamiltonian into the independent single electron Hamiltonian terms and the fact that $\psi_m(\bar{\boldsymbol{r}}; \bar{\boldsymbol{R}})$ has to respect Pauli's exclusion principle, which mathematically, translates to the imposed antisymmetry of $\psi_m(\bar{\boldsymbol{r}}; \bar{\boldsymbol{R}})$ under the permutation of two electrons (that is to say, $\psi_m(\boldsymbol{r}_1, .., \boldsymbol{r}_j, .., \boldsymbol{r}_k, .., \boldsymbol{r}_{Ne}; \bar{\boldsymbol{R}}) = -\psi_m(\boldsymbol{r}_1, .., \boldsymbol{r}_k, .., \boldsymbol{r}_j, .., \boldsymbol{r}_{Ne}; \bar{\boldsymbol{R}})$).

Thus, the problem can be solved in the case of non interacting electrons, the term defining the Coulomb interaction of each electron with every other electron, V_e, being our 'only' problem. The Hamiltonian for the system can now be written as

$$H_e = \sum_{i=1}^{N_e} H_e^i + V_e, \tag{2.23}$$

which can be seen as the sum of two terms, the first one describing each single electron, and the second describing multi electronic interaction effects. To solve this problem, V_e is usually replaced by a mean "effective" potential, applied to each single electron, noted V_{eff}^i. This way, the system Hamiltonian can be decomposed as the sum of single electron Hamiltonians

$$H_{eff} = \sum_{i=1}^{N_e} H_e^i + V_{eff}^i(\boldsymbol{r}_i) = \sum_{i=1}^{N_e} H_{eff}^i, \tag{2.24}$$

and, the same way as for eq. 2.22, Schrödinger's equation can be written for each electron of the system as

$$H_{eff}^i \phi_{eff}^i(\boldsymbol{r}_i; \bar{\boldsymbol{R}}) = \varepsilon_{eff}^i \phi_{eff}^i(\boldsymbol{r}_i; \bar{\boldsymbol{R}}). \tag{2.25}$$

This approach allows the eigenstates of H_{eff}, $\psi_m^{eff}(\bar{\boldsymbol{r}}; \bar{\boldsymbol{R}})$, to be written as a product of single electron wave functions. Examples of methods using such formalism to solve the problem are the Hatree and Hartree-Fock methods. However, in these methods, the energy from the multi electronic interactions is written as

$$E_H = e^2 \int d\boldsymbol{r} d\boldsymbol{r}' \frac{\rho(\boldsymbol{r})\rho(\bar{\boldsymbol{r}}')}{|\boldsymbol{r} - \boldsymbol{r}'|} \tag{2.26}$$

defined using

$$V_{eff}^i(\boldsymbol{r}_i) = V_H^i = e^2 \int d\boldsymbol{r}' \frac{\rho(\boldsymbol{r}')}{|\boldsymbol{r} - \boldsymbol{r}'|} \tag{2.27}$$

and where the electronic density $\rho(\boldsymbol{r})$ is written using the single electron wave functions

$$\rho(\boldsymbol{r}) = \sum_{i=1}^{N_e} |\phi_i^{eff}(\boldsymbol{r}_i; \bar{\boldsymbol{R}})|^2 \tag{2.28}$$

The Hartree energy E_H, however, is not rigorously equal to the energy the V_e term would produce. First, the V_H term includes self interaction, that is to say, the interaction of one electron with itself, which should not be the case, and does not happen in V_e. Moreover, the eigenstates of H_{eff} are not antisymmetric and thus do not respect Pauli's exclusion principle. Though the Hartree-Fock method adds a term that allows to compensate the self interaction and restore Pauli's exclusion principle, the multielectronic interaction energy still is different from the energy produced by V_e because of spin correlation not being taken into account.

Density Functional Theory constitutes a further attempt to solve the problem of N_e interacting electrons. This system is described by the Hamiltonian of eq. 2.17, where the constant term V_N is ignored. As a reminder, this Hamiltonian is written

$$H_e = T_e + V_{eN} + V_e, \tag{2.29}$$

where the V_{eN} term can be seen as the sum of the same external potential created by the specific configuration $\bar{\boldsymbol{R}}$ applied to each individual electron of the system (see eq. 2.19). The V_{eN} term will thus be referred to as the external potential V_{ext} from now on. The dependence on the parameter $\bar{\boldsymbol{R}}$ is also implicit in what follows. DFT allows to take the electronic density instead of the electron's position (the collective electron coordinates $\bar{\boldsymbol{r}}$) as a variable of the problem. This allows to reduce the number of variables to 3 instead of $3N_e$ while also allowing to get all the needed physical information on the system. DFT is built using the Hohenberg-Kohn double theorem (25) as its foundations. They are the following:

1^{st} Theorem: The (non-degenerate) ground state electron density ρ_0 of the N_e electron system uniquely determines (to a constant) the external potential V_{ext}.

2^{nd} Theorem: There is a universal electron density density functional $F[\rho]$, not depending explicitly on V_{ext}, and defined as

$$F[\rho] = T_e[\rho] + V_e[\rho]. \tag{2.30}$$

The energy of the system is described by $F[\rho]$, such that the energy of the system E in a functional of the electron density ρ

$$E[\rho] = F[\rho] + \int d\boldsymbol{r} V_e xt(\boldsymbol{r})\rho(\boldsymbol{r}) \tag{2.31}$$

which is minimal for the ground state electronic density ρ_0. $E[\rho_0] = E_0$ is then the ground state energy of the system of N_e electrons. The electronic density must of course verify $\int d\boldsymbol{r}\rho(\boldsymbol{r}) = N_e$.

At this point, DFT is an exact theory, which allows access to the exact ground state energy of the system of N_e electrons in interaction. However, this requires to know the functional F, which in turns requires to know V_e exactly, which was already a problem before.

An approach to solve this problem, proposed by W. Kohn and L. J. Sham (26) is to once again consider the fictitious case of non interacting electrons. Indeed, since the Hohenberg-Kohn theorems are valid for any N_e electron system, then they are for the system where electrons are non interacting (i.e when $V_e = 0$). The idea is that for this fictitious system, there exists an external potential, noted V_{KS}, associated (see Hohenberg-Kohn 1^{st} theorem) to the same electron density produced by the real system of N_e interacting electrons.

The fictitious system is described by the Kohn-Sham Hamiltonian

$$H^{KS} = -\frac{\hbar^2\nabla^2}{2m} + V^{KS}(\boldsymbol{r}), \tag{2.32}$$

where the first term is the kinetic energy term and the second term is the Kohn-Sham potential, producing the same real N_e interacting electron density. The problem is that we don't know how to express $V^{KS}(\boldsymbol{r})$ so that it is associated to the real system electron density yet. The fictitious system is described by the following Schrödinger equation

$$H^{KS}\phi_i^{KS}(\boldsymbol{r}_i) = \varepsilon_i^{KS}(\boldsymbol{r}_i)\phi_i^{KS}(\boldsymbol{r}_i), \tag{2.33}$$

where $\phi^{KS}(\boldsymbol{r}_i)$ and $\varepsilon^{KS}(\boldsymbol{r}_i)$ are the single electron eigenstates and eigen energies, respectively. Using this new formalism, the density of the Kohn-Sham fictitious system is given by

$$\rho(\boldsymbol{r}) = \sum_{i=1}^{N_e} |\phi_i^{KS}(\boldsymbol{r}_i)|^2 \tag{2.34}$$

and its kinetic energy is written as

$$T_{KS}[\rho] = \sum_{i=1}^{N_e} \langle \phi_i^{KS}(\boldsymbol{r}_i)| - \frac{\hbar^2 \nabla^2}{2m} |\phi_i^{KS}(\boldsymbol{r}_i)\rangle = -\frac{\hbar^2}{2m} \sum_{i=1}^{N_e} \int \phi_i^{KS}(\boldsymbol{r}_i)^* \nabla^2 \phi_i^{KS}(\boldsymbol{r}_i) d\boldsymbol{r} \tag{2.35}$$

The functional of ρ, F (see eq. 2.30) can then be rewritten as

$$F[\rho] = T_{KS}[\rho] + V_e[\rho] + (T_e[\rho] - T_{KS}[\rho]). \tag{2.36}$$

By taking the Hartree energy (defined with the Hartree potential, see equations 2.26 and 2.27) which is the part we know how to calculate in the $V_e[\rho]$ term, we get

$$F[\rho] = T_{KS}[\rho] + E_H[\rho] + (T_e[\rho] - T_{KS}[\rho] + V_e[\rho] - E_H[\rho]). \tag{2.37}$$

The term in parenthesis $T_e[\rho] - T_{KS}[\rho] + V_e[\rho] - V_H[\rho]$ is called the exchange and correlation energy, E_{xc}. It contains all the quantum effects accounting for the difference between the real energy term stemming from electron-electron interactions, defined by the V_e (eq.2.13), and the Hartree energy, calculated in the case of non interacting electrons in a the Hartree potential. Those effects include for instance the Pauli exclusion, and the spin correlation. The total energy functional defined in eq. 2.31 can then be rewritten as

$$E[\rho] = T_{KS}[\rho] + E_H[\rho] + E_{xc}[\rho] + \int d\boldsymbol{r} V_{ext}(\boldsymbol{r})\rho(\boldsymbol{r}). \tag{2.38}$$

Minimising $E[\rho]$ in this equation allows to find the ground state energy of the system. In practice, a self-consistent cycle is established using the Kohn-Sham equations. The first of these equations is eq. 2.33 where H_{KS} is rewritten to explicit V_{KS}

$$\left[-\frac{\hbar^2\nabla^2}{2m} + V_{xc}(\boldsymbol{r}_i) + V_H(\boldsymbol{r}_i) + V_ext(\boldsymbol{r}_i)\right]\phi_i^{KS}(\boldsymbol{r}_i) = \varepsilon_i^{KS}(\boldsymbol{r}_i)\phi_i^{KS}(\boldsymbol{r}_i), \tag{2.39}$$

where the exchange and correlation potential is defined as the functional derivative of the exchange and correlation energy

$$V_{xc}(\boldsymbol{r}_i) = \frac{\delta E_{xc}}{\delta\rho(\boldsymbol{r}_i)}. \tag{2.40}$$

The second equation allows to calculate the electron density given the Kohn-Sham eigenstates and is given in eq. 2.34.

If every term and every functional is known, then the DFT is still an exact theory. However, the exchange and correlation functional does not have an exact expression. Several approximations, such as the Local Density Approximation (LDA) or Generalised Gradient Approximation (GGA), to the expression of the exchange and correlation functional.

In the LDA, the exchange and correlation functional is expressed as

$$E_{xc} = \int f_{xc}[\rho(\boldsymbol{r})]\rho(\boldsymbol{r})d\boldsymbol{r} \tag{2.41}$$

where $f_{xc}[\rho(\boldsymbol{r})]$ is the exchange correlation in the case of an homogeneous electron gas, of density $\rho(\boldsymbol{r})$. In that sense, DFT is still exact, in the LDA, for an homogeneous electron gas.

In the GGA, the gradient of the density is also taken into account, and the exchange and correlation energy is written as

$$E_{xc} = \int f_{xc}[\rho(\boldsymbol{r}), \nabla\rho(\boldsymbol{r})]\rho(\boldsymbol{r})d\boldsymbol{r}, \tag{2.42}$$

which adds additional term to the exchange and correlation energy as expressed the LDA.

2.2.2 Pseudopotential framework and PAW formalism

In the previous section (2.2.1), we have seen that the DFT allows to calculate the ground state energy of a system of N_e electron, thanks to Schrödinger's equation, applied to a fictitious system of N_e non interacting electron, subjected to an as much fictitious external potential V_{KS}. V_{KS} is chosen so that the fictitious system, described by single electron Kohn-Sham orbitals $\phi_i^{KS}(\boldsymbol{r}_i)$, has the same electron density $\rho(\boldsymbol{r})$ as the real system. This Schrödinger equation and the equation defining the electron density of the system (respectively equations 2.39 and 2.34, are referred to as the Kohn-Sham equations. Thus, solving the Kohn-Sham equations allows to find the density of both the fictitious and the real system, which in turn permits calculation of the properties of the system such as the energy of the ground state thanks to the energy functional of ρ (eq. 2.38).

In practice, XRS or XAS spectra calculations featured in this thesis are made with the Quantum ESPRESSO suite of codes, more precisely using the pw.x and XSpectra.x codes. They rely on a DFT and single electron framework, but using periodic boundary conditions, and expanding the electron orbitals using plane wave basis. Plane waves are very convenient to use for calculations but also suffer from a serious problem. Indeed, correctly describing a rapidly varying function, for instance a core level orbital or the Coulomb potential in the region close to the nucleus, would require a very high number of plane waves. To counter this problem, Quantum ESPRESSO relies on the use of pseudopotentials. The use of pseudpotentials leads to defining a cut-off radius r_{cut} which separates the core and valence regions. The contribution of the valence electrons is treated explicitly, while that of the core electrons is not, which is sometimes referred to as the 'frozen core' approximation. In practice, pseudised wave functions are equal to the real (also referred to as *all electron*) wave functions after the cut-off radius, and more or less approximated before the cut-off radius where it varies too rapidly for plane waves expansion. By reducing the number of plane waves needed for plane wave expansion, calculations are much faster and the memory requirements are much smaller. For illustration purposes, the example of all electron and pseudised atomic orbitals, taken from the pseudopotential of sulphur used in chapter 4, is presented in Fig. 2.4. This figure clearly shows how, beyond the cut-off radius r_{cut}, the pseudised atomic orbitals are equal to the all electron ones, and not before. Moreover, this figure also shows how the pseudised orbitals are increasingly different from the all electron atomic orbitals for the rapidly varying ones (i.e for the $3s$ and $3p$).

However, the use of pseudopotentials, though it brings clear advantages in terms of computational costs when using plane waves basis sets, also brings problems. Indeed, as seen before in

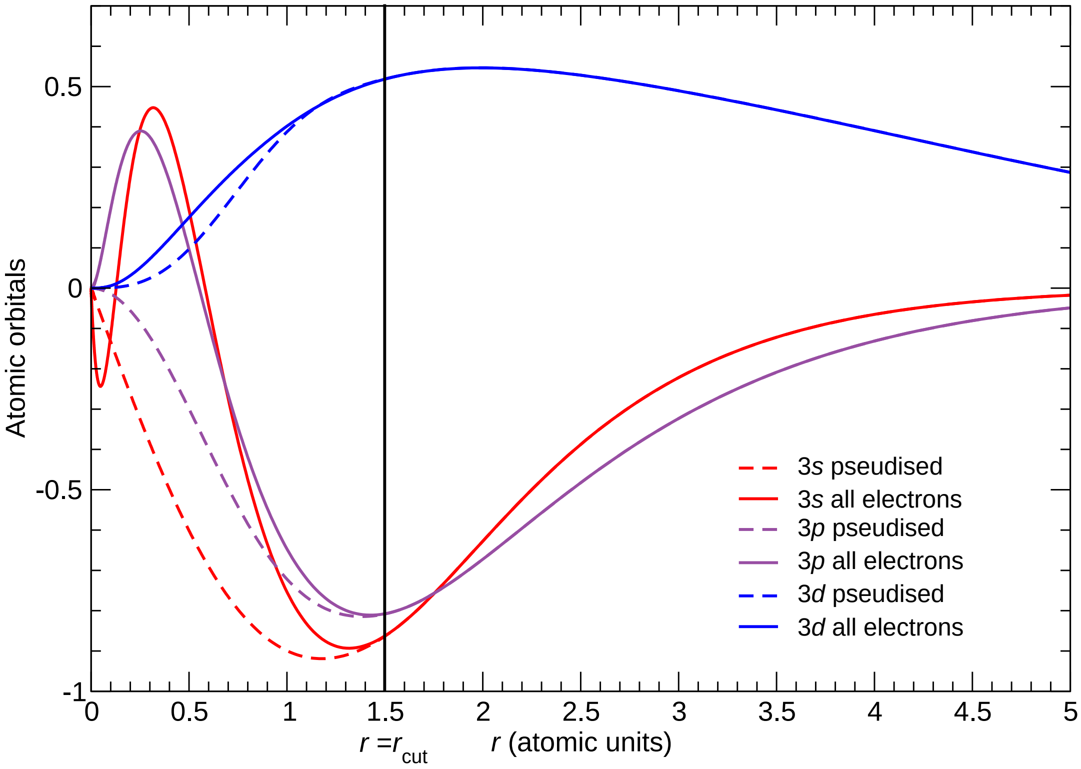

Figure 2.4: All electron (plain lines) and peudised (dotted lines) $3s$, $3p$ and $3d$ atomic taken from the pseudopotential describing a sulphur atom. The demarcation between the regions before and after the cut-off radius is marked by a vertical straight black line.

equations 2.3 and 2.5, the XAS cross section $\sigma(\hbar\omega)$ and the dynamic structure factor $S(\boldsymbol{q},\omega)$, are both proportional to the sum over the final states, of a squared matrix element $\langle f|\mathcal{O}|i\rangle$, where $\mathcal{O}$ is the XAS or XRS transition operator, and $|i\rangle$ and $|f\rangle$ the initial and final states, respectively, involved in the transition of the core electron. It is also important to remember that $\hbar\omega$ is the incident X-ray photon energy in the case of XAS and the energy transfer in the case of XRS. Thus, $|i\rangle$ and $|f\rangle$ are in fact $|\psi_i\rangle$ and $|\psi_f\rangle$, where ψ_i and ψ_f are the N_e electron wave functions describing the initial state and the excited state including a core hole, respectively. In the single electron framework brought by DFT, the N_e electron wave functions ψ, calculated for a specific configuration of the nuclei $\bar{\boldsymbol{R}}$, are treated as Slater determinants using the single electron wave functions ϕ. Thus, in practice, the required matrix elements can be written as $|\langle\phi_f|\mathcal{O}|\phi_i\rangle|$, where ϕ_i and ϕ_f are the single electron orbitals involved in the transition. More precisely, ϕ_i is the core level orbital excited by the X-rays and ϕ_f is the orbital that becomes occupied after the transition. For instance, for a K edge, and a dipole transition involving the p states, ϕ_i is a $1s$ orbital and ϕ_f is any p orbital. ϕ_i (a $1s$ orbital in the K edge example) is easily obtained, and ϕ_f is calculated with a core hole placed on the excited core level, as in XAS or XRS, as the presence of a core hole is usually required for a better agreement with experience. However, using pseudopotentials gives access to pseudised wave functions of the final states, $\tilde{\phi}_f$, rather than the all electron final states wave functions ϕ_f. Without going too much into details, this causes a problem because the calculation of the matrix element $\langle\phi_f|\mathcal{O}|\phi_i\rangle$ involves the calculation of a radial integral term involving the atomic orbitals of the initial and final states. The atomic orbital of the core state is necessarily localised in the core region, where the pseudised atomic orbital of the final state, as shown by Fig.2.4, can be very different from their all electron counterparts. This means that a priori, the use of pseudopotentials makes accurate calculation of the transition matrix element, and thus of the spectrum intensity, impossible.

On another note, it should be mentioned that chapter 4, and more precisely sections 4.1 and 4.2, features the detailed expression of the matrix element in the case of the $L_{2,3}$ edges in XRS, including the radial term mentioned above. Of course, the calculation of an XRS $L_{2,3}$ edge and of a XAS K edge involve different initial states and transition operators, but in principle, these two calculations involve the same kind of terms, and thus this chapter, and the two mentioned sections can give a more detailed insight regarding the above discussion.

The solution to this problem caused by the use of the pseudopotentials, is the PAW (Projector-Augmented Wave) method. Introduced by P. E. Blöchl (27), the PAW method allows to reconstruct the final states all electron wave functions ϕ_f (that is to say, obtained by considering all the electrons and not just the valence electrons, and thus, not approximated for $r < r_{cut}$) by applying a linear operator T on the pseudised final states wave functions $\tilde{\phi}_f$, and ultimately allows to write a new expression for the matrix element, $\langle \phi_f | \mathcal{O} | \phi_i \rangle$, which features $\tilde{\phi}_f$, instead of ϕ_f. We briefly describe the method in the rest of this section. The PAW formalism defines the relation between $\tilde{\phi}_f$ and ϕ_f as follows

$$|\phi_f\rangle = T|\tilde{\phi}_f\rangle. \tag{2.43}$$

The linear operator T is defined by Blöchl as

$$T = 1 + \sum_{\boldsymbol{R},n} \left[|\varphi_{\boldsymbol{R},n}\rangle - |\tilde{\varphi}_{\boldsymbol{R},n}\rangle \right] \langle \tilde{p}_{\boldsymbol{R},n}|. \tag{2.44}$$

In this equation, $\boldsymbol{R}$ indicates that the second term of the linear operator T can be considered as a sum of local, atom-centered terms $T_{\boldsymbol{R}_I}$ (each atom position being defined by a specific position vector $\boldsymbol{R}_I$):

$$T = 1 + \sum_{\boldsymbol{R}_I,n} T_{\boldsymbol{R}_I} \tag{2.45}$$

with

$$T_{\boldsymbol{R}_I} = \left[|\varphi_{\boldsymbol{R}_I,n}\rangle - |\tilde{\varphi}_{\boldsymbol{R}_I,n}\rangle \right] \langle \tilde{p}_{\boldsymbol{R}_I,n}|. \tag{2.46}$$

The local terms $T_{\boldsymbol{R}_I}$ only act within an augmentation range, noted $\Omega_{\boldsymbol{R}_I}$. $\varphi_{\boldsymbol{R}_I,n}$ and $\tilde{\varphi}_{\boldsymbol{R}_I,n}$ are called the all electron partial wave functions and the pseudised partial wave functions, respectively. They are chosen as the atomic orbital (and the pseudised partial atomic orbital) for the isolated atom. Outside the augmentation range, the all electron and pseudised partial wave functions are equal. The augmentation region is analogous to the cut-off principle used for the pseudopotentials described earlier, where the all electron wave functions ϕ are equal to the pseudised wave functions $\tilde{\phi}$ outside the cut-off radius, r_{cut}, and different inside (in fact, $\Omega_{\boldsymbol{R}_I}$ and r_{cut} are the same in our case). $\tilde{p}_{\boldsymbol{R}_I,n}$, called projectors, define how the pseudised wave function of the final states $\tilde{\phi}_f$ can be expanded in terms of the pseudised partial wave functions $\tilde{\varphi}_{\boldsymbol{R}_I,n}$:

$$|\tilde{\phi}_f\rangle = \sum_{\boldsymbol{R}_I,n} |\tilde{\varphi}_{\boldsymbol{R}_I,n}\rangle\langle\tilde{p}_{\boldsymbol{R}_I,n}|\tilde{\phi}_f\rangle. \tag{2.47}$$

Because of equation 2.43, $\tilde{p}_{\boldsymbol{R}_I,n}$ can also be defined using

$$|\phi_f\rangle = \sum_{\boldsymbol{R}_I,n} |\varphi_{\boldsymbol{R}_I,n}\rangle\langle\tilde{p}_{\boldsymbol{R}_I,n}|\tilde{\phi}_f\rangle. \tag{2.48}$$

Both equations (2.47 and 2.48) hold inside the augmentation region $\Omega_{\boldsymbol{R}_I}$. In other words, the projectors are such that $\langle\tilde{p}_{\boldsymbol{R}_I,n}|\tilde{\phi}_f\rangle$ are the coefficients of the expansion of $\tilde{\phi}_f$ on the basis composed by each $\tilde{\varphi}_{\boldsymbol{R}_I,n}$. The index n indicates several pieces of information: the quantum orbital numbers l and m, as well as an additional index in case there are several projectors for the same l, m couple. The projectors and the pseudised partial wave functions also satisfy

$$\langle\tilde{p}_{\boldsymbol{R}_I,n}|\tilde{\varphi}_{\boldsymbol{R}'_I,n'}\rangle = \delta_{\boldsymbol{R}_I\boldsymbol{R}'_I,nn'}. \tag{2.49}$$

Thus, thanks to the linear operator T, it is possible to obtain the all electron final state wave functions from the pseudised final state wave functions. More precisely, it is possible to rewrite the matrix element describing the transition from the initial state ϕ_i to the final state ϕ_f needed to model a XAS or XRS spectrum, $\langle\phi_f|\mathcal{O}|\phi_i\rangle$ (where $\mathcal{O}$ is the XAS or XRS transition operator), as explained in (58). In the PAW formalism, we get the final state all electron wave function by applying T to the pseudised final state wave function: $|\phi_f\rangle = T|\tilde{\phi}_f\rangle$. Using this expression of $|\phi_f\rangle$ to rewrite the matrix element $\langle\phi_f|\mathcal{O}|\phi_i\rangle$, we get

$$\begin{aligned}\langle\phi_f|\mathcal{O}|\phi_i\rangle &= \langle\tilde{\phi}_f|\mathcal{O}|\phi_i\rangle + \sum_{\boldsymbol{R}_I,n}\langle\tilde{\phi}_f|\tilde{p}_{\boldsymbol{R}_I,n}\rangle\langle\varphi_{\boldsymbol{R}_I,n}|\mathcal{O}|\phi_i\rangle \\ &\quad - \sum_{\boldsymbol{R}_I,n}\langle\tilde{\phi}_f|\tilde{p}_{\boldsymbol{R}_I,n}\rangle\langle\tilde{\varphi}_{\boldsymbol{R}_I,n}|\mathcal{O}|\phi_i\rangle\end{aligned} \tag{2.50}$$

We should note here that since ϕ_i is localised on a specific atom for which a core level is excited by X-ray photons, the sum should only be evaluated for that precise atom. Moreover, from eq. 2.47, we can see that inside the augmentation region, the first and third term of eq. 2.50 cancel out. From there, we can define a new wave function, noted $\tilde{\phi}_0$

$$|\tilde{\phi}_0\rangle = \sum_n |\tilde{p}_{\boldsymbol{R}_0,n}\rangle\langle\varphi_{\boldsymbol{R}_0,n}|\mathcal{O}|\phi_i\rangle, \tag{2.51}$$

where $\boldsymbol{R}_0$ defines the absorbing (or scattering) atom, and such that the needed matrix element is now rewritten in terms of the pseudised final state wave function $\tilde{\phi}_f$, and not the all electron one, the use of pseudpotential only allowing access to the former:

$$\langle\phi_f|\mathcal{O}|\phi_i\rangle = \langle\tilde{\phi}_f|\tilde{\phi}_0\rangle \tag{2.52}$$

On a final note, it was mentioned earlier that Quantum ESPRESSO is based on periodic boundary conditions. Indeed, the cell chosen to describe the studied material is replicated infinitely by working in the reciprocal space. This, however, poses another problem, as the pseudised final state wave function $\tilde{\phi}_f$ is calculated with a core hole on the absorbing atom, created by removing a core level electron when generating the absorbing atom pseudopotential. This means that because of the periodic boundary conditions, supercells of the materials, rather than the conventional unit cell, must in general be used to isolate the core hole from its replications.

2.2.3 Recursive Lanczos algorithm

The previous sections explained how DFT, thanks to the PAW formalism which was required due to the use of pseudopotentials, allowed calculation of the matrix element $\langle\phi_f|\mathcal{O}|\phi_i\rangle$ needed to calculate the intensity of a XAS or XRS spectrum. However, as shown in eq. 2.3 and 2.5, the squared matrix element is summed over the final states. This can be computationally very expensive, especially for large energy range, which with the need to use supercells to isolate the core hole can become problematic. That is why, in Quantum ESPRESSO, and more precisely in the XSpectra module, the XAS cross section or XRS dynamic structure factor are calculated as a continued fraction, using a recursive method proposed by R. Haydock, V. Heine and M. J.

Kelly (28) and based on the Lanczos algorithm. The method is described precisely in (58).

The problem is first rewritten using the Green operator of the system, $\tilde{G}(E)$

$$\tilde{G}(E) = (E - \tilde{H} + i\gamma)^{-1}, \tag{2.53}$$

where $\tilde{H}$ is the pseudo Hamiltonian of the system, defined by

$$\tilde{H} = T^{\dagger} H T, \tag{2.54}$$

and the energy E is given by $E = E_i + \hbar\omega$. By using the relation

$$\sum_f |\tilde{\phi}_f\rangle \delta(E_f - E) \langle\tilde{\phi}_f| = -\frac{1}{\pi}\mathfrak{Im}[\tilde{G}(E)] \tag{2.55}$$

is it possible to rewrite the sum over the final states of the squared matrix element:

$$\sum_f |\langle\tilde{\phi}_f|\tilde{\phi}_0\rangle|^2 \delta(E_f - E_i - \hbar\omega) = -\frac{1}{\pi}\mathfrak{Im}[\langle\tilde{\phi}_0|\tilde{G}(E)|\tilde{\phi}_0\rangle] \tag{2.56}$$

From there, the lanczos algorithm evaluates $\langle\tilde{\phi}_0|\tilde{G}(E)|\tilde{\phi}_0\rangle$ as a continued fraction. The algorithm sets up a basis where the pseudo Hamiltonian is tridiagonal. This Lanczos basis is created by repeatedly applying the pseudo Hamiltonian to the initial basis vector noted $|u_o\rangle$, defined by

$$|u_o\rangle = \frac{|\tilde{\phi}_0\rangle}{\sqrt{\langle\tilde{\phi}_0|\tilde{\phi}_0\rangle}}, \tag{2.57}$$

and the next iterations of the basis vectors. The recurrence relation is as follows:

$$\tilde{H}|u_i\rangle = a_i|u_i\rangle + b_{i+1}|u_{i+1}\rangle + b_i|u_{i-1}\rangle. \tag{2.58}$$

The real paramaters a_i and b_i are, respectively, the diagonal and non-diagonal elements of the representation of $\tilde{H}$ in the Lanczos basis, that is to say

$$a_i = \langle u_i|\tilde{H}|u_i\rangle \tag{2.59}$$

and

$$b_i = \langle u_{i-1}|\tilde{H}|u_i\rangle = \langle u_i|\tilde{H}|u_{i-1}\rangle. \tag{2.60}$$

This representation of $\tilde{H}$ in the Lanczos basis allows to write $\langle\tilde{\varphi}_{\boldsymbol{R}_0,n}|\tilde{G}(E)|\tilde{\varphi}_{\boldsymbol{R}_0,n}\rangle$ as a continued fraction

$$\langle\tilde{\phi}_0|\tilde{G}(E)|\tilde{\phi}_0\rangle = \frac{\langle\tilde{\phi}_0|\tilde{\phi}_0\rangle}{a_0 - E - i\gamma - \frac{b_1^2}{a_1 - E - i\gamma - \frac{b_2^2}{\cdots}}}, \tag{2.61}$$

which in turn allows evaluating the XAS cross section or the XRS cross section. As the fraction is infinite, a terminator is needed, or in other words, a condition that allows the calculation to stop. If N_c is the number of iterations required for convergence of $\langle\tilde{\phi}_0|\tilde{G}(E)|\tilde{\phi}_0\rangle$, then the coefficients a_i and b_i for subsequent iterations $i > N_c$ are all set equal to a_{N_c} and b_{N_c}, respectively. This allows for an analytical expression of the continued fraction (29). The broadening parameter, γ, which represents the core hole lifetime, has a large impact on the number of iterations required for convergence. However, since the algorithm is based on only evaluating repeatedly the action of the pseudo Hamiltonian on a single vector, it is very cost efficient compared to other operations, like diagonalising a matrix for each final state, for instance, and which would be required to evaluate the sum over the final states involved in the spectrum intensity calculation, without using the continued fraction rewriting.

2.2.4 Case of ultrasoft pseudopotentials

In the two previous sections (2.2.2 and 2.2.3), we explained in detail how to calculate XRS or XAS spectra intensity, from a DFT foundation, and when using pseudopotentials. More specifically, first, section 2.2.2 describes the principle behind the use of pseudopotentials and the PAW formalism used to rewrite the matrix element, involved in the sprectrum intensity calculation, in an expression suitable to the use of pseudopotentials. Section 2.2.3 presents, in a second time, the computationally efficient Lanczos procedure which allows to calculate the spectrum intensity as a continued fraction. The PAW formalism and Lanczos procedure presented in these two sections are developed for a specific kind of pseudopotentials called norm-conserving pseudopotentials. These pseudpotentials are generated such that the norm of the pseudised wave functions is the same as the norm of the corresponding all electron wave functions, hence the name.

However, XSpectra also works with another kind of pseudopotentials, refered to as ultrasoft, designed so the number of plane waves in the basis for the wave functions expansion is reduced compared to norm-conserving pseudopotentials. The norm of the pseudised wave functions is not the same as the corresponding all electron wave functions, contrary to norm-conserving pseudopotentials. Though the use of ultrasoft pseudpotentials allows to reduce computational costs (time consumed and memory), the PAW formalism and Lanczos procedure developed in the two previous sections do not hold for ultrasoft pseudopotentials. The new formulation of the PAW formalism and the Lacnzos procedure suited to ultrasoft pseudopotentials is described in detail in (59). Here (in this section), we briefly present the essential changes necessary to make the PAW formalism and the Lanczos procedure suited the use of ultrasoft pseudopotentials.

When using ultrasoft pseudopotentials, it is usual to define the integrated augmentation charge, noted $q_{bfR,nm}$, as

$$q_{bfR,nm} = \langle \varphi_{\boldsymbol{R},n} | \varphi_{\boldsymbol{R},m} \rangle - \langle \tilde{\varphi}_{\boldsymbol{R},n} | \tilde{\varphi}_{\boldsymbol{R},m} \rangle, \tag{2.62}$$

using all electron and pseudised partial wavefunctions first defined in section 2.2.2. Using the integrated augmented charge, an operator S is defined as

$$S = 1 + \sum_{\boldsymbol{R},m,n} |\tilde{p}_{\boldsymbol{R},n}\rangle \, q_{bfR,nm} \, \langle \tilde{p}_{\boldsymbol{R},m}|. \tag{2.63}$$

Just like for equation 2.44 in section 2.2.2, this sum can be seen as a sum of local, atom-centered terms noted $Q_{\boldsymbol{R}_I}$, each atom being referred to by its specific position vector $\boldsymbol{R}_I$, allowing to write S as

$$S = 1 + \sum_{\boldsymbol{R}_I} Q_{\boldsymbol{R}_I} \tag{2.64}$$

with

$$Q_{\boldsymbol{R}_I} = |\tilde{p}_{\boldsymbol{R}_I,n}\rangle\, q_{bfR_I,nm}\, \langle\tilde{p}_{\boldsymbol{R}_I,m}|. \tag{2.65}$$

The operator S is then used to modify the Lanczos procedure described in section 2.2.3 for norm-conserving pseudopotentials. More specifically, the Green operator, described in the norm-conserving scheme by equation 2.53, is now instead written as, in the ultrasoft scheme

$$\tilde{G}(E) = S^{-1/2} \frac{1}{E - S^{-1/2}\tilde{H}S^{-1/2} - i\gamma} S^{-1/2}, \tag{2.66}$$

where $E = E_i + \hbar\omega$ and $\tilde{H}$ is the pseudohamiltonian defined in equation 2.54. Given this expression of $\tilde{G}(E)$, and using the identity

$$\sum_f |\tilde{\phi}_f\rangle \delta(E_f - E) \langle\tilde{\phi}_f| = \frac{1}{\pi} \lim_{\gamma\to 0} \mathfrak{Im}[\tilde{G}(E)], \tag{2.67}$$

the sum over the final states of the squared matrix element used to calculate the spectrum intensity (given that the matrix element can be written thanks to the use of pseudopotentials as $\langle\phi_f|\phi_0\rangle$), can be written as

$$\sum_f |\langle\tilde{\phi}_f|\tilde{\phi}_0\rangle|^2 \delta(E_f - E) = \frac{1}{\pi} \lim_{\gamma\to 0} \mathfrak{Im}[\langle\tilde{\phi}_0|\tilde{G}(E)|\tilde{\phi}_0\rangle], \tag{2.68}$$

yielding a very similar expression for the sum over the final states of the squared matrix element in the case of norm-conserving pseudopotentials, though it is important to remember that the Green operator's expression is not the same in the norm-conserving and ultrasoft scheme. From there, just like for norm-conserving pseudopotentials, the quantity $\langle\tilde{\phi}_0|\tilde{G}(E)|\tilde{\phi}_0\rangle$ is expressed as a continued fraction thanks to the Lanczos procedure

$$\langle\tilde{\phi}_0|\tilde{G}(E)|\tilde{\phi}_0\rangle = \frac{\langle\tilde{\phi}_0|S^{-1}|\tilde{\phi}_0\rangle}{a_0 - E - i\gamma - \frac{b_1^2}{a_1 - E - i\gamma - \frac{b_2^2}{\cdots}}}. \tag{2.69}$$

Just like for the case of the norm-conserving scheme, the continued fraction is computed thanks to a repeated application of $\tilde{H}$ on Lanczos vectors. The initial Lanczos vector, noted $|u_0\rangle$, is defined as

$$|u_0\rangle = \frac{S^{-1/2}|\tilde{\phi}_0\rangle}{\sqrt{\langle\tilde{\phi}_0|S^{-1}|\tilde{\phi}_0\rangle}}, \tag{2.70}$$

and the recurrence relation giving the next Lanczos vectors is

$$S^{-1/2}\tilde{H}S^{-1/2}|u_i\rangle = a_i|u_i\rangle + b_{i+1}|u_{i+1}\rangle + b_i|u_{i-1}\rangle. \tag{2.71}$$

This time, the a_i and b_i coefficients are defined by the following relations

$$a_i = \langle u_i|S^{-1/2}\tilde{H}S^{-1/2}|u_i\rangle, \tag{2.72}$$

$$b_i = \langle u_i|S^{-1/2}\tilde{H}S^{-1/2}|u_{i-1}\rangle. \tag{2.73}$$

These equations describe a very similar Lanczos process as the one described in the previous section, but where instead of $\tilde{H}$ the representation of $S^{-1/2}\tilde{H}S^{-1/2}$ in the Lanczos basis is considered, and in the definition of the initial Lanczos vector $|u_0\rangle$, $|\tilde{\phi}_0\rangle$ was replaced by $S^{-1/2}|\tilde{\phi}_0\rangle$.

On a final note regarding the ultrasoft scheme, in practice, the Lanczos vectors that are used in XSpectra are not the $|u_i\rangle$ vectors, but instead another of vectors $|t_i\rangle$, obtained by defining $|t_0\rangle$ as

$$|t_0\rangle = S^{1/2}|u_0\rangle, \tag{2.74}$$

and using the recurrence relation

$$\tilde{H}S^{-1}|t_i\rangle = a_i|t_i\rangle + b_{i+1}|t_{i+1}\rangle + b_i|t_{i-1}\rangle. \tag{2.75}$$

This allows for a faster computation of the continued fraction. Indeed, using the $|u_0\rangle$ vectors leads to having to both apply $\tilde{H}$ and multiplying by the $S^{-1/2}$ matrix two times at each step of the Lanczos algorithm to get the coefficients a_i and b_i. On the other hand, by using the $|t_i\rangle$

vectors, the $S^{1/2}$ matrix has to be used only once at the first step to get $|t_0\rangle$. Then, each of the vectors are obtained by the recurrence relation. Though the $|t_i\rangle$ vectors, contrary to the original Lanczos vectors $|u_i\rangle$, are not orthogonal, by definition we have $\langle t_i|S^{-1}|t_j\rangle = \delta_{i,j}$, which means that at each step of the Lanczos algorithm the coefficients needed to compute the continued fraction can be obtained as

$$a_i = \langle\tilde{t}_i|\tilde{H}|\tilde{t}_i\rangle, \tag{2.76}$$

and

$$b_i = \langle\tilde{t}_i|\tilde{H}|\tilde{t}_{i-1}\rangle, \tag{2.77}$$

where the auxiliary vectors $|\tilde{t}_i\rangle$ are defined by

$$|\tilde{t}_i\rangle = S^{-1}|t_i\rangle. \tag{2.78}$$

This means that instead of two multiplications involving the $S^{-1/2}$ matrix, there is now only one multiplication by the S^{-1} matrix for each step (as well as applying $\tilde{H}$ in both cases) of the Lanczos algorithm when using the $|t_i\rangle$ vectors instead of the $|u_i\rangle$ vectors. This unfortunately comes at the cost of additional memory required to store the $|\tilde{t}_i\rangle$ vectors in addition to the $|t_i\rangle$ ones. However, given that the S matrix is of the same order as the $\tilde{H}$ matrix, which dimension is given by the number of plane waves used to expand the wave functions (i.e the energy cut-off, chosen in the input file of XSpectra), the time gained by the reduced computational cost is not negligible.

2.3 Conclusion

In this chapter, the general theoretical framework on which the calculations performed in all the next chapters of this thesis are based on was developed, to give an overview of the approximations and limitations they are subjected to. The first section was focused on briefly presenting the two core level spectroscopies this thesis focuses on, X-Ray Absorption Spectroscopy and X-Ray Raman Scattering. It was highlighted how the two techniques, both relying on the excitation of core level electrons by x-ray photons, could be modelled by calculating their intensity, which could be expressed thanks to Fermi's golden rule, as two similar expressions, respectively the absorption cross section for XAS and the dynamic structure factor for XRS. Both expressions feature a squared transition matrix element, which depends on the XAS or XRS transition operator as well as the initial and excited states involved in the electronic transition caused by the x-ray photon. The next section explains how, from the exact N-body problem, several approximations allowed to develop the Density Functional Theory framework used by the Quantum ESPRESSO suite of codes to perform all calculations featured in this thesis. Moreover, the pseudopotential formalism, allowing to work with a plane wave basis set to develop the wave functions used to describe our system, was presented and explained. The expression of the different ingredients necessary to compute the absorption cross section and the dynamic structure factor was rewritten according to this formalism. Finally, the Recursive algorithm used to efficiently compute the spectrum intensity as a continued fraction was also presented. Additionally, since calculations performed during this thesis made use of ultrasoft pseudopotentials rather than norm conserving ones, related necessary changes to the formalism developed in the previous sections were presented. The expression of the XAS and XRS transition operators were not yet detailed because detailing them at this point would not bring any necessary information needed to understand the theoretical framework hidden behind the calculations presented in the next chapters. However, that is not to say that their expression is irrelevant. Indeed, the decomposition of the calculated XAS and XRS spectra into different multipole contributions, each stemming from a specific kind of electronic transition, is a consequence of the expansion of the XAS and XRS transition operators into several terms. These expressions will be developed later, when necessary to better understand the different calculations and results presented in the next chapters.

3 Assessment of thermal vibration effects on multipolar contributions in XAS and XRS *K* edges

This chapter is dedicated to the assessment of quantum thermal vibrations of the nuclei in materials on the multipole transition channels available to two core level spectroscopies in particular, X-ray Absorption Spectroscopy (XAS) and X-ray Raman Scattering (XRS). Those effects are studied for K edges (excitation of a $1s$ core electron) on the monopole ($1s \rightarrow s$), dipole ($1s \rightarrow p$) and quadrupole ($1s \rightarrow d$) transition channels. This assessment relies on the study of two reference materials: α-Al_2O_3 and the rutile phase of TiO_2. For the former, the Al K edge was measured at room temperature on a powder sample using XRS, while the Ti K edge of the latter was measured using XAS, for different temperatures ranging from 6 to 698K. The second experiment was also designed to more specifically focus on the pre-edge region of the spectrum, and more precisely on the temperature dependence of the anisotropy of the empty $3d$ states of Ti. Indeed, in the specific experimental set-up which will be described later, the anisotropy of the empty $3d$ states of the absorbing Ti atom create signature features in the pre-edge region. This measurement of the Ti K edge of rutile TiO_2 allows to underline the strong effect of temperature on the pre-edge region of a transition metal K edge. This is even more important given how this region of the spectrum is routinely used to determine pieces of information regarding the probed element in a specific sample, such as concentration, valence, or even symmetry, this region being a signature of the environment of the probed sample. To model the thermal vibration effects in core level spectroscopies, a method based on Density Functional Theory is used, consisting in averaging a number of spectra calculated for atomic configurations of the material, where atoms have been moved from their equilibrium positions according to both temperature and vibrational properties of the material (phonons). This method allows to reproduce temperature variations of the different measured spectra with very better agreement than standard calculation processes. However, the finite number of atomic configurations used, though allowing good modelling of thermal vibrations effects on the spectra, also causes a loss of symmetry in the material. As we will explain later, this may lead to unexpected problems when studying and trying to reproduce the angular dependence of a measured spectrum using this method, because the angular dependence of the measured spectrum is dictated by the crystal symmetry of the studied material. A method based on group theory was designed to correct these unexpected problems, allowing to obtain a final calculated spectrum which both include thermal vibration effects (i.e correctly reproduce the temperature dependence of the spectrum) and keep the theoretically expected angular dependence.

3.1 Theoretical elements and method

This section presents general theoretical elements regarding the XRS and XAS spectra calculations as well as how vibrations are taken into account in those calculations.

3.1.1 Standard spectrum calculation

The goal of the following section is to give essential theoretical elements regarding, precisely, the x-ray absorption and x-ray Raman Scattering transition operators, and how they affect the expression of the x-ray absorption absorption cross section and the x-ray Raman scattering dynamic structure factor respectively. More details on both spectroscopies, as well as the theoretical framework used to make calculations, are available in section 2.

3.1.1.1 X-ray Absorption Cross section

In the case of X-ray absorption spectroscopy, The transition operator $\mathcal{O}^{\mathrm{XAS}}$ describing the photon absorption is the sum of the electric-dipole (E1) and electric-quadrupole (E2) transition operators (53), which respectively read:

$$\mathcal{O}^{\mathrm{XAS}}_{\mathrm{dip}} = \hat{\boldsymbol{\varepsilon}} \cdot \boldsymbol{r}\,, \tag{3.1}$$

$$\mathcal{O}^{\mathrm{XAS}}_{\mathrm{quad}} = \frac{\mathrm{i}}{2}\,\hat{\boldsymbol{\varepsilon}} \cdot \boldsymbol{r}\,\boldsymbol{k} \cdot \boldsymbol{r}. \tag{3.2}$$

In those equations, i is the imaginary unit, and $\hat{\varepsilon}$ and $\boldsymbol{k}$ are the polarisation and the wave vector of the incident X-ray beam, respectively. In the case of non-magnetic materials and a linear polarisation of the X-ray beam, the absorption cross section can be written as the sum of the E1 and E2 terms (53). More precisely,

$$\begin{aligned}\sigma(\hbar\omega) &= 4\pi^2\alpha_0\,\hbar\omega \\ &\quad\times \sum_f \left[|\langle f|\hat{\boldsymbol{\varepsilon}} \cdot \boldsymbol{r}|i\rangle|^2 + \frac{1}{4}\,|\langle f|\hat{\boldsymbol{\varepsilon}} \cdot \boldsymbol{r}\,\boldsymbol{k} \cdot \boldsymbol{r}|i\rangle|^2 \right] \\ &\quad\times \delta(E_f - E_i - \hbar\omega)\,, \end{aligned} \tag{3.3}$$

where α_0 is the fine structure constant and $\hbar\omega$ is the energy of the incident X-ray photon. The E1 and E2 terms (respectively on the left and right in the brackets of Eq. 3.3) are governed by different transition rules and give rise to different transition channels. The E1 term stems from dipole transitions, dictated by the $\Delta l = \pm 1$ transition rule, where l is the azimuthal quantum number and Δl describes the evolution of l during the electronic transition provoked by the absorption of X-ray photons (in the case of XRS, the electronic transition is provoked by X-ray photon scattering, of course). For a K edge, since the initial state is described (in our single electron framework) by a $1s$ state, defined by $l_i = 0$, and l has to be positive, we only have the case $\Delta l = 1$. This corresponds to $1s \to p$ electronic transitions. The E2 term stems from quadrupole transitions dictated by the selection rule $\Delta l = \pm 2$, where once again, because for a K edge $l_i = 0$, only the $\Delta l = 2$ case is possible. This corresponds to $1s \to d$ electronic transitions. These E2 transitions mainly contribute to spectral features located in the pre edge region in the case of transition metals such as Ti.

3.1.1.2 X-ray Raman Scattering dynamic structure factor

In the case of XRS, there is an inelastic scattering of the incident X-ray photon. The transition operator describing this inelastic scattering of the photon is given by:

$$\mathcal{O}^{\mathrm{XRS}} = e^{\mathrm{i}\boldsymbol{q}\cdot\boldsymbol{r}}\,, \tag{3.4}$$

where $\boldsymbol{q} = \boldsymbol{k}_{\mathrm{in}} - \boldsymbol{k}_{\mathrm{out}}$ is the scattering vector. $\mathcal{O}^{\mathrm{XRS}}$ can be expanded in terms of spherical Bessel functions j_l and complex spherical harmonics Y_l^m. More details regarding this expansion are given in section 4.1.2. To understand the study presented in this section, it is only relevant to know that this expansion of the XRS transition operator leads to different terms for $\mathcal{O}^{\mathrm{XRS}}$:

$$\mathcal{O}^{\mathrm{XRS}}_{\mathrm{mono}} = j_0(qr)\,, \tag{3.5}$$

$$\mathcal{O}^{\mathrm{XRS}}_{\mathrm{dip}} = j_1(qr)\,4\mathrm{i}\pi \sum_{\lambda=-1}^{1} (-1)^{\lambda} Y_1^{-\lambda}(\hat{\boldsymbol{q}}) Y_1^{\lambda}(\hat{\boldsymbol{r}}), \tag{3.6}$$

$$\mathcal{O}^{\mathrm{XRS}}_{\mathrm{quad}} = -j_2(qr)\,4\pi \sum_{\lambda'=-2}^{2} (-1)^{\lambda'} Y_2^{-\lambda'}(\hat{\boldsymbol{q}}) Y_2^{\lambda'}(\hat{\boldsymbol{r}}). \tag{3.7}$$

This decomposition is important because once again, the different terms represent different transition channels, imposed by the different transition rules specific to each terms. For instance, the monopole and dipole terms are respectively governed by the $\Delta l = 0$ and $\Delta l = \pm 1$ selection rule, respectively. This corresponds, for the monopole and dipole terms, to $1s \to s$ and $1s \to p$ electronic transitions, respectively. However, as shown in Ref. (47), it is safe to neglect the quadrupole contribution to the XRS K edge spectrum of light elements such as Al. From Eq. 3.5 to 3.7, it can be seen that while the monopole term only depends on the norm q of vector $\boldsymbol{q}$, the dipole (and quadrupole) terms depend on both the norm and direction of vector $\boldsymbol{q}$. Any potential angular dependence of the XRS spectrum thus stem from the dipole (and quadrupole) terms. When considering a powder sample, cross-terms cancel and the XRS dynamic structure factor can be written as a sum of the monopole and dipole contibutions (47).

$$S(\boldsymbol{q},\hbar\omega) = \sum_f \left[\left|\langle f|\mathcal{O}^{\mathrm{XRS}}_{\mathrm{mono}}|i\rangle\right|^2 + \left|\langle f|\mathcal{O}^{\mathrm{XRS}}_{\mathrm{dip}}|i\rangle\right|^2\right] \times \delta(E_f - E_i - \hbar\omega), \tag{3.8}$$

where $\hbar\omega$ is the energy transfer taking place during the photon scattering. It should be noted that monopole transitions are forbidden in XAS. Thus, studying the effects of vibrations on both XRS and XAS allows to assess these effects on the monopole, dipole and quadrupole transition channels.

3.1.2 Modelling the effects of thermal quantum vibrations of the nuclei

As was just explained, the intensity of XAS and XRS spectra is calculated using Eq. 3.3 or Eq. 3.8. Chapter two gives the necessary information regarding how these expressions are calculated in the framework of both the DFT and the PAW formalism required by the use of pseudopotentials, which the Quantum ESPRESSO suite of codes is based on. In standard XAS and XRS spectrum calculation using Quantum ESPRESSO, the only required input is the equilibrium cell of the material, as well as pseudopotentials describing all the different chemical species. This standard calculation thus does not consider effects related to cell dynamics, including thermal vibrations of the nuclei.

To take temperature effects into account in the calculation of core-level spectroscopies spectra, a method developed by Nemausat *et al.* (41; 42) is used. The method allows to take thermal quantum vibrations of the nuclei into account, when modelling XAS and XRS spectroscopies, by considering both the finite temperature and the vibrational properties of the material. It was previously used to probe nuclei quantum thermal vibrations in XAS for several light oxides on the one hand, for example in the temperature-dependent measurement of Mg K edge spectra in MgO. On the other hand, it also allowed to study the effects of those vibrations on changes in chemical shifts in NMR (Nuclear Magnetic Resonance) also in the case of light element oxides.

This method consists in calculating the spectrum as an average of a number of configuration spectra, which are themselves calculated for different out of equilibrium atomic configurations of the material. Each of these configurations is generated so that the atoms are moved away from their equilibrium positions according to both the vibrational properties of the studied material and the quantum statistics at a given finite temperature.

The theoretical framework of this model is briefly given in what follows. More information can be obtained in articles detailing studies performed by R. Nemausat (41; 42), as well as his thesis work. In this model, the Born-Oppenheimer approximation is adopted and the total energy of the considered cell of the material is a function of the nuclear positions, and thus depends on which configuration of the material is considered. The configuration of the material is defined by the vector containing the nuclei positions along the three cartesian axis. If the considered cell of the crystal contains N nuclei, this vector then contains $3N$ coordinates. It is convenient to define the collective position vectors, defined as $\bar{\boldsymbol{R}} = (\boldsymbol{R_1}, ..., \boldsymbol{R_N})$. The dynamical properties of the material are given by the corresponding dynamical matrix, whose components read at the Γ point of the first Brillouin zone:

$$D_{IJ}^{\alpha,\beta} = \frac{1}{\sqrt{M_I M_J}} \frac{\partial^2 E(\bar{\boldsymbol{R}})}{\partial u_I^\alpha u_J^\beta}\bigg|_{\boldsymbol{u}=0} \tag{3.9}$$

where M_I is the mass of the I_{th} atom, $E(\bar{\boldsymbol{R}})$ is the energy of the considered cell configuration, and $\boldsymbol{u}_I$ is the displacement from its equilibrium position $\boldsymbol{R}_{I,eq}$ of the I_{th} nucleus, such that the position of the I_{th} atom can be written as $\boldsymbol{R}_I = \boldsymbol{R}_{I,eq} + \boldsymbol{u}_I$. α and β simply index ($\alpha = 1..3$, $\beta = 1..3$) the coordinates of the displacement vectors $\boldsymbol{u}_I$. The phonon modes frequencies ω_μ and polarisation vectors $\boldsymbol{e}_{I,\mu}$ can then be obtained from the following relation:

$$\sum_{J=1}^{N} \sum_{\beta=1}^{3} D_{IJ}^{\alpha,\beta} e_{J,\mu}^{\beta} = \omega_\mu^2 e_{I,\mu}^{\alpha} \tag{3.10}$$

where μ indexes the phonon modes, and

$$\sum_{I=1}^{N} |\boldsymbol{e}_{I,\mu}|^2 = 1. \tag{3.11}$$

At a given finite temperature T, the probability $P(\bar{\mathbf{R}})$ of finding the crystal with its nuclei at the positions defined by $\bar{\mathbf{R}}$ (and also used to calculate the phonon properties) is given by

$$P(\bar{\mathbf{R}}) = A\exp\left[-{\sum_{\mu}}' \frac{\left(\sum\limits_{I=1}^{N}\sqrt{M_I}\boldsymbol{e}_{I,\mu}\cdot\boldsymbol{u}_I\right)^2}{2a_\mu}\right] = A\exp\left[-{\sum_{\mu}}'\sum_{\alpha,\beta,I,J}\sqrt{M_IM_J}e^{\alpha}_{I,\mu}e^{\beta}_{J,\mu}u^{\alpha}_{I}u^{\beta}_{J}\right] \tag{3.12}$$

where A is a normalisation constant, ${\sum_{\mu}}'$ is the sum over the $3N-3$ optical phonon modes and

$$a_\mu = \sqrt{\frac{\hbar}{2\omega_\mu}\coth\left(\frac{\beta\hbar\omega_\mu}{2}\right)} \tag{3.13}$$

is the normal length of the μth phonon mode at the T finite temperature. T is represented in Eq 3.13 by the β constant, defined by $\beta = \frac{1}{k_BT}$ with k_B the Botlzmann constant.

Monte Carlo sampling of $P(\bar{\mathbf{R}})$ allows to generate the configurations of the material which are then used to include thermal vibration effects in the spectrum calculation. More precisely, in practice, a set of material configurations defined by $\bar{\boldsymbol{R}}^i$, with i ranging from 1 to N_c with N_c the number of configurations, is generated. They are then used to simulate the nuclei vibrations effects on the observable $O(\bar{\boldsymbol{R}})$. In our case, the observable can be either the X-ray absorption cross section, $\sigma(\omega)$ or the dynamic structure factor $S(\boldsymbol{q},\omega)$. The configurations are generated by generating a set of N_c random Gaussian numbers with unit variance and zero expectation, $\{x^i_\mu\}_{i=1..N_c}$, for each μ phonon mode. The nuclei position vectors are then defined by, for each i_{th} configuration:

$$\boldsymbol{R}^i_I = \boldsymbol{R}^i_{I,eq} + {\sum_{\mu}}' \frac{1}{\sqrt{M_I}}\boldsymbol{e}_{I,\mu}a_\mu x^i_\mu \tag{3.14}$$

At last, the quantum statistical average of O at T is computed according to the following approximation used in other applications before (78; 77):

$$O(T) = \int d\bar{\mathbf{R}} P(\bar{\mathbf{R}}) O(\bar{\mathbf{R}}) \simeq \frac{1}{N_c} \sum_{i=1}^{N_c} O(\bar{\mathbf{R}}^i) \tag{3.15}$$

This procedure is referred to as the Quasi Harmonic Approximation (QHA) procedure in the rest of this chapter, which is the name given to the general method summarised here in (42).

3.2 XRS at the Al *K* edge in corundum (α-Al$_2$O$_3$)

3.2.1 Experimental set up and details

The measure of the Al K-edge XRS spectrum was recorded at room temperature on a powder sample of α-Al$_2$O$_3$ was made available thanks to S. Huotari. The experiment was performed at the ID20 beamline of the European Synchrotron Radiation Facility (ESRF) in Grenoble, France, using the large-solid angle XRS spectrometer.(50) The synchrotron ring was operating at 200 mA and the beam was monochromated by a combination of Si(111) double-crystal cryogenically cooled premonochromator and a Si(311) channel-cut postmonochromator. The total energy resolution was about 0.6 eV. A total of 24 analyzer crystals using the Si(660) reflection were utilized at a mean scattering vector norm of 9.5 Å^{-1}± 0.5 Å^{-1}, a high value enhancing monopole transitions. α-Al$_2$O$_3$ crystallises in the trigonal system, with the space group $R\bar{3}c$.

3.2.2 Computational and calculation details

3.2.2.1 computational details

In this part, general computational and calculation details are given. We used the QHA model described in section 3.1.2 to account for vibrations and their effects on the XRS dynamic structure factor. The phonon calculation was performed on the room temperature cell of α-Al$_2$O$_3$ (75) using the PH code from the QUANTUM ESPRESSO suite of codes.

The PH calculation follows a self-consistent field (SCF) calculation, performed using the pw.x code included in Quantum ESPRESSO, to get charge density and atomic forces in the room temperature cell, using the PW module of Quantum ESPRESSO. The ultrasoft pseudopotentials (68) from the PSLIBRARY (69) used for this calculation were generated in the Rappe, Rabe, Kaxiras and Joannopoulos (70) formalism. The SCF charge density calculation was made in the generalised Gradient Approximation and using the Perdew, Burke and Ernzerhof parametrization (GGA-PBE) (74), with a 4×4×4 k-point grid to sample the Brillouin zone. 50 atomic configurations of the $2{\times}2{\times}2$ α-Al$_2$O$_3$ supercell were generated at room temperature to average the final spectrum, according to results from the phonon calculation, using an external code to Quantum ESPRESSO, courtesy of M. Lazzeri of IMPMC. This number of configurations is found to be enough to converge the final spectrum, whose calculation process is detailed further below. Fig. 3.1 shows this convergence with an increasing number of configurations used to average the final spectrum, from 2 to 50.

The XRS spectra were calculated in two steps. The charge density was first obtained from a SCF charge density calculation, and the spectrum was subsequently calculated using a modified version of the XSpectra module of QUANTUM ESPRESSO, in which the calculation of the XRS dynamic structure factor calculation for K edges was previously implemented (47). The SCF charge density calculations for each configuration were performed at the Γ point, and energy cutoffs were set to 50 Ry and 500 Ry for the electronic wave function and density, respectively. The same pseudopotentials were used as the ones used for the SCF calculation preceding the phonon calculation, however, each XRS K edge spectrum used for the QHA model calculation process was calculated for an excited state with a $1s$ core hole on the absorbing (excited) atom. The $1s$ core-hole was generated in the absorbing Al atom pseudopotential by setting the $1s$ core-orbital occupation to one instead of two. To avoid interaction between the absorbing Al atom core-hole and its replicas during calculation, the absorbing atom was isolated in a supercell. This is why each atomic configuration was generated as a $2{\times}2{\times}2$ supercell of α-Al$_2$O$_3$, containing 80 atoms (2 units of Al$_2$O$_3$ per uni cell). This provided enough distance between the absorbing atom and each of its replicas to minimize the interaction of the core hole and its images on the replicas of the absorbing atom. Fig. 3.2 shows an image of the α-Al$_2$O$_3$ supercell used to perform the SCF charge density calculations. Fig. 3.3 shows a comparison between the equilibrium supercell of α-Al$_2$O$_3$ and one of the configuration of the supercell in which atoms were moved from their equilibrium positions, where the supercells are shown along the 3-fold

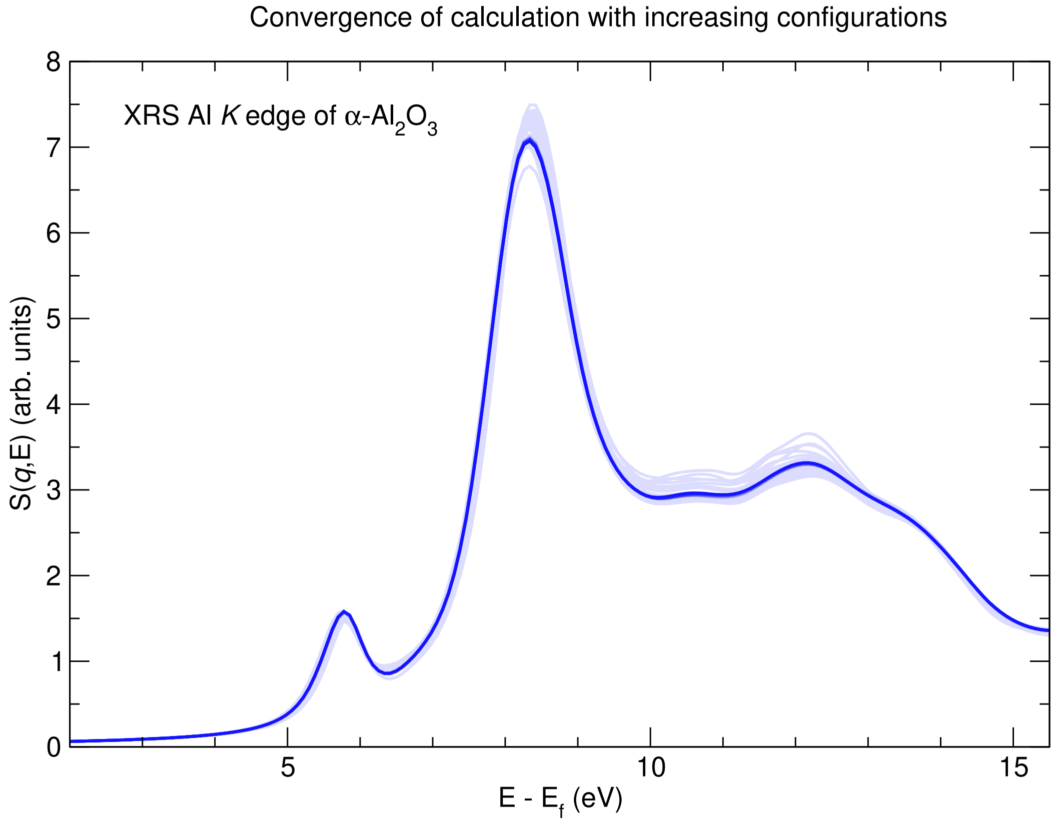

Figure 3.1: Convergence of the calculated Al K edge spectrum of α-Al_2O_3 with an increasing number of configurations. For the spectrum obtained by averaging 50 configurations, the darkest blue color is used. Then progressively lighter blue shades are used until the spectrum obtained by averaging 40 configuration spectra. Then, the lightest blue shade is used for all the spectra obtained by averaging 2 to 39 configurations.

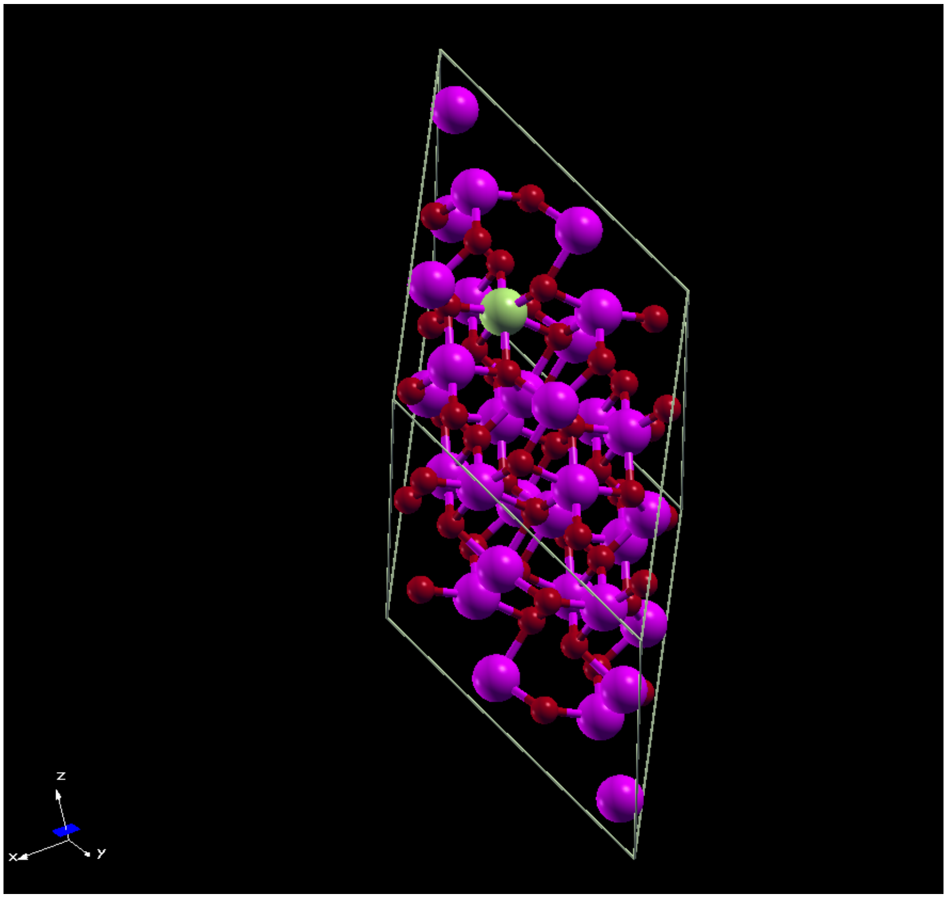

Figure 3.2: Image of the 2×2×2 equilibrium cell at room temperature of Al_2O_3. The oxygen atoms are red and the aluminium atoms are purple. An Al atom was higlighted to show the octahedral coordination with the surrounding O atoms. The image was obtained using XCrysden (96).

symmetry axis.

The XRS K edge spectra were calculated using a 4×4×4 k-points grid to sample each configuration supercell Brillouin zone, a module q of the scattering vector $\boldsymbol{q}$ of 10 Å^{-1} to match the experiment, and a broadening parameter of 0.3 eV. The measurement was done at high q value so that the monopole transition, stemming from $1s \rightarrow s$ electronic transitions, would have a high enough intensity.

Both the monopole and dipole contributions to the spectra were calculated separately. The monopole contribution of the spectrum, as shown before (see section 3.1.2, does not depend on the direction of the scattering vector $\boldsymbol{q}$, but the dipole part does. The isotropic dipole contribu-

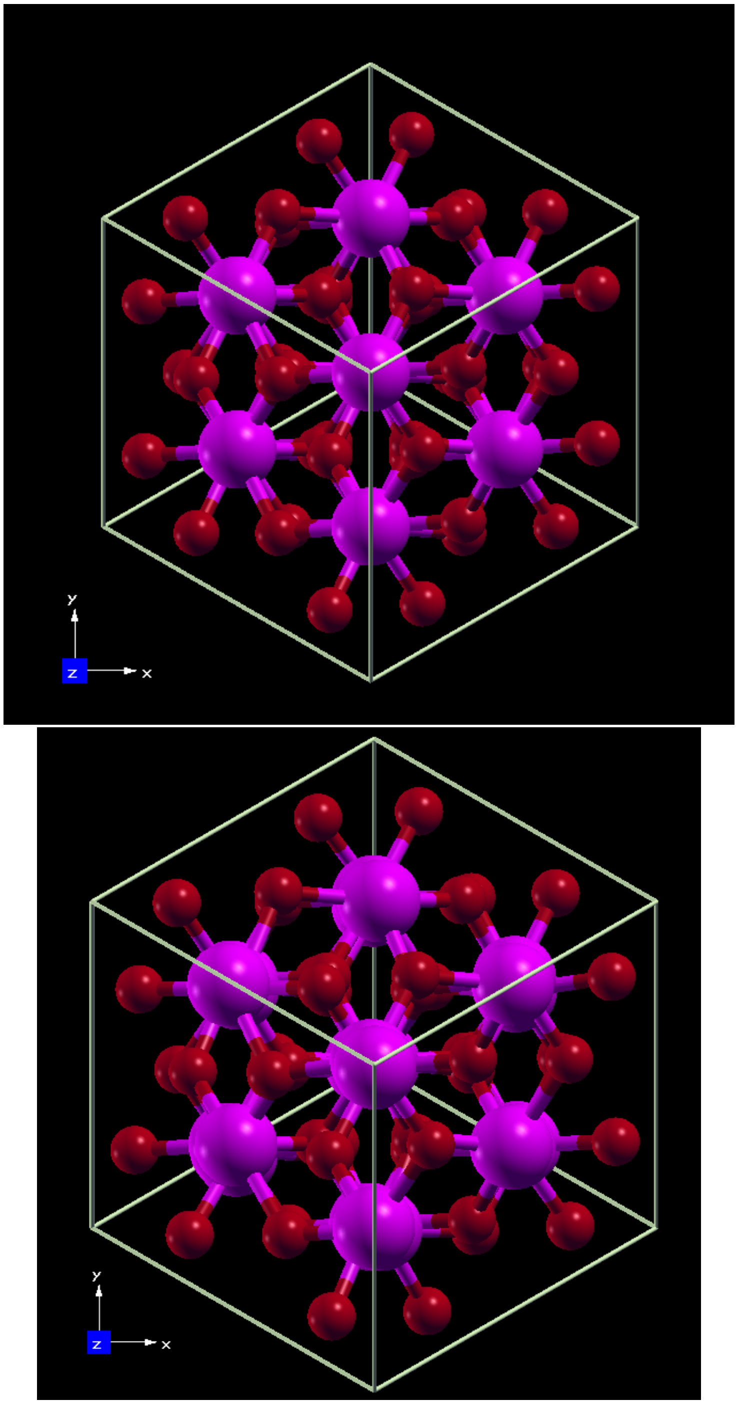

Figure 3.3: Comparison between the equilibrium supercell of α-Al_2O_3 (top) and the supercell representing a configuration used in the QHA model to account for thermal vibration effects in the XRS K edge spectrum (bottom). The supercells are shown along the z axis, which is a 3-fold symmetry axis of the corundum structure.

tion to the spectrum was obtained as an average of the dipole contributions obtained for three directions of $\boldsymbol{q}$, $\hat{q}_x$, $\hat{q}_y$ and $\hat{q}_z$ parallel to the [100], [010] and [001] directions, respectively. All spectra were calculated in the FCH (Full Core-Hole) approximation, where the positive charge on the absorbing atom, caused by the $1s$ core-hole, is compensated in the material by a uniform negative background charge in the supercell. This is equivalent to treating the excited core level electron as promoted to the continuum, and thus missing from the material, hence the name.

A calculation was also performed on the $2{\times}2{\times}2$ supercell of the room temperature α-Al_2O_3 structure. This was done in order to compare the spectrum obtained with atoms fixed at their room temperature equilibrium positions with the one obtained from calculations done according to the QHA model. By doing so, the effects of taking into account thermal vibrations of the atoms, instead of just taking thermal expansion of the cell into account, on the calculated spectrum are emphasised.

3.2.2.2 Realignment and averaging

As mentioned earlier (see section 3.1.2), the final spectrum is obtained by averaging all the spectra calculated for each atomic configuration of the material. However, because only valence electronic states are explicitly calculated in our formalism, the energy scale used for the spectrum and calculated by the SCF calculation is not absolute. Moreover, because each atomic configuration spectrum is obtained from a different configuration of the α-Al_2O_3 supercell, each spectrum is thus calculated on a specific energy scale with a specific energy origin, most likely different from the other spectra energy origin. To make a long story short, each different configuration of the Al_2O_3 supercell can be considered as a different compound. In other words, the different spectra calculated for the i_{th} configuration (dipole and monopole contribution, for every different $\hat{q}$) all having the same energy zero specific to the i_{th} configuration of the supercell.

Thus, to average all the configuration spectra, they must first be realigned on a same energy scale, taken as the energy scale of a chosen reference spectrum. To do so, the so-called ΔSCF (76) procedure is used. A core-level shift (CLS) value is calculated for each configuration spectrum, and then applied to their energy. To calculate the core-level shift value, for each configuration, a SCF calculation must be performed in both the GS (Ground State) and XCH (eXcited core-Hole) approximations. The GS approach is just a ground-state calculation, with no core-hole on the absorbing atom. In the XCH approach, the absorbing atom has a $1s$ core-hole but, unlike the FCH approximation where the $1s$ core electron was promoted to the continuum and the positive charge it left compensated by a background negative charge, the system is still neutrally charged, and the excited core level electron is promoted to the lowest level in the conduction band.

The core-level shift is calculated as such, for the configuration i with regards to reference configuration 0:

$$\Delta^{i}_{\mathrm{CLS}} = (E^{i}_{\mathrm{tot,XCH}} - E^{i}_{\mathrm{tot,GS}}) - (E^{0}_{\mathrm{tot,XCH}} - E^{0}_{\mathrm{tot,GS}}). \tag{3.16}$$

E_{tot} refers to the total energy obtained from the SCF calculations, with additional indexes and exponent specifying, respectively, the approximation the calculation was done in and the configuration it was done for. This core-level shift takes into account the difference in the energy it takes to promote the $1s$ electron to the lowest conduction band, for each different configuration of the material. This way, the specific energy scale of each spectrum can all be realigned to that of the chosen reference spectrum. However, the XSpectra module places the energy zero, by default, at the highest occupied band energy, ϵ_{homo}. The core-level shift value calculated in 3.16 aligns each different spectra with regards to the lowest conduction band energy for each configuration of the material, ϵ_{lumo}. So, for the realignment to make sense, if the keyword xe0 was not set to $\epsilon^{i}_{\mathrm{lumo}}$ manually in the XSpectra calculations so that the energy zero of each spectra was taken as the corresponding $\epsilon^{i}_{\mathrm{lumo}}$, another term has to be added to the core-level shift calculation:

$$\Delta^{i}_{\mathrm{CLS}} = (E^{i}_{\mathrm{tot,XCH}} - E^{i}_{\mathrm{tot,GS}}) - (E^{0}_{\mathrm{tot,XCH}} - E^{0}_{\mathrm{tot,GS}}) + \Delta^{i}_{\mathrm{gap}} \tag{3.17}$$

where

$$\Delta^{i}_{\mathrm{gap}} = (\epsilon^{i}_{\mathrm{lumo}} - \epsilon^{i}_{\mathrm{homo}}) - (\epsilon^{0}_{\mathrm{lumo}} - \epsilon^{0}_{\mathrm{homo}}) \tag{3.18}$$

From then, the realigned spectrum energy of the configuration i, with regards to the reference chosen configuration 0, is defined as

$$E^i_{\mathrm{CLS}} = E^i + \Delta^i_{\mathrm{CLS}}, \tag{3.19}$$

Where E^i is the enegy of the spectrum calculated for the i configuration.

The last step before averaging is simply to interpolate the energies of each spectrum and the energy of a chosen reference spectrum, since after the core-level shift every spectrum now have different energy values. Each contribution (monopole and dipole) were averaged separately as well as summed, so that the final spectrum can also be separated into its different contributions, like any spectrum obtained from conventional calculations. The final spectrum including vibration effects (referred to as average in Fig. 3.4) was then realigned to the experiment spectrum by matching the position of its main edge peak (peak B in Fig. 3.4) The spectrum calculated with atoms fixed at their equilibrium positions was shifted by the same energy, after the ΔSCF procedure was applied to it to rescale it on the same energy scale as the final spectrum including vibration effects.

3.2.3 Results and discussion

In this part, we show the results obtained at the Al XRS K edge of corundum α-Al_2O_3, by comparing experiment and the calculations performed as described above. The decomposition of the calculated spectrum in its monopole and dipole contributions is also provided to assess thermal vibration effects on the two multipole contributions explored by this measurement, the dipole and monopole contributions. PDOS calculations were also performed and are alwo shown later, to help understand the results and confirm and/or complete this assessment.

3.2.3.1 Comparison between calculation and experiment

The comparison of the measurement of the XRS spectrum at the Al K edge in Al_2O_3 with the calculation can be seen on the Fig. 3.4. The measurement, as well as both calculation taking thermal vibrations of atoms using the QHA model and taking only thermal expansion effects

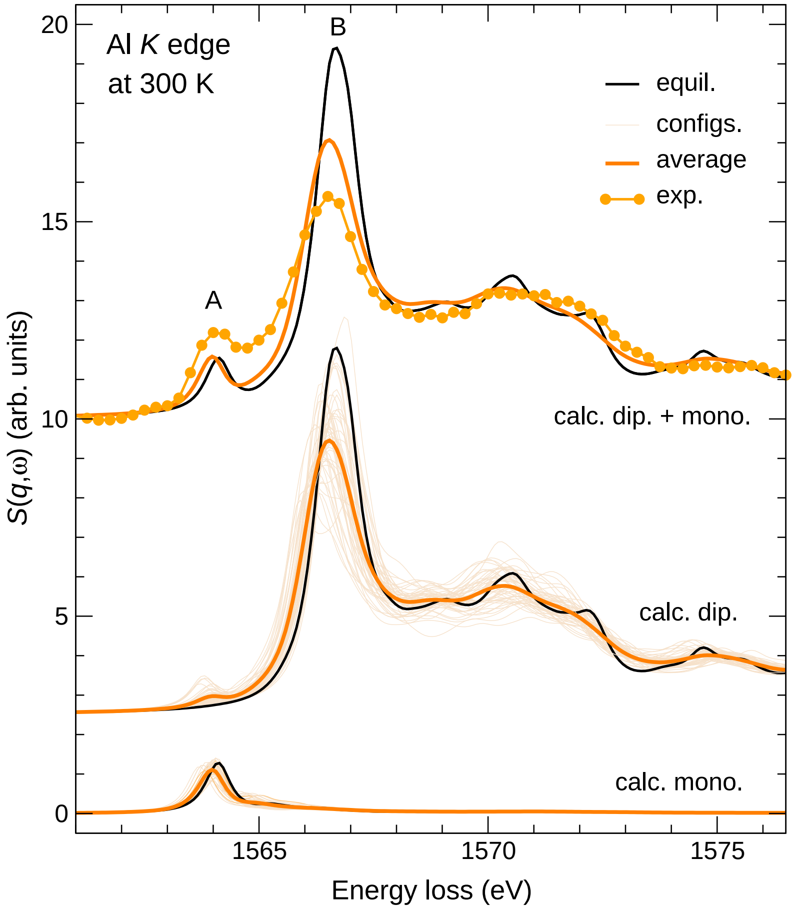

Figure 3.4: Comparison between the measured XRS spectrum at the Al K edge in corundum Al_2O_3 (orange dotted line) and the calculated spectrum. Both calculation taking into account thermal vibration effects (darker orange line) and with atoms fixed at their equilibrium positions (black line) are shown. Calculations were performed at 300K and at a scattering vector $\boldsymbol{q}$ value of 10 Å^{-1}. The monopole and dipole contributions are also separately shown and shifted vertically for more clarity.

into account are shown on the top of the figure. On the same figure, the monopole and dipole contributions were also shown and shifted vertically, bellow the experiment and total calculated spectra for more clarity.

The measured Al K edge XRS spectrum (orange dotted line) consists in two main spectral features, in the form of a pre-edge peak named A and a main edge peak named B, located at respectively 1964 and 1967 eV. The theoretical spectra obtained for the equilibrium cell at room temperature (black line) and using the QHA model (orange line) both reproduce the two features. Explicitly taking thermal vibrations into account however significantly improves the relative intensities of the A and B peaks, because the intensity of the B peak, largely overestimated in the equilibrium cell calculation, is far closer to the measured B peak intensity. The A peak intensity, on the other hand, is almost unaffected by explicitly taking thermal vibrations into account during the spectrum calculation. The spectrum beyond the B peak is also better described using the QHA model rather than the standard equilibrium cell calculation. It should also be noted, that compared to the standard calculation procedure, the QHA model calculation leads to a small shift towards the lower energies of the whole spectrum (both the dipole and monopole contribution) by about 0.3 eV. This shift was also observed, for spectra calculated using the QHA model, during the thesis work of R. Nemausat (41).

3.2.3.2 Results analysis

By comparing the calculation performed using the QHA model and the calculation performed in the standard way, the effect of vibrations can be assessed on both the monopole and dipole contributions. Each individual configuration spectrum can also be seen, both for the total spectrum as well as the monopole and dipole contribution, in light orange. It can already be observed that thermal vibrations of the atoms mainly affect the dipole contribution.

The most obvious difference stems from the dipole contribution to the spectrum and concerns the B peak intensity, or more precisely, the A/B peak intensity ratio. Calculations with atoms fixed at their equilibrium positions (black line) greatly overestimate this ratio, which is far closer to the experiment when looking at the calculation performed using the QHA model. This allows a far better agreement with experiment when using the QHA calculation, than the standard calculation. The more important but less obvious result concerning the dipole contribution is the new contribution to the A peak, which is purely a monopole at equilibrium. The monopole contribution, in contrast, is only very slightly changed by taking into account those vibrations, with a dampening of about 14% only of the A peak feature and no new contributions anywhere in the spectrum. It should also be noted, that compared to the standard calculation procedure, the QHA calculation leads to a small shift towards the lower energies of the whole spectrum (both the dipole and monopole contribution) by about 0.3 eV.

PDOS calculations for the equilibrium supercell, as well as the corresponding spectrum calculation, can be seen on Fig. 3.5. This calculation confirms that at equilibrium, the nature of the A peak is solely monopolar as only the unoccupied s states of the excited (absorbing) Al atom (panel two from the top) are present at its energy, which in turns mean only $1s \rightarrow s$ eletronic transitions can be its origin. A clear correlation between the absorbing atom unoccupied p states (panel four) and the B peak (main edge) feature.

Since the Al site is not centrosymmetric (point group C_3), *local* mixing can occur between the s and p states of the same atom. However, for calculations performed using the cell with atoms at their equilibrium positions, no such hybridisation occurs. Indeed, in Fig. 3.5, the absorbing Al atom, calculations at the equilibrium symmetry show that the unoccupied s and p states are located at different energies, and more precisely, the empty p states are absent at the A peak energies, where only s states are located. Moreover, *non local* s-p hybridisation do not take place either as the s empty states of the excited atom and the p states of the neighbour (unexcited) Al atom are located at different energies. The explanation for the dipole contribution to the A peak when taking thermal vibrations into account is that thermal vibrations enables the *local* s-p mixing to take place and induce a new dipole contribution to the A peak, otherwise (at least for calculations using the equilibrium cell) signature only of the empty s states. This particular result is similar to what was already observed in previous use of this method to study the effect of thermal vibrations on the XAS dipole K edge of oxides of light elements (case of the Mg K edge of MgO, for instance) (41; 42).

This figure, in addition, shows how important the effect of the core-hole on the excited atom is. Indeed, panels three and five can show how different the states projected on the neighbour atom, without any core-hole, are from the states projected on the excited atom, bearing a core-

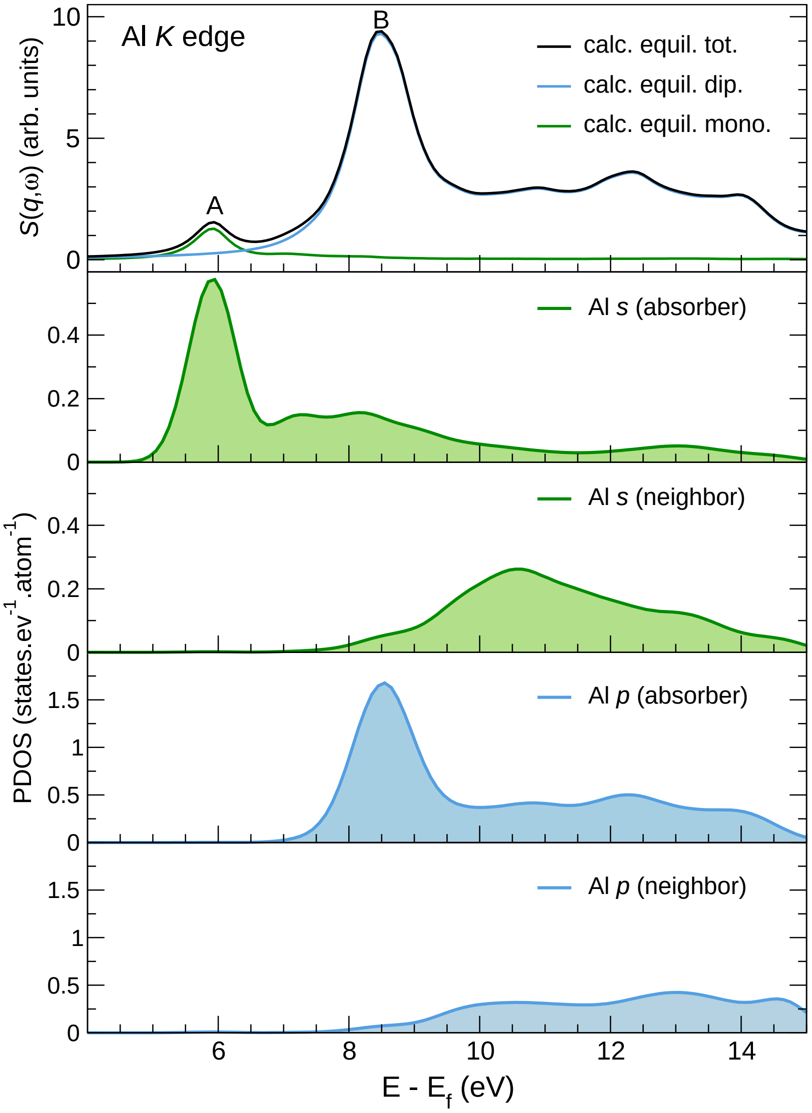

Figure 3.5: Display of calculated density of states projected on the absorbing Al atom, as well as on neighbour Al atoms with no core hole. On the top panel, the equilibrium calculation of the XRS Al K edge of corundum spectrum is shown, as well as its monopole and dipole contribution, respectively in black, green and blue. On the bottom panels, projected density of states (PDOS) are shown. From top to bottom, respectively, the s states projected on the absorbing and neighbour Al atoms, and the p states projected on the absorbing and neighbour Al atom are shown.

hole. The A and B peak placement and intensity, for example (that is to say, the pre-edge and edge regions) are mostly defined by the empty states of the excited atom, which the core-hole presence has significantly pulled towards lower energies, and on a smaller energy range.

3.3 XAS at the Ti *K* edge in rutile $\mathrm{TiO_2}$

3.3.1 Experimental set up and details

Ti K-edge spectra of rutile $\mathrm{TiO_2}$ were measured by S. Collins at the I16 beam line of the Diamond Light Source using a synthetic single crystal. Rutile $\mathrm{TiO_2}$ crystallizes in the tetragonal system with space group $P4_2/mnm$ (n. 136), the 4-fold symmetry axis being parallel to the [001] direction. The experimental setup was designed to study the angular and temperature dependence of the pre-edge region of the Ti K edge by using a resonant elastic x-ray scattering geometry, as shown in Fig. 3.6a. The sample ($10\times10\times1$ mm square) was mounted on the cold finger of a closed-cycle ARS cryofurnace and oriented by x-ray diffraction. Sample rotations about the [001] axis were carried out while maintaining angles of 10 and 70 degrees between the sample surface, and incident and scattered beams, respectively, in the scattering σ polarisation configuration (polarisation vector perpendicular to the scattering plane, which is the plane containing the [001] axis and the wave vector $\boldsymbol{k}$). In this setup geometry, polarisation vector $\hat{\varepsilon}$ was kept normal to the 4-fold symmetry axis of the crystal, so that only electric-quadrupole angular dependence was expected (53). The angular-dependent spectra were recorded for different temperatures ranging from 6 K to 698 K, by detecting the total fluorescence signal using a Pilatus 100K area detector. Fig. 3.6b displays XAS spectra in the pre-edge region recorded at 6 K for a π rotation of azimuthal angle φ. The A1 peak, known to be due to E2 transitions (87), does exhibit the expected $\pi/2$ periodicity (53). The maximum and minimum intensities of peak A1 define the two spectra that are considered in the following. The minimum intensity of the pre-edge first peak is measured when the [100] axis is in the scattering plane. The maximum pre-edge first peak intensity is then obtained when the sample is rotated by 45° around the [001] axis. The wave vector and polarisation vector for which these two cases were measured are denoted ($\hat{\varepsilon_0}$, $\boldsymbol{k_0}$) and ($\hat{\varepsilon_1}$, $\boldsymbol{k_1}$) respectively. Their average and difference are denoted *E2 in-plane mean spectrum* and *E2 in-plane dichroic signal*, respectively, and are the two signals that

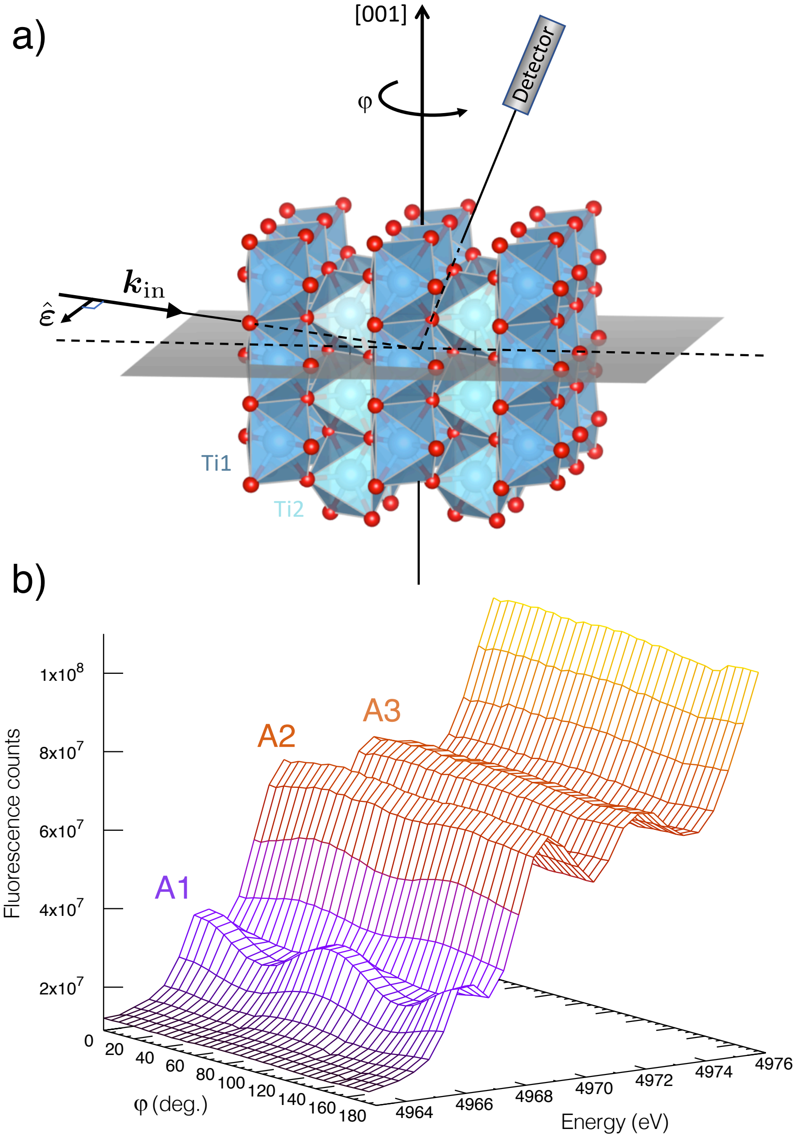

Figure 3.6: a) Experimental setup used to record the polarization-dependent x-ray absorption spectra at the Ti K-edge of TiO_2 rutile, as a function of temperature. As the polarization remains in the plane perpendicular to the crystal [001] direction, in-plane dichroism only arises from electric quadrupole E2 transitions. The image of the supercell of TiO_2 was obtained using Vesta (97). b) Spectra obtained at 6 K for azimuthal angle φ varying from 0 to π. The minimum and maximum intensity of peak A1 identify the two φ values that are considered in this study to define the *in-plane mean spectrum* and *in-plane dichroic signal*.

will be reproduced by calculations. Self-absorption correction were applied using the process described in Ref. (49).

3.3.2 Computational and calculation details

The calculation processes in the case of the XAS Ti K edge of TiO_2 are slightly different from the case of Al_2O_3, because of both the different experimental set up of the experiment, and a problem occurring during phonon calculations. However, the calculations process still mainly follow the QHA model. Details are given in the following sections.

3.3.2.1 Computational details

The phonon calculation caused some problems in the case of the rutile phase of TiO_2. Indeed, when performing phonon calculation using the GGA-PBE approximation, it has been observed (72; 73) that the $\mathrm{A_{2u}}$ phonon mode is predicted to be unstable, leading to discrepancies between the observed and calculated properties of this compound. This led to the choice of performing the SCF calculation required for the phonon calculation in the local density approximation (LDA), using ultrasoft pseudopotentials from the PSLIBRARY also generated in the Rappe, Rabe, Kaxiras and Joannopoulos (RRKJ) formalism. LDA predicts a stable structure of this compound, at a slightly lower equilibrium unit cell volume (and thus lower cell parameters) than observed, and also provides the correct description of its lattice dynamics. The phonon calculation was performed on the fully relaxed unit cell of rutile TiO_2 containing 6 atoms. Thus, thermal expansion effects, unlike the case of Al_2O_3 where the unit cell was describing the room temperature structure, were neglected. This choice was made because, at higher temperatures, some phonon frequencies would be calculated as negative due to the aforementioned problem, leading to imaginary modes. Unlike the case of Al_2O_3, the calculation process thus does not exactly correspond to the QHA model developed by R. Nemausat and used in (41; 42). In the case of TiO_2, temperature is only taken into account when generating the atomic displacement in the different configurations of the fully relaxed TiO_2 supercell. Besides phonon calculations, all SCF charge density calculations were also performed using the fully relaxed supercell of TiO_2. The calculation procedure in this case is thus referred to as the modified QHA model, to remind this main difference with the proper QHA model used in the case of Al_2O_3. The modified QHA model still allows, as detailed later, good reproduction of thermal effects in the Ti K edge spectrum of rutile TiO_2.

A set of 40 configurations of the $2\times2\times3$ supercells of the fully relaxed rutile TiO_2 unit cell were generated at three temperatures, chosen in the same temperature range in which the XAS Ti K edge in TiO_2 was measured: 15K, 300K, 715K (close to the ”low”, ”medium” and ”high” temperatures of the experiment). The atomic configurations were generated as supercells to isolate the core hole from its replicated images. They were not chosen exactly the same as the temperatures of the experiment because in the QHA model, calculations should have been performed on supercells of rutile TiO_2 with experimental cell parameters, measured at finite temperatures. The chosen temperatures are thus temperatures close enough to temperatures of the experiment, for which experimental cell parameters of rutile TiO_2 were available in literature.

The XAS spectra were obtained after a SCF charge density calculation, with energy cutoffs for the electronic wave functions and charge density of 50 Ry and 500 Ry, respectively, performed at the Γ point. The XAS calculations were performed using a $4\times4\times4$ k-points grid to sample the Brillouin zone of each configuration of the TiO_2 supercell and a broadening parameter of 0.7 eV, slightly higher than the value in Tables (51), but found to properly reproduce the pre-edge features of the measured spectrum. The spectra were calculated in the FCH approximation, with a $1s$ core-hole in the excited Ti atom pseudopotential and a background charge in the supercell to compensate the resulting positive charge. This is the same approximation used to model the core hole for the calculation of the XRS spectrum of Al_2O_3 at the Al K edge at room temperature.

The dipole and quadrupole contributions to the spectra were calculated separately. The dipole contribution depends solely on the polarisation vector ($\hat{\varepsilon}$) of the incident x-rays while the quadrupole contribution to the spectrum depends on both the incident polarisation and wave vector $\boldsymbol{k}$. Consequently, the spectra were calculated for two specific couples of $(\hat{\varepsilon}, \boldsymbol{k})$ chosen to match the particular experimental set-up, and supposed to allow reproducing the angular dependence of the XAS Ti K pre-edge that was measured. Moreover, since the measurement was performed on an oriented single crystal, calculations were performed for both sites of the

Ti atom which are, crystallographically speaking, equivalent, but oriented differently in the supercell, and thus yield different signals according to the specific orientation of $(\hat{\varepsilon})$.

3.3.2.2 Final spectrum and angular dependence signal

As for the case of corundum, the use of the modified QHA model implies that a spectrum was calculated for each atomic configuration of the $2\times2\times3$ TiO_2 supercell. This amounted, for each configuration, to a calculation for the two Ti sites, of both contributions, and for both $(\hat{\varepsilon}, \boldsymbol{k})$ couples. The two $(\hat{\varepsilon}, \boldsymbol{k})$ couples, noted $(\hat{\varepsilon}_1, \boldsymbol{k}_1)$ and $(\hat{\varepsilon}_0, \boldsymbol{k}_0)$ were chosen so that they correspond to the polarisation yielding, respectively, the maximum and minimum first pre-edge peak (peak A1 of Fig. 3.6) intensity. Thus, as for the case of corundum, each spectrum calculated for a specific configuration of the TiO_2 supercell has a different energy zero (see section 3.2.2.2 for the explanation in the case of the Al XRS K edge). Moreover, this is also true for the different spectra obtained for the same configuration of the supercell, but with the excited atoms placed at different sites. Thus, a core-level shift step was performed to realign all calculated spectra, i.e calculated for each multipole contribution, for each $(\hat{\varepsilon}, \boldsymbol{k})$ couple, and for each different Ti site, with regards to a single chosen reference spectrum. This means that compared to the case of α-Al_2O_3, the core level shift must be calculated twice for each configuration instead of once, because the core level shift that must be applied to the calculated spectra is different for the two different sites. For the configuration i and for the site j, the core-level shift value is calculated as, with regards to a reference configuration 0 (to be clear, the index 0 actually refers to both a configuration of the supercell and one of the two possible Ti sites chosen for the excited atom)

$$\Delta^{i,j}_{\mathrm{CLS}} = (E^{i,j}_{\mathrm{tot,XCH}} - E^{i}_{\mathrm{tot,GS}}) - (E^{0}_{\mathrm{tot,XCH}} - E^{0}_{\mathrm{tot,GS}}) + \Delta^{i,j}_{gap} \tag{3.20}$$

where

$$\Delta^{i,j}_{gap} = (\epsilon^{i,j}_{\mathrm{lumo}} - \epsilon^{i,j}_{\mathrm{homo}}) - (\epsilon^{0}_{\mathrm{lumo}} - \epsilon^{0}_{\mathrm{homo}}) \tag{3.21}$$

In Eq. 3.20, the total ground-state energy calculated for the supercell configuration i does not show the chosen site j index because, with no core-hole on the excited atom, the calculated total supercell energy does not depend on the chosen site.

As for the case of α-Al$_2$O$_3$, the configuration spectra, for each possible Ti site, is then realigned to the reference spectrum by applying the specific calculated core-level shift value to its energy:

$$E^{i,j}_{\mathrm{CLS}} = E^{i,j} + \Delta^{i,j}_{\mathrm{CLS}}, \tag{3.22}$$

After the shifting process, the energy of each spectrum is interpolated with regards to a reference spectrum energy so that the needed manipulations can be performed on the calculated data. Two kinds of spectrum were measured at the Ti K edge for the different temperatures explored by the experiment (see section 3.3.1 for more details). All calculated spectra were used to model these two different kind of spectra. The calculated *in-plane mean spectrum* was obtained by averaging the contributions obtained from calculations using the two $(\hat{\varepsilon}, \boldsymbol{k})$ couples. The calculated *in-plane dichroic signal* was obtained by subtracting the spectrum obtained using the $(\hat{\varepsilon}_0, \boldsymbol{k_0})$ couple to the spectrum obtained using the $(\hat{\varepsilon}_1, \boldsymbol{k_1})$ couple. The in-plane mean spectrum was then realigned to the experimental spectrum with regards to the position of the A3 peak, and the same energy realignment was then applied to the in-plane dichroic calculated spectrum.

3.3.3 Results for the in-plane mean signal

In this part, the XAS spectrum calculation at the Ti K edge in rutile TiO$_2$ obtained following details given above is compared to the measured spectrum. Both the in-plane mean signal and a close-up of this signal in the pre-edge region are shown. As for for the case of corundum, the different contributions (electric dipole E1 and electric quadrupole E2) to the calculated spectrum are also shown. After comparing experiment and calculations, an analysis of the pre-edge is conducted so that vibrations effects on both contributions to the K XAS spectrum can be properly assessed. The analysis also relies on PDOS calculations, performed on the fully relaxed equilibrium cell of rutile TiO$_2$.

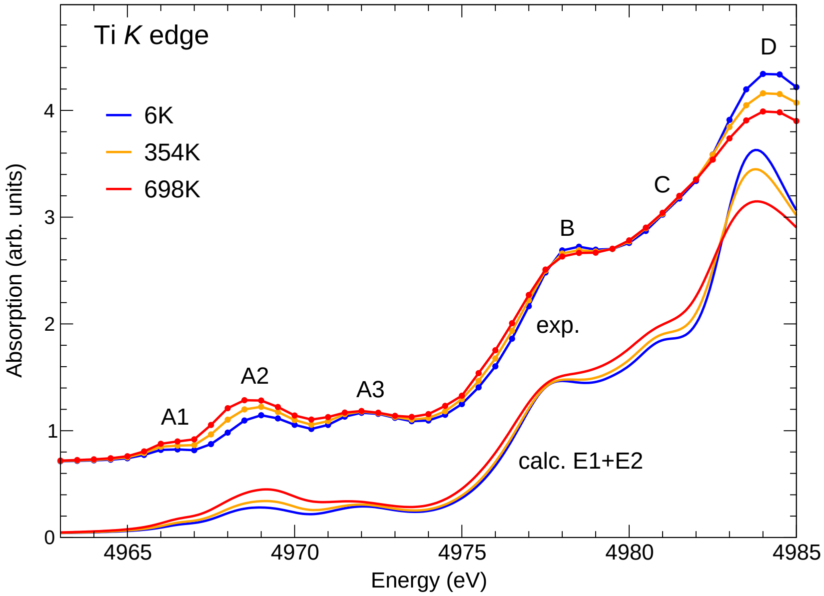

Figure 3.7: Comparison between the experimental and the calculated Ti-K edge in rutile TiO_2, carried out in XAS for three different temperatures. The experimental spectra (full lines with data points) were shifted vertically for clarity. The red, yellow and blue colour refer to measurement or calculation performed at high, medium and low temperatures of the experiment temperature range, respectively.

3.3.3.1 Experiment and calculation comparison

A comparison between the calculated Ti K edge in-plane mean spectra in TiO_2 XAS spectra for three temperatures and the measurement of the same Ti K edge for corresponding temperatures is shown in Fig. 3.7. Fig. 3.8 shows a zoom of this figure in the pre-edge region, which is a signature of the empty $3d$ states for many transition metals, to which titanium belongs.

The three main features of the pre-edge region are well reproduced: the A1, A2 and A3 peaks are present and with rather good relative energy placement. The pre-edge first peak (A1) is, however, reproduced at a slightly higher energy than expected according to the measurement. The main edge region is also well reproduced, with both the main edge (D) and the clear shoulder feature (B) well reproduced in terms of relative energy position (to each other) and relative intensity. It can be noted, however, than the whole calculated spectra is slightly contracted compared to the experiment as the main edge calculated features and placed at lower energies than the measured ones, unlike the pre-edge first peak. The calculated C feature, though, is a little too intense as well as impacted by temperature compared to the experiment.

Concerning the temperature dependence, the variations of the in-plane mean signal spectrum of the Ti K edge as temperature increases reproduced by calculations in the modified QHA model are in good agreement with the experiment. Indeed, the increasing intensity of the pre-edge is well reproduced, with a main effect on the A2 peak, and a lesser effect on the A1 and A3 peak. The effect of temperature on the A3 peak is slightly overestimated compared to experiment however. The decrease of the main edge peak D as temperature increases is also well reproduced. The calculated B feature is unaffected by temperature, which is consistent with the experiment. However, the C feature, seemingly invisible in the experiment, is produced in the calculated spectrum and shown to be increasing as temperature increases. Thermal expansion effects are found to be negligible next to the other effects provoked by the thermal vibrations of the nuclei when trying to reproduce temperature dependence in such calculations. Indeed, Fig. 3.9 shows calculation of the Ti K edge of rutile TiO_2 using the fully relaxed equilibrium cell, but with cell parameters of the experimental TiO_2 structure found for the corresponding temperature in literature (81; 82). This figure, by comparing the calculated spectra obtained for the various different temperatures, and chosen close to temperatures for which the Ti K

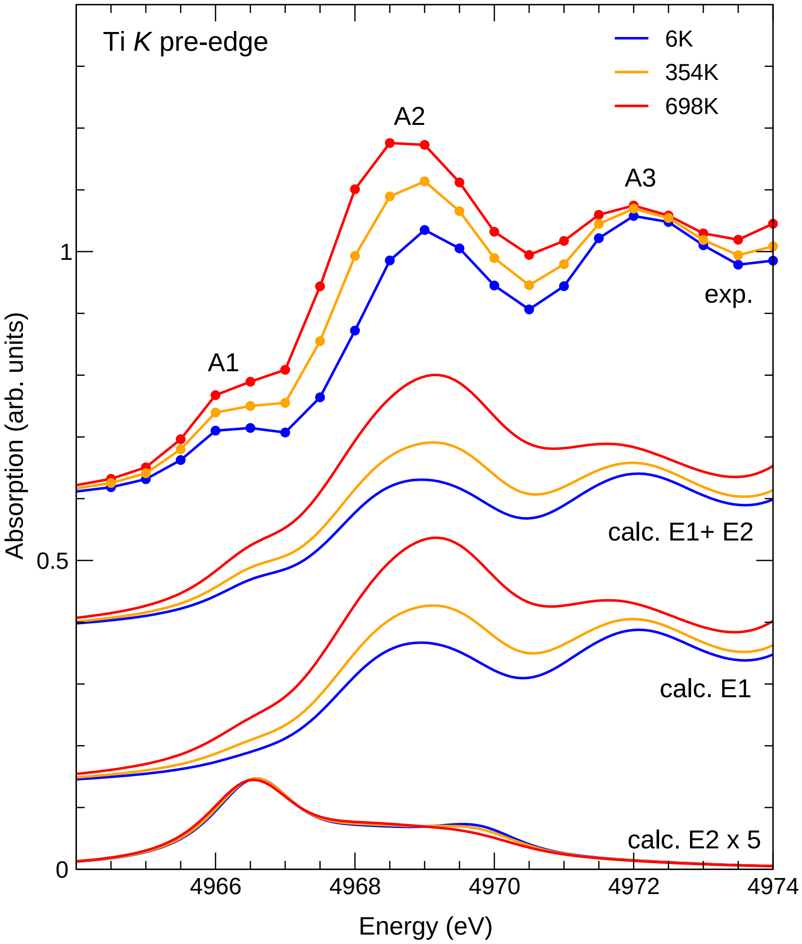

Figure 3.8: Temperature dependence of the Ti-K pre-edge region in rutile TiO_2, obtained from a zoom in the pre-edge region of Fig. 3.7. Calculated E1 and E2 contributions as well as their sum (solid lines), are compared to experiment (solid lines with data points) for three different temperatures represented by different colours. Measured spectra were vertically shifted for clarity.

edge spectra were measured, shows almost no effect from the thermal expansion of the cell parameters. Thus, Fig. 3.7 shows how taking into account thermal vibrations of the atoms in the supercell is of paramount importance to grasp the variations affecting the spectrum as temperature increases. It should be noted, finally, that despite the temperature variations exhibited by the measured Ti K edge are generally very well reproduced, the slight redshift measured for the A2 peak as temperature increases is not reproduced by calculation.

3.3.3.2 Pre-edge analysis and discussion

The pre-edge region of a spectrum, in XAS, gives insight regarding the local and electronic structure of the excited element. In particular, for transition metals such as Ti, the pre-edge region is related to the empty $3d$ states of the studied metal. As shown by Fig. 3.8, the pre-edge peaks A1, A2 and A3 are the results of both the E1 and E2 contributions. More specifically, the A1 and A2 peaks are the result of both the E1 and E2 contributions, that is to say respectively from $1s{\rightarrow}p$ and $1s{\rightarrow}d$ electronic transitions, while the A3 peak stems purely from the E1 contribution, and thus from $1s{\rightarrow}p$ transitions. This is true for all the explored temperatures, and it can be noted that the dipole contribution is strongly affected by the temperature while the quadrupole contribution remains virtually unchanged, for all explored temperatures. Thus, the temperature variation measured for the A1 and A2 peak, as shown by calculation, can be attributed solely to the effects of thermal vibrations on the dipole contribution to the spectrum.

Another important point to know is that the E1 (dipole) transitions have either a *local* or *non-local* character. In more detailed words, the dipole transitions can on one hand involve the empty p states of the excited atom, mixed with its empty $3d$ states, in which case the are referred to as *local*. On the other hand, dipole transitions can also involve the excited atom empty p states, hybridized with the empty $3d$ states of the neighbour Ti atom, in which case they are refered to as *non-local*. This is important because the point group of the Ti atoms, D_{2h}, is centrosymmetric. This forbids on-site $p-d$ mixing, which in turn should make the local E1 transitions described earlier forbidden, and thus invisible in the Ti XAS K edge of rutile TiO_2. However, by taking into account the vibrations, the site symmetry is broken, and the formerly symmetry-forbidden on-site $p-d$ mixing becomes available. This also means that in our case, even though it is not true for the equilibrium structure of rutile TiO_2, the vibration-enabled local

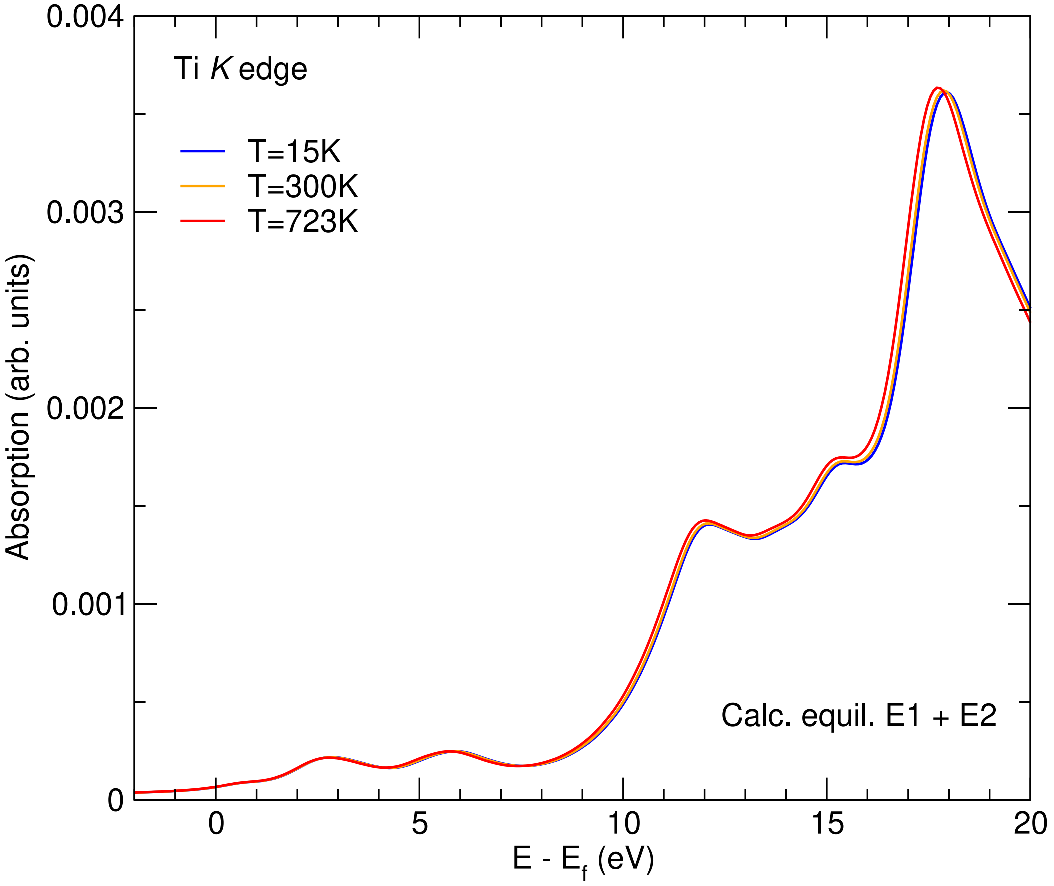

Figure 3.9: Calculation of the Ti K edge spectrum of rutile TiO_2 for the fully relaxed equilibrium cell. However, cell parameters were replaced by cell parameter of experimental rutile TiO_2 structure close to the temperatures of the measured experimental Ti K edge spectra, and to those used for the calculations performed using the modified QHA model shown in Fig. 3.7 and 3.8. These figure thus highlight the almost non-existent effets on the calculated spectra of the thermal expansion of the cell parameters of the TiO_2 equilibrium supercell.

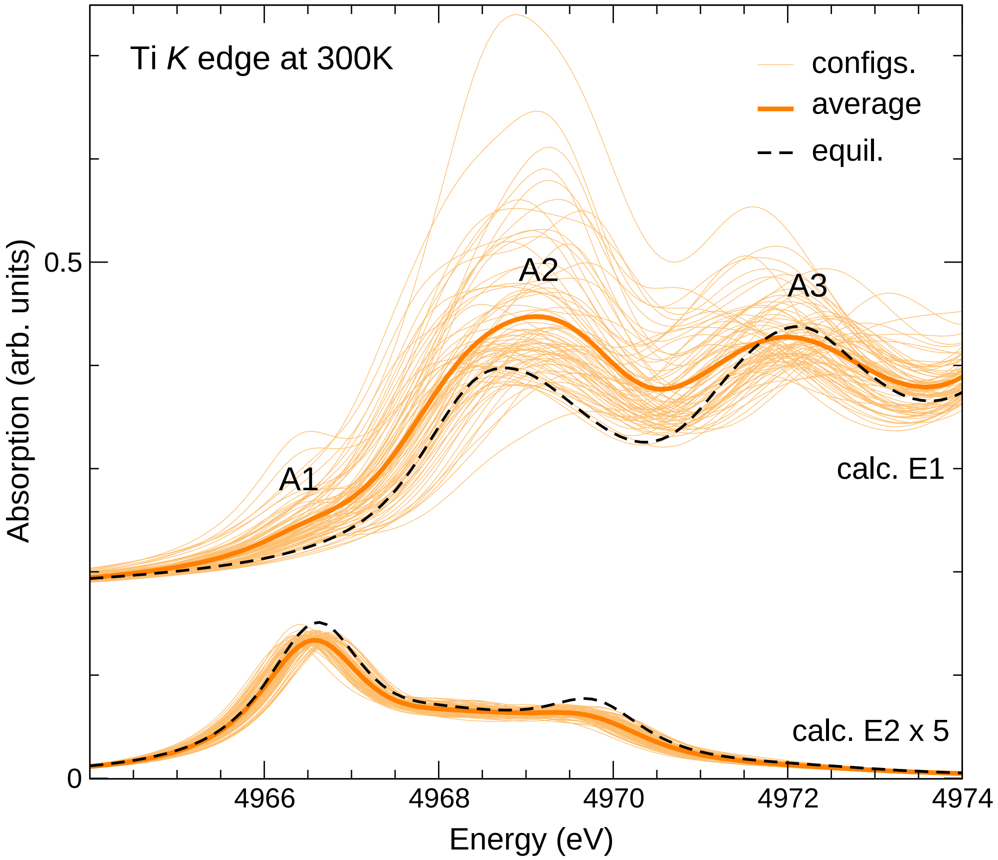

Figure 3.10: Theoretical Ti K pre-edge structures in rutile TiO_2 at 300K: comparison between spectra performed with atoms at equilibrium positions (black dashed line) and obtained when taking vibrations into account (orange thick line). Each configuration spectrum used for averaging is also displayed in light orange. The E1 and E2 contributions are shown separately and shifted vertically for clarity.

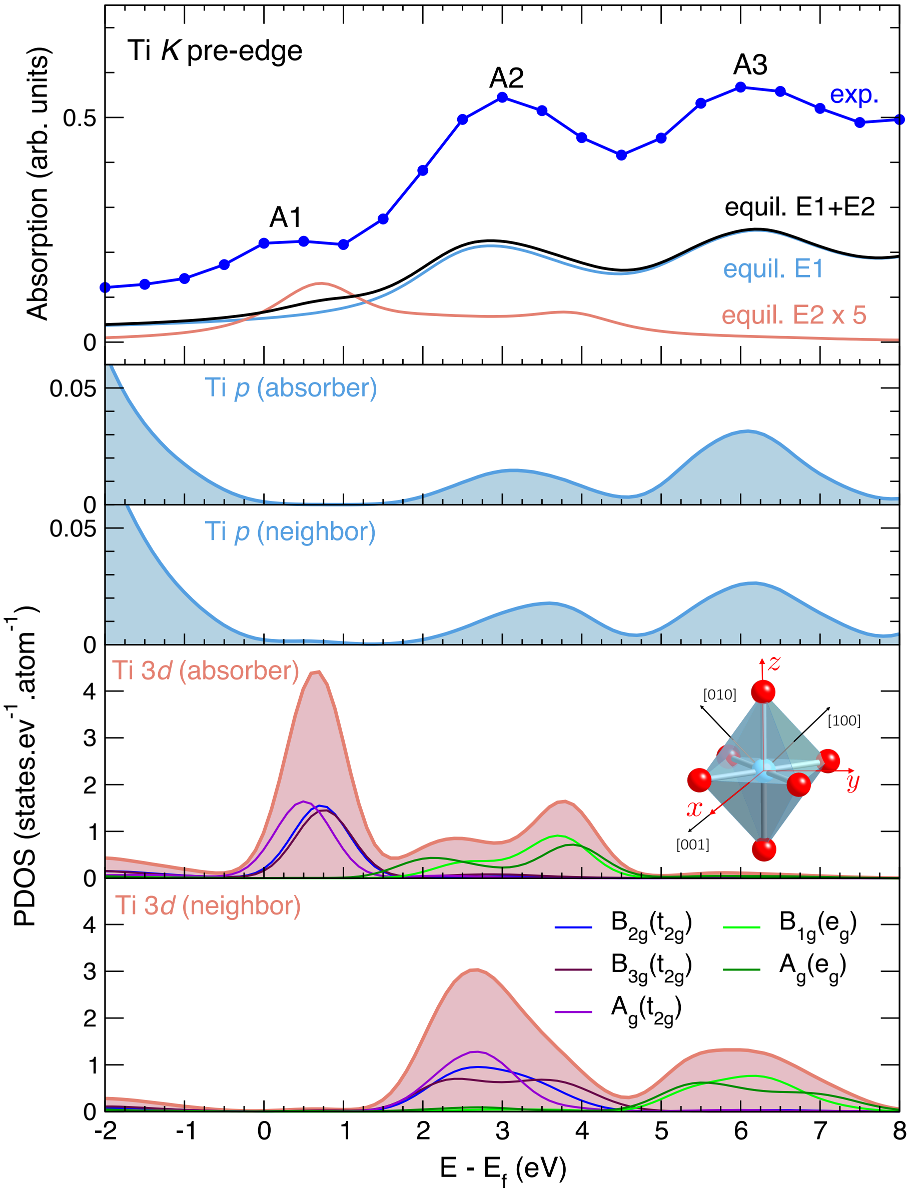

Figure 3.11: Top panel: experimental (6K) and calculated Ti K pre-edge XAS spectra in rutile. Panels below: partial p and $3d$ densities of states projected on absorber Ti and one of its first Ti neigbour. The supercell used for XAS and PDOS calculations was built with atoms at their equilibrium positions, using the fully relaxed crystal structure.

E1 transition can contribute to the pre-edge region of the calculated Ti K edge. Of course, it is expected that these local E1 contributions to the spectrum will be visible for pre-edge feature that were already a signature of the empty $3d$ states of the excited atom, since they are the result of temperature-induced on-site $p - d$ mixing.

As we just explained, the measured temperature variation of the XAS Ti K edge of the rutile phase of TiO_2 mainly come from the dipole contribution to the spectrum (thus, from $1s \rightarrow p$ transitions). It is more precise, however, to say that the temperature variations in fact manly stems from the local E1 contribution to the spectra. It should be noted that these local contributions, by definition, are only featured in the spectra calculated using the modified QHA model, but not in the one calculated following standard procedure and the equilibrium cell (this is true even when taking into account thermal expansion of the cell). .The effects of the vibrations on the multipole contribution to the spectrum as well as the origin of its temperature variations, can be confirmed by using Fig. 3.10. Fig. 3.10 shows a comparison between two calculations, performed with (using the modified QHA model, orange) and without (calculation for the fully relaxed equilibrium cell, black dotted line) vibrations taken into account. First, this figure shows that peak A1, for the spectrum calculated with the equilibrium cell without taking vibrations into account, is a purely quadrupole feature. More precisely, it shows that the A1 peak only presents a dipole contribution when thermal vibrations are taken into account, which enables symmetry-forbidden local E1 contributions to contribute to the spectrum. Moreover, the figure also shows that vibrations also have a significant effect on the A2 peak, and a far weaker effect on the A3, compared to the equilibrium calculation. Thus, by comparing the spectra calculated with and without vibrations taken into account, we can confirm that the effects of vibrations on the dipole contribution, in the pre-edge region, is indeed adding a symmetry-forbidden local E1 contribution, to the peaks that are at least partly quadrupole features. This is shown by how the A1 and A2 peaks, respectively purely and partly quadrupole in nature, are affected more than the A3 peak, which is a purely dipole feature. This is explained by the breaking of Ti site symmetry, which induces on-site $p - d$ mixing and thus new local E1 contributions, but only for pre-edge features already stemming (at least in part) from quadrupole electronic transitions, i.e for the pre-edge features that are a signature of the excited atom empty $3d$ states. The added E1 local contributions to those A1 and A2 peaks increase in intensity as temperature grows, as shown on Fig. 3.8, and create the temperature variation measured by the experiment. Finally, we can confirm by looking at Fig/ 3.10, thanks to the different configuration spectra being displayed for both the E1 and E2 contribution to the spectrum, that the thermal vibrations of the atoms in the supercell mainly affect the E1 contribution while leaving the E2 contribution mainly unchanged, saved for a slight broadening of the features, as was the case of the monopole contribution of the XRS Al K edge of α-$\mathrm{Al_2O_3}$.

Inspection of the projected density of states (PDOS) on the excited Ti atom and one of its neighbour, in the equilibrium cell, confirms those results. Moreover, combined with the described effects of vibrations on the multipole contributions to the spectrum, this inspection also allows to attribute, precisely and to each pre-edge feature, its origin in terms of electronic transitions. PDOS calculation can be seen on Fig. 3.11. The top panel of Fig. 3.11 is a comparison of the pre-edge regions of the equilibrium calculation (no vibrations) and the measurement of Ti K edge un rutile $\mathrm{TiO_2}$, for $\mathrm{T} = 6$ K. Once again, the E1 and E2 contributions are shown, but not shifted vertically. On the panels below, the density of states projected on the empty $3d$ and p states of the excited and one of the first neighbour Ti are shown. For the $3d$ states, a decomposition of the states is also shown, and according to the $\mathrm{D_{2h}}$ symmetry of the Ti site(98). The $3d$ states, in that symmetry, are decomposed into non-degenerate states $\mathrm{A_g}$, $\mathrm{B_{2g}}$ $\mathrm{B_{3g}}$ and the $\mathrm{A_g}$ and $\mathrm{B_{1g}}$ states. The first are referred to as "t_{2g}-like" orbitals and the last two as "e_g-like" orbitals, by reference to the well-known decomposition in the $\mathrm{O_h}$ symmetry. We used this reference because, for convenience, we approximate the Ti site symmetry (corresponding to a distorted centrosymmetric octahedron) to the $\mathrm{O_h}$ symmetry (perfect octahedron), as the t_{2g}-e_g splitting of the $3d$ states, theoretically valid for the $\mathrm{O_h}$ symmetry, is very well known and common. The coordinate system used for the decomposition is shown in the inset of Fig. 3.11. This figure confirms how at equilibrium, the only contribution to the A1 pre-edge feature stems from quadrupole electronic transitions, as only the excited Ti t_{2g}-like states are present in this energy range. This is in agreement with most previous studies of the XAS Ti K pre-edge of $\mathrm{TiO_2}$ (43; 83; 84; 85; 86; 87; 88; 89; 90). Fig. 3.11 also confirms the mixed nature of the A2 pre-edge feature. Indeed, the figure shows that at equilibrium, only the excited Ti atom $3d$ e_g-like states and the neighbour Ti $3d$ t_{2g}-like states are present in the A2 peak energy range, making it the result of both those E2 transitions and non-local E1 transitions For the A3 peak,

Peak labels	Probed states	Electronic transitions
A1	absorbing Ti $3d$ (t_{2g}-like) **absorbing Ti $\mathbf{3d}$ ($\boldsymbol{t_{2g}}$-like)**	E2: $1s \rightarrow 3d$ **E1 *local*: $\mathbf{1s \rightarrow 4p}$ mixed with $\mathbf{3d}$ of absorbing Ti**
A2	absorbing Ti $3d$ (e_g-like) **absorbing Ti $\mathbf{3d}$ ($\boldsymbol{e_g}$-like)** neighboring Ti $\mathbf{3d}$ ($\boldsymbol{t_{2g}}$-like)	E2: $1s \rightarrow 3d$ **E1 *local*: $\mathbf{1s \rightarrow 4p}$ mixed with $\mathbf{3d}$ of absorbing Ti** E1 *non-local*: $\mathbf{1s \rightarrow 4p}$ mixed with $\mathbf{3d}$ of neighboring Ti
A3	neighboring Ti $3d$ (e_g-like)	E1 *non-local*: $1s \rightarrow 4p$ mixed with $3d$ of neighboring Ti

Table 3.1: Nature of the electronic transitions at the origin of the Ti K pre-edge structures in rutile TiO_2. Transitions induced by nuclear thermal fluctuations are indicated in bold.

since only the neighbour Ti $3d$ e_g-like states are present in its energy range, it is confirmed to be purely a purely dipole feature, with a non-local E1 transition at its origin. The effects of the thermal vibrations on the dipole and quadrupole transition channels, which we described earlier, allow to complete the inventory of the empty states represented in each pre-edge features, by adding the symmetry-forbidden local E1 contribution to both the A1 and A2 pre-edge peaks, which also increases as temperature increases. Table 3.1 summarises the precise origin of each pre-edge peak in terms of electronic transitions, and also details which empty states are involved in the transitions, as well as the nature of each electronic transitions (local or non local). The temperature-induced local E1 contributions to the spectrum are added to the contributions already present at equilibrium, and emphasised by using a bold format.

The temperature-induced local E1 contribution to the A1 peak, caused by the mixing of the excited atom empty p states with its t_{2g}-like states, has often been overlooked by previous studies of the pre-edge region of the XAS Ti Kedge of rutile. This can be explained both by how its intensity is low compared to the already present E2 contribution to the A1 peak, and the fact that the temperature-induced $p - d$ mixing is not reproduced vy standard calculation processes. It should be noted however that some studies (91; 92) assign a dipole contribution to the A1 pre-edge peak; however this could be caused by artifacts introduced by the muffin-tin approximation (87). Moreover, a recent in-depth study (93) of the linear dichroism of this edge however, based on high-energy-resolution measurements, confirms the presence of a weak E1 contribution to the A1 peak, although the authors did not relate it explicitly to finite temperature effects.

The most visible temperature-induced local E1 contribution is the one present on the A2 pre-edge peak, this time caused by the mixing of the absorber empty p states with its e_g-like states. It is indeed the A2 peak that shows the most variation in intensity as temperature increases. It should be noted that the the strong temperature dependence variations to states related to the excited $e - g$ like states has also been observed for other Ti compounds, such as SrTiO$_3$ (94) or PbTiO$_3$ (10). Concerning the A2 peak, as mentioned earlier, calculations in the modified QHA model do not manage to reproduce the redshift affecting the measured A2 peak as temperature increases. A qualitative explanation can be given by considering the core-hole treatment in DFT. Indeed, as can be seen in Fig. 3.11, the excited atom bearing the core-hole, compared to the neighbour Ti atom which does not bear one, sees its empty d states placed at lower energies. This is explained by a potential that is more attractive for the $3d$ states because of the core-hole. However, DFT is known to often overestimate the screening of the core-hole by the valence electrons, as was already reported for different transition metals K edges (like the K edge of scandium for example), and appears as the main drawback of the method (43; 95). Because of this problem, the empty $3d$ states of the absorbing atom are not pulled at low enough energies, and thus, the local E1 contribution to the A1 and A2 peaks, caused by the thermal vibrations, and are dependent on the empty $3d$ states of the absorbing atom, end up at higher energies than expected. In particular, for the A2 peak, this causes the E1 local contribution to the A2 peak to be at about the same energies as the non-local E1 contribution to the A2 peak, linked to the energy position of the empty $3s$ t_{2g}-like states of the neighbour Ti atom (cf Fig. 3.11 and the placement of the absorbing atom $3d$ e_g-like states and the neighbour Ti atom $3d$ t_{2g}-like states). The temperature-induced E1 local contribution, which grows as temperature increases, thus grows at higher energies than if the core-hole was a little more attractive, and at the same energy location as the non-local E1 contribution, which does not increase as temperature increases. This is what causes the redshift observed on the A2 peak for the experiment not to be reproduced by calculations in the modified QHA model, even though the other temperature variations of the spectrum are well reproduced. A slightly more attractive core-hole would lower the energy position of the local E1 contribution, which in turn would increase in intensity as temperature increases at slightly lower energies than the non-local E1 contribution, which would allow to restore the redshift as temperature increases.

3.3.4 Angular dependence signal

As mentioned earlier, in the case of the Ti K edge of the rutile phase of TiO_2, the measurement was performed in a very specific set-up that allowed to measure both an in-plane mean signal and the anisotropy of the $3d$ states of the excited Ti atom by measuring an in-plane dichroic signal. In this part, a comparison between the measured in-plane dichroic signal and the calculation performed using the modified QHA model and aiming to reproduce the signal. Additionally, we discuss the fact that the use of atomic configurations to model thermal vibrations effect, while allowing to correctly reproduce temperature variations for the in-plane mean signal, also causes unexpected problems when looking at the angular dependence of the pre-edge region of the Ti K edge.

3.3.4.1 Comparison between first calculations and experiment

We are reminded here that both the in-plane mean and dichroic signals are obtained thanks to the final spectra obtained by using the modified QHA model described earlier. The in-plane dichroic signal, more specifically, is obtained by subtracting the spectrum obtained using the $(\hat{\varepsilon}_0, \boldsymbol{k_0})$ couple to the spectrum obtained using the $(\hat{\varepsilon}_1, \boldsymbol{k_1})$ couple. A comparison of the measured in-plane dichroic signal and the one calculated using the modified QHA model, using 40 atomic configurations of the supercell (20 for each of the two Ti sites) can be seen on Fig. 3.12, and for reference regarding the dichroic signal energy localisation, the in-plane mean signals are shown in dotted lines using a 1/10 scale. The measured in plane dichroic signal is non zero only for the A1 and A2 peaks, which are the only quadrupole peaks (even if only partly in the case of the A2 peak). This is, of course, expected because the experiment was designed so that the measured in plane dichroic signal would represent the anisotropy of the $3d$ states of the excited Ti atom (see section 3.3.1). As a matter of fact, taking into account the crystal symmetry (D_{4h}) and the experimental set-up, the E1 contribution of the in plane dichroic signal is theoretically expected to be zero. This signal is positive for the first peak (by construction) but negative for the second peak; it means that the intensity of the second peak varied in an opposite way to that of the first peak as the sample was rotated by 90°. In other words, while the intensity of the A1 peak decreased, the intensity of the A2 peak increased. The measurement also shows that, as temperature increases, this angular dependence signal slightly decreases.

These results are well reproduced by the calculations in the modified QHA model, when only looking at the E2 component of the calculated in-plane dichroic signal. Indeed, save for a slight shift towards higher energy which is consistent with the slight shift also observed for the calculated in-plane mean signal, the shape of the signal is well reproduced. It is non zero only for the A1 and A2 peaks as measured, and positive for the A1 peak and negative for the A2 peak. The variation of the signal when temperature increases is also well reproduced. However, an unexpected E1 contribution to the signal is also present. It is non zero, and in particular, presents a non negligible feature at the A3 peak energy, where the measurement and the E2 calculated signal are both zero. This signal is both unexpected theoretically according to the symmetry, and not measured by experiment. Thus, it is related to a calculation problem, not yet identified.

First, the hypothesis of a convergence problem was tested. Indeed, as was shown earlier when discussing the in-plane mean signal, individual contributions mainly show variations for the E1 contribution and not the E2 contribution. Thus, at this point, it was possible that for subtle effects (the in-plane mean and dichroic signals are shown simultaneously in Fig. 3.12 but the in-plane mean signal is at a 1/10 scale) to be properly reproduced, and not just the global temperature dependence of the in-plane mean spectrum, more configurations were needed.

3.3.4.2 Convergence of the in-plane dichroic signal

Thus, more configurations were used to generate the in-plane dichroic signal. The goal was to check if the convergence of the E1 contribution to the in-plane dichroic signal to zero was attainable with a reasonable number of atomic configurations, and thus confirming our non-zero E1 contribution problem as a convergence problem. To create more different configurations of the material, the absorbing Ti was placed on the two possible sites, equivalent but oriented differently, in the $2\times2\times3$ supercell of TiO_2. This amounted to 480 possible different configurations of the material (240 per different oriented Ti site). The results of these calculations can be seen on Fig. 3.13. The E1 and E2 contributions as well as their sum is shown in blue and shifted vertically from each other, in shades of blue; The darker the color, the more configurations were

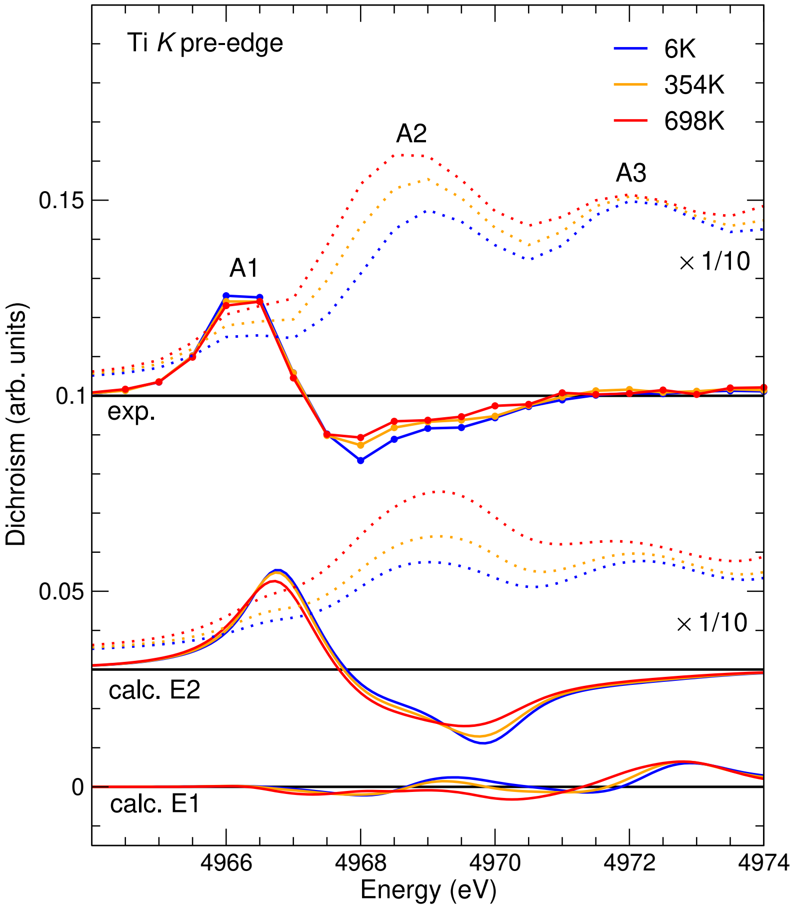

Figure 3.12: Experimental and calculated in-plane dichroic signal (from the spectra calculated using the modified QHA model) of the Ti-K pre-edge region in rutile TiO_2 for three different temperatures. The intensity of the dichroic signal is in the same units as those used for the XAS spectra in Fig. 3.8. As for previous figures, calculations (and its separated contributions) as well as the experiment were shifted vertically for clarity. Zero lines (in black) have been added for measured and calculated dichroism, which have been vertically shifted for clarity. For reference purposes, the XANES spectra are also displayed in dotted lines, but using a factor 1/10.

used for the modified QHA model calculation process described earlier.

This figure shows that taking too few configurations, for this kind of subtle effect related to the angular dependence of the pre-edge region, leads to a non converged signal. As expected, the figure also confirms once again the very low effect of thermal vibrations on the E2 contribution, as all the configuration numbers tested yield the same E2 in-plane dichroic signal. Strikingly, the figure also shows that even after using a significant amount of configurations (given the fact that for each of those an SCF calculation as well as an E1 and E2 spectrum calculation, for each orientation, is needed to get in-plane mean and dichroic signals) seemingly does not lead to a convergence to zero of the E1 contribution, and that is expected theoretically. This leads to a worse agreement with the measured in-plane dichroic signal because the E1 contribution has to be taken into account in the comparison. More precisely, the unexpected non zero E1 contribution creates equally unexpected contributions around the energies of the A2, and more visibly, A3 peaks. Thus, simply reproducing the in-plane dichroic signal using the spectra calculated using the modified QHA model, and more precisely by subtracting the final spectrum obtained using the $(\hat{\varepsilon}_0, \boldsymbol{k_0})$ couple to the final spectrum obtained using the $(\hat{\varepsilon}_1, \boldsymbol{k_1})$ couple, does not allow in our case reproduction of the measured in-plane dichroic signal, using a reasonable number of atomic configurations to average the spectrum.

Consequently, the modified QHA model, when using a reasonable number of configurations to average the final spectrum, does not allow to simultaneously reproduce the correct signal, and the correct temperature dependence of the signal. The breaking of symmetry caused by the modified QHA model allows local $p - d$ mixing to occur on the absorbing Ti atom. This enabled new dipole contributions in the pre-edge region of the in-plane mean spectrum of the Ti K edge, which allowed reproducing the measured data and its temperature dependence with good accuracy. However, this breaking of symmetry also affects the crystal symmetry, and the measured angular dependence of the Ti K edge of rutile TiO_2 is not reproduced by calculation, even when using even a high and beyond reasonable number of configurations. Thus, the problem caused by the use of atomic configurations of the material to model quantum thermal vibration effects goes beyond a simple convergence problem. However, even in temperature experiment, the expected angular dependence of K edges spectra is always observed. Thus, the problem must be solved. To that end, we devised a method to recover the crystal symmetry that

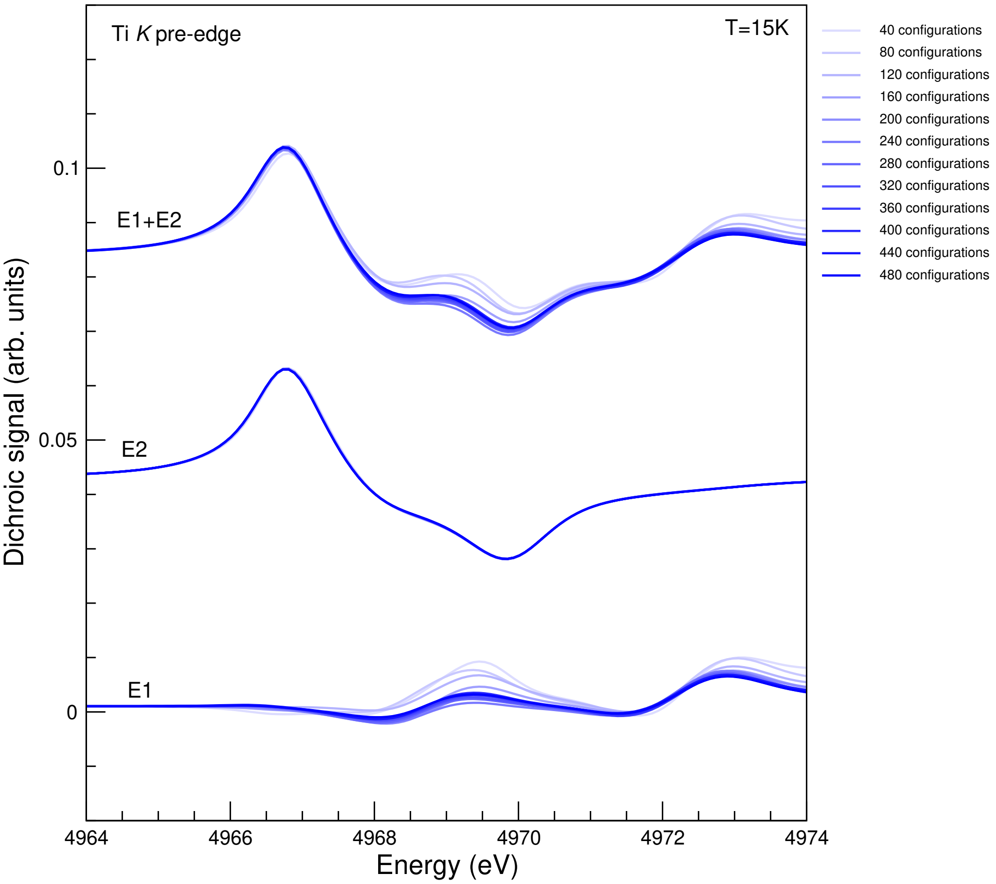

Figure 3.13: Convergence of the calculated in-plane dichroic signal with respect to the number of atomic configurations used. Each configuration number N means N/2 configurations for each of the two differently oriented Ti sites. Once again, the E1 and E2 contributions of the signal, and the signal itself were all shifted for more clarity. The darker the color of the signal, the more configurations were used.

has been lost by the use of atomic configurations, based on group theory. We justify and detail this method in the next section, and use it to correct the angular dependence signal problem, while keeping all previous results and conclusions.

3.3.4.3 Average cross section symmetry properties

In this section, the method used to recover the crystal symmetry lost because of the atomic configurations is justified, then explained in practice. First, we show that the x-ray absorption cross section calculated with the modified QHA model, as an average of configuration cross sections and noted $\sigma_{average}$, must have the same properties as that of the crystal, even when taking into account thermal vibration effects. More precisely, we prove that the average cross section has symmetry properties imposed by the point group of the crystal. This justifies recovering the symmetry of the crystal for the averaged cross section, which seemingly can not be done using a reasonable number of configurations when using the modified QHA model. Then, the procedure followed to actually recover symmetry is explained in details.

First, we recall the necessary theoretical ingredients of the QHA model used to calculate the average cross section (see also section 3.1.2). The crystal is seen as N nuclei of mass M_I and charge q_I and N_e electrons of mass m. The position vectors of the nuclei and electrons are noted, respectively, $\boldsymbol{R_I}$ and $\boldsymbol{r_i}$ ($I = 1, ..., N$ and $i = 1, ..., N_e$). In what follows, to lighten notations, collective coordinates $\bar{\boldsymbol{R}} = (\boldsymbol{R}_1, ..., \boldsymbol{R}_N)$ and $\bar{\boldsymbol{r}} = (\boldsymbol{r}_1, ..., \boldsymbol{r}_{N_e})$ were used. The system is described by wave functions $\Psi(\bar{\boldsymbol{R}}, \bar{\boldsymbol{r}})$ of energy E.

The XAS cross section including thermal vibrations at temperature T can be written as, for incoming x-ray photons of energy $\hbar\omega$:

$$\sigma(\hbar\omega) = 4\pi^2\alpha_0\,\hbar\omega\,\frac{1}{Z}\sum_{m,n,i,j} e^{-E^i_m/k_{\mathrm{B}}T}|\langle\Psi^j_n|\mathcal{O}(\bar{\boldsymbol{r}})|\Psi^i_m\rangle|^2\,\delta(E^j_n - E^i_m - \hbar\omega) \tag{3.23}$$

where α_0 and k_{B} are the fine structure and Boltzmann constants, respectively, and where the partition function Z reads:

$$Z = \sum_{m,i} e^{-E^i_m/k_{\mathrm{B}}T}. \tag{3.24}$$

In Eq. 3.23, $\mathcal{O}(\bar{\boldsymbol{r}})$ is the XAS transition operator, that reads

$$\mathcal{O}(\bar{\boldsymbol{r}}) = \sum_j e^{\mathrm{i}\boldsymbol{k}\cdot\boldsymbol{r}_j} \left(\hbar\hat{\boldsymbol{\varepsilon}} \cdot \nabla_j - \frac{g}{2}\,\boldsymbol{s}_j \cdot (\boldsymbol{k} \times \hat{\boldsymbol{\varepsilon}})\right) \tag{3.25}$$

which, when expanded, gives the electric dipole (E1) and electric quadrupole (E2) terms. The wave functions $\Psi^i_m(\bar{\boldsymbol{R}}, \bar{\boldsymbol{r}})$ are described using the Born-Oppenheimer and harmonic approximations.

In the Born-Oppenheimer approximation, we assume that wave functions $\Psi(\bar{\boldsymbol{R}}, \bar{\boldsymbol{r}})$ can be factorized as, by considering the nuclei and electron coordinates independent:

$$\Psi^i_m(\bar{\boldsymbol{r}}, \bar{\boldsymbol{R}}) \quad = \quad \chi^i_m(\bar{\boldsymbol{R}})\psi_m(\bar{\boldsymbol{r}}; \bar{\boldsymbol{R}}). \tag{3.26}$$

In this equation (Eq. 3.26), the electronic wavefunction $\psi_m(\bar{\boldsymbol{r}}; \bar{\boldsymbol{R}})$ is the solution of Schrödinger equation with nuclei clamped at position $\bar{\boldsymbol{R}}$

$$H_e(\bar{\boldsymbol{r}}; \bar{\boldsymbol{R}})\psi_m(\bar{\boldsymbol{r}}; \bar{\boldsymbol{R}}) = \epsilon_m(\bar{\boldsymbol{R}})\psi_m(\bar{\boldsymbol{r}}; \bar{\boldsymbol{R}}).$$

The electronic Hamiltonian $H_e(\bar{\boldsymbol{r}}; \bar{\boldsymbol{R}})$ is written as

$$H_e(\bar{\boldsymbol{r}}; \bar{\boldsymbol{R}}) = -\frac{\hbar^2}{2m}\sum_{i=1}^{N_e} \Delta_i + V_e(\bar{\boldsymbol{r}}) + V_{eN}(\bar{\boldsymbol{r}}, \bar{\boldsymbol{R}}) + V_N(\bar{\boldsymbol{R}}), \tag{3.27}$$

V_e being the Coulomb potential between the different electrons, V_{eN} the Coulomb potential between nuclei and electrons and V_N the Coulomb potential between the different nuclei.

In the harmonic approximation, the vibrational wavefunctions $\chi^i_m(\bar{\boldsymbol{R}})$ (Eq. 3.26) are the solutions of

$$H_m(\bar{\boldsymbol{R}}, \bar{\boldsymbol{R}}^0)\chi^i_m(\bar{\boldsymbol{R}}) = \left(E^i_m - \epsilon_m(\bar{\boldsymbol{R}}^0)\right)\chi^i_m(\bar{\boldsymbol{R}}), \tag{3.28}$$

where $\bar{\boldsymbol{R}}^0$ are the equilibrium positions of the nuclei for quantum states ψ_m. The hamiltonian

$H_m(\bar{\boldsymbol{R}}, \bar{\boldsymbol{R}}^0)$ reads

$$H_m(\bar{\boldsymbol{R}}, \bar{\boldsymbol{R}}^0) = -\sum_{I=1}^{N} \frac{\hbar^2}{2M_I}\Delta_{\boldsymbol{R}_I} + \frac{1}{2}\sum_{I,J}(\boldsymbol{R}_I - \boldsymbol{R}_I^0)\cdot \frac{\partial^2 \epsilon_m(\bar{\boldsymbol{R}})}{\partial \boldsymbol{R}_I \partial \boldsymbol{R}_J}\Big|_{\bar{\boldsymbol{R}}=\bar{\boldsymbol{R}}^0}(\boldsymbol{R}_J - \boldsymbol{R}_J^0). \tag{3.29}$$

If we assume that the experimental resolution is much larger than the vibrational energies (31), then the final states vibrations can be neglected, and we can focus on the ground state vibrational energies given by solving Eq. 3.28 for $m=0$ only. In this framework, the cross section including vibration effects at finite temperature, $\sigma(\hbar\omega)$ (Eq. 3.23) becomes an average over individual cross sections $\sigma_{\bar{\boldsymbol{R}}}(\hbar\omega)$ calculated for individual configurations of the material (see section 3.1.2 for details):

$$\sigma_{\rm av}(\hbar\omega) = Z^{-1}\sum_i e^{-E_0^i/k_{\rm B}T}\int d\bar{\boldsymbol{R}}\,|\chi_0^i(\bar{\boldsymbol{R}})|^2\,\sigma_{\bar{\boldsymbol{R}}}(\hbar\omega), \tag{3.30}$$

with

$$\sigma_{\bar{\boldsymbol{R}}}(\hbar\omega) = 4\pi^2\alpha_0\,\hbar\omega\sum_f |\langle\psi_f|\mathcal{O}(\bar{\boldsymbol{r}})|\psi_0\rangle|^2\,\delta(\epsilon_f-\epsilon_0-\hbar\omega). \tag{3.31}$$

Now, let us consider the effect of applying an isometry D on the collective coordinates $\bar{\boldsymbol{R}}$ on the average cross section $\sigma_{\rm av}(\hbar\omega)$. The isometry D can always be written as $D\boldsymbol{r} = \mathcal{S}\boldsymbol{r} + \boldsymbol{t}$ for any $\boldsymbol{r}$, and where $\boldsymbol{t}$ is a translation vector and $\mathcal{S}$ a rotation or a roto-inversion. Applying D to $\bar{\boldsymbol{R}}$ in Eq. 3.30 gives:

$$\begin{aligned}\sigma_{\rm av}(\hbar\omega) &= Z^{-1}\sum_i e^{-E_0^i/k_{\rm B}T}\\ &\quad\times\int d\bar{\boldsymbol{R}}\,|\chi_0^i(D\bar{\boldsymbol{R}})|^2\,\sigma_{D\bar{\boldsymbol{R}}}(\hbar\omega),\end{aligned} \tag{3.32}$$

where we used $dD\bar{\boldsymbol{R}} = d\bar{\boldsymbol{R}}$ because isometries conserve volume. As we can see, both the configuration cross section $\sigma_{D\bar{\boldsymbol{R}}}(\hbar\omega)$ as well as the ground state vibrational wavefunction $\chi_0^i(D\bar{\boldsymbol{R}})$ are affected. We investigate separately both cases.

First, let us investigate what applying D to $\bar{\boldsymbol{R}}$ changes for the configuration cross section

$\sigma_{D\bar{\boldsymbol{R}}}(\hbar\omega)$. Since isometries do not change length and scalar product and since the $V_{eN}(\bar{\boldsymbol{r}}, \bar{\boldsymbol{R}})$ and $V_N(\bar{\boldsymbol{R}})$ Coulomb terms of Eq. 3.27 are functions of length of type $|\boldsymbol{r}_i - \boldsymbol{R}_I|$ and $|\boldsymbol{R}_I - \boldsymbol{R}_J|$, respectively, we can easily show that

$$H_e(\bar{\boldsymbol{r}}; D\bar{\boldsymbol{R}}) = H_e(D^{-1}\bar{\boldsymbol{r}}; \bar{\boldsymbol{R}}). \tag{3.33}$$

The electronic wavefunctions ψ_m satisfy both

$$H_e(\bar{\boldsymbol{r}}; D\bar{\boldsymbol{R}})\psi_m(\bar{\boldsymbol{r}}; D\bar{\boldsymbol{R}}) = \epsilon_m(D\bar{\boldsymbol{R}})\psi_m(\bar{\boldsymbol{r}}; D\bar{\boldsymbol{R}})$$

and

$$H_e(D^{-1}\bar{\boldsymbol{r}}; \bar{\boldsymbol{R}})\psi_m(D^{-1}\bar{\boldsymbol{r}}; \bar{\boldsymbol{R}}) = \epsilon_m(\bar{\boldsymbol{R}})\psi_m(D^{-1}\bar{\boldsymbol{r}}; \bar{\boldsymbol{R}}).$$

Since the two hamiltonians in those equations are identical (cf Eq. 3.33), then we can always order the eigenvalues (as long as they are not degenerate (99)) so that we have

$$\epsilon_m(D\bar{\boldsymbol{R}}) = \epsilon_m(\bar{\boldsymbol{R}}), \tag{3.34}$$

and $\psi_m(\bar{\boldsymbol{r}}; D\bar{\boldsymbol{R}})$ equal to $\psi_m(D^{-1}\bar{\boldsymbol{r}}; \bar{\boldsymbol{R}})$ up to a phase. Using these symmetry properties of the electronic states and eingenvalues, we can now calculate $\sigma_{D\bar{\boldsymbol{R}}}(\hbar\omega)$ starting from Eq. 3.31. We have:

$$\begin{aligned}
& \left|\langle\psi_f(\bar{\boldsymbol{r}}; D\bar{\boldsymbol{R}})|\mathcal{O}(\bar{\boldsymbol{r}})|\psi_0(\bar{\boldsymbol{r}}; D\bar{\boldsymbol{R}})\rangle\right|^2 \delta\big(\epsilon_f(D\bar{\boldsymbol{R}}) - \epsilon_0(D\bar{\boldsymbol{R}}) - \hbar\omega\big) \\
= & \left|\langle\psi_f(D^{-1}\bar{\boldsymbol{r}}; \bar{\boldsymbol{R}})|\mathcal{O}(\bar{\boldsymbol{r}})|\psi_0(D^{-1}\bar{\boldsymbol{r}}; \bar{\boldsymbol{R}})\rangle\right|^2 \delta(\epsilon_f(\bar{\boldsymbol{R}}) - \epsilon_0(\bar{\boldsymbol{R}}) - \hbar\omega) \\
= & \left|\langle\psi_f(\bar{\boldsymbol{r}}; \bar{\boldsymbol{R}})|\mathcal{O}(D\bar{\boldsymbol{r}})|\psi_0(\bar{\boldsymbol{r}}; \bar{\boldsymbol{R}})\rangle\right|^2 \delta(\epsilon_f(\bar{\boldsymbol{R}}) - \epsilon_0(\bar{\boldsymbol{R}}) - \hbar\omega).
\end{aligned} \tag{3.35}$$

To calculate $\mathcal{O}(D\bar{\boldsymbol{r}})$ in Eq. 3.35, we use Eq. 3.25 for the XAS transition operator. In Eq. 3.25, gradient ∇ is translation invariant and $\boldsymbol{t}$ applied on term $e^{i\boldsymbol{k}\cdot\boldsymbol{r}}$ only brings a phase $e^{i\boldsymbol{k}\cdot\boldsymbol{t}}$, which disappears in the modulus in Eq. 3.35.

Then, using the identity

$$\boldsymbol{q} \cdot (\mathcal{S}\bar{\boldsymbol{r}}) = (\mathcal{S}^{-1}\boldsymbol{q}) \cdot \bar{\boldsymbol{r}}, \tag{3.36}$$

and considering both cases $\boldsymbol{q} = \hat{\varepsilon}$ and $\boldsymbol{q} = \boldsymbol{k}$, we obtain the following symmetry property of the configuration cross section:

$$\sigma_{D\bar{\boldsymbol{R}}}(\hbar\omega, \hat{\varepsilon}, \boldsymbol{k}) = \sigma_{\bar{\boldsymbol{R}}}(\hbar\omega, \mathcal{S}^{-1}\hat{\varepsilon}, \mathcal{S}^{-1}\boldsymbol{k}). \tag{3.37}$$

In a second time, we investigate the effect of applying D onto $\bar{\boldsymbol{R}}$ in the $H_0(\bar{\boldsymbol{R}}, \bar{\boldsymbol{R}}_0)$ harmonic nuclear Hamiltonian, defined by Eq. 3.29 for $m = 0$ (vibrations of the ground state only). The invariance of $\boldsymbol{r} \cdot \nabla$ under invertible linear transformations, the translation invariance of $\boldsymbol{R}_I - \boldsymbol{R}_I^0$ and ∇, and Eq. 3.34 imply

$$H_0(D\bar{\boldsymbol{R}}, D\bar{\boldsymbol{R}}_0) = H_0(\bar{\boldsymbol{R}}, \bar{\boldsymbol{R}}_0), \tag{3.38}$$

for any isometry D. If, moreover, D is a symmetry element of the space group of the crystal, then we have $D\bar{\boldsymbol{R}}_0 = \bar{\boldsymbol{R}}_0$ and, as a consequence, Eq. 3.38 becomes:

$$H_0(D\bar{\boldsymbol{R}}, \bar{\boldsymbol{R}}_0) = H_0(\bar{\boldsymbol{R}}, \bar{\boldsymbol{R}}_0). \tag{3.39}$$

This means that $\chi_0^i(\bar{\boldsymbol{R}})$ and $\chi_0^i(D\bar{\boldsymbol{R}})$ are eigenstates of the same Hamiltonian and, if they are non-degenerate, $\chi_0^i(D\bar{\boldsymbol{R}})$ and $\chi^i(\bar{\boldsymbol{R}})$ are equal up to a phase:(101)

$$\left|\chi_0^i(D\bar{\boldsymbol{R}})\right|^2 = \left|\chi_0^i(\bar{\boldsymbol{R}})\right|^2. \tag{3.40}$$

Besides, $\chi_0^i(D\bar{\boldsymbol{R}})$ and $\chi_0^i(\bar{\boldsymbol{R}})$ have the same energy E_0^i, which also means that they have the same Boltzmann weight in Eq. 3.23.

We can now draw a conclusion regarding the average XAS cross section $\sigma_{av}(\hbar\omega)$ calculated using the (modified) QHA model, and defined in Eq. 3.30, when D is applied to $\bar{\boldsymbol{R}}$ and if D is a symmetry operation of the crystal space group. Using the symmetry properties described in equations 3.40 and 3.37, we can now see that

$$\int d\bar{\boldsymbol{R}}\,|\chi_0^i(D\bar{\boldsymbol{R}})|^2\,\sigma_{D\bar{\boldsymbol{R}}}(\hbar\omega,\hat{\boldsymbol{\varepsilon}},\boldsymbol{k}) = \int d\bar{\boldsymbol{R}}\,|\chi_0^i(\bar{\boldsymbol{R}})|^2\,\sigma_{\bar{\boldsymbol{R}}}(\hbar\omega,\mathcal{S}^{-1}\hat{\boldsymbol{\varepsilon}},\mathcal{S}^{-1}\boldsymbol{k}), \tag{3.41}$$

where S is the rotation or roto-inversion part of D, that is to say, a symmetry operation of the crystal point group.

Using the new Eq. 3.41, in Eq. 3.32 we finally obtain

$$\sigma_{\mathrm{av}}(\hbar\omega,\hat{\boldsymbol{\varepsilon}},\boldsymbol{k}) = \sigma_{\mathrm{av}}(\hbar\omega,\mathcal{S}^{-1}\hat{\boldsymbol{\varepsilon}},\mathcal{S}^{-1}\boldsymbol{k}). \tag{3.42}$$

In other words, the average cross section, which takes quantum thermal effects of the nuclei into account in the (modified) QHA model framework, has the same angular dependence (i.e same symmetry properties) as the cross section calculated with nuclei at their equilibrium positions. That is to say that we managed to prove that even though quantum thermal vibrations are into play, the average cross section calculated using the (modified) QHA model must keep the angular dependence of the equilibrium cross section. This justifies the method described thereafter aiming to recover the equilibrium cross section angular dependence, that cannot be obtained using a reasonable number of atomic configurations.

3.3.4.4 Recovering the cross section symmetry

In the previous section, we justified how the average cross section $\sigma_{av}(\hbar\omega)$ calculated using the (modified) QHA model, should have the same symmetry properties as the cross section calculated with atoms at their equilibrium positions, which is dictated by the crystal symmetry. As a reminder, $\sigma_{av}(\hbar\omega)$ is calculated by averaging a number of cross sections, each calculated for a configuration of the material generated for a finite temperature, and where atoms were moved from their equilibrium positions according to both the finite temperature and vibrational properties of the material calculated beforehand. We also showed earlier that, using a reasonable number of atomic configurations, whereas temperature effects could be reproduced, accurately reproducing expected angular dependence, especially for the dipole contribution to the signal, seemed out of reach. We now explain the method used to manually recover the symmetry properties expected for the average cross section $\sigma_{av}(\hbar\omega)$, and thus the correct angular dependence.

To recover the angular dependence, we used a method based on group theory. To sum it up, calculations using the modified QHA model calculations for the $(\hat{\varepsilon}_0, \boldsymbol{k}_0)$ and $(\hat{\varepsilon}_1, \boldsymbol{k}_1)$ couples are replaced by a linear combination calculations in the modified QHA model, for well chosen new $(\hat{\varepsilon}, \boldsymbol{k})$ couples, which yield the expected expressions of the absorption cross section for the $(\hat{\varepsilon}_0, \boldsymbol{k}_0)$ and $(\hat{\varepsilon}_1, \boldsymbol{k}_1)$ couples under the $\mathrm{D_{4h}}$ symmetry of the $\mathrm{TiO_2}$ crystal in the rutile phase. The method uses the formalism based on spherical tensors operators developped by C. Brouder (53).

To explain the method, we will first consider the simpler case of the electric dipole (E1) part of the absorption cross section. According to ref (53) (Eq. 4.4), in our experimental set up, the cross section calculated for the crystal with atoms at their equilibrium positions, that is to say, with the $\mathrm{D_{4h}}$ symmetry, can be expressed as:

$$\sigma^{\mathrm{E1}}_{\mathrm{D_{4h}},\perp} = \sigma^{\mathrm{D}}(0,0) + 1/\sqrt{2}\,\sigma^{\mathrm{D}}(2,0). \tag{3.43}$$

Note that to get this result from Eq. 4.4 from (53), we used pieces of information taken from the experimental set up the measurement was performed in. In ref. (53), $\hat{\varepsilon}$ is given as, in a orthonormal frame bound to the crystal:

$$\hat{\varepsilon} = \begin{pmatrix} \sin\theta\cos\varphi \\ \cos\theta\sin\varphi \\ \cos\theta \end{pmatrix}, \tag{3.44}$$

where θ and φ are the spherical coordinates of $\hat{\varepsilon}$: θ is the angle between $\hat{\varepsilon}$ and the z axis, which corresponds to the [001] four-fold axis of the $\mathrm{TiO_2}$ crystal, and φ the azimuthal angle. In our case, since the polarisation vector is always in the scattering plane and thus perpendicular to the [001] axis (around which the sample is rotating), we used $\theta = \frac{\pi}{2}$ to naturally get Eq. 3.43 from Eq. 4.4 from (53).

In comparison, in the general case of a crystal with no symmetry (corresponding to the situation of each atomic configuration used in QHA calculations (either the modified model or not) where atoms are moved from their equilibrium positions), the cross section instead reads, with θ kept as $\frac{\pi}{2}$ to respect the experimental set up (Eq. 4.7 of ref. (53))

$$\sigma_{\perp}^{\mathrm{E1}}(\varphi) = \sigma^{\mathrm{D}}(0,0) + 1/\sqrt{2}\sigma^{\mathrm{D}}(2,0) - \sqrt{3}\left[\cos 2\varphi\, \sigma^{\mathrm{Dr}}(2,2) + \sin 2\varphi \sigma^{\mathrm{Di}}(2,2)\right]. \tag{3.45}$$

As we can see, the difference between the two cases (Eqs. 3.43 and 3.45) are the terms in brackets. These terms are the ones responsible for the difference between the expected and calculated E1 contributions to the angular dependence signal. Indeed, according to Eq. 3.43, and with the experimental set up taken into account, the E1 contribution to the Ti K edge in the rutile phase of $\mathrm{TiO_2}$ does not change as the angle φ varies (i.e when the sample rotates around the [001] axis). It follows that E1 contribution to both the measured in-plane dichroic signal, and the calculated in-plane dichroic signal obtained by standard calculation process (single equilibrium supercell), must be zero (see section 3.3.1 for more details). On the contrary, in the general case corresponding to the atomic configurations, calculating the in-plane dichroic signal does not yield a 0 signal:

$$\begin{aligned} \sigma_{\perp}^{\mathrm{E1}}(\hat{\varepsilon}_1) - \sigma_{\perp}^{\mathrm{E1}}(\hat{\varepsilon}_0) &= \sigma_{\perp}^{\mathrm{E1}}(\varphi_{\hat{\varepsilon}_1}) - \sigma_{\perp}^{\mathrm{E1}}(\varphi_{\hat{\varepsilon}_0}) \\ &= \sqrt{3}\left[\sigma^{\mathrm{Di}}(2,2) - \sigma^{\mathrm{Dr}}(2,2))\right]. \end{aligned} \tag{3.46}$$

The goal here, is to obtain the symmetry properties (i.e the angular dependence) for the average cross section $\sigma_{av}(\hbar\omega)$ (the general case) corresponding to the ones expected for a $\mathrm{D_{4h}}$ symmetry. To do so, instead of performing calculations for the polarisation vectors used in the experimental set up, a little change is needed. This change is of course justified because we proved in the previous section (section 3.3.4.3) that even with the thermal vibrations taken into account in the Quasi Harmonic Approximation, the average cross section must keep the symmetry properties given by the crystal. In the case of the dipole contribution, instead of just $\hat{\varepsilon}_0$ and $\hat{\varepsilon}_1$ used before (and defined in section 3.3.1), we use two other orientations for the polarisation vector, noted $\hat{\varepsilon}_2$ and $\hat{\varepsilon}_3$. They were obtained by a $\frac{\pi}{2}$ rotation of $\hat{\varepsilon}_0$ and $\hat{\varepsilon}_1$, respectively, in the plane perpendicular to the z-axis. This corresponds, in terms of θ and φ, to keep $\theta = \frac{\pi}{2}$ for both $\hat{\varepsilon}_2$ and $\hat{\varepsilon}_3$, and getting the φ values of $\hat{\varepsilon}_2$ and $\hat{\varepsilon}_3$ by adding $\frac{\pi}{2}$ to the φ values of $\hat{\varepsilon}_0$ and $\hat{\varepsilon}_1$, respectively. Using the new polarisation vectors, we manage to recover the expected dipole cross section for a $\mathrm{D_{4h}}$ symmetry, using calculation performed with atomic configurations (no symmetry):

$$\begin{aligned}
1/2\left[\sigma_{\perp}^{\mathrm{E1}}(\hat{\varepsilon}_0)+\sigma_{\perp}^{\mathrm{E1}}(\hat{\varepsilon}_2)\right] &= 1/2\left[\sigma_{\perp}^{\mathrm{E1}}(\varphi_{\hat{\varepsilon}_0})+\sigma_{\perp}^{\mathrm{E1}}(\varphi_{\hat{\varepsilon}_2})\right]\\
&= \sigma^{\mathrm{D}}(0,0)+1/\sqrt{2}\,\sigma^{\mathrm{D}}(2,0)\\
&= \sigma_{\mathrm{D_{4h}},\perp}^{\mathrm{E1}}(\hat{\varepsilon}_0)\\
&= \sigma_{\mathrm{D_{4h}},\perp}^{\mathrm{E1}}, \qquad (3.47)
\end{aligned}$$

and

$$\begin{aligned}
1/2\left[\sigma_{\perp}^{\mathrm{E1}}(\hat{\varepsilon}_1)+\sigma_{\perp}^{\mathrm{E1}}(\hat{\varepsilon}_3)\right] &= 1/2\left[\sigma_{\perp}^{\mathrm{E1}}(\varphi_{\hat{\varepsilon}_1})+\sigma_{\perp}^{\mathrm{E1}}(\varphi_{\hat{\varepsilon}_3})\right]\\
&= \sigma^{\mathrm{D}}(0,0)+1/\sqrt{2}\,\sigma^{\mathrm{D}}(2,0)\\
&= \sigma_{\mathrm{D_{4h}},\perp}^{\mathrm{E1}}(\hat{\varepsilon}_1)\\
&= \sigma_{\mathrm{D_{4h}},\perp}^{\mathrm{E1}}, \qquad (3.48)
\end{aligned}$$

In other words, to recover $\mathrm{D_{4h}}$ symmetry properties of the average cross section calculated with the (modified) QHA model, we must replace calculations performed for the $\hat{\varepsilon}_0$ polarisation vector by the average of the calculations performed on the $\hat{\varepsilon}_0$ and $\hat{\varepsilon}_2$ polarisation vectors. Similarly, we must replace calculations performed for the $\hat{\varepsilon}_1$ polarisation vector by the average of the calculations performed on the $\hat{\varepsilon}_1$ and $\hat{\varepsilon}_3$ polarisation vectors. Using these changes, the calculated dichroic signal becomes:

$$\begin{aligned}
&1/2\left[\sigma_{\perp}^{\mathrm{E1}}(\hat{\varepsilon}_1)+\sigma_{\perp}^{\mathrm{E1}}(\hat{\varepsilon}_3)\right]-1/2\left[\sigma_{\perp}^{\mathrm{E1}}(\hat{\varepsilon}_0)+\sigma_{\perp}^{\mathrm{E1}}(\hat{\varepsilon}_2)\right]\\
=\;&1/2\left[\sigma_{\perp}^{\mathrm{E1}}(\varphi_{\hat{\varepsilon}_1})+\sigma_{\perp}^{\mathrm{E1}}(\varphi_{\hat{\varepsilon}_3})\right]-1/2\left[\sigma_{\perp}^{\mathrm{E1}}(\varphi_{\hat{\varepsilon}_0})+\sigma_{\perp}^{\mathrm{E1}}(\varphi_{\hat{\varepsilon}_2})\right]\\
=\;&0, \qquad (3.49)
\end{aligned}$$

and yields a zero signal as expected theoretically.

For the E2 (electric quadrupole) contribution, it is a bit more complicated but the principle stays the same. For a crystal with the $\mathrm{D_{4h}}$ point group symmetry, the absorption cross section is defined by (Eq. 5.7 of Ref. (53) with $\theta = \pi/2$)

$$\begin{aligned} \sigma^{\mathrm{E2}}_{\mathrm{D_{4h}},\perp}(\varphi,\psi) &= \sigma^{\mathrm{Q}}(0,0) + \sqrt{5/14}\left(3\sin^2\psi - 1\right)\sigma^{\mathrm{Q}}(2,0) \\ &\quad +1/\sqrt{14}\left(5\sin^2\psi - 4\right)\sigma^{\mathrm{Q}}(4,0) \\ &\quad -\sqrt{5}\,\sin^2\psi\,\cos 4\varphi\,\sigma^{\mathrm{Qr}}(4,4). \end{aligned} \tag{3.50}$$

In Eq. 3.50, the angle ψ, which was not involved in the electric dipole E1 equations, represents the direction of the wave vector $\boldsymbol{k}$ in the plane perpendicular to the polarisation vector. In other words, ψ represents the orientation of the wave vector $\boldsymbol{k}$ in the scattering plane and represents the 10° incidence of $\boldsymbol{k}$ to the crystal surface (see section 3.3.1). It should be noted that since the wave vector keeps the same incidence to the crystal during the sample rotation, ψ stays the same during all the experiment.

The in-plane dichroic signal, observed experimentally and obtained as the difference between $\sigma^{\mathrm{E2}}_{\mathrm{D_{4h}},\perp}(\varphi_{\hat{\varepsilon}_1},\psi)$ and $\sigma^{\mathrm{E2}}_{\mathrm{D_{4h}},\perp}(\varphi_{\hat{\varepsilon}_0},\psi)$, yields in this case:

$$\begin{aligned} \sigma^{\mathrm{E2,dic}}_{\mathrm{D_{4h}},\perp} &= \sigma^{\mathrm{E2}}_{\mathrm{D_{4h}},\perp}(\hat{\varepsilon}_1,\boldsymbol{k_1}) - \sigma^{\mathrm{E2}}_{\mathrm{D_{4h}},\perp}(\hat{\varepsilon}_0,\boldsymbol{k_0}) \\ &= \sigma^{\mathrm{E2}}_{\mathrm{D_{4h}},\perp}(\varphi_{\hat{\varepsilon}_1},\psi) - \sigma^{\mathrm{E2}}_{\mathrm{D_{4h}},\perp}(\varphi_{\hat{\varepsilon}_0},\psi) \\ &= 2\sqrt{5}\,\sin^2\psi\,\sigma^{\mathrm{Qr}}(4,4). \end{aligned} \tag{3.51}$$

In comparison, for a crystal with no symmetry (case of the atomic configurations), the E2 absorption cross section, given the experimental set up, reads (Eq. A.38 of Ref. (53) with $\theta = \pi/2$):

$$\begin{aligned}
\sigma_{\perp}^{\mathrm{E2}}(\varphi,\psi) \;=\;& \sigma^{\mathrm{Q}}(0,0)+\sqrt{5/14}\,(3\sin^2\psi-1)\sigma^{\mathrm{Q}}(2,0)+1/\sqrt{14}\,(5\sin^2\psi-4)\sigma^{\mathrm{Q}}(4,0)\\
&+2\sqrt{15/7}\sin\psi\cos\psi\left[\sin\varphi\,\sigma^{\mathrm{Qr}}(2,1)-\cos\varphi\,\sigma^{\mathrm{Qi}}(2,1)\right]\\
&-\sqrt{15/7}\cos^2\psi\left[\cos 2\varphi\,\sigma^{\mathrm{Qr}}(2,2)+\sin 2\varphi\,\sigma^{\mathrm{Qi}}(2,2)\right]\\
&+\sqrt{10/7}\sin\psi\cos\psi\left[\sin\varphi\,\sigma^{\mathrm{Qr}}(4,1)-\cos\varphi\,\sigma^{\mathrm{Qi}}(4,1)\right]\\
&+2\sqrt{5/7}\cos^2\psi\left[\cos 2\varphi\,\sigma^{\mathrm{Qr}}(4,2)+\sin 2\varphi\,\sigma^{\mathrm{Qi}}(4,2)\right]\\
&-\sqrt{10}\,\sin\psi\cos\psi\left[\sin 3\varphi\,\sigma^{\mathrm{Qr}}(4,3)-\cos 3\varphi\,\sigma^{\mathrm{Qi}}(4,3)\right]\\
&-\sqrt{5}\,\sin^2\psi\left[\cos 4\varphi\,\sigma^{\mathrm{Qr}}(4,4)+\sin 4\varphi\,\sigma^{\mathrm{Qi}}(4,4)\right].
\end{aligned}\tag{3.52}$$

In this case, the in-plane dicroic signal, if calculated as the difference signal between $\sigma_{\perp}^{\mathrm{E2}}(\varphi_{\hat{\varepsilon}_1},\psi)$ and $\sigma_{\perp}^{\mathrm{E2}}(\varphi_{\hat{\varepsilon}_0},\psi)$, yields:

$$\begin{aligned}
\sigma_{\perp}^{\mathrm{E2}}(\varphi_{\hat{\varepsilon}_1},\psi)-\sigma_{\perp}^{\mathrm{E2}}(\varphi_{\hat{\varepsilon}_0},\psi) \;=\;& 2\sqrt{15/7}\sin\psi\cos\psi\left[(1-\sqrt{2}/2)\sigma^{\mathrm{Qr}}(2,1)-\sqrt{2}/2\,\sigma^{\mathrm{Qi}}(2,1)\right]\\
&-\sqrt{15/7}\cos^2\psi\left[-\sigma^{\mathrm{Qr}}(2,2)+\sigma^{\mathrm{Qi}}(2,2)\right]\\
&+\sqrt{10/7}\sin\psi\cos\psi\left[(1-\sqrt{2}/2)\sigma^{\mathrm{Qr}}(4,1)-\sqrt{2}/2\,\sigma^{\mathrm{Qi}}(4,1)\right]\\
&+2\sqrt{5/7}\cos^2\psi\left[-\sigma^{\mathrm{Qr}}(4,2)+\sigma^{\mathrm{Qi}}(4,2)\right]\\
&-\sqrt{10}\,\sin\psi\cos\psi\left[-(1+\sqrt{2}/2)\sigma^{\mathrm{Qr}}(4,3)+\sqrt{2}/2\,\sigma^{\mathrm{Qi}}(4,3)\right]\\
&+2/\sqrt{5}\,\sin^2\psi\,\sigma^{\mathrm{Qr}}(4,4).
\end{aligned}\tag{3.53}$$

As we can see, in the case of an atomic configuration with no symmetries, both the absorption cross section for a specific polarisation (Eq. 3.52) and the in-plane dichroic signal calculated the same way it was measured (Eq. 3.53) are very different from what the are expected to be in the $\mathrm{D_{4h}}$ symmetry. Looking closely at the equations, these differences consist in additional terms, that appear when symmetry is lost. To recover the symmetry, the same process we used to recover symmetry for the E1 contribution of the signal is used: a linear combination of calculations performed for well chosen polarisation vectors replaces calculations performed only for $\hat{\varepsilon}_0$ and $\hat{\varepsilon}_1$. Using a total of eight polarisation vectors (including $\hat{\varepsilon}_0$ and $\hat{\varepsilon}_1$, and noted $\hat{\varepsilon}_i$ ($i = 0\ ..\ 7$)) we manage to recover the expression of the E2 absorption cross section expected

Index i	$\hat{\varepsilon}$	$\boldsymbol{k}$
0	$[0\bar{1}0]$	$(\sin\psi, 0, -\cos\psi)$
1	$[1\bar{1}0]$	$\left(\frac{-1}{\sqrt{2}}\sin\psi, \frac{1}{\sqrt{2}}\sin\psi, -\cos\psi\right)$
2	$[100]$	$(0, \sin\psi, -\cos\psi)$
3	$[\bar{1}\bar{1}0]$	$\left(\frac{1}{\sqrt{2}}\sin\psi, \frac{-1}{\sqrt{2}}\sin\psi, -\cos\psi\right)$
4	$[010]$	$(-\sin\psi, 0, -\cos\psi)$
5	$[\bar{1}10]$	$\left(\frac{-1}{\sqrt{2}}\sin\psi, \frac{-1}{\sqrt{2}}\sin\psi, -\cos\psi\right)$
6	$[\bar{1}00]$	$(0, -\sin\psi, -\cos\psi)$
7	$[110]$	$\left(\frac{-1}{\sqrt{2}}\sin\psi, \frac{1}{\sqrt{2}}\sin\psi, -\cos\psi\right)$

Table 3.2: The eight different ($\hat{\varepsilon}$, $\boldsymbol{k}$) couples employed in the present calculations to extract the $\mathrm{D_{4h}}$ in-plane mean and dichroic components of the Ti K edge in rutile $\mathrm{TiO_2}$ from calculations performed using the modified QHA model, i.e with no crystal symmetry. The angle ψ specifies the direction of the wavevector $\boldsymbol{k}$ in the plane perpendicular to $\hat{\varepsilon}$.

in the $\mathrm{D_{4h}}$ symmetry, for the $\hat{\varepsilon}_0$ and $\hat{\varepsilon}_1$ polarisation vectors, as

$$\begin{aligned}
\sigma^{\mathrm{E2}}_{\mathrm{D_{4h}},\perp}(\hat{\varepsilon}_0, \boldsymbol{k_0}) &= \sigma^{\mathrm{E2}}_{\mathrm{D_{4h}},\perp}(\varphi_{\hat{\varepsilon}_0}, \psi) \\
&= 1/4\ \left[\sigma^{\mathrm{E2}}_{\perp}(\hat{\varepsilon}_0, \boldsymbol{k_0}) + \sigma^{\mathrm{E2}}_{\perp}(\hat{\varepsilon}_2, \boldsymbol{k_2}) + \sigma^{\mathrm{E2}}_{\perp}(\hat{\varepsilon}_4, \boldsymbol{k_4}) + \sigma^{\mathrm{E2}}_{\perp}(\hat{\varepsilon}_6, \boldsymbol{k_6})\right] \\
&= 1/4\ \left[\sigma^{\mathrm{E2}}_{\perp}(\varphi_{\hat{\varepsilon}_0}, \psi) + \sigma^{\mathrm{E2}}_{\perp}(\varphi_{\hat{\varepsilon}_2}, \psi) + \sigma^{\mathrm{E2}}_{\perp}(\varphi_{\hat{\varepsilon}_4}, \psi) + \sigma^{\mathrm{E2}}_{\perp}(\varphi_{\hat{\varepsilon}_6}, \psi)\right]
\end{aligned} \tag{3.54}$$

and

$$\begin{aligned}
\sigma^{\mathrm{E2}}_{\mathrm{D_{4h}},\perp}(\hat{\varepsilon}_1, \boldsymbol{k_1}) &= \sigma^{\mathrm{E2}}_{\mathrm{D_{4h}},\perp}(\varphi_{\hat{\varepsilon}_1}, \psi) \\
&= 1/4\ \left[\sigma^{\mathrm{E2}}_{\perp}(\hat{\varepsilon}_1, \boldsymbol{k_1}) + \sigma^{\mathrm{E2}}_{\perp}(\hat{\varepsilon}_3, \boldsymbol{k_3}) + \sigma^{\mathrm{E2}}_{\perp}(\hat{\varepsilon}_5, \boldsymbol{k_5}) + \sigma^{\mathrm{E2}}_{\perp}(\hat{\varepsilon}_7, \boldsymbol{k_7})\right] \\
&= 1/4\ \left[\sigma^{\mathrm{E2}}_{\perp}(\varphi_{\hat{\varepsilon}_1}, \psi) + \sigma^{\mathrm{E2}}_{\perp}(\varphi_{\hat{\varepsilon}_3}, \psi) + \sigma^{\mathrm{E2}}_{\perp}(\varphi_{\hat{\varepsilon}_5}, \psi) + \sigma^{\mathrm{E2}}_{\perp}(\varphi_{\hat{\varepsilon}_7}, \psi)\right]
\end{aligned} \tag{3.55}$$

for $\hat{\varepsilon}_0$ and $\hat{\varepsilon}_1$, respectively. These linear combinations allow to cancel all the additional terms added when symmetry was lost. As was the case for the E1 contribution, the new polarisation vectors $\hat{\varepsilon}_2, \hat{\varepsilon}_4, \hat{\varepsilon}_6$ and $\hat{\varepsilon}_3, \hat{\varepsilon}_5, \hat{\varepsilon}_7$ are obtained from successive $\frac{\pi}{2}$ rotations of $\hat{\varepsilon}_0$ and $\hat{\varepsilon}_1$, respectively, in the plane perpendicular to the z-axis of the crystal. All the $(\hat{\varepsilon}, \boldsymbol{k})$ couples used to recover the crystal symmetry, for both the E1 and E2 contributions, are presented in Table 3.2.

Finally, the in-plane dichroic signal is simply calculated as the difference between Eq. 3.55

and Eq. 3.54, calculations using the modified QHA model and performed for the eight $(\hat{\varepsilon}_i, \boldsymbol{k}_i)$ couples ($i = 0$ .. 7).

Using this method, we theoretically are able to obtain a calculated spectrum that both includes thermal vibrations of the nuclei, but also respects the angular dependence dictated by the rutile $\mathrm{TiO_2}$ crystal symmetry which is lost because of the use of atomic configurations. This is true for both the in-plane mean and dicroic signals. It should be noted that the method is already applied to obtain the in-plane mean spectra shown in section 3.3.3 to recover the correct angular dependence. The measured in-plane mean signal was obtained as the average of the signal measured for the $(\hat{\varepsilon}_0, \boldsymbol{k}_0)$ and $(\hat{\varepsilon}_1, \boldsymbol{k}_1)$ couples. Eq. 3.47 and Eq. 3.48, which both describe how to recover the $\mathrm{D_{4h}}$ angular dependence of the dipole contribution (that is to say, no variations as the φ angle varies), show that both $1/2\left[\sigma_{\perp}^{\mathrm{E1}}(\hat{\varepsilon}_0) + \sigma_{\perp}^{\mathrm{E1}}(\hat{\varepsilon}_2)\right]$ and $1/2\left[\sigma_{\perp}^{\mathrm{E1}}(\hat{\varepsilon}_1) + \sigma_{\perp}^{\mathrm{E1}}(\hat{\varepsilon}_3)\right]$ can be used to get the correct angular dependence for the E1 contribution of the in-plane mean signal. The E2 contribution of the in-plane mean signal is calculated as the average of Eq. 3.55 and Eq. 3.54, using the calculations from the modified QHA model for the eight $(\hat{\varepsilon}_i, \boldsymbol{k}_i)$ couples ($i = 0$ .. 7).

The in-plane dichroic signal obtained after applying the crystal symmetry recovery method can be seen in Fig. 3.14, decomposed in its E1 and E2 contributions, in the same way the dichroic signal obtained with the modified QHA model before applying to method to recover symmetry was applied is shown in Fig. 3.12. As can be seen by comparing the two figures, the E2 signal obtained after recovering angular dependence is still in very good agreement with the measured signal. Moreover, the temperature effect on the E2 contribution is still a slight decrease of the signal intensity as temperature increases, which is still consistent with the experiment results. The method had very little effect on the E2 contribution, which is not surprising given how it was barely affected by taking into account thermal vibrations (see section 3.3.3.2, Fig. 3.10). On the contrary, the E1 contribution sees a big change after angular dependence is recoverd, as it becomes a zero signal, as expected according to the $\mathrm{D_{4h}}$ symmetry of the crystal. This result confirms that the method we used is able to keep the thermal vibration effects included in calculated spectra, while also recovering the expected angular dependence of both the in-plane mean and in-plane dichroic signals, which allows better modelling of the measured spectra.

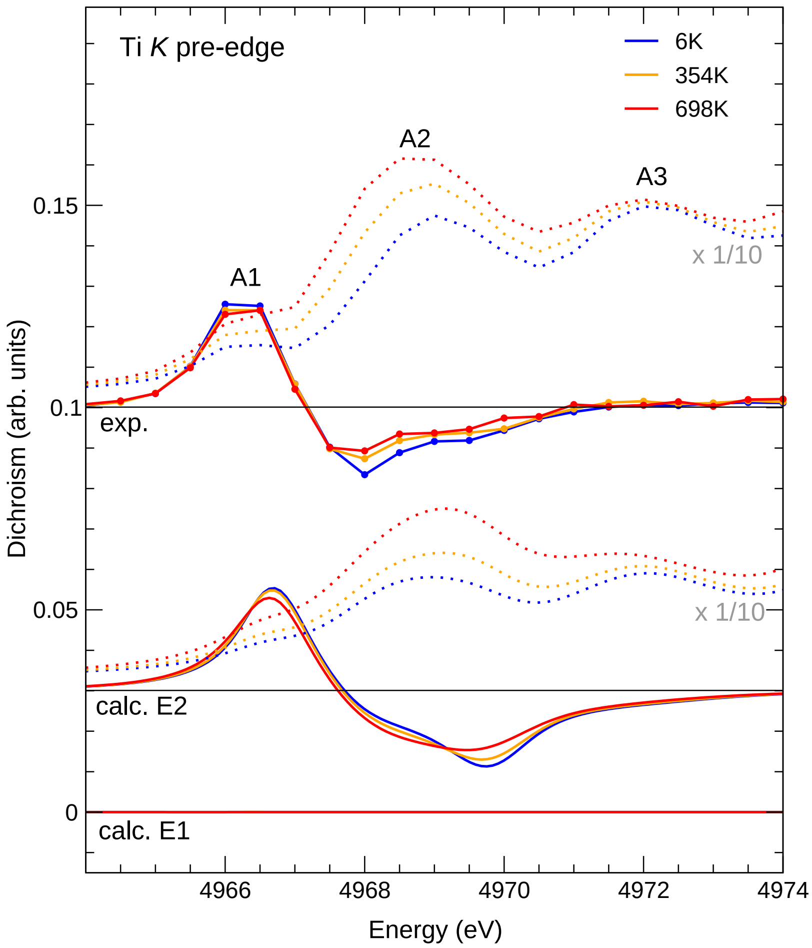

Figure 3.14: Same figure as Fig. 3.12, but using signals obtained after recovering crystal symmetries. As before, contributions are shown separately and calculation and experiment are shifted vertically for clarity. For reference purposes, zero lines (black) and in-plane mean measured and calculated signals (dotted lines) are shown at a 1/10 scale.

3.4 Conclusion

In this chapter, the effects of the quantum thermal vibrations of the nuclei on the multipole contributions to XAS and XRS K edge spectra were studied. The study relies on the comparison between measured K edge XAS or XRS spectra of well known materials, the rutile phase of TiO_2 and corundum α-Al_2O_3, at finite temperature, and calculated spectra using the QHA model. A slightly modified QHA model was used in the case of TiO_2, where thermal expansion effects are not taken into account. The need to slightly modify the QHA model was caused by a problem when calculating phonons on the rutile TiO_2 at finite temperature. The QHA model (both the regular QQHA model and and the modified QHA model using in the case of rutile) allows to explicitly account for these thermal vibrations, by calculating the spectrum as an average of individual spectra, each calculated for an out of equilibrium configuration of the material. In these configurations, atoms are moved away from their equilibrium positions using both previously calculated phonons in the material, and a specific finite temperature. Spectra and phonon calculations were performed using Quantum ESPRESSO, a DFT based open source suite of codes. In both the cases of TiO_2 and α-Al_2O_3, taking quantum thermal vibrations of the nuclei into account greatly improve the agreement between theory and experiment. Additionally to the overall slight shift towards lower energies, and a slight broadening of the spectra features visible on the whole calculated spectra, the study also highlights how the quantum thermal vibrations mainly affect the dipole contribution to the K edge XRS or XAS spectra that were studied, and in contrast only have minor effects on the monopole or quadrupole contributions. Indeed, the temperature is observed to have a strong effect on the dipole contribution by either greatly modifying the intensity of spectral features already present in calculations performed for the equilibrium cell (case of α-Al_2O_3) and/or by adding new spectral features to the dipole contribution, which contribute to a better reproduction of the measured variation of the spectra with varying temperatures (case of rutile TiO_2, and in a lesser extent of corundum). While the modification of spectral weight is predominantly visible on the main edge of the studied spectra, the latter effects essentially arise from on-site hybridisation between the absorber p and s or d states. This leads to the appearance of spectral features, invisible for a standard calculation performed using the equilibrium cell even when taking into account thermal expansion. The affected regions of the spectra are thus the regions dominated by those states, i.e, for example, in the pre-edge region of the Ti K spectrum of rutile TiO_2. In comparison, the monopole and quadrupole contributions to the Al K edge spectra of corundum and to the Ti K edge or rutile TiO_2, respectively, were barely affected and only suffered a slight broadening effect. In addition the inspection of Projected Density Of States (PDOS) allowed to highlight the effects of the presence of a core hole on the absorbing atom in DFT. In the presence of a core hole, the states of the absorbing atom are indeed pulled to lower energies in the conduction band, as well as concentrated on a smaller energy interval. These effects of presence of a core hole on the absober atom, in the case of the Ti K edge spectrum of TiO_2, were explained as a possible reason for not being able to reproduce the slight shift of one of the pre-edge peak as temperature increased, when the measured temperature variation of the spectrum was otherwise correctly reproduced. Finally, in the case of TiO_2, the study allowed to highlight how using this method based on averaging atomic configurations, while allowing better reproduction of temperature dependent Ti K data, also lead to the loss of the expected angular dependence according to the crystal symmetry of TiO_2. This problem was made visible when trying to reproduce a signal measured during the experiment, designed to represent the anisotropy of the $3d$ states of Ti and thus, tighly related to the angular dependence properties of the spectrum. We justified and developed a method that can be used to recover the symmetry properties of the average cross section calculated using the (modified) QHA protocol, and used it to correctly reproduce the angular dependence of the experimental signal.

4 Implementation of XRS calculation at the $L_{2,3}$ edge in QUANTUM Espresso

X-Ray Raman Scattering (XRS) is a core-level spectroscopy (that is to say, which relies on the excitation of a core-level electron), much like XAS. It has recently been increasingly popular to investigate light element edges in diverse materials. The fact that highly energetic 'hard' x-rays are used, whereas in XAS 'soft' x-rays are used to measure the K edge of light elements, makes for easier experimental conditions, for instance making *in situ* measurements possible or making measurement possible without needing any sort of vacuum. This section is dedicated to presenting the implementation of XRS calculation of the $L_{2,3}$ edges in the Quantum ESPRESSO suite of codes, more precisely in the XSpectra module of quantum ESPRESSO, as well as exploring its capacity to reproduce experimental data at the $L_{2,3}$ edge of various sulphur compounds. Indeed, one of the objectives is to evaluate how well XSpectra can reproduce XRS $L_{2,3}$ edge spectra, at various values of q, where the monopole and dipole contribution to the spectrum do not have the same relative weight. This work follows, and completes, the previous implementation of the XRS K edge calculations in Quantum ESPRESSO by Emmanuelle de Clermont Gallerande during her PhD thesis. In ref. (47), the implementation is briefly explained and the XRS K edge of various light elements in lithium compounds are modelled and found in good agreement with experiment. Moreover, not only XRS K edge spectra calculations were already made possible for XSpectra, but the XSpectra module was also able to properly reproduce measured XAS $L_{2,3}$ edge spectra, for example in the case of diverse Cu compounds, though it should be kept in mind that DFT suffers from inherent limitations when treating the case of the $L_{2,3}$ edges of the other transition metals. Thus, expanding XRS calculations in

Quantum ESPRESSO by implementing calculations of XRS $L_{2,3}$ edge spectra would provide a potentially interesting additional theoretical tool to help analyse measured XRS $L_{2,3}$ edges spectrum data, at least for cases outside the limitations imposed by DFT. After reminding of important theoretical aspects regarding $L_{2,3}$ edges in XRS, some details will be given regarding the implementation. Finally, performed calculations, including validation tests, will be shown and discussed.

4.1 Theoretical details

In this section, the theoretical elements needed to properly implement the calculation of XRS $L_{2,3}$ edges are reminded, developed and/or introduced.

4.1.1 Double differential cross section and dynamic structure factor

As we already discussed in an earlier section (see section 3.1.1.2) to model an XRS spectrum, we need to calculate its intensity, which is proportional to the dynamic structure factor $S(\boldsymbol{q}, \omega)$. We start by reminding of some elements regarding the dynamic structure factor. The intensity of a spectrum measured using XRS is in fact proportional to the double differential cross section per solid angle and frequency (pulsation), which can be written as (15; 14)

$$\frac{d^2\sigma}{d\Omega d\omega} = \left(\frac{d\sigma}{d\Omega}\right)_{Th} S(\boldsymbol{q}, \omega). \tag{4.1}$$

In Eq. 4.1, the double differential cross section involves two different terms, $\left(\frac{d\sigma}{d\Omega}\right)_{Th}$ and $S(\boldsymbol{q}, \omega)$. The first term is the Thomson scattering cross section, which depends on the characteristics of the incident and scattered X-ray photons. $\left(\frac{d\sigma}{d\Omega}\right)_{Th}$ is written as

$$\left(\frac{d\sigma}{d\Omega}\right)_{Th} = r_e^2 \left(\hat{\varepsilon}_{in} \cdot \hat{\varepsilon}_{out}\right)^2 \frac{\omega_{out}}{\omega_{in}}, \tag{4.2}$$

where r_e the classical radius of the electron, expressed as $r_e = \frac{e^2}{4\pi\varepsilon_0 m_e c^2}$, with e the elementary charge, ε_0 the vacuum permittivity, m_e the mass of the electron and c the speed of light in vacuum. In eq. 4.2, the incident and scattered x-ray photon polarisation vectors are noted $\hat{\varepsilon}_{in}$

$\hat{\varepsilon}_{out}$ respectively. $\hbar\omega_{in}$ and $\hbar\omega_{out}$ are the incident and scattered photon energy, respectively. The second term of eq. 4.1 is the dynamic structure factor $S(\boldsymbol{q},\omega)$. For an x-ray photon scattering causing an excitation from an initial state $|i\rangle$ of energy E_i to a final state $|f\rangle$ of energy E_f, the dynamic structure factor can be expressed using Fermi's golden rule as (14)

$$S(\boldsymbol{q},\omega) = \sum_f \left|\langle f|e^{i\boldsymbol{q}\cdot\boldsymbol{r}}|i\rangle\right|^2 \delta(E_f - E_i - \hbar\omega). \tag{4.3}$$

We remind here that since we are in a DFT single particle framework, $|i\rangle$ is the atomic orbital of a core level state (in the case of an $L_{2,3}$ edge, a $2p$ state) and $|f\rangle$ is any of the unoccupied electronic state orbitals calculated with a core hole on the excited core level. In eq. 4.3, $\boldsymbol{q}$ is the scattering vector defined by $\boldsymbol{q} = \boldsymbol{k}_{in} - \boldsymbol{k}_{out}$, with $\boldsymbol{k}_{in}$ and $\boldsymbol{k}_{out}$ the incident and scattered x-ray photon wave vectors, respectively. $\hbar\omega = \hbar\omega_{in} - \hbar\omega_{out}$ is the energy transfer occurring during the scattering of the x-ray photon. $e^{i\boldsymbol{q}\cdot\boldsymbol{r}}$ is the XRS transition operator discussed in section 3.1.1.2, where it is noted $\mathcal{O}^{\mathrm{XRS}}$.

This factorisation into two terms of the double differential cross section (eq. 4.1) is useful because it allows to separate the terms depending on the incident and scattered beam characteristics only (included in the Thomson scattering cross section $\left(\frac{d\sigma}{d\Omega}\right)_{Th}$) from those dictating the light matter interactions (dynamic structure factor $S(\boldsymbol{q},\omega)$). Moreover, describing these two terms also allows to explain more easily why the Thomson scattering term is neglected in the spectra calculation. In a scattering experiment, the polarisation of the incident beam is constant and the polarisation of the scattered beam can be chosen as constant, and thus the scalar product between $\hat{\varepsilon}_{in}$ and $\hat{\varepsilon}_{out}$ is a constant term. r_e is also, obviously, a constant term. The only non constant term is $\frac{\omega_{out}}{\omega_{in}}$. Indeed, as the energy transfer $\hbar\omega = \hbar\omega_{in} - \hbar\omega_{out}$ probed to measure the edge increases, then ω_{out} decreases since ω_{in} is constant. However, the edges are usually measured on a small enough energy range (around some tens of eV), that $\frac{\omega_{out}}{\omega_{in}}$ can also be considered constant in the case of non resonant scattering, i.e where the measured edge energy is far from in incident energy. For instance, for the $L_{2,3}$ edges of sulphur at around 163 eV, and an incident beam energy of 10 keV, the relative difference between $\frac{\omega_{out}}{\omega_{in}}$ at the beginning of the S $L_{2,3}$ energy range ($\omega_{out} \simeq (10000 - 163)$ eV $=$ 9837 eV) and at the end of the energy range ($\omega_{out} \simeq$ 9787 eV) is approximately 0.5 %. For the same spectrum, but measured instead on a

100 eV energy range, the difference would still only amount to approximately 1%.

On a final note, we can already notice that the differences between K and $L_{2,3}$ edges lie in the initial and final states $|i\rangle$ and $|f\rangle$ involved in the excitation of the core-level electron. For K edges, $|i\rangle$ is a $1s$ state while it is a $2p$ state for $L_{2,3}$ edges.

4.1.2 Expansion of the XRS transition operator

For our purpose of implementing calculations at the $L_{2,3}$ edges into the XSpectra module of Quantum ESPRESSO, it is however more useful to develop the transition operator $\mathcal{O}^{\mathrm{XRS}} = e^{i\boldsymbol{q}\cdot\boldsymbol{r}}$ using Bessel spherical functions and spherical harmonics. This decomposition allows to separate the XRS transition operator into several terms, associated to different transition channels. The decomposition will thus allow the implementation of each transition channel separately, the same way it is already done for the calculation of XAS K and $L_{2,3}$ edges spectra and XRS K edge spectra in the XSpectra module of Quantum ESPRESSO.

In order to take into account each different multipole contribution to the XRS $L_{2,3}$ edge spectrum separately (i.e calculate separately the monopole and dipole contributions to the spectrum), the general expansion of $e^{i\boldsymbol{q}\cdot\boldsymbol{r}}$ on spherical harmonics Y_λ^μ must first be considered. The general expression for this expansion is

$$e^{i\boldsymbol{q}\cdot\boldsymbol{r}} = 4\pi \sum_{\lambda=0}^{+\infty} \sum_{\mu=-\lambda}^{\lambda} i^\lambda Y_\lambda^{\mu\,*}(\hat{q}) Y_\lambda^\mu(\hat{r}) j_\lambda(qr), \tag{4.4}$$

where $\hat{q}$ and $\hat{r}$ are the unit vectors of $\boldsymbol{q}$ and $\boldsymbol{r}$, respectively, such that $\boldsymbol{q} = q\hat{q}$ and $\boldsymbol{r} = r\hat{r}$. We also remind here that $Y_\lambda^{\mu\,*} = (-1)^\mu Y_\lambda^{-\mu}$. The spherical Bessel functions j_λ are defined by their Taylor series expansion (in terms of qr):

$$j_\lambda(qr) = \sum_{k=0}^{\infty} \frac{(-1)^k}{2^k k!(2k+2\lambda+1)!!} (qr)^{2k+\lambda}. \tag{4.5}$$

To get a useful expression for the implementation of $L_{2,3}$ edges (and of K edge beforehand), only the terms obtained for $\lambda = 0$, $\lambda = 1$ and $\lambda = 2$ are kept in eq. 4.4. However, the $\lambda = 2$ term was only kept for the implementation of K edge calculation in XRS in XSpectra by E. De Clermont Gallerande (47), where it corresponds to a contribution stemming from quadrupole electronic transitions ($\Delta l = 2$ where l is the orbital quantum number, i.e $1s \rightarrow d$ electronic transitions). The $\lambda = 2$ term has not yet been implemented in XSpectra for XRS $L_{2,3}$ edge calculations, though it also leads to monopole transitions in the case of XRS $L_{2,3}$ edges. The implementation of the $\lambda = 2$ term was scheduled to come after the first implementation of XRS $L_{2,3}$ edge calculation was done and first calculations by the modified XSpectra module were performed. For an $L_{2,3}$ edge, keeping the $\lambda = 0$ and $\lambda = 1$ terms means only keeping contributions stemming from $2p \rightarrow p$ ($\Delta l = 0$), and $2p \rightarrow s$ and/or d transitions ($\Delta l \pm 1$), respectively. Writing the XRS transition operator up the $\lambda = 2$ yields to the following expression, useful for our implementation purposes

$$e^{i\boldsymbol{q}\cdot\boldsymbol{r}} \approx j_0(qr) + 4i\pi j_1(qr) \sum_{\mu=-1}^{1} Y_1^{\mu}(\hat{q})^* Y_1^{\mu}(\hat{r}) - 4\pi j_2(qr) \sum_{\mu'=-2}^{2} Y_2^{\mu'}(\hat{q})^* Y_2^{\mu'}(\hat{r}). \tag{4.6}$$

4.1.3 Particular case of low angular scattering vector values

The specific case of low values for the norm of the scattering vector is of particular interest to us. Indeed, we can show that in the $qr \ll 1$ limit, then the XRS transition operator and the XAS transition operator are equivalent when interchanging $\boldsymbol{q}$ and $\hat{\varepsilon}$, the only difference between the two being a multiplicative constant.

First, in the Bessel Taylor series expansions, if only the first terms for each contribution are kept (i.e only qr terms up to the second order), then the spherical Bessel functions, for up to $\lambda = 2$, are expressed as

$$j_0(qr) \approx 1 - \frac{(qr)^2}{6}, \tag{4.7}$$

$$j_1(qr) \approx \frac{1}{3} qr, \tag{4.8}$$

and

$$j_2(qr) \approx \frac{(qr)^2}{15}. \tag{4.9}$$

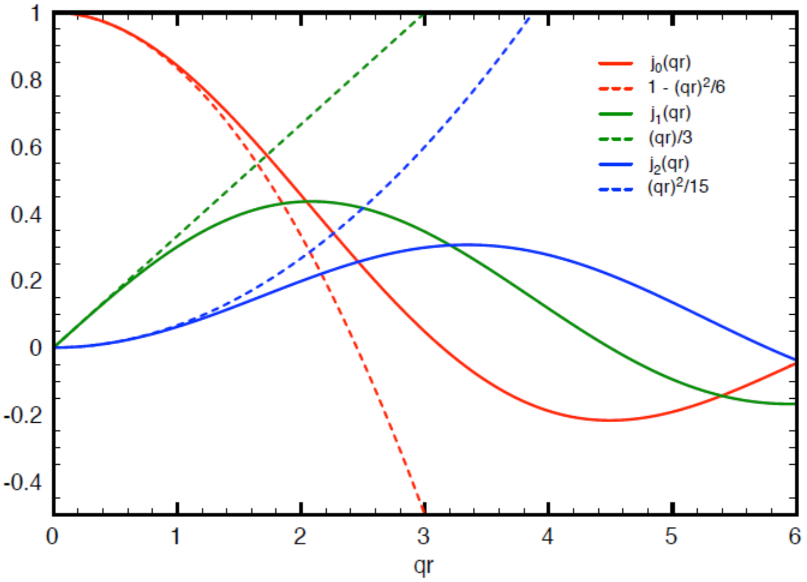

Figure 4.1: Comparison of the spherical Bessel functions with the expression of their development into Taylor expansion series up until the second order in qr terms. Courtesy of G. Radtke.

Fig.4.1 shows the comparison between these expressions and the complete spherical Bessel functions.

Injecting these expressions in eq. 4.4, and only keeping terms up to $\lambda = 2$, yields the following expression for the XRS transition operator:

$$e^{i\boldsymbol{q}\cdot\boldsymbol{r}} \approx 1 - \frac{(qr)^2}{6} + i\frac{4\pi}{3}qr \sum_{\mu=-1}^{1} Y_1^{\mu}(\hat{q})^* Y_1^{\mu}(\hat{r}) - \frac{4\pi}{15}(qr)^2 \sum_{\mu'=-2}^{2} Y_2^{\mu'}(\hat{q})^* Y_2^{\mu'}(\hat{r}). \tag{4.10}$$

In the $qr \ll 1$ limit, we can keep only the zeroth and first order (in qr) terms, such that only the monopole and dipole contributions are non zero. Indeed, the $(qr)^2$ terms are now negligible, and the Bessel functions Taylor expansion now yield

$$j_0(qr) \approx 1, \tag{4.11}$$

$$j_1(qr) \approx \frac{1}{3}qr, \tag{4.12}$$

and

$$j_2(qr) \approx 0, \tag{4.13}$$

which leads to the XRS transition operator being expressed as a sum of the monopole and dipole terms:

$$\mathcal{O}_{\mathcal{XRS}}(\boldsymbol{q}) = e^{i\boldsymbol{q}\cdot\boldsymbol{r}} \approx 1 + iqr\frac{4\pi}{3}\sum_{\mu=-1}^{1} Y_1^{\mu}(\hat{q})^* Y_1^{\mu}(\hat{r}). \tag{4.14}$$

However, since the spectrum intensity is proportional to a squared matrix element $\left|\langle f|\mathcal{O}^{XRS}(\boldsymbol{q})|i\rangle\right|^2$ (see eq. 2.5, where $|i\rangle$ and $|f\rangle$ the initial and final states, respectively, involved in the core excitation, are orthogonal (i.e $\langle f|i\rangle = 0$), then the monopole term doesn't contribute to the spectrum intensity and thus, in the $qr \ll 1$ limit the XRS spectrum is expected to mainly stem from dipole transitions.

The XAS operator is the sum of a dipole and quadrupole term, defined in equations 3.1 and 3.2:

$$\mathcal{O}^{\text{XAS}} = \mathcal{O}^{XAS}_{dip} + \mathcal{O}^{XAS}_{quad} = \hat{\boldsymbol{\varepsilon}}\cdot\boldsymbol{r} + \frac{i}{2}\hat{\boldsymbol{\varepsilon}}\cdot\boldsymbol{r}\ \boldsymbol{k}\cdot\boldsymbol{r}. \tag{4.15}$$

The scalar products of equation 4.15 can be expressed in terms of spherical harmonics, which leads to the following expressions for the dipole and quadrupole parts of the XAS transition operator:

$$\mathcal{O}_{dip}^{\mathrm{XAS}} = r\frac{4\pi}{3}\sum_{\lambda}(-1)^{\lambda}Y_1^{-\lambda}(\hat{\varepsilon})Y_1^{\lambda}(\hat{r}) \tag{4.16}$$

$$\mathcal{O}_{quad}^{\mathrm{XAS}} = ir^2k\frac{4\pi\sqrt{2\pi}}{3\sqrt{15}}\sum_{\lambda,\mu}Y_1^{-\lambda}(\hat{\varepsilon})Y_1^{-\mu}(\hat{k}) \times\sum_{\nu}(-1)^{\nu}(1\lambda1\mu|2\nu)Y_2^{\nu}(\hat{r}), \tag{4.17}$$

where we used $\boldsymbol{k} = k\hat{k}$ and $\boldsymbol{r} = r\hat{r}$. The quadrupole contribution, however, is often negligible in terms of intensity compared to the dipole contribution. By comparing equations 4.14 (remembering that the 1 term does not contribute to the spectrum intensity) and 4.16, we can see that the XRS and dipole part of the XAS operator are indeed equivalent, if we interchange $\hat{\varepsilon}$ and $\hat{q}$, the only difference being the iq factor appearing in the XRS transition operator. Thus, provided that the dipole contribution dominates the spectrum, any XAS spectrum measured at any edge should be equivalent, to a multiplicative constant, to the XRS spectrum measured at the same edge in the $qr \ll 1$ limit.

This fact was very useful in the implementation of XRS $L_{2,3}$ edge calculation in XSpectra because the calculation of XAS $L_{2,3}$ edge spectra is already implemented in XSpectra. Thus, we were able to verify, once the implementation of XRS $L_{2,3}$ edge calculation in XSpectra was finished, that the XRS $L_{2,3}$ edge and the XAS dipole contribution to the $L_{2,3}$ edge spectra, calculated by XSpectra and at low q values in the case of the XRS spectrum, were indeed equivalent, save for an intensity factor.

4.1.4 Differences between the K and $L_{2,3}$ edges

In this section, we briefly explain the main differences between K edges, which the previous chapter of this thesis focuses on and whose calculation for XRS were already implemented in XSpectra, and $L_{2,3}$ edges from a theoretical point of view. This allows to evaluate consequences of those differences for the implementation of XRS $L_{2,3}$ edge calculation in XSpectra, as an introduction to the next section which focuses, in more details, on the implementation.

4.1.4.1 Specificities of the $L_{2,3}$ compared to the K edge

In this section, the differences (as obvious as they may seem) between K and $L_{2,3}$ edges are explained, and their different consequences, as well as the different choices they lead to make, for the implementation of $L_{2,3}$ edge spectra calculations in XSpectra are briefly presented. The main differences between a K edge and an $L_{2,3}$ edge (for both XAS and XRS) essentially stem from the fact that they stem from the excitation of different core levels. A K edge, as seen earlier, stems from the transition of a $1s$ to the available empty states. The $L_{2,3}$ edges instead stem from the transitions of $2p$ electrons to available empty states. The first glaringly obvious differences between XRS K and $L_{2,3}$ edges spectra are a direct consequence of their respective origin. Firstly, Since the K and $L_{2,3}$ edges stem from the transitions of electrons from different core levels, then the same multipole contributions (defined by specific selection rules) to the XRS K and $L_{2,3}$ edge spectra do not allow to probe the same empty states. While, for instance, the dipole contribution ($\Delta l = \pm 1$, with l the orbital quantum number) to XRS K edge spectra allows to probe empty p states, the same contribution to XRS $L_{2,3}$ edge spectra allows to probe empty s and d states instead (of course, for clarity here we do not consider possible *local* or *non-local* $p - d$ or $p - s$ mixing discussed in Chapter three). The monopole and quadrupole contributions (respectively, governed by selection rules $\Delta l = 0$ and $\Delta l = 2$) to the XRS $L_{2,3}$ edge spectra allow to probe empty p and empty f states. This difference in the empty states probed by each contribution is interesting to note because the relative weight of each contribution is related to the norm q of the scattering vector $\boldsymbol{q}$. Secondly, for the same element, the $1s$ and $2p$ core levels have very different energies. Thus, the energy loss at which these edges are found are usually very different from each other. These first differences mainly explain the potentially very different energy positions and shapes of the XRS K and $L_{2,3}$ edge spectra for the same element.

Another less obvious difference was illustrated by the dipole contribution example developed earlier. Indeed, for K edges, the monopole, dipole and quadrupole (though the latter was completely neglected in XRS K edge calculations presented in the previous chapter, see section 3.2) contributions only allow direct probing of empty states defined by one specific l : s states for the monopole, p states for the dipole, etc. In the case of $L_{2,3}$ edges however, the sole dipole contribution allows to probe both empty s and empty d states. That is to say, a single contribution can lead to probing states defined by different l. This possibly leads, when calculating the squared transition matrix element needed to obtain spectrum intensity, to cross terms, for instance in the case of the dipole contribution, between the $l = 0$ and $l = 2$ terms.

The last, but not the least difference between the K and $L_{2,3}$ edges, is that the $L_{2,3}$ edge is in fact two separate edges, the L_2 and L_3 edges while the K edge is one single edge. This stems from the fact that for $L_{2,3}$ edges, the excited core level state is the $2p$ state, defined by $l = 1$. Thus, the spin-orbit interaction, describing the interaction between the angular momentum of the electron and its spin, is responsible for a splitting of the $2p$ states. The spin-orbit Hamiltonian, noted H_{SO}, can be written as

$$H_{SO} = \xi(r)\mathbf{L} \cdot \mathbf{S} \tag{4.18}$$

where $\xi(r)$ is a constant depending on r only, and $\mathbf{L}$ and $\mathbf{S}$ are the orbital angular and spin angular momenta of the electron. By introducing the total angular momentum, $\mathbf{J}$, and defined as $\mathbf{J} = \mathbf{S} + \mathbf{L}$, then we can rewrite Eq. 4.18 as

$$H_{SO} = \frac{\xi(r)}{2}\left(\mathbf{J}^2 - \mathbf{L}^2 - \mathbf{S}^2\right) \tag{4.19}$$

The eigenstates are no longer defined by the usual quantum numbers n, l, s, m_l and m_s. Instead, they are defined by n, l, s, j and m_j, given that H_0, $\mathbf{L}^2$, $\mathbf{S}^2$, $\mathbf{J}^2$ and J_z all commute with each other, and noted $|n, l, s, j, m_j\rangle$. j and m_j are the quantum numbers associated to the total angular momentum $\mathbf{J}$ and its projection along the z axis J_z. j is either 1/2 or 3/2 in the case of $2p$ states ($j = |l + s|$), leading to the $2p_{1/2}$ and $2p_{3/2}$ states giving rise respectively to the L_2 and L_3 edges, with the possible values of m_j going from $-j$ to j. Thus, for $j = 3/2$, then m_j can be $-3/2, -1/2, 1/2$ and $3/2$. for $j = 1/2$, then m_j can be $-1/2$ and $1/2$. Applying the spin-orbit Hamiltonian to the $2p_{1/2}$ and $2p_{3/2}$ states yields, respectively

$$\begin{aligned}
& \langle 2,1,1/2,1/2,m_j|\; H_{SO}\; |2,1,1/2,1/2,m_j\rangle \\
= \;& \langle 2,1,1/2,1/2,m_j|\; \frac{\xi(r)}{2}\; (\mathbf{J}^2 - \mathbf{L}^2 - \mathbf{S}^2)\; |2,1,1/2,1/2,m_j\rangle \\
= \;& \hbar^2 \frac{\xi(r)}{2}((1/2)(1/2+1) - 1(1+1) - (1/2)(1/2+1)) \\
= \;& -\hbar^2\, \xi(r) \qquad (4.20)
\end{aligned}$$

and

$$\begin{aligned}
& \langle 2,1,1/2,3/2,m_j|\; H_{SO}\; |2,1,1/2,3/2,m_j\rangle \\
= \;& \langle 2,1,1/2,3/2,m_j|\; \frac{\xi(r)}{2}\; (\mathbf{J}^2 - \mathbf{L}^2 - \mathbf{S}^2)\; |2,1,1/2,1/2,m_j\rangle \\
= \;& \hbar^2\; \frac{\xi(r)}{2}((3/2)(3/2+1) - 1(1+1) - (1/2)(1/2+1)) \\
= \;& \hbar^2\; \frac{\xi(r)}{2} \qquad (4.21)
\end{aligned}$$

leading to an energy difference between the $2p_{1/2}$ and $2p_{3/2}$ states of $\Delta E = (3/2)\,\hbar^2\,\xi(r)$. In equations 4.20 and 4.21, the quantum number m_j is left as is because it does not affect the spin-orbit coupling energy calculation. The multiplicity of the $2p_{1/2}$ and $2p_{3/2}$ is 4 and 2, respectively $(2j+1)$. Thus, in our single electron scheme, the $L_{2,3}$ edges are calculated as two times the same edge, but shifted from one another by the energy difference $(3/2)\,\hbar^2\,\xi(r)$ and with a relative intensity ratio of 1:2. The lower energy level is the $2p_{1/2}$ level, and thus the L_2 edge is the edge placed at higher energies than the L_3 edge. See Fig.4.2 for a illustration of the spin-orbit coupling at the $2p$ level.

4.1.4.2 Consequences for the implementation in the XSpectra module

All the differences between the K and $L_{2,3}$ described earlier have consequences, of varying degrees, in the implementation of XRS $L_{2,3}$ edge calculation in XSpectra. While the next section explains in more detail the implementation, we begin discussing here the general implications of those differences. In a general way, the implementation was done so the calculations of the different contributions was done is the most separate way possible.

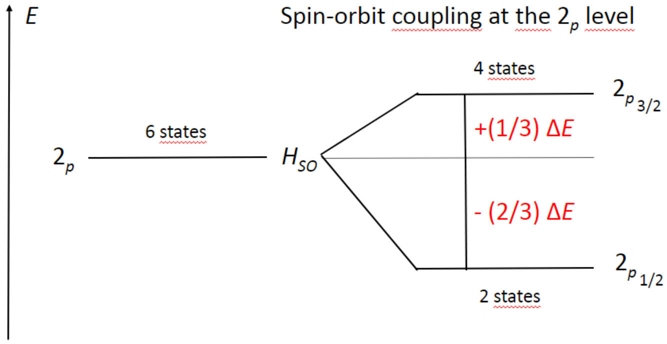

Figure 4.2: Diagram recapitulating the splitting of the $2p$ states into the $2p_{1/2}$ and $2p_{3/2}$ states, giving rise respectively to the L_2 and L_3 states.

The most impacting difference is that the $L_{2,3}$ edge is in fact the sum of two edges, the L_2 and L_3 edges, whereas the K edge is only one edge. Since these two edges stem from the excitation of the $2p_{1/2}$ and $2p_{3/2}$ states, the calculation of the total $L_{2,3}$ edge is necessarily done by calculating both the L_2 and L_3 edges they give rise to. In XSpectra, two different squared matrix elements $\left|\langle f|e^{i\boldsymbol{q}\cdot\boldsymbol{r}}|i\rangle\right|^2$ thus need to be calculated, as $|i\rangle$ can be either the $2p_{1/2}$ or $2p_{3/2}$ state. The implementation was done so the two edges can be calculated, in separate calculations. It should be noted that one Lanczos (see section 2.2 and more particularly section 2.2.3) algorithm is performed for each possible m_j value ($m_j = -j, .., j$). Thus, technically, there is twice the number of Lanczos recursions performed for the calculation of an L_3 edge than that of an L_2 edge. This is why, when testing the implementation, mainly L_2 calculations were used.

Only the monopole and dipole contributions to the XRS spectrum at the $L_{2,3}$ edge were implemented. Calculations of the monopole and dipole contributions were implemented in separate subroutines, which means that a different calculation needs to be ran to obtain both the dipole and monopole contribution. This also means that cross terms between the monopole and dipole contributions are neglected, which was not very important at the first step of the implementation (and testing) since they cancel for powder samples, and our available data used to compare calculations and experiment were measured on powder samples. However, this is an important point to keep in mind. For the dipole contribution, that stems from transitions to both empty s and d states, it was decided in a first time to implement the calculation of dipole transitions to the empty s and d states in two separate cases, and calculate the dipole contribution as the sum of these two separate cases (it is equivalent to say we 'divided' the selection rule $\Delta l = \pm 1$ in the cases $\Delta l = 1$ and $\Delta l = -1$). Though these two cases are calculated separately, they are however both calculated each time a dipole contribution is calculated, and it is not (yet) possible to obtain the separate contributions from the $2p \rightarrow s$ and $2p \rightarrow d$ transitions. Moreover, this also suggests neglecting eventual s/d cross terms that may arise when calculating the whole dipole contribution directly, but those were not the priority, as the most important goal at the time was to get XRS $L_{2,3}$ edges calculations properly implemented in the modified XSpectra module.

Finally, it is important to note that while the calculation of $L_{2,3}$ edges spectra technically requires to calculate both the L_2 and L_3 edges, the theoretical framework Quantum ESPRESSO relies on should lead to the L_2 edge being exactly half the L_3 edge, and thus, only the L_2 edge calculation (which is faster, as seen earlier) is really needed to obtain the $L_{2,3}$ edges. This suggests however needing to perform basic data manipulation of the L_2 edge to obtain the $L_{2,3}$ edge. More explicitly, the L_3 edge must be obtained by multiplying the L_2 edge by two and shifted by the energy difference Δ mentioned earlier, and then summed to the L_2 edge spectrum. These operations for now have to be 'handmade'.

Now that all the theoretical details and generalities have been explained, the implementation of XRS $L_{2,3}$ edges calculations in the modified XSpectra module can be properly presented in the next section.

4.2 Implementation details

In this section, based on the discussions developed in section 4.1, the implementation of XRS $L_{2,3}$ edge calculation in the XSpectra module of Quantum ESPRESSO is detailed. First, we develop the expression of the pseudo wave function used to calculate an XRS $L_{2,3}$ edge spectrum intensity, resulting from the pseudopotential framework and PAW formalism, on which Quantum ESPRESSO and XSpectra are based (the pseudopotential framework and PAW formalism are described in subsection 2.2.2). Then, more technical details are given on how this expression is used to calculate the spectrum intensity. In other words, the objective of this section is to explain how the XRS $L_{2,3}$ spectrum is calculated, using both the theoretical framework explained in the second chapter (2.2), and the theoretical details relevant to XRS $L_{2,3}$ edges given in section 4.1.

4.2.1 Expression of the pseudo wave function for an $L_{2,3}$ edge in XRS

In the previous section, the expression of the XRS dynamic structure factor $S(\boldsymbol{q}, \omega)$ was given in equation 4.3. It involves the transition matrix element $\langle f|e^{i\boldsymbol{q}\cdot\boldsymbol{r}}|i\rangle$. in our DFT single electron framework, $|i\rangle$ is the atomic orbital of the core level state which is excited during the electronic transition. For clarity, we remind that $|i\rangle$ is noted $|\phi_i\rangle$ in section 2.2. $|f\rangle$ is any of the unoccupied electronic state orbitals, usually calculated with a hole on the excited core level. It is noted $|\phi_f\rangle$ in section 2.2. In the pseudopotential framework used by Quantum ESPRESSO, we only have access to pseudised wave functions (noted for instance, for the final state, $|\tilde{\phi}_f\rangle$ instead of $|\phi_f\rangle$), where only valence or semi-core electrons are taken into account explicitly, while the cores of the atoms are frozen, instead of the all electron wave functions (calculated with all the electrons taken into account explicitly). *A priori*, the calculation of the transition matrix element requires the all electron wave functions $|\phi_f\rangle$ instead of the pseudised wave functions $|\tilde{\phi}_f\rangle$. However, in subsection 2.2.2, we described how, using the PAW formalism, the transition matrix element can be rewritten (see equations 2.50 to 2.52 in the said subsection) in terms of the pseudised final state wave functions, as $\langle\tilde{\phi}_f|\tilde{\phi}_0\rangle$, where $|\tilde{\phi}_0\rangle$ is defined in equation 2.51, and reminded here

$$|\tilde{\phi}_0\rangle = \sum_n |\tilde{p}_{\boldsymbol{R}_0,n}\rangle\langle\varphi_{\boldsymbol{R}_0,n}|\mathcal{O}|\phi_i\rangle. \tag{4.22}$$

In this equation, $|\tilde{p}_{\boldsymbol{R}_0,n}\rangle$ are called projectors, $|\varphi_{\boldsymbol{R}_0,n}\rangle$ are called partial wave functions and chosen as the atomic orbitals of the isolated absorbing atom, indicated by $\boldsymbol{R}_0$, and the index n contains the quantum orbital numbers l and m as well as a quantum spin number σ, and an additional index p if there is more than one projector per l channel. In order to properly implement calculation of XRS $L_{2,3}$ edges in XSpectra, it is necessary to properly rewrite $|\tilde{\phi}_0\rangle$. We start by rewriting the different wave functions appearing in the expression of $|\tilde{\phi}_0\rangle$, and by expressing $|\tilde{\phi}_0\rangle$ in the most general way possible. The atomic orbitals of the isolated atom at position $\boldsymbol{R}_0$ (the "partial wave functions" of section 2.2.2), are defined by

$$\langle \boldsymbol{r}|\varphi_{\boldsymbol{R}_0,p,l,m,\sigma}\rangle = R_{p,l,\sigma}(r)\, Y_l^m(\hat{r})\, \chi_\sigma^s(s_z), \tag{4.23}$$

where the first, second and third terms are respectively the radial, angular and spin parts ($\chi_\sigma^s(s_z) = \delta_{\sigma,s_z}$) of the wave function. Similarly, we define the initial state wave function

$$\langle \boldsymbol{r}|\phi_i\rangle = \sum_{m_i=-l_i}^{li} \sum_{m_s=-1/2}^{1/2} (l_i, m_i, s, m_s|j, m_j) R_{n_i,l_i,m_s}(r)\, Y_{l_i}^{m_i}(\hat{r})\, \chi_{m_s}^s(s_z), \tag{4.24}$$

once again defined by a radial, angular and spin term. In this expression, $(l_i, m_i, s, m_s|j, m_j)$ is a Clebsch-Gordan coefficient. In this case, the wave function, because it represents the initial state involved in the core electron transition, is also defined by quantum numbers n_i and l_i, as well as the couple of quantum numbers (j, m_j), resulting from the spin orbit coupling in the general case where l_i can be non zero (which is in fact the case for a $L_{2,3}$ edge as discussed earlier). By injecting those two expressions into equation 4.22, we get a new expression for $|\tilde{\phi}_0\rangle$, indexed by the quantum numbers n_i, l_i, j, m_j

$$\begin{aligned} |\tilde{\phi}_0^{n_i,l_i,j,m_j}\rangle &= \sum_{p,l,m,\sigma} |\tilde{p}_{\boldsymbol{R}_0,p,l,m,\sigma}\rangle (l_i, m_j - \sigma, s, \sigma|j, m_j) \\ &\quad \times \int R_{p,l,\sigma}(r)\, Y_l^{m\,*}(\hat{r})\, \mathcal{O}_{XRS}(\boldsymbol{r})\, R_{n_i,l_i,\sigma}(r)\, Y_{l_i}^{m_j-\sigma}(\hat{r})\, d\boldsymbol{r}. \end{aligned} \tag{4.25}$$

To obtain this expression, we used $\chi_\sigma^s(s_z) = \delta_{\sigma,s_z}$ and $\chi_{m_s}^s(s_z) = \delta_{m_s,s_z}$ which impose $m_s = \sigma$, which in turn yields $m_j = m_i + m_s = m_i + \sigma$ and thus $m_j - \sigma = m_i$. From there, to obtain the final general expression for $|\tilde{\phi}_0^{n_i,l_i,j,m_j}\rangle$, the expansion of $\mathcal{O}^{\mathrm{XRS}}(\boldsymbol{r}) = e^{i\boldsymbol{q}\cdot\boldsymbol{r}}$ described in equation 4.4 can be injected into equation 4.25, which yields the following expression

$$\begin{aligned} |\tilde{\phi}_0^{n_i,l_i,j,m_j}\rangle &= 4\pi \sum_{\lambda=0}^{\infty} \sum_{\mu=-\lambda}^{\lambda} i^\lambda Y_\lambda^{\mu\,*} \sum_{\sigma=-1/2}^{1/2} (l_i, m_j - \sigma, s, \sigma|j, m_j) \\ &\quad \times \sum_{p,l} \mathcal{J}_{p,l,n_i,l_i,\sigma}^{\lambda} \sum_{m=-l}^{l} \mathcal{G}_{\lambda,\mu,l_i,m_j-\sigma}^{l,m} |\tilde{p}_{\boldsymbol{R}_0,p,l,m,\sigma}\rangle. \end{aligned} \tag{4.26}$$

In equation 4.26, $\mathcal{G}^{l,m}_{\lambda,\mu,l_i,m_j-\sigma}$ is a Gaunt coefficient, defined as the integral over three spherical harmonics:

$$\mathcal{G}^{l,m}_{\lambda,\mu,l_i,m_j-\sigma} = \int Y_l^{m\,*}(\hat{r})\, Y_\mu^\lambda(\hat{r})\, Y_{l_i}^{m_j-\sigma}(\hat{r})\, d\hat{r}. \tag{4.27}$$

The term $\mathcal{J}^{\lambda}_{p,l,n_i,l_i,\sigma}$ is a radial integral, including the terms depending on r, and expressed as

$$\mathcal{J}^{\lambda}_{p,l,n_i,l_i,\sigma} = \int R_{p,l,\sigma}(r) R_{n_i,l_i,\sigma}(r) j_\lambda(qr) r^2 dr. \tag{4.28}$$

Interestingly, it is also the term that includes the dependence on the norm q of the scattering vector $\boldsymbol{q}$. The value of q directly impacts this term via the spherical Bessel functions $j_\lambda(qr)$, and has an effect on the relative weight of the various multipole contributions to XRS $L_{2,3}$ spectra. To get a clearer idea of this effect, in the particular case of sulphur compounds studied later in this chapter, the radial integral defined in Eq.4.28 was calculated for the case of $2p \rightarrow 4s$, $2p \rightarrow 3p$ and $2p \rightarrow 3d$ transitions. The needed all electron core ($2p$) and atomic orbitals were obtained using the ld1.x code included in Quantum ESPRESSO with the pseudopotential describing the sulphur atom, and used as input for XRS $L_{2,3}$ edges spectrum calculations shown this chapter. The radial integral was calculated for several values of q, ranging from 2 Å^{-1} to 12 Å^{-1}, corresponding to the range of values of q used later in the chapter. The calculations are shown in Fig.4.3. The figure allows to expect a dipole-dominated spectrum at low q values and, for higher values of q, a rapid increase of the monopole contribution weight, leading to a monopole-dominated spectrum at higher q values. Interestingly, the variation of the radial integral term is not linear with q, and for very high q values, the weight of the monopole contribution starts rapidly decreasing again. On another note, the radial integral of the monopole contribution in the $\lambda = 2$ term, not yet implemented in XSpectra, was also calculated. The radial term of the monopole contribution from the $\lambda = 2$ term does not follow the exact same evolution as the value of q increase. Indeed, it reaches its maximum before the monopole contribution from the $\lambda = 1$ does, and also starts decreasing at lower values of q. It is moreover shown to be negligible compared to the monopole contribution from the $\lambda = 1$ term at the values of q where the monopole contribution from the $\lambda = 1$ term dominates the XRS spectrum.

Of course, this is the most general expression for $|\tilde{\phi}_0^{n_i,l_i,j,m_j}\rangle$ and as explained in sec-

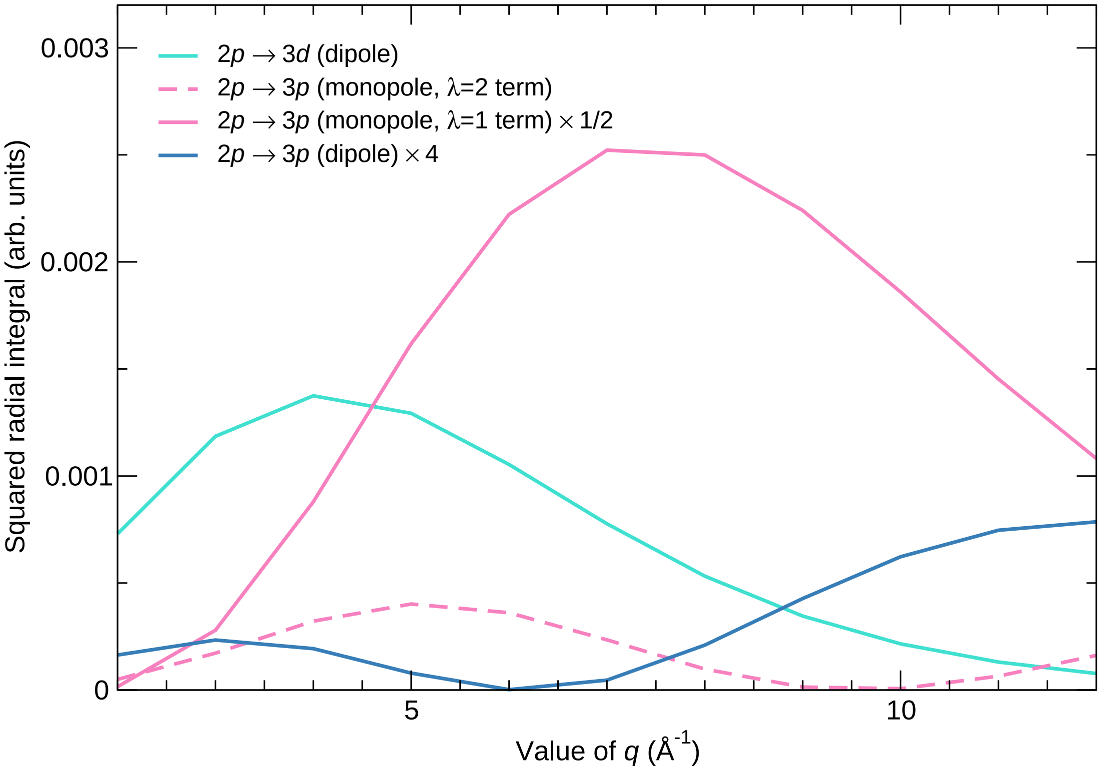

Figure 4.3: Calculation of the radial integral term for different electronic transitions, from a $2p$ core level, at several values of q. The core and atomic orbitals were taken from the pseudopotential describing a sulphur atom, and which is later used for XRS $L_{2,3}$ edge spectra calculations in this chapter.

tion 4.1.2, we only need the terms $\lambda = 0$ and $\lambda = 1$ in order to calculate the monopole and dipole contributions to the spectrum, respectively.

The expression of $|\tilde{\phi}_0^{n_i,l_i,j,m_j}\rangle$ obtained for $\lambda = 0$ is detailed in the following equation, after removing terms cancelled by a null Gaunt coefficient:

$$\begin{aligned} |\tilde{\phi}_0^{n_i,l_i,j,m_j}\rangle_{\lambda=0} &= \sqrt{4\pi}\sum_{\sigma=-1/2}^{1/2}(l_i,m_j-\sigma,s,\sigma|j,m_j) \\ &\quad \times \sum_p \mathcal{J}^0_{p,l,n_i,l_i,\sigma}\mathcal{G}^{l_i,m_j-\sigma}_{0,0,l_i,m_j-\sigma}|\tilde{p}_{\boldsymbol{R}_0,p,l_i,m_j-\sigma,\sigma}\rangle. \end{aligned} \tag{4.29}$$

In the slightly more complicated case of $\lambda = 1$, then we get the following expression for $|\tilde{\phi}_0^{n_i,l_i,j,m_j}\rangle$ instead, again after removing terms cancelled by a null Gaunt coefficient:

$$\begin{aligned} |\tilde{\phi}_0^{n_i,l_i,j,m_j}\rangle_{\lambda=1} &= 4\pi i\sum_{\mu=-1}^{1}Y_1^{\mu\,*}(\hat{q})\sum_{\sigma=-1/2}^{1/2}(l_i,m_j-\sigma,s,\sigma|j,m_j) \\ &\quad \times\sum_p \sum_{\substack{l=|l_i-1| \\ [l+l_i+1\mathrm{even}]}}^{l_i+1} \mathcal{J}^1_{p,l,n_i,l_i,\sigma} \sum_{\substack{m=-l \\ [m=\mu+m_j-\sigma]}}^{l} \mathcal{G}^{l,m}_{1,\mu,l_i,m_j-\sigma}|\tilde{p}_{\boldsymbol{R}_0,p,l,m,\sigma}\rangle. \end{aligned} \tag{4.30}$$

These two expressions were implemented in XSpectra for the calculation of XRS $L_{2,3}$ edges, using $n_i = 1$ and $l_i = 1$, to represent the initial $2p$ core state. Then, both cases of the $2p_{3/2}$ (L_3 edge) and $2p_{1/2}$ (L_2 edge) initial states must be considered. In the first case, we use $j = 3/2$ and $m_j = \{-3/2, -1/2, 1/2, 3/2\}$ and in the second case we use $j = 1/2$ and $m_j = \{-1/2, 1/2\}$. As explained earlier, the calculation of both these edges is separated in the code. On another note, we can see that these terms can be seen as the product of a radial term (mainly, the radial integral) and angular term. The angular dependence of $|\tilde{\phi}_0^{n_i,l_i,j,m_j}\rangle$, and thus, of the calculated spectrum, is included in the spherical harmonics depending on $\hat{q}$. We can note that the monopole contribution shows no angular dependence, unlike the dipole contribution (equations 4.29 and 4.30, respectively). The details regarding the implementation of this expression in XSpectra are given in the next section.

4.2.2 Technical details of the implementation in XSpectra

In the previous section, the expression of $|\tilde{\phi}_0^{n_i,l_i,j,m_j}\rangle$ in both the monopole and dipole case, was given. This expression was used to implement calculation of XRS $L_{2,3}$ edges in XSpectra. In this section, we first give a brief overview of the $L_{2,3}$ edge calculation process performed by the XSpectra module. Then, for each important part of the process, more details are given and discussed.

As an introduction, and from the most global point of view, the $L_{2,3}$ edge calculation was implemented so that either the dipole or the monopole contribution to the spectrum is calculated from one run of XSpectra. Additionally, one XSpectra calculation currently provides either the L_2 or L_3 edge, separately. Finally, each calculation is made, specifically, for a specified orientation of the scattering vector $\boldsymbol{q}$ (i.e, for one specific $\hat{q}$) and for one specified value of its norm q. The calculation of K edges is done in the same way, ignoring the separation of the calculation of L_2 and L_3 edges. In that sense, because (as explained in section 4.1.4) the $L_{2,3}$ edge can be obtained from either the L_2 or L_3 edge, the calculation protocol is the same for XRS K or $L_{2,3}$ edges when using using XSpectra.

On another note, and as a reminder (see chapter 3 and more precisely sections 3.2.2 and 3.3.2), a XAS or XRS spectrum calculation using XSpectra always follows a Self-Consistent Field (SCF) calculation of the charge density in the material, performed by the PW code of Quantum ESPRESSO. It is from this SCF calculation that the different physical properties of the material like, for instance, the charge density, and needed for the spectrum calculation, are obtained. The only requirements for this SCF calculation are the positions of the atoms in the material supercell, as well as the pseudopotentials describing each atom, including in our case, the absorbing or scattering atom. Once this calculation has been performed, it can then be used to perform as many XSpectra calculations as needed, for instance, for different orientations or norm of the scattering vector $\boldsymbol{q}$.

From a more technical point of view, the calculation of the L_2 or L_3 edge is a multi-step process. The steps are briefly described in what follows. These steps can be performed in the main program of the XSpectra code, or by specialised parts in the code called subroutines. A lot of those steps are common for all spectra calculations, such as reading the input file or the output file from the SCF calculation, writing the beginning of the output file of XSpectra, etc. However, for the calculation of a specific edge, namely the L_2 or L_3 edge in our case, there are mainly two steps that are particularly important. A set of subroutines were thus created to perform those two steps in the case of an XRS L_2 or L_3 edge calculation.

The first step of the process is the calculation of the pseudo wave function $|\tilde{\phi}_0^{n_i,l_i,j,m_j}\rangle$ detailed in the previous subsection, which is then used to initialise the Lanczos algorithm used to calculated the spectrum intensity as a continued fraction. The first step is the the calculation of $|\tilde{\phi}_0^{n_i,l_i,j,m_j}\rangle$, and is divided into two parts. First, the radial part of $|\tilde{\phi}_0^{n_i,l_i,j,m_j}\rangle$, which contains the radial integral defined in equation 4.28, is calculated. In a second step, the angular part of $|\tilde{\phi}_0^{n_i,l_i,j,m_j}\rangle$, which contains all the terms not included in the radial integral, is calculated. $|\tilde{\phi}_0^{n_i,l_i,j,m_j}\rangle$ is then computed as the product of these two terms, according to the expression described in equations 4.29 and 4.30 for the monopole and dipole case, respectively. The pseudo wave function $|\tilde{\phi}_0^{n_i,l_i,j,m_j}\rangle$ has to be calculated for all j and m_j indices, according to the calculated edge ($j = 3/2$ and $m_j = \{-3/2, -1/2, 1/2, 3/2\}$ for the L_3 edge and $j = 1/2$ and $m_j = \{-1/2, 1/2\}$ for the L_2 edge) to account for the spin-orbit coupling occurring in our case. This is why the calculation of the radial part is done before the calculation of the angular part: since it does not depend on the indices j and m_j, then it does not need to be included in the loop incrementing the m_j index in the program, which would result in needlessly calculating the same radial integral several times. Once $|\tilde{\phi}_0^{n_i,l_i,j,m_j}\rangle$ is calculated, for each possible m_j, it is used to initialise a Lanczos algorithm in order to be able to calculate the spectrum intensity. Indeed, we remind here that, as explained in the second chapter (2.2), it is possible to calculate the spectrum intensity (that is to say, the sum over the final states of the squared transition matrix element, according to the expression of the dynamic structure factor $S(\boldsymbol{q}, \omega)$) using the Green operator of the system:

$$\sum_f |\langle\tilde{\phi}_f|\tilde{\phi}_0\rangle|^2 \delta(E_f - E_i - \hbar\omega) = -\frac{1}{\pi}\mathfrak{Im}[\langle\tilde{\phi}_0|\tilde{G}(E)|\tilde{\phi}_0\rangle]. \tag{4.31}$$

From there, the spectrum intensity can then be rewritten as a continued fraction,

$$\langle\tilde{\phi}_0|\tilde{G}(E)|\tilde{\phi}_0\rangle = \frac{\langle\tilde{\phi}_0|\tilde{\phi}_0\rangle}{a_0 - E - i\gamma - \frac{b_1^2}{a_1 - E - i\gamma - \frac{b_2^2}{\dots}}}, \tag{4.32}$$

where the coefficients a_i and b_i are the diagonal and non diagonal coefficients of the matrix representing the pseudohamiltonian $\tilde{H}$, using a specific Lanczos basis. In this Lanczos basis, the matrix of $\tilde{H}$ is tridiagonal, and the Lanczos vectors are obtained by successive application of $\tilde{H}$ on the Lanczos vectors, using a recurrence relation (equation 2.58). The first Lanczos vector used to initialise the recurrence is defined using $|\tilde{\phi}_0^{n_i,l_i,j,m_j}\rangle$. For more details, see section 2.2.3. Consequently, because in our case, $|\tilde{\phi}_0^{n_i,l_i,j,m_j}\rangle$ is calculated for each possible m_j, then a specific set of coefficients a_i and b_i is calculated for each possible m_j using a Lanczos subroutine, and stored in their own variable. The broadening parameter of the spectrum calculation, representing the lifetime of the core hole created during the electronic transition, plays a direct role in the expression of the spectrum intensity as a continued fraction and has a large impact on the convergence of the Lanczos algorithm.

From there, the much simpler second step, performed by another subroutine, is to compute the spectrum intensity as a continued fraction for each possible m_j and to obtain the total spectrum intensity. It should be noted that the energy range over which the spectrum is calculated is specified in the XSpectra input file. It is specified in reference to an energy 0 that can be chosen in the input file. By default, XSpectra sets the energy 0 of the spectrum as the energy of the Fermi level. The Fermi energy, calculated during the SCF calculation, is the energy of the highest occupied level found during the calculation. The energy range is then defined in the input file by choosing its upper and lower bounds, in reference to the energy 0. For instance, to obtain a spectrum calculated over a 70 eV energy range, and starting from 10 eV before the energy origin, then the lower bound should be set to -10 eV and the upper bound to 60 eV. The step between each energy point of the range can also be specified, and determines, with the energy range width, how many energy points the spectrum is calculated for. For each of energy point, each spectrum intensity calculated as a continued fraction for each possible m_j, is then summed to obtained the spectrum intensity at this energy. The calculated spectrum is finally written in its own file, named 'nrixs.dat', in a two column format, one for the energy and one for the spectrum intensity at that energy value.

4.3 Calculations at the $L_{2,3}$ edge

In this section, XRS calculations at the $L_{2,3}$ edge, performed using the modified XSpectra module, are presented. For clarity's sake, it should be kept in mind that calculations performed using two different XSpectra modules will be shown in this section. The 'modified XSpectra module' refers to the XSpectra module that was previously modified to include XRS calculations at the K edge by E. De Clermont Gallerande, and which was modified during this thesis to include XRS calculations at the $L_{2,3}$ edge. XAS calculations at the $L_{2,3}$ edge, on the other hand, are performed using the XSpectra module from the current version of Quantum ESPRESSO. It will be referred to as the 'regular version' of the XSpectra module. First, the modified XSpectra module is tested by performing diverse calculations. In the first subsection (4.3.1), calculations on a simple test case are presented. These calculations were performed to check that XRS calculations at the $L_{2,3}$ edge worked properly after implementation. More precisely, the XRS $L_{2,3}$ calculations were compared to XAS $L_{2,3}$ calculations at the $L_{2,3}$ edge performed on the same test case using the regular version of the XSpectra module, for the case of low $\boldsymbol{q}$ norm (i.e q) values. This is because we know that the XRS and XAS transition operators are equivalent for low q values (see section 4.1.3). Thus, the calculated XRS (for low q values) and XAS spectra should also be equivalent if XRS $L_{2,3}$ edges calculation was implemented correctly, which makes this comparison a good first validation test. In this section, the same test case is also used to verify that the 1:2 branching ratio between the L_2 and L_3 edge, which is expected in a single electron framework such as DFT, is obtained. In the following sections, XRS calculations performed at the S $L_{2,3}$ edge of Li_2SO_4 and pure sulphur (alpha structure of S_8) are shown. These calculations are compared to available measured data and used to assess the capacity of the modified XSpectra module to properly reproduce XRS $L_{2,3}$ edges, for various values of q. Indeed, compared to the calculation of XAS $L_{2,3}$ edge spectra, the variation of the norm of q have an impact on the relative weight of the monopole and dipole contribution. Finally, calculations performed for several other sulphur compounds (realgar, pyrite, orpiment and arsenopyrite).

4.3.1 First Verification tests: Cu $L_{2,3}$ edge in Cu

After (and during !) the implementation of XRS $L_{2,3}$ edge calculations, one of the test case suggested in the Quantum ESPRESSO suite for the XSpectra module, and whose function is usually to perform first calculations and get more familiar with the XSpectra module, was used to verify that the modified XSpectra ran properly and gave reasonable results. The final results of these very first calculations performed using the modified XSpectra are shown in this section.

The test case consists in calculating the XRS $L_{2,3}$ edge of Cu in pure copper. It should be noted that as this is a test case, the parameters of the calculation are not optimised to get realistic results, like they were in the Work of Bunau et al. (60). Instead, this test case focuses on efficiency (i.e a short calculation time), allowing us to quickly verify that the modified XSpectra module runs properly. Thus, comparison with experiment would not, in that case, make much sense, as the calculation is optimised for calculation efficiency at the cost of reliability of the results. However, this test case can still serve as a first validation test for the implementation of XRS $L_{2,3}$ calculations in the modified XSpectra module.

Indeed, as explained before, the XRS transition operator for small $\boldsymbol{q}$ norm value (more precisely, in the $qr \ll 1$ limit) is equivalent to the dipole part of the XAS transition operator, save for a constant factor. This result stems partly from the fact that in this limit, the monopole contribution to the XRS spectrum is expected to be negligible (see section 4.1.3 for more details). Thus, calculation of the XRS Cu $L_{2,3}$ edge as described in this test case will not only allow to quickly check that the modified XSpectra module runs properly, but also that it calculates the expected spectrum, at least for low q values. In practice, this check consists in comparing the XRS Cu $L_{2,3}$ edge, calculated by the modified XSpectra module, to the XAS Cu $L_{2,3}$ edge, calculated by the XSpectra module of the current official version of Quantum ESPRESSO, in which the XAS $L_{2,3}$ edge calculation is already implemented, and detailed in Bunau et al. (60). Moreover, this test case also allows checking that the calculated L_2 and L_3 edges are equivalent, and the branching ratio value, that is to say the ratio of the intensity of the L_2 edge over the intensity of the L_3 edge. Indeed, we remind about the fact that for our calculation relying on a DFT framework, i.e a single particle approach, where the electrons are not explicitly interacting with each other, the L_2 and L_3 edges should be equivalent and that the branching ratio should be 1:2, according to the degeneracy of the $2p_{1/2}$ and $2p_{3/2}$ states. Thus, while this test case (because it is no converged) does not yield reliable results for a physical study of solid Cu, it instead makes for an efficient first test to partly validate the implementation of XRS $L_{2,3}$ edge calculations in XSpectra.

The necessary SCF charge density calculation was performed for a unit cell of the material with no core hole, containing two atoms, as pure Cu crystallises in the face-centered cubic system. The energy cut-offs were set to 20 Ry and 200 Ry for the electronic wave functions and charge density, respectively. The Brillouin zone was sampled using a 3×3×3 k-points grid, as suggested by the test case. The XRS (or XAS, when needed) calculations were then performed, to calculate both the L_2 and L_3 edges separately. The calculations were performed for a small value of the norm of $\boldsymbol{q}$, in order to be compared with the XAS calculation performed using the same SCF calculation. More precisely, the q value was set to 0.5 Å^{-1}. The broadening parameter was set to 0.5 eV, for both XAS and XRS calculations. Both the monopole and dipole contributions were calculated for each edge. The isotropic dipole contribution is usually calculated as the average of three spectra, calculated in the dipole approximation, for $\boldsymbol{q}$ oriented respectively along the x, y and z axes. However, because of the fcc symmetry of the unit cell of Cu, calculation for one of those orientation was enough (chosen arbitrarily as the orientation along the x axis). Moreover, since the monopole contribution does not show any angular dependence as seen earlier (see section 4.2.1, eq. 4.29), it was only calculated for $\boldsymbol{q}$ oriented arbitrarily along the x axis. the total spectrum is calculated as the sum of the average dipole and monopole contributions. For XAS spectrum calculations, the L_2 and L_3 edges were calculated following the same process, replacing the indicated orientation of the scattering vector $\boldsymbol{q}$ by the same orientation of the polarisation vector $\hat{\varepsilon}$. Only the dipole contribution to the XAS $L_{2,3}$ edge was calculated.

The results of the calculations performed for this test case, using both the modified XSpectra module for the XRS spectrum calculations and the regular version of the XSpectra module for the XAS spectrum calculations, are shown in figures 4.4 and 4.5.

Figure 4.4 shows a comparison between the calculated XRS Cu L_2 and L_3 edge in solid Cu, calculated using the modified XSpectra module. The comparison clearly shows that the L_2 and L_3 edges are equivalent, and display 1:2 branching ratio. This confirms that after implementa-

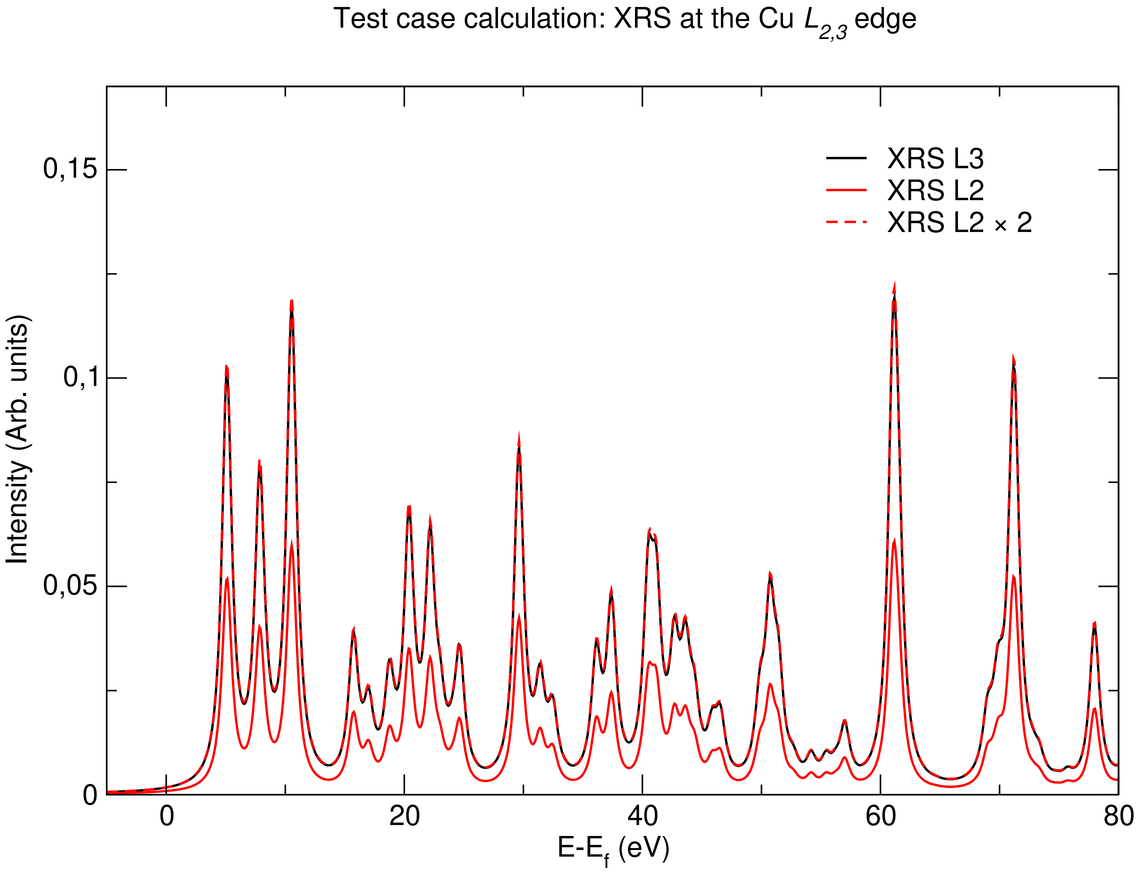

Figure 4.4: Comparison between the XRS spectra of solid Cu calculated at the Cu L_2 and L_3 edges. This figure illustrates how the test case calculations performed by the modified version verify the expected branching ratio between the L_2 and L_3 edges, i.e an intensity ratio between the L_2 and L_3 edges of 1:2. To clearly show this result, both the L_2 and L_3 edge spectra are shown separately, in red and black respectively, the L_3 edge spectrum having been slightly shifted vertically. The L_2 edge is also shown, after being multiplied by two, and in the same colour, as a dashed line spectrum over the L_3 edge spectrum.

tion of XRS $L_{2,3}$ edge calculation, the modified XSpectra module calculates L_2 and L_3 edges properly related to each other according to the expected branching ratio.

To obtain the complete $L_{2,3}$ edge, calculation of only one of the two edges, preferably the L_2 edge since it is computationally cheaper (less Lanczos algorithm loops needed), is needed. Indeed, the other edge can then be obtained from the calculated edge, which then allows to obtain the complete $L_{2,3}$ edge by performing elementary operations on the L_2 edge, as explained in section 4.1.4.2. After calculating the XRS Cu L_2 edge, the Cu L_3 edge was obtained by multiplying its intensity by two, and shifting it by -19.6 eV, which is the tabulated energy difference between the Cu L_3 and L_2 edges. Indeed, since in DFT the L_2 and L_3 edges are calculated at the same energy, this shift must be applied before summing the two edges, which is the final step to obtain the $L_{2,3}$ edge. The same process was used to obtained the XAS Cu $L_{2,3}$ edge from the calculated XAS Cu L_2 edge. The energies of the different edges were found in the Quantum ESPRESSO and compiled by Gwyn P. Williams using several references (65; 66; 67). Figure 4.5 shows the comparison of the XAS and XRS spectra calculated at the Cu $L_{2,3}$ edge. The XAS spectrum intensity was multiplied by a constant to match the intensity of the XRS spectrum. Since the L_3 edge is shifted by -19.6 eV compared to the L_2 edge, the energy range shown in figure 4.5 is also shifted by -19.6 eV compared to the energy range shown in figure 4.4. In other words, the L_2 edge energy zero would be at 19.6 eV in figure 4.5. This comparison thus clearly shows that for a low q value, the XAS and XRS spectra are equal, save for a constant intensity factor.

To summarise, the Cu test case allowed checking that two important and expected properties of $L_{2,3}$ edges were indeed verified for the calculated XRS spectra obtained using the modified version of XSpectra. First, the calculated XRS L_2 and L_3 are equivalent, and the intensity ratio between the L_3 and L_2 edges is 2:1. This is expected for calculations in a single particle framework. In a second time, we could also check that the XRS Cu $L_{2,3}$ edge calculated by the modified version of XSpectra for low q values is equal, save for an intensity factor, to the XAS Cu $L_{2,3}$ edge calculated by the regular version of the XSpectra module. This was also expected because of the equivalence of the dipole part of the XAS transition operator to the XRS transition operator in the small q value ($qr \ll 1$) limit. This allows partial validation of the implementation of XRS $L_{2,3}$ edge calculation in XSpectra. However, results also need to be

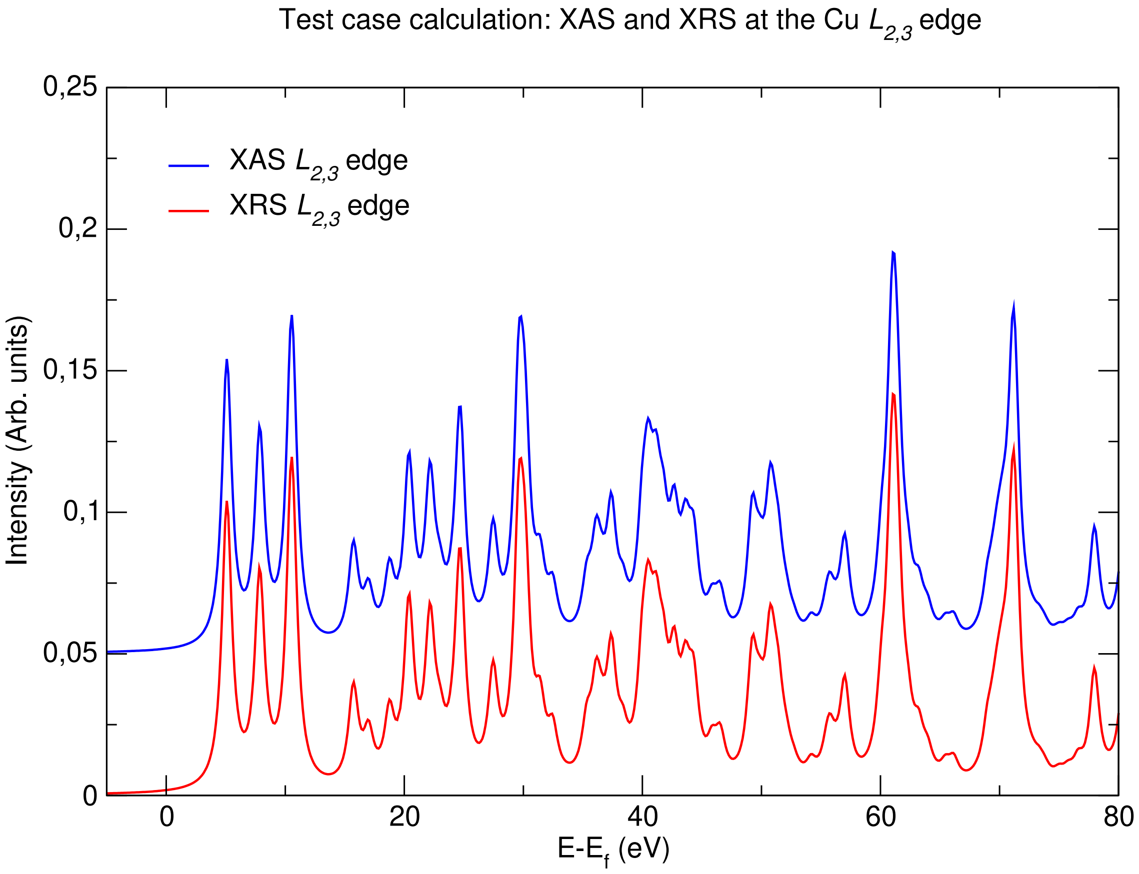

Figure 4.5: Comparison between the XAS (blue) and XRS (red) Cu $L_{2,3}$ edges in solid Cu. The XAS spectrum was slightly shifted vertically for an easier comparison. To be able to show the XRS and XAS $L_{2,3}$ edge spectra on the same energy range as Fig. 4.4, they were shifted by the energy difference between the L_3 and L_2 edges, i.e 19.6 eV.

compared to experimental data for a complete validation. Indeed, for instance, comparison with XAS $L_{2,3}$ edge spectra cannot validate the implementation in the case of calculation at higher q values, for which the XAS and XRS transition operators are no longer equivalent.

Thus, the two next sections are dedicated to studying the ability of the modified XSpectra module to calculate the XRS spectrum, at the S $L_{2,3}$ edge of $\mathrm{Li_2SO_4}$, and of pure sulphur in the α structure, respectively. More precisely, it is the ability of the modified XSpectra module to accurately reproduce measured XRS $L_{2,3}$ edge data, for different values of q and using different core hole approximations for the SCF charge density calculation preceding the spectrum calculation, that is studied in the next two sections. To do so, the spectra calculated by the modified version of the XSpectra module are compared to available experimental data, measured at the ID20 beamline of the European Synchrotron Radiation Facility (ESRF) for different values of q, as well as experimental XAS data found in literature.

4.3.2 Calculation at the S $L_{2,3}$ edge of $\mathrm{Li_2SO_4}$

In this section, the calculation of the S $L_{2,3}$ edge of $\mathrm{Li_2SO_4}$ performed using the modified version of the XSpectra module, for different q values, are detailed and then compared to the measured XRS S $L_{2,3}$ edge spectrum of $\mathrm{Li_2SO_4}$. $\mathrm{Li_2SO_4}$ crystallises in the the monoclinic system, with the studied structure in the $P2_1/a$ (n. 14) space group. The XRS spectrum of $\mathrm{Li_2SO_4}$ at the S $L_{2,3}$ edge was measured on a powder sample at the ID20 beamline of the European Synchrotron Radiation Facility (ESRF). Since the spectrum was measured for different values of the scattering vector $\boldsymbol{q}$, the measured data was very interesting to assess the capability of the freshly modified XSpectra module to reproduce the q dependence of XRS $L_{2,3}$ edges.

4.3.2.1 Computational details

Though DFT does not allow to explicitly treat core hole electron interactions, several approximations were tested for the SCF calculations performed with a core hole on the absorbing S atom. More specifically, spectra were calculated using SCF charge density calculations performed in the FCH (Full Core Hole) and XCH (eXcited Core Hole) approximations, as well as SCF calculations with no core hole present on the absorbing S atom, referred to as GS calcula-

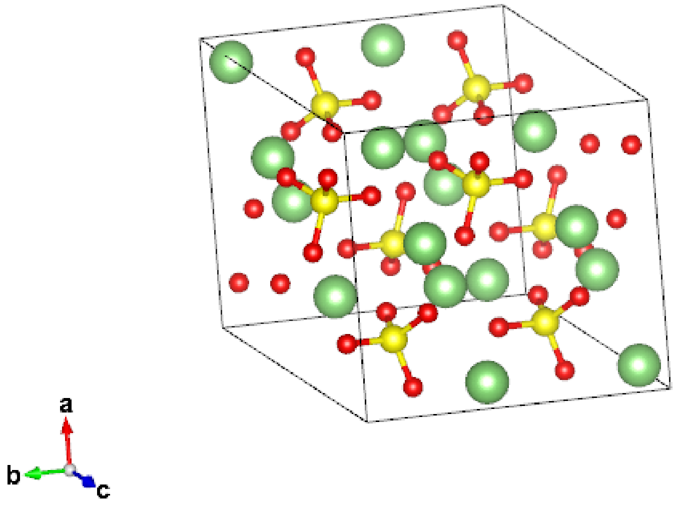

Figure 4.6: Image of the 1×2×1 supercell of $\mathrm{Li_2SO_4}$ used to perform the SCF charge density calculation. The sulfur atoms, in yellow, are in tetragonal coordination with the surrounding oxygen atoms, in red. The image was obtained using Vesta.

tions. In so doing, the effect of these different core hole 'modelling' in DFT on the calculated XRS $L_{2,3}$ edge spectrum could be studied. In the FCH approximation, the excited $2p$ electron is promoted to the continuum and the missing charge is compensated by a background negative charge. In the XCH approximation, the material is still neutrally charged because the excited $2p$ electron is instead promoted to the lowest unoccupied level. The core hole present on the absorbing S atom needed to be isolated during the SCF calculations, so that it did not interact with its periodic replications. To do so, a supercell was created from the unit cell of the material.

Thus, SCF calculations were performed, at the Γ point of the Brillouin zone, on a $1{\times}2{\times}1$ supercell of the material, containing 56 atoms. The cell parameters were as follow: $a = 8.25$ Å, $b = 9.90$ Å, $c = 8.44$ Åand $\beta = 107.9$ °. The pseudopotentials used for the different atoms were taken from the PSLIBRARY, and generated following the RRKJ (Rappe, Rabe, Kaxiras and Joannopoulos) formalism. In the case where the absorbing atom had a $2p$ core hole, the occupancy of the $2p$ shell was reduced by one. The energy cut-offs were set to 60 Ry and 720 Ry for the electronic wave functions and charge density, respectively. Fig. 4.6 shows an image of the Li2SO4 supercell.

The spectrum calculations were performed using a $4{\times}4{\times}4$ k-points grid sampling the Brillouin zone. The total dipole contribution was calculated as the average between three individual dipole contributions, calculated for $\boldsymbol{q}$ oriented along the x, y and z axis respectively, while the monopole contribution was calculated for $\boldsymbol{q}$ oriented along the arbitrarily chosen x axis, since the monopole contribution does not show any angular dependence. The final spectrum was then calculated as the sum of the total dipole and monopole contributions. To reproduce the different values of q at which the XRS S $L_{2,3}$ edge of Li_2SO_4 was measured (equal to, according to the experimenters, approximately 3.5, 6.3 and 8.1 Å^{-1}), the spectrum was calculated for q values of 2, 6 and 9 Å^{-1}, and are referred to as calculated at 'low', 'medium' and 'high' q values in what follows. Calculations were performed for the L_2 edge, and then used to obtain the L_3 edge by multiplying its intensity by two, and shifting its energy by -1.1 eV, which is the tabulated value of the energy difference between the L_2 and L_3 edges found in Quantum ESPRESSO. The $L_{2,3}$ edge was then obtained as the sum of the L_2 and L_3 edges, after interpolating the energy values of the L_2 edge on those of the L_3 edge to make the sum possible. To be compared with experiment, spectrum calculations using FCH SCF calculations were performed using a varying broadening parameter over the spectrum energy range. The broadening parameter starts at a value of 0.5 eV in the first 20 eV of the spectrum, then ramps up linearly to 3 eV for the next 10 eV, before staying constant at 3 eV for the rest of the spectrum energy range. When studying the effects of the core hole approximation on the calculated spectrum, a constant broadening parameter of 0.5 eV, which was found to properly reproduce the A feature broadness (see Fig. 4.7, was used instead.

Finally, to compare the total spectra obtained for the different q values and the experimental spectra whose areas were normalised in the measured energy range, the calculated spectra areas were also normalised, using the area of a reference spectrum, over the same energy range. The reference spectrum was arbitrarily chosen as the experimental spectrum measured for the lowest q value. The measured spectra were also shifted in energy, to match the first peak of the measured spectrum, located at around 174 eV. The results obtained after the calculations are presented in the rest of this section.

4.3.2.2 Comparison between calculations and experiment

Figure 4.7 shows a comparison of the measured and calculated XRS S $L_{2,3}$ edge of Li_2SO_4. The spectra calculated using the FCH approximation for the core hole were chosen since they best reproduce the measured data, especially at low q values. The measured spectra mainly contains

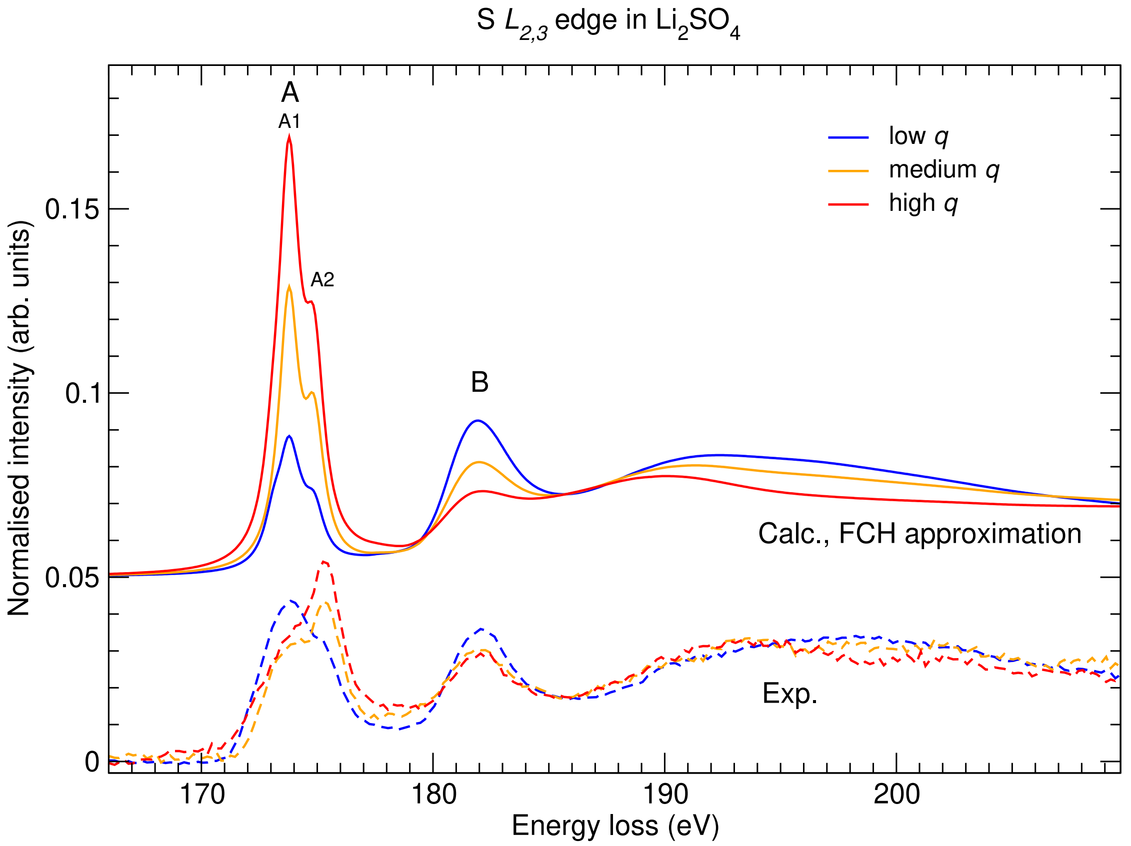

Figure 4.7: Comparison of the XRS spectrum of Li_2SO_4, measured (dotted lines) and calculated at (solid lines) the S $L_{2,3}$ edge. The blue, orange and red colours are used to refer to spectrum measured or calculated at a low, medium or high norm of the scattering vector $\boldsymbol{q}$.

two spectral features in the measured energy range, named A and B, respectively located at roughly 174 and 182 eV. The A feature contains two distinct peaks, noted A1 and A2 separated by about 1.5 eV, while the B feature is formed by a single and slightly broader peak. The A and B features show a clear variation as the value of q increases, far more pronounced than the variation of the spectra in the rest of the measured energy range. This is especially true for the A feature. Measured data shows that the A feature becomes more intense at higher q values. Moreover, the relative intensities of the two peaks in the A feature change so that the A2 peak, lower than the A1 peak at low q value, becomes more intense for higher q values. On the contrary, as the q value increases, the intensity of the B feature as well as the tail of the spectrum gets lower. This causes the B feature intensity, higher than the A feature intensity for the lowest q value, to become lower for the two higher q values. The calculation manages to reproduce the measured spectra with good accuracy regarding several points. The general shape of the spectrum, that is to say, the energy placement of the A and B features, as well as the shape of the tail of the spectrum, is accurately reproduced. The separation of the A feature into two separate peaks is also well reproduced. The low q spectrum, especially, is reproduced with a very good accuracy, the only problem being that the relative intensity of the A and B features. While measurement at low q values show that the A feature is slightly higher in intensity than the B feature, the calculated spectrum reproduce for the lowest q value a B feature slightly higher in intensity than the A feature. Regarding the q value variation of the spectrum, though the variation is more intense than for the measured spectra, the calculation manages to reproduce the decrease of the B feature intensity as q increases. The slight decrease of intensity of the tail of the spectrum is also reproduced. However, the q variation of A feature is not accurately reproduced. Indeed, the reproduced intensity variation of the A feature is far greater than the measured one. Moreover, the fact that the first peak of the A feature is first more intense than the second peak, which is then reversed as q increases with the second peak of the A feature becoming more intense is not reproduced at all. The reproduced A feature always shows the first peak higher in intensity than the second peak, with a roughly constant relative intensity.

4.3.2.3 Decomposition of the calculated spectra

Fig. 4.8 and Fig. 4.9 show the decomposition of the calculated XRS spectra shown in Fig. 4.7, into the separate L_2 and L_3 edges, and into the monopole and dipole contributions to the $L_{2,3}$ edge, respectively. Fig. 4.8 allows to highlight that the A1 and A2 peaks of the A feature in the calculated $L_{2,3}$ spectrum stem from the L_3 and L_2 edges, respectively, in the case of the spectra calculated in the FCH approximation. This is true for all q values used to calculated the S $L_{2,3}$ edge spectrum. Moreover, it allows to understand why only the A feature is split in two peaks while the B feature consists in a broader peak. Indeed, the B peaks of the L_3 and L_2 edges are broader than the A feature of the individual L_3 and L_2 edges. Moreover, the energy difference between the S L_2 and L_3 edges is only 1.1 eV. Thus, the sum of the L_2 and L_3 edges yields a seemingly non-split and broader B feature while it yields a split A feature, for which clear separation of the individual A peaks from the L_2 and L_3 edges, which are narrower than the B peaks, is made easier. Fig. 4.9 shows the variation of the dipole and monopole contributions to the S $L_{2,3}$ edge spectrum as the value of q increases. It allows to highlight how, at low q values, the spectrum is largely dominated by the dipole contribution (i.e by $p \rightarrow s$ and $p \rightarrow d$) electronic transitions, shown in blue, while the monopole ($p \rightarrow p$ electronic transitions) contribution is virtually zero. This is part of the reason why the XRS S $L_{2,3}$ edge spectrum equivalent to the XAS S $L_{2,3}$ edge spectrum for low q values. It also highlights how, in contrast, the calculated XRS spectrum quickly becomes dominated by the monopole contribution (i.e by $p \rightarrow p$ electronic transitions). Indeed, as the q value increases, the figure clearly shows how the red contribution to the total spectrum becomes predominant compared to the blue contribution to the total spectrum. More precisely, the shape of the A feature, entirely stemming from the dipole contribution at low q values, becomes largely dominated by the monopole contributions for the medium and high q values. The A feature is the part of the spectrum that changes the most as the value of q increases. It can thus be argued that the monopole contribution, thanks to its increase in intensity relatively to the dipole contribution intensity, is the main factor behind the variation of the XRS S $L_{2,3}$ edge spectrum of $\mathrm{Li_2SO_4}$ as the value of q increases. Additionally, while the B feature and the tail of the spectrum are not as dominated by the monopole contribution at medium and high q values as the A feature, they still correspond to an equal mixing of the monopole and dipole contributions, instead of just stemming from the dipole contribution.

To summarise, Fig. 4.9 thus highlights that the variations of the calculated XRS S $L_{2,3}$ edge spectrum with an increase in the q value mainly stems from the varying relative weights of the monopole and dipole contributions to the spectrum. While the spectrum calculated for the low q value is largely dominated by the dipole contribution, the monopole contribution rapidly becomes the dominant contribution to the spectrum, and especially to the A feature, at high q values. This strong variation of the relative weights of the dipole and monopole contributions to the calculated spectrum with the value of q was also observed for calculations based on solving the Bethe-Salpeter equations, in the case of the Na and Si XRS $L_{2,3}$ edge spectrum of a polycrystalline sample of Na and pure Si, respectively (64).

In summary, this section shows that calculations performed by the modified XSpectra module and using the FCH approximation manage to reproduce the measured XRS S $L_{2,3}$ edge spectra at low q values (where it is equivalent to the XAS S $L_{2,3}$ edge spectrum), as well as its variations, with increasing values of q, of the spectrum for the B feature energy range and higher. In contrast, the variation of the A feature as the value of q increases is not reproduced accurately. More precisely, for low q values, calculations show the A feature to be the sum of two separate contributions from the L_3 and L_2 edges, only slightly overlapping each other. The A1 peak is indeed shown to stem mainly from the L_3 edge and the A2 peak from the L_2 edge. The measured A1 and A2 peaks are separated by approximately the same energy as the calculated A1 and A2 peaks, which is the tabulated energy difference of the L_3 and L_2 edges. Moreover, the relative intensity ratio of the measured A1 and A2 peak is approximately the same as the relative intensity ratio of the calculated A1 and A2 peaks. Thus, the measured A feature can be considered as the sum of the L_3 and L_2 edge contributions, slightly overlapping each other, which give rise respectively to the A1 and A2 peaks, with the expected branching ratio of 2:1 between the L_3 and L_2 edge contributions (i.e the L_3 edge contribution is two times more intense as the L_2 contribution). However, for higher q values, this description of the A feature which still applies to the calculated A feature, does not allow to reproduce the measured A feature accurately. Indeed, though the energy separation of the A1 and A2 peaks is still consistent with the energy difference between the L_3 and L_2 edges, the relative intensities of the A1 and A2 peaks, which is reversed as the value of q increases, no longer allow the measured A feature to be simply described as the sum of the L_3 and L_2 edge contributions, each contributing

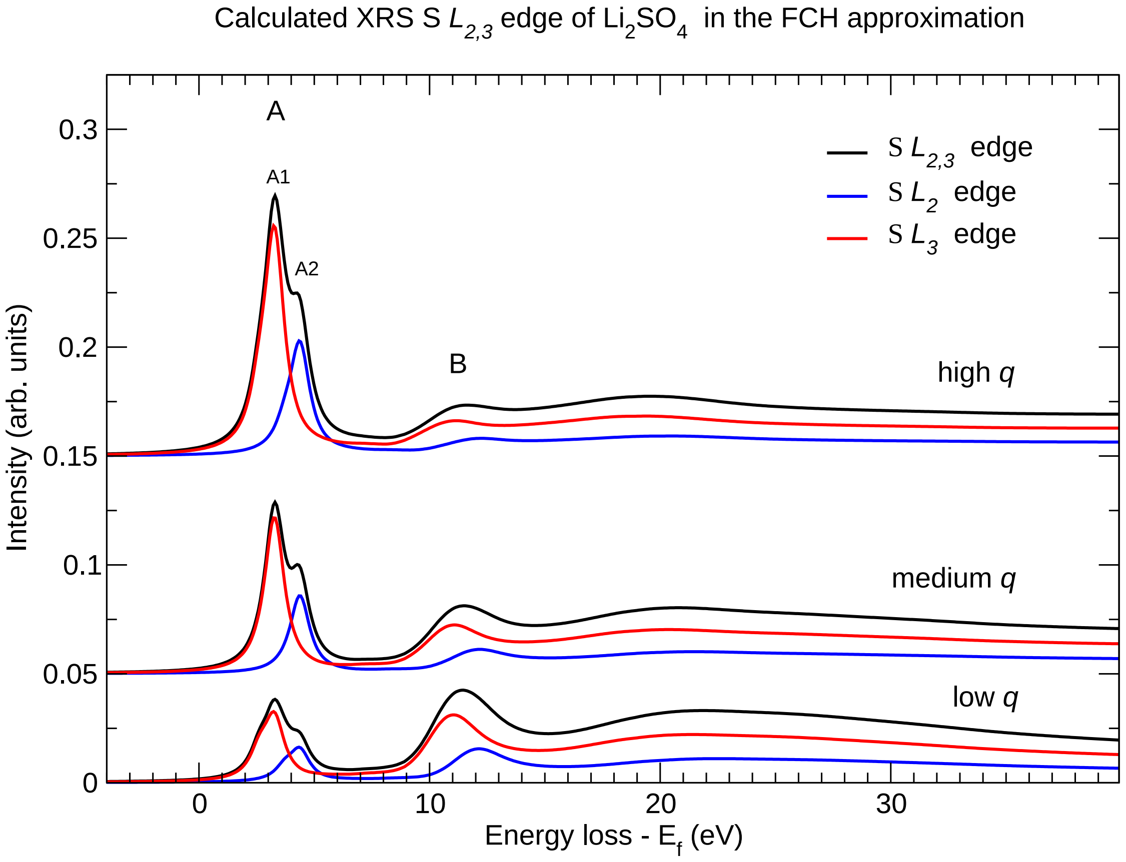

Figure 4.8: Decomposition of the calculated XRS spectrum of Li_2SO_4, calculated at the S $L_{2,3}$ edge, and using the FCH approximation for the core hole treatment for the SCF charge density calculation, into the separate L_2 and L_3 edges, for all q values. The black, blue and red colours refer to the total $L_{2,3}$ edge, and single L_2 and L_3 edges, respectively. The total spectrum calculated for the low, medium and high q values are normalised on the shown energy range, and the respective L_2 and L_3 edge contributions are multiplied by an intensity factor consistent with the applied normalisation.

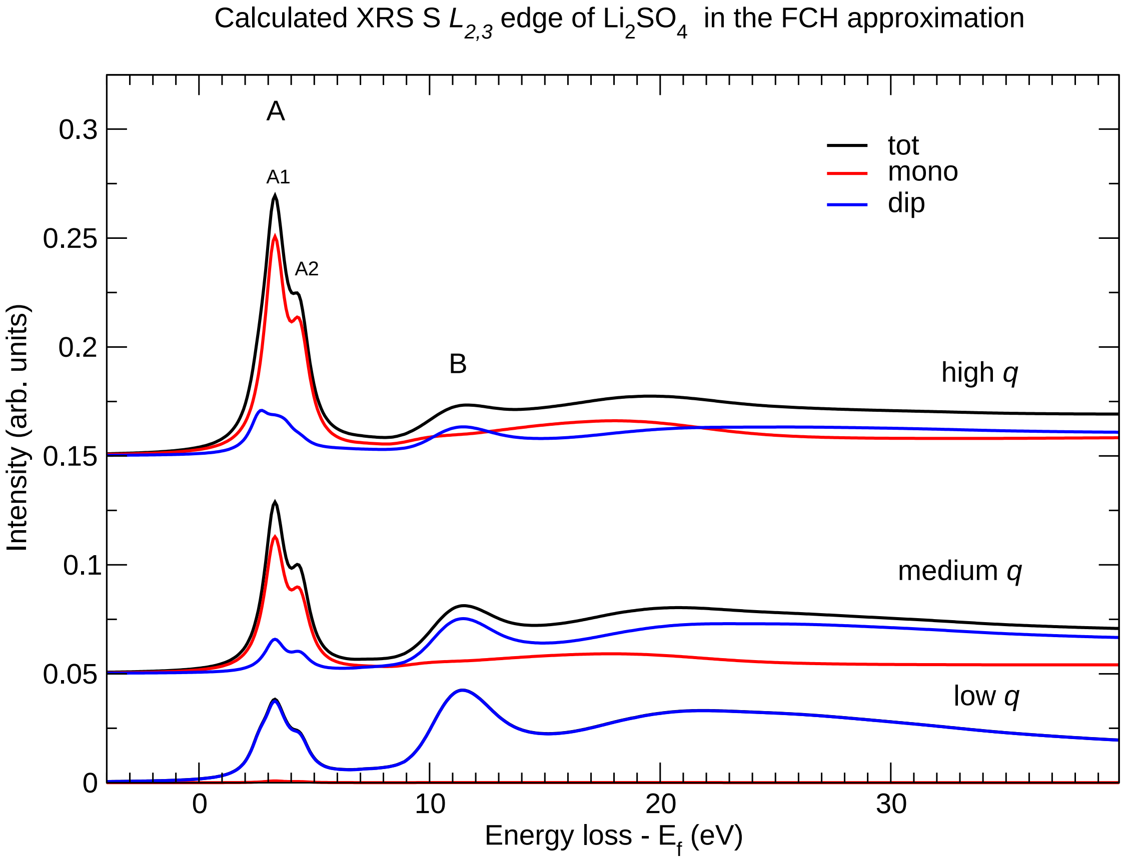

Figure 4.9: Decomposition of the calculated XRS spectrum of Li_2SO_4, calculated at the S $L_{2,3}$ edge, and using the FCH approximation for the core hole treatment for the SCF charge density calculation, into the separate monopole and dipole contributions, for all q values. The black, blue and red colours refer to the total $L_{2,3}$ edge, and single L_2 and L_3 edges, respectively. The total spectrum calculated for the low, medium and high q values are normalised on the shown energy range, and the respective monopole and dipole contributions are multiplied by an intensity factor consistent with the applied normalisation.

to only to the A1 and A2 peak respectively. That does necessarily mean, however, that the 2:1 branching ratio, yielding good results for low q values, changed for high q values. Indeed, while this would mean that DFT, always yielding a 2:1 branching ratio, could not properly describe the measured spectrum at high q values, there is little reason the increase of the value of q could change the branching ratio, which only changes from the 2:1 value when many electrons effect come into play. Instead, since the A feature becomes dominated by the monopole contribution as the value of q increases, the inability to reproduce the variations of the A feature measured as q increases are more likely related to not properly reproducing the monopole contribution, at least for high values of q.

To complete the analysis provided by the separation of the calculated XRS spectrum into the separate L_2 and L_3 edges as well as into its dipole and monopole contributions, the effect of the core hole approximation used in the SCF charge density calculation previous to the spectrum calculation is explored. This allows to assess the effect of each possible core hole approximation on the ability of the modified XSpectra module to reproduce the measured signal, for different values of q. Moreover, PDOS (Projected Density Of States, where the partial density of states is projected on the absorbing atom) calculations were performed on the supercell of the material, using a 4×4×4 k-points grid to sample the Brillouin zone, and using a 0.5 eV broadening parameter. This allows to identify each feature in terms of electronic transitions, especially for the A peak, for which calculation apparently cannot accurately reproduce the variations for an increasing value of q.

4.3.2.4 Effects of the different core hole approximations on the calculated spectrum

The effects of the different core hole approximations on the calculated spectrum is shown in Fig.4.10. From top to bottom, respectively, the calculated XRS S $L_{2,3}$ edge spectrum using the GS, XCH and FCH core hole approximations are shown, for the same three q values used to calculate the spectra shown in the previous comparison to the measured XRS data. The broadening parameter was kept at a constant 0.5 eV for these calculations. Fig. 4.10 shows that the FCH and XCH approximations yield virtually identical spectra, save for the fact that the B feature seems to split more clearly in two peaks in the XCH approximation, while for the FCH approximation the B feature still appears as a single wide peak. This stems from

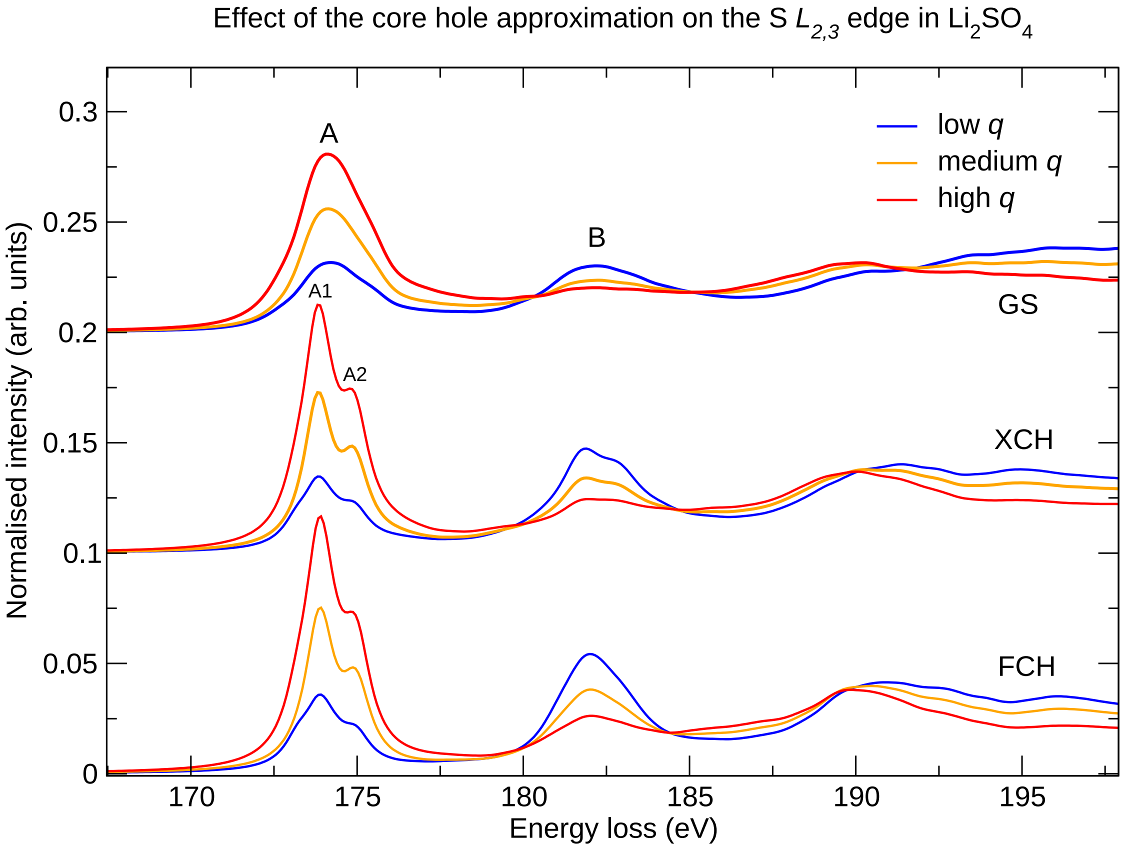

Figure 4.10: Comparison of the XRS spectrum of Li_2SO_4, calculated at the S $L_{2,3}$ edge, using several approximations for the core hole treatment for the SCF charge density calculation. The blue, orange and red colours are used to refer to spectrum measured or calculated at a low, medium or high norm of the scattering vector $\boldsymbol{q}$. The spectra calculated for different core hole approximations were shifted vertically for more clarity.

the fact that while using the XCH approximation, the calculated B peaks of the L_2 and L_3 edges are slightly less broad than those calculated using the FCH approximation, which leads to the L_2 and L_3 edge contributions to the $L_{2,3}$ B feature to be more clearly separated. The GS approximation, in contrast, leads to the A feature resembling more a single peak, while in calculations performed using the FCH and XCH approximations, as well as in the measured data, the A feature clearly is split in two different peaks. This stems from the GS approximation yielding broader A peaks in the individual L_2 and L_3 edges. The GS approximation also yields a less intense and broader B feature in the calculated spectrum, than the B features in the spectra obtained using the FCH and XCH approximations. Looking at the variations of the spectrum as q increases, for all core hole approximations, the same changes to the calculated spectrum as q increases are observed. With an increasing q value, the A feature intensity greatly increases while the intensity of the B feature, and of the spectrum at higher energies, decrease. This is consistent with the previous comparison between calculated and measured data. Astudying the core hole approximation effects on the calculated spectrum shows that the FCH approximation proves a better approximation for comparison with the experiment at lows q values. However, though the variation of the B feature and of the high energy range spectrum is well reproduced using the FCH approximation, none of the core hole approximations allows reproducing the inversion of the relative intensity of the A1 and A2 peaks of the A feature as q increases, and which was described earlier.

4.3.2.5 Projected density of states calculations

Fig. 4.11 shows a display of PDOS, shown with the XRS S $L_{2,3}$ spectra calculated for the three q values, and using the FCH approximation for the core hole modelling, as a reference for the energy placement of the A and B features. PDOS calculations allow to see the energy distribution of partial density of states, projected on the absorbing atom, on the energy range of the calculated spectrum. This figure thus provides the origin of the A and B features in terms of electronic transitions. It can also help explain the differences between the spectral features A and B in the spectra calculated using the FCH, XCH and GS approximations. For all core hole approximations adopted for the SCF charge density calculation, the figure shows that the A feature stems mainly from electronic transitions to p states, and in a less pronounced manner on

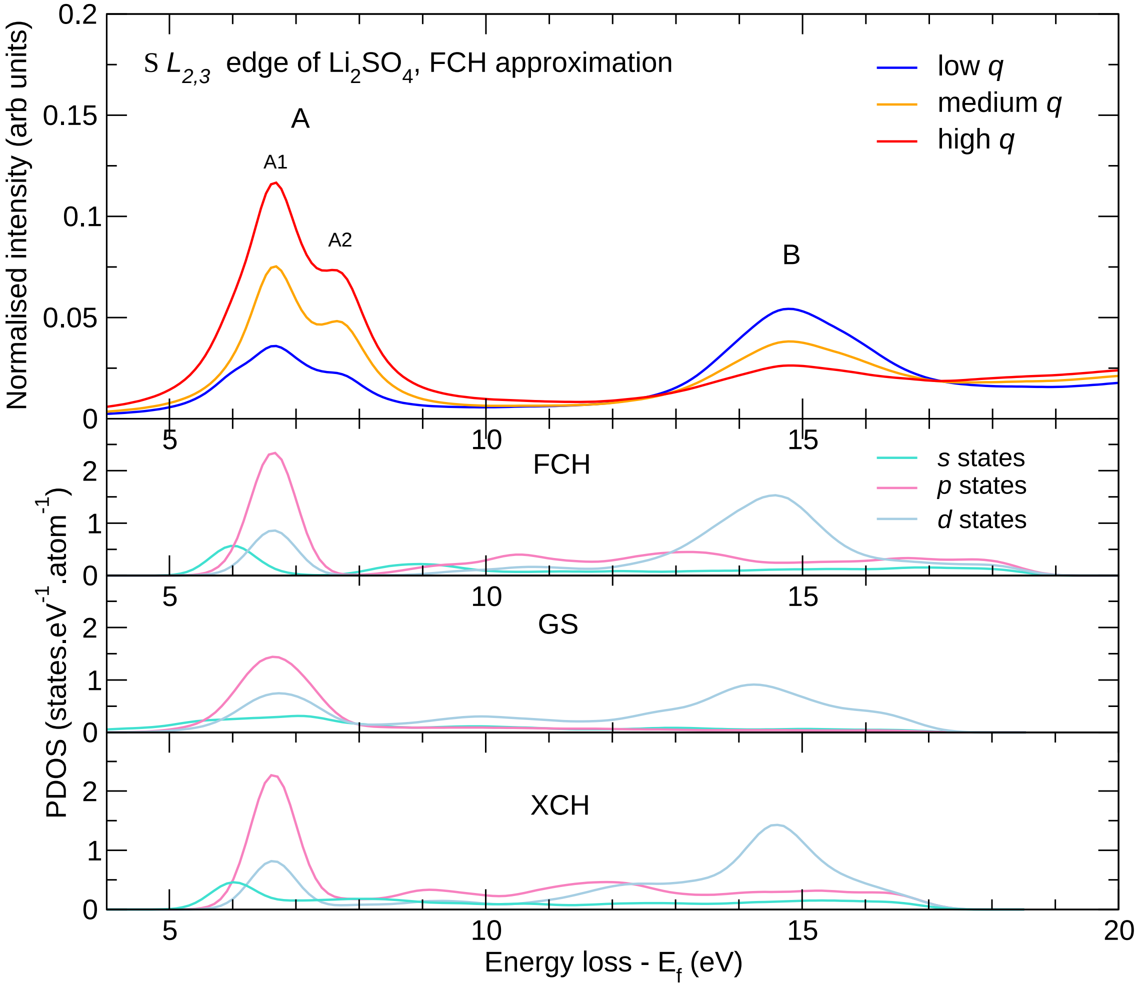

Figure 4.11: Calculation of density of states projected on the absorbing S atom. The spectrum calculated using the FCH approximation is also shown on the top panel, for energy placement of the A and B features. Then, from top to bottom, the panels display the s, p and d, density of states projected on the absorbing S atom, for a core hole described in the FCH, GS and XCH approximation, respectively.

transitions to s and d states. In contrast, the B feature mainly stems from electronic transitions to d states and, in an even less pronounced manner, transitions to s and p states. In the case of calculations performed using the GS approximation, it should be noted that the energy range of the B feature is almost devoid of s and p states. The described energy distribution of the s, p and d states suggests that the high variation of the A feature is correlated with a strong density of p states, which is consistent with the previous discussion, where we showed how the variation of the spectrum with the increase of the value of q was mainly caused by the rapidly changing relative weights of the monopole ($p \rightarrow p$ transition channel contribution) and dipole ($p \rightarrow s$ and $p \rightarrow d$ transition channel contribution) contributions to the total spectrum. The strong density of d states in the B feature energy range explains why, even when the monopole contribution dominates the spectrum at high q values, the dipole contribution still contributes to the B feature in a non-negligible way. Overall, SCF charge density calculations performed in the GS approximation lead to states being located on larger energy intervals, which in turns lead to the broader spectral features of the spectrum compared to the spectral features of spectrum calculated using the FCH or XCH approximation. This in turn leads, as discussed earlier, to a single peak A feature for the S $L_{2,3}$ edge spectrum calculated using the GS approximation, as opposed to the S $L_{2,3}$ edge spectra calculated using the FCH or XCH approximations, where the A feature is split in the A1 and A2 peaks, each peak stemming from the L_3 and L_2 edge, respectively. The density of the s p and d states, at the energies of the A feature, are virtually identical for the FCH and XCH approximations, which explains the identical A feature calculated using both these approximations, and displayed in Fig 4.10. In contrast, the d states occupy a broader energy range around the B feature energies in the case of the FCH approximation than in the case of the XCH approximation. This leads, as discussed earlier, to the B feature appearing split in the spectrum calculated using the XCH approximation while it appears as a single peak in the spectrum calculated using the FCH approximation. The differences between the PDOS calculated in the FCH and XCH approximations and the PDOS calculated in the GS approximation can be attributed to the attractive effect of the presence of a core hole on the excited atom. Indeed, as seen in the previous chapter, the presence of a core hole on the excited atom attracts the empty states at lower energies and localises them in a sharper energy distribution. We would like to note that since the spectra calculated using different core hole approximations were shifted independently in energy to best match the measured spectra, the relative placement of empty states calculated with different core hole approximations should not be taken into account, as the PDOS were subjected to the same energy shift. This is why, though the core hole should attract empty states at lower energies, all the PDOS appear at similar energy ranges. Only the change of shape of the energy distribution of the empty states, or the relative placement of different empty states calculated for the same core hole approximations, should be considered here.

Thus, PDOS calculations allows not only to confirm the previous discussion regarding the origin of the variation of the XRS S $L_{2,3}$ edge of Li_2SO_4 with the increase of the value of the norm of the scattering vector, q, but also to explain the origin of the A and B features in terms of electronic transitions. More importantly however, they also allow to explain the differences between the shapes of the calculated spectra obtained using the different core hole approximations (GS, FCH and XCH). More specifically, the differences between the calculated PDOS for each approximation can be studied in the energy range of the A feature, to try and understand the precise reasons behind the change of shape of the A feature when using the XCH or FCH approximation, rather than the GS approximation. Indeed, while the A features of the spectra obtained using the FCH and XCH approximations are virtually identical, they are however very different from the A feature obtained using the GS approximation as discussed earlier. PDOS calculations show that the XCH and FCH approximation lead to the same energy distribution of the density of s, p and d states in the A feature energy range, but in contrast very different from the density of s p and d states energy distribution obtained using the GS approximation. More precisely, the s states are placed at slightly lower energies (0.5 to 1 eV) than the p states in the FCH and XCH approximations. In the GS approximation, on the contrary, the s and p states occupy the same range, and are distributed on a larger energy interval. Thus, the difference between the shapes of the A feature of the spectra obtained using the XCH or FCH approximation and the A feature of the spectrum obtained using the GS approximation is caused by both a different relative energy placement of the s and p states, as well as the s and p states occupying a larger energy interval in the case of the GS approximation than in the case of the XCH or FCH approximation. In other words, calculations failing to reproduce the correct relative energy placement of the monopole and dipole contributions, as well as the correct broadness of these contributions to the A feature, may be responsible for failing to reproduce the evolution of the A feature as the value of q increases. The results suggest that the energy placement and the energy size of the monopole contribution, more specifically, are of paramount importance to properly reproduce the evolution of the A feature as q increases. Indeed, it was shown in previous discussions that the monopole contribution to the A feature quickly dominates the dipole contribution to the A feature when the value of q increases.

4.3.2.6 Conclusion

To summarise, using the FCH approximation for the core hole, calculations by the modified XSpectra module allow to reproduce accurately the XRS S $L_{2,3}$ edge spectrum of $\mathrm{Li_2SO_4}$ for low q values. The variation of the B feature as well as of the high energy range of the spectrum as the value of q increases is also reproduced. However, calculations performed using any of the core hole approximation fail to accurately reproduce the evolution of the A feature as the value of q increases. Indeed, at low q values, calculations show that the separation of the measured A feature into the A1 and A2 peaks stem from the clear separation between the L_3 and L_2 edges contributions to the $L_{2,3}$ edge, respectively, and that their relative intensities is consistent with the 2:1 branching ratio expected theoretically in a single electron scheme such as DFT. With the increase of the value of q however, the relative intensities of the A1 and A2 peak is reversed, which means that the scheme where the A1 and A2 peaks stem from separated L_3 and L_2 contributions, with a 1:2 branching ratio, and which yields good results for low q values, does not hold anymore for higher q values. Calculations showed that the monopole contribution becomes the dominant contribution to the A feature at higher q values.

PDOS calculations and spectrum decompositions showed that it is likely that the inability to reproduce the measured evolution of the A feature as the value of q increases is caused by the inability of the XCH, GS or FCH approximation to properly reproduce the correct energy placement of the monopole contribution to the A feature, relatively to the dipole contribution, as well as the broadness of the monopole contribution to the A feature. Indeed, the dipole contribution of the XRS S $L_{2,3}$ edge spectrum is well reproduced at low q values when using the FCH and XCH approximations, which indicate that the presence of a core hole lead to accurate reproduction of the empty s and d energy distribution in the A feature energy range.

In other words, the failure to reproduce the correct energy distribution of the empty p states, specifically, in the presence of a core hole. It is thus possible that this problem is more closely related to the limitations imposed by the theoretical framework Quantum ESPRESSO is based on. Since, however, no satisfactory agreement was obtained at high q values, it is difficult at this stage to draw definitive conclusions. To continue exploring the capacity of the modified XSpectra module to reproduce XRS measured data at the S $L_{2,3}$ edge, and more specifically the measured change of these data as the value of q increases, calculations were also performed for pure sulphur in the alpha structure, and compared to experimental data measured at the ID20 beamline of ESRF.

4.3.3 Calculation at the S $L_{2,3}$ edge of S_8 in the α structure

The modified XSpectra module was also used to calculate the XRS S $L_{2,3}$ edges of α-sulphur (chemical formula S_8), as measured data was also available for different values of the norm of the scattering vector $\boldsymbol{q}$. This also meant that the ability of the modified XSpectra module to reproduce the variations of the measured spectrum with an increase of the value of q could be further tested. The XRS spectrum of α-sulphur was measured at the S $L_{2,3}$ edge at the ID20 beamline at the ESRF different values of q: 2.1, 4.0, 5,3, 8.0 and 12.0 Å^{-1}.

4.3.3.1 computational details

To calculate the XRS S $L_{2,3}$ edge of α-sulphur, a similar calculation process as the one used to calculate the XRS S $L_{2,3}$ edge of Li_2SO_4 was used. The SCF calculations needed for spectrum calculation were performed on the unit cell containing 128 atoms, at the Γ point of the Brillouin zone. α-sulphur, which is the most common form of S_8 found in nature, crystallises in the orthorombic system, in the space group 70 ($Fddd$). The cell parameters of the unit cell are as follow : $a = 10.46460$Å^{-1}, $b = 12.86600$ Å^{-1}, $c = 24.48600$ Å^{-1}. The SCF calculations were once again performed using the GS, XCH and FCH approximations to model the core hole, so that the effect of those different approximations on the calculated XRS $L_{2,3}$ edges could be assessed. However, given the size of the unit cell, no supercell was needed to isolate the core hole from its periodic replications, as they were separated by at least 10 Å^{-1}. The

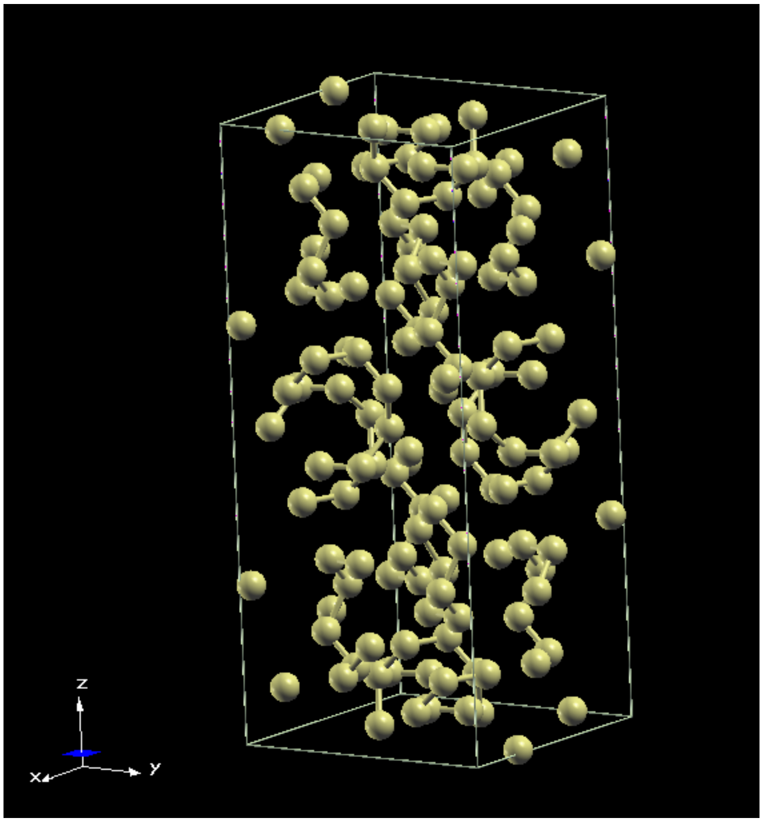

Figure 4.12: Image of the unit cell of α-sulphur used to perform the SCF charge density calculation, obtained using the XCrysden program. The sulphur atoms form cycles of 8 atoms.

pseudopotential used to describe the S atom was taken from the PSLIBRARY and generated using the RRKJ formalism (same pseudopotential as the one used in the previous section). When a core hole was included on the absorbing atom, the pseudopotential was generated with an occupancy on the $2p$ shell reduced by one. The energy cut-offs for the electronic wave functions and charge density were once again set to 60 Ry and 720 Ry, respectively. However, unlike the structure of Li_2SO_4, the α-structure of pure sulphur presents four non-equivalent possible sites for the S atoms, and thus SCF calculations were performed independently for each of these possible sites. Fig. 4.12 shows an image of the unit cell of α-sulphur.

Spectrum calculations were then performed using the modified XSpectra module, using the SCF calculations performed for each non-equivalent site. They were performed using a $4\times4\times4$ k-points grid to sample the Brillouin zone, and a constant broadening parameter of 0.5 eV, which yielded good results in the previous case of Li_2SO_4. The monopole contribution was calculated for an arbitrary orientation of the scattering vector $\boldsymbol{q}$ while the dipole contribution was obtained as the average of the spectra calculated for $\boldsymbol{q}$ oriented along the x, y and z axis, respectively.

For each non-equivalent site, the total spectrum was then obtained by summing the monopole and dipole contributions. The final spectrum was then obtained by a weighted sum of the total spectra obtained for each non-equivalent site. Since all the non-equivalent sites have the same multiplicity in the unit cell (i.e there are 32 S atoms in each type of non-equivalent sites in the unit cell), then the spectra calculated for each of the sites were given the same weight and the final spectra was simply obtained as an average of the total spectra calculated for each of the sites. Before averaging, because the SCF calculation does not calculate absolute energies, the spectra calculated for each inequivalent site must be shifted in energy, with respect to an arbitrary spectrum (chosen as spectra obtained for the first inequivalent site), using the ΔSCF procedure for compounds with multiple inequivalent sites, already described in section 3.3.2.2. To match the different values of the norm of the scattering vector $\boldsymbol{q}$ for which the spectrum was measured, the S $L_{2,3}$ edge spectrum was calculated for q values of 2.1, 4.0, 5,3, 8.0 and 12.0 Å^{-1} when using the GS approximation, as preliminary calculations for a 'low' and 'high' q value ($q = 4.0$Å^{-1} and $q = 12.0$Å^{-1}, respectively) suggested a better general agreement with experiment when using this approximation rather than the others. When using the FCH and GS approximation, the spectrum was only calculated for $q = 4.0$ Å^{-1} and $q = 12.0$ Å^{-1}, so that a spectrum was available at a 'low' and 'high' value of q, making the study of the effects of the different core hole approximations on the calculated spectrum possible at these two values of q..

Only the XRS S L_2 edge spectrum of α-sulphur was calculated following the above indications. Indeed, once it was also verified for this compound that the expected relation was obtained between the calculated L_2 and L_3 edges, the L_3 edge was from this point obtained from the L_2 edge by multiplying its intensity by two and shifting its energy towards lower energies by 1.1 eV, which is the energy difference between the S L_2 and L_3 edges tabulated in Quantum ESPRESSO. The $L_{2,3}$ edge spectrum was then obtained as the sum of the L_2 and L_3 edges, after interpolating the L_2 edge values on the energy range of the L_3 edge.

The calculated spectra are shown in the rest of this section. More precisely, the calculated

XRS S $L_{2,3}$ edge of α-sulphur is compared with the measured data, as well as the XAS S $L_{2,3}$ edge of α-sulphur found in the literature (79). It should be kept in mind however, that the comparison with XAS data is only relevant for the XRS spectrum measured or calculated at low q values, as the XAS and XRS cross sections are only equivalent in the $qr \ll 1$ limit (see section 4.1.3). Additionally, the effect of the core hole approximation on the calculated spectrum is once again studied, by comparing the different spectra obtained using the FCH, XCH and GS approximations during the SCF calculations. PDOS calculations, performed using a 4×4×4 k-points grid to sample the Brillouin zone of the unit cell of the material, and a 0.5 eV broadening parameter, are also used to help complete the analysis of the results. Indeed, as the partial density of states were projected on the absorbing S atom, it is possible to assess the effects of each core hole approximation on the relative energy placement of the density of the different states.

4.3.3.2 Comparison between calculation and experiment

Fig. 4.13 shows the comparison between the calculated XRS S $L_{2,3}$ edge spectrum of α-sulphur and the measured data, for all q values at which the spectrum was measured, as well as the XAS data found in literature (79). All the XRS spectra (calculated and measured) were normalised using their area on the energy range of the measured XRS spectrum, using a common reference spectrum, arbitrarily chosen. The XAS spectrum, since its energy range is different from the measured XRS data, was simply scaled using a constant intensity factor to best match the XRS experiment data. The general shape of the measured XRS S $L_{2,3}$ edge spectrum of α-sulphur is similar to the XRS S $L_{2,3}$ of Li_2SO_4 discussed in the previous section (see section 4.3.2). Indeed, the XRS S $L_{2,3}$ of α-sulphur can be described as featuring two distinct spectral features separated by approximately 8 eV, which are located respectively at around 165 and 177 eV. In contrast to the XRS S $L_{2,3}$ edge spectrum of Li_2SO_4 however, the second spectral feature referred to as the B feature, is less intense than the rest of the spectrum at a higher energy range, and it varies very little as the value of q increases. Indeed, in the case of Li_2SO_4 (see Fig. 4.7), the second spectral feature B showed a clear decrease in intensity as q increased and was its intensity was higher than the high energy range spectrum intensity. The first feature, referred to as the A feature, varies greatly with the value of q, and is split in two distinct peaks (similarly

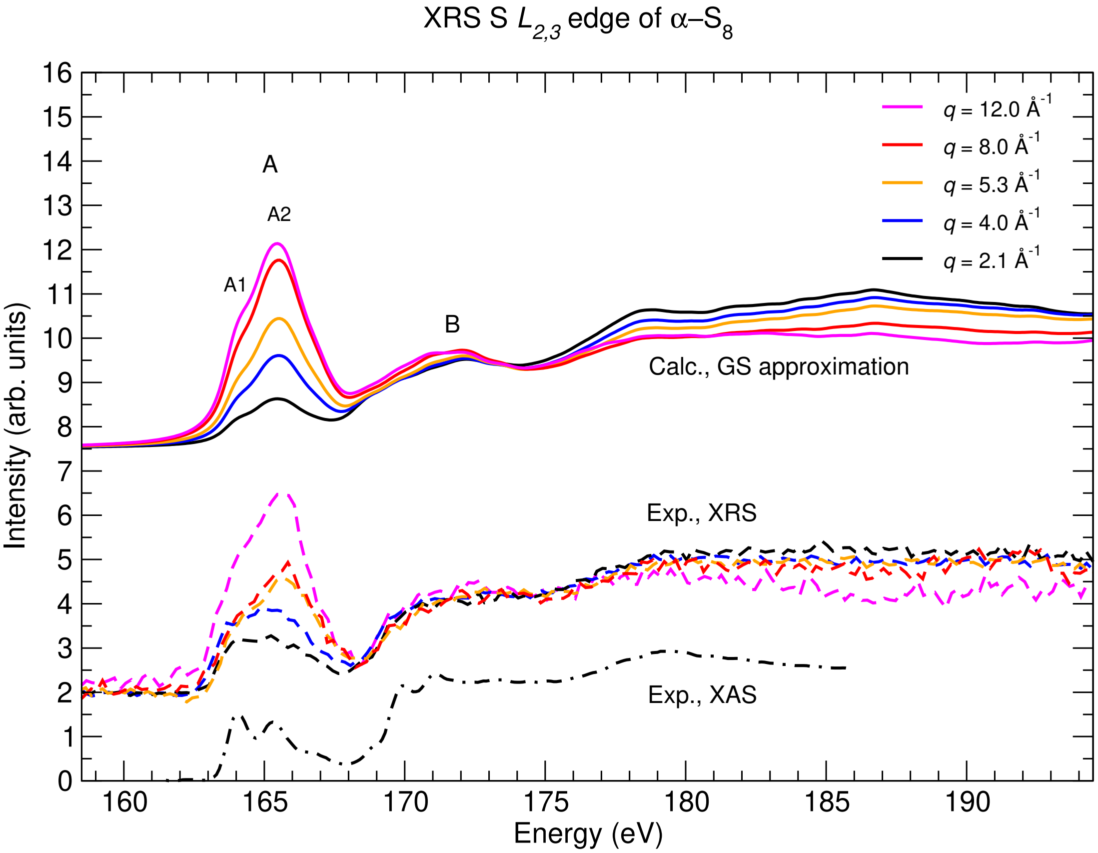

Figure 4.13: Comparison of the XRS spectrum of α-sulphur, calculated at the S $L_{2,3}$ edges, using the GS approximation for the core hole treatment during the SCF charge density calculation, with available experiment data, for different values of q. Additionally, the XAS S $L_{2,3}$ spectrum of α-sulphur, found in literature, is also shown in the figure. The calculated spectra (plain lines) were vertically separated from the measured data (dotted lines) for more clarity.

to the case of $\mathrm{Li_2SO_4}$) noted A1 and A2. For the lower q values, the separation between the A1 and A2 peaks is harder to see due to noise and experimental energy resolution. However, the split between the A1 and A2 peaks seem to increase, from approximately 1 eV for the lowest value of q to approximately 2 eV for the highest value of q. As the value of q increases, the intensity of the A feature also sees a large increase. For the q values of 5.3 and 8.0 Å^{-1}, the A feature of the measured XRS spectrum seem to have the same intensity, but this could very well be attributed to experiment noise. Indeed, from a global point of view, the evolution of the intensity of the A feature is otherwise very gradual for all the other q values. In comparison, the B feature remains mainly unaffected, while the intensity of the higher energy range spectrum slightly decreases, as the value of q increases. The equivalence of XAS and XRS, at low values of q, make the comparison between the XRS spectrum measured at $q = 2.1\tilde{A}A^{-1}$, and the XAS data found in the literature, pertinent. Save for a broadening parameter caused by the lower energy resolution of the XRS experiment, the two spectra are indeed in good agreement. In more details, the overall shape of the XAS spectrum is very close to the shape of the XRS spectrum. Moreover, the A feature of both those spectra is comparable in intensity and the XAS A feature is also split in two peaks, spaced by approximately 1 eV. Strikingly, the modified XSpectra module best manages to reproduce experimental data by using the GS approximation for the SCF calculations. Indeed, the general shape of the spectrum is very well reproduced by calculations, with the A and B feature reproduced at the correct energies, and a correct relative intensity for all q values. The general change of the shape of the spectrum with the increase of q is also well reproduced, when looking at both the large increase of the A feature intensity and the slight decrease of the high energy range spectrum. The fact that the B feature is unaffected by the increase of the q value is also reproduced. It is very surprising because, as explained earlier, the GS approximation consists in calculating the spectrum with no core hole on the excited core level shell of the absorbing atom. However, XRS (as well as XAS) is based on the excitation of a core level electron and thus, better agreement with experiment is expected when taking into account the presence of a core hole rather than not. Moreover, when the modified XSpectra module was first modified in order to include XRS K edge calculation (47), better agreement was obtained by taking into account a core hole (or half core hole) on the excited core level. While very surprising, this is, however, not entirely unheard of, as the XSpectra module, for instance, better reproduces the Cu $L_{2,3}$ edges spectra of metallic Cu without introducing a core hole on the absorbing Cu atom (60). The agreement between calculation and experiment is especially good at high q values, in contrast with the previous case of $\mathrm{Li_2SO_4}$ (where no matter which core hole approximation was used, calculations could never reproduce accurately the data measured at high q values).

However, looking more closely at the calculated and measured XRS spectra for the low q values (2.1 and 4.0 Å^{-1}), as well as the XAS spectrum), a similar problem as the one highlighted in the case of $\mathrm{Li_2SO_4}$ arises. Indeed, while it shows that the overall agreement between calculation (in the GS approximation) and experiment is good for all q values, Fig 4.13 also shows a specific evolution of the A feature with the increase of the q value, and more specifically of the A1 and A2 peaks relative intensity. More precisely, for the XRS spectrum measured at the lowest q value and for the XAS measured spectrum, the A1 peak intensity is equal to, or slightly higher than, the A2 peak intensity. As the value of q increases, experiment shows that the A1 peak intensity becomes smaller than the A2 peak intensity. The A feature of the measured XRS S $L_{2,3}$ edge of α-sulphur thus behaves similarly to the the A feature of the XRS S $L_{2,3}$ edge of $\mathrm{Li_2SO_4}$ as the value of q increases. Unfortunately, for the calculated XRS S $L_{2,3}$ edge spectra of α-sulphur, the A1 peak is less intense than the A2 peak for all q values.

Thus, though in the case of α-sulphur the agreement between measured data and calculation (in the GS approximation) is far better than in the case of $\mathrm{Li_2SO_4}$, especially at high q values, the relative intensity of the A1 and A2 peaks is not correctly reproduced by the modified XSpectra module for lower q values. This is similar to the problem encountered in the previous section, where the agreement between calculated and measured XRS S $L_{2,3}$ edge of $\mathrm{Li_2SO_4}$ was good for lower q values, whereas calculation at higher q values reproduced inaccurate relative intensity of the two A1 and A2 peaks. To continue investigating this issue, the effect of the core hole approximation on the calculated spectrum is then studied, for a low and high value of q (4.0 and 12.0 Å^{-1}, respectively). The spectra will also be decomposed into the individual L_2 and L_3 edges, as well as into their monopole and dipole contributions, to try and gain more insight regarding the A feature, part of whose evolution as the q value increases is not reproduced by calculation.

4.3.3.3 Effect of the different core hole approximations on the calculated spectrum

Fig. 4.10 shows a comparison between the calculations of the XRS S $L_{2,3}$ edge spectrum of α-sulphur performed using, from top to bottom, the GS, XCH and FCH approximations. Calculations performed using each approximations were shifted vertically for easier comparison. For each core hole approximation, both calculations performed at $q = 4.0$ Å^{-1} and $q = 12.0$ Å^{-1} are shown, also shifted vertically from one another. The XRS S $L_{2,3}$ edge spectrum of α-sulphur measured at these two values of q are also shown, in dotted line, in each case, for comparison purposes. Fig. 4.10 shows how, as indicated earlier, the GS approximation yield the best overall agreement with experiment.

Indeed, for the higher q value, the spectrum calculated using the GS approximation yields almost perfect agreement with the measured A feature, while spectra calculated with a core hole on the excited atom (i.e using the FCH and XCH approximations) do not show the correct shape for the A feature. Indeed, for the spectra calculated with a core hole, the A1 and A2 peaks of the A feature are slightly too close to each other compared to experiment (about 0.5 eV closer than the A1 and A2 peaks of the experiment), especially for the high value of q. Moreover, spectra calculated with a core hole on the excited atom for the higher q values do not show the correct relative intensities of the A1 and A2 peaks. The A features calculated using the XCH and FCH approximations, however, closely resemble each other, the only difference being a slightly more intense A1 peak in the case of the FCH approximation than the XCH approximation. For the higher q value, finally, calculated spectra show a similar agreement to the measured spectra in the B feature energy range, as well as in the higher energy range, no matter which core hole approximation is used.

As for the spectra calculated for the lower q value, once again the better overall agreement is obtained using the GS approximation rather than the FCH and XCH approximations. This result is however more nuanced for the lower q value than for the higher q value. Indeed, for the lower q value, the intensity of the A feature obtained using the GS approximation is far closer to the measured A feature than the A features obtained using the FCH or XCH approximations, which are only approximately half as intense as the measured A feature. Moreover, the A1 and A2 peaks are once again, in the case of the FCH and XCH approximations, slightly closer

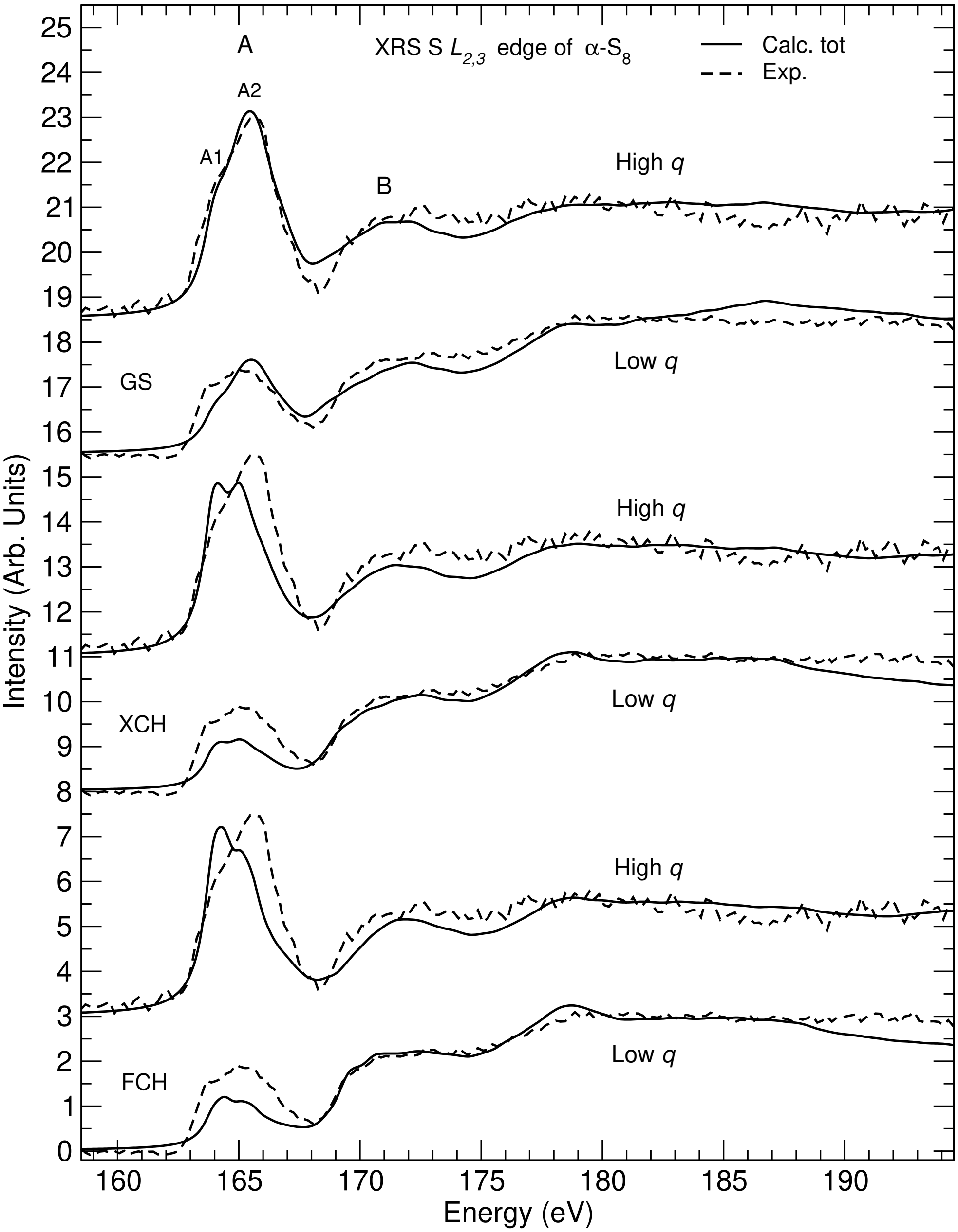

Figure 4.14: Comparison of the XRS spectrum of α-sulphur, calculated at the S $L_{2,3}$ edges, using the GS, FCH and XCH approximations for the core hole treatment during the SCF charge density calculation. The spectra calculated using different core hole approximations were shifted vertically for more clarity. For each core hole approximation, both spectra calculated for $q = 4.0\text{Å}{-}1$ and $q = 12.0\text{Å}{-}1$ are shown, referred to as the 'low q' and 'high q' spectra. For a comparison reference, the measured data at the same q values are shown in dotted lines.

to each other than the measured A1 and A2 peaks. However, as we have seen previously, for the lower q value, calculations performed with no core hole (GS approximation) do not yield the accurate shape of the A feature, because they yield incorrect relative intensities of the A1 and A2 peaks compared to the measured A feature. More precisely, the calculated A1 peak is too low in intensity and the A2 peak too high in intensity compared to the measured A feature for which the A1 and A2 peaks have a similar intensity. In comparison, the overall shape of the A feature, and more precisely the relative intensities of the A1 and A2 peaks, regardless of the overall intensity of the calculated A feature, is better reproduced using the XCH and FCH approximations approximation, as they both lead to the A1 and A2 peaks having similar intensities. Additionally, it should be noted that the A features calculated using the FCH and XCH approximations are also closer in shape to the measured A feature of the XAS data shown in Fig. 4.13, which we know to be equivalent to the XRS spectra in the low q value limit. Finally, the agreement with measured data in the B feature energy range, as well as in the higher energy range, is slightly better for calculations performed with a core hole (FCH and XCH approximations) rather than no core hole (GS approximation) in the case of the lower q value.

To summarise, Fig. 4.10 shows that calculations performed using the GS approximation lead to a better overall agreement with the measured data, with a especially good agreement in the case of the higher q value between the measured and calculated A feature. Calculations performed with a core hole on the excited atom (i.e using the FCH and XCH approximations) on the other hand lead to an overall worse agreement with experiment, as they are not able to reproduce the shape of the A feature for the higher q value. However, for the lower q value, they reproduce a shape of the A feature more closely related to the measured A feature than the A feature reproduced by calculations with no core hole (GS approximation), though its intensity is far lower than the measured A feature for the same q value. This is however, not entirely unexpected as in the case of Li_2SO_4 discussed in the previous section, calculations with a core hole indeed lead to a good agreement with the measured spectrum for the lowest q value. Moreover, calculations performed in the FCH approximation also failed reproducing the change in the shape of the A feature of the S $L_{2,3}$ edge spectrum of Li_2SO_4 at higher q values.

4.3.3.4 Decomposition of the calculated spectra

The spectra shown in Fig. 4.10 were also decomposed into their individual monopole and dipole contributions, as well as into contributions from the individual L_3 and L_2 edges, as shown, respectively, in Fig. 4.9 and in Fig. 4.16. These two new figures follow the same organisation as Fig. 4.10, with only the new decomposition of the calculated spectra appearing on the new figures.

The decomposition into the monopole and dipole contributions shows the origin of the evolution of the XRS S $L_{2,3}$ edge spectrum of α-sulphur as the value of q increases to be the same as the origin of the evolution discussed in the case of the XRS S $L_{2,3}$ edge spectrum of Li_2SO_4. Indeed, for each different core hole approximation, the calculated spectra is mainly dominated by the dipole contribution for the low q value. This is especially true for the B feature and the high energy range of the spectra. The A feature is a mix between the dipole and the monopole contribution, but not especially dominated by either of the two in the case of calculations performed using the FCH and XCH approximations. For the spectrum calculated using the GS approximation however, the monopole contribution to the A feature is already dominating the dipole contribution to the A feature. It can be argued that this is because the 'low' value of q, chosen here as 4.0 $Å^{-1}$, is already high enough to allow a significant growth of the monopole contribution to the spectrum compared to the dipole contribution (102). In contrast, for the higher value of q, the spectrum becomes mainly dominated by the monopole contribution to the spectrum. This is especially true for the A feature, which, for the calculated spectra with or without a core hole on the excited atom, clearly has the same shape as the monopole contribution, and get most of its intensity from the said contribution. At most, the dipole contribution constitutes approximately one fourth of the A feature intensity of the total (i.e sum of the monopole and dipole contributions) spectrum. This indicates that the failure to reproduce the A feature at higher q values when using the XCH and FCH approximations is directly correlated to a failure to properly reproduce the monopole contribution in these approximations. Indeed, as the value of q increases, and the monopole contribution to the A feature becomes dominant, the failure to properly reproduce the monopole contribution naturally translates to the wrong shape and/or intensity for the A feature.

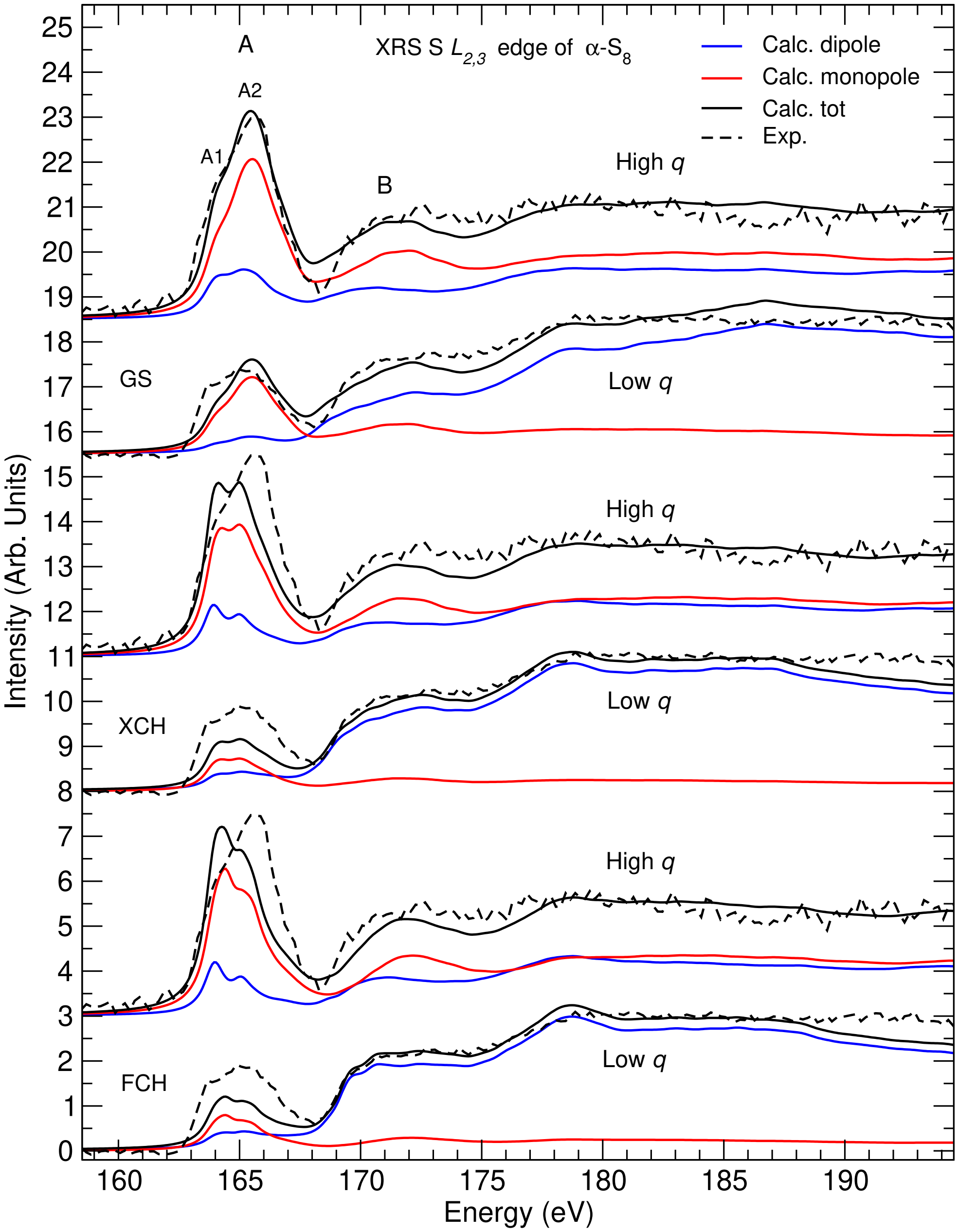

Figure 4.15: Decomposition of the calculated spectra shown in Fig. 4.10 into the individual monopole and dipole contributions to the $L_{2,3}$ edge.

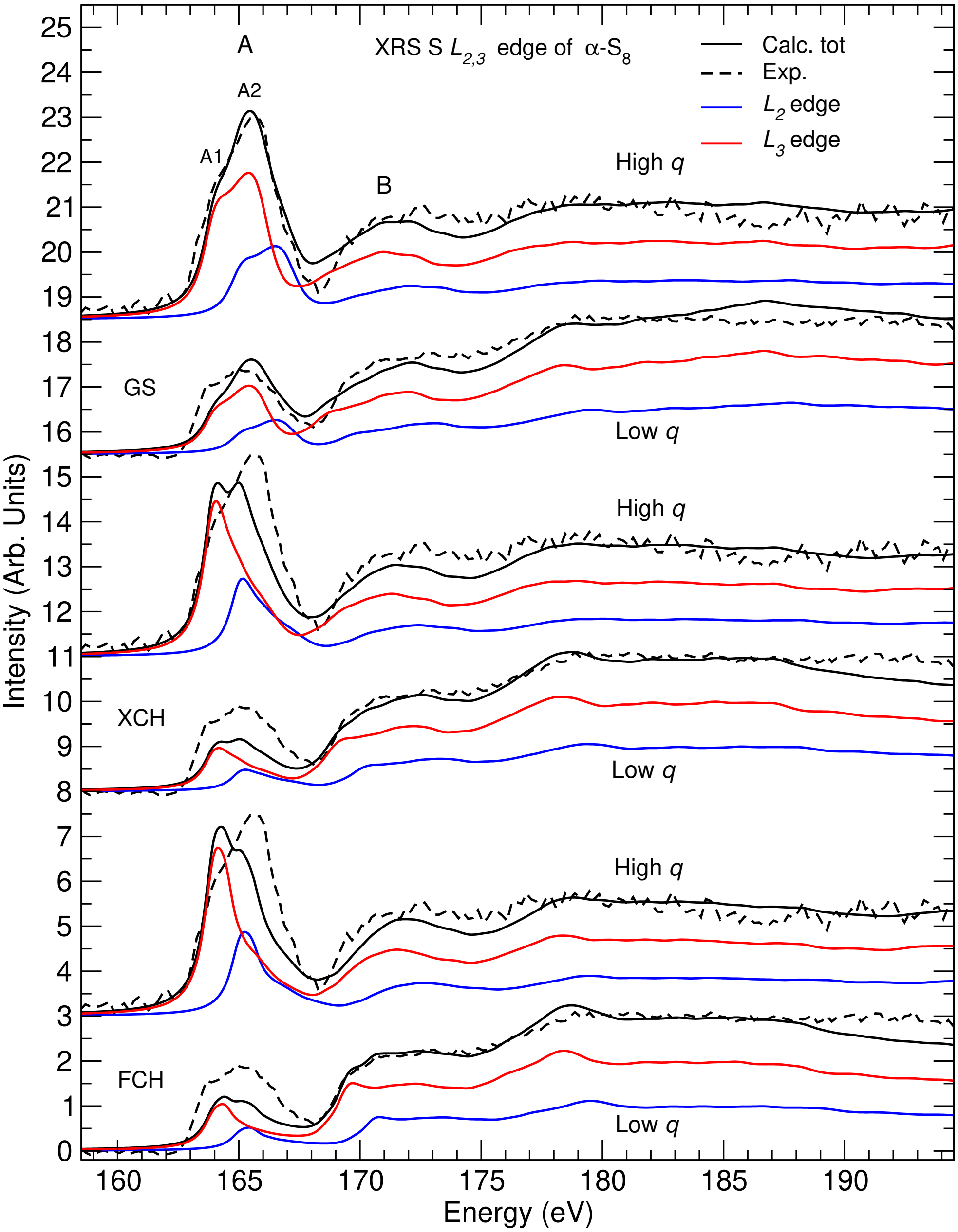

Figure 4.16: Decomposition of the calculated spectra shown in Fig. 4.10 into the individual L_3 and L_2 edges.

Decomposing the calculated spectra in the separate L_3 and L_2 edges is especially interesting in the case of α-sulphur. Indeed, unlike case of Li_2SO_4, XAS data found in the literature (79) was available for the $L_{2,3}$ edge of sulphur, and in this reference, the A1 and A2 peaks (which are noted 1 and 2 in the reference) are explicitly interpreted as signature contributions from the L_2 and L_3 edge. This interpretation is consistent with the decomposition of the XRS S $L_{2,3}$ spectrum of Li_2SO_4 calculated using the FCH (and XCH) approximation(s) into the separate L_3 and L_2 edges shown in Fig. 4.8 (see previous section). This is also consistent for the decomposition of the S $L_{2,3}$ spectrum of α-sulphur, calculated in the FCH and XCH approximations, into the separate L_3 and L_2 edges shown in Fig. 4.16. Indeed, the aforementioned decompositions of the calculated spectra clearly show that their A1 and A2 peaks stem respectively from separate contributions from the L_3 and L_2 edges, with only a slight overlapping of both contributions. However, in the case of the S $L_{2,3}$ edge spectra of α-sulphur calculated using the GS approximation instead (see top of figure Fig. 4.16), the decomposition into the separate L_3 and L_2 edges show that the contributions of each edge to the A feature cannot simply be reduced to the A1 and A2 peaks, respectively. Indeed, instead of the L_3 edge creating the A1 peak and the L_2 edge creating the A2 peak of the A feature, the L_3 edge mainly contributes to both the A1 and A2 peaks while the L_2 edge contributes only to the A2 peak. Thus, for calculation using the GS approximation and at any q values, the simple description of the L_2 and L_3 edge contributing to the A feature respectively in the form of the A1 peak and the A2 peak, and which is valid for low q values in the cases of the measured XRS (and XAS !) S $L_{2,3}$ edge of α-sulfur is no longer valid. Given the overall agreement between the measured XRS data and the calculations performed using the GS approximation, especially at high q values, it is safe to argue that this also holds for the measured A feature for the high values of q.

To summarise, calculations performed with a core hole and yielding two clearly separated L_3 and L_2 edge contributions to the A1 and A2 peaks of the A feature, respectively, lead to reproducing an accurate shape of the A feature at low q values, for the XRS S $L_{2,3}$ edge spectrum of α-sulphur (though it should also be noted that the intensity of the reproduced A feature is too small compared to the measured A feature). This, on a side note, also holds for the XRS $L_{2,3}$ edge spectrum of Li_2SO4. In contrast, the same calculations lead to a poor agreement with experiment at higher q values, and instead, calculations performed with no core hole and yielding L_3 and L_2 edge contributions to the $L_{2,3}$ edge spectrum that are broader and no longer clearly separate into the A1 and A2 peaks, respectively, yield a better agreement with the measured data. Since the decomposition shows that the monopole contribution dominates the A feature of the calculated spectra, the inability of either core hole approximation to accurately reproduce the measured spectra at all possible values of q is very likely related to the energy distribution of the density of p states. This is consistent with the previous analysis made for the case of Li_2SO_4, which suggested that that inability to reproduce the correct shape of the A feature for high values of q was related to the inaccurate reproduction of the energy placement, and energy size, of the monopole contribution to the A feature. PDOS calculations were thus used to help understanding the shape of the A feature, in terms of electronic transitions to the different available s, p or d states.

4.3.3.5 Projected density of states calculations

Fig. 4.17 shows a display of the partial density of states projected on the excited S atom, for each different core hole approximations, as well as the S $L_{2,3}$ edge XRS spectrum of α-sulphur as a reference for the energy placement of the A feature. The figure allows to assess the origin of each spectral feature in terms of electronic transitions of the excited core level electron to the empty s, p or d states of the excited atom in the conduction band. Before describing and discussing the results, we remind of the fact that the featured spectrum contains the contributions from both the L_2 and L_3 edges. In contrast, the shown PDOS should be seen as the origin of the individual L_2 and L_3 edges, which explain why the PDOS shown on the figure may look like they are only present on half the A feature. We are particularly interested in the origin of the A feature here, because as we have discussed earlier, the B feature of the measured or calculated S $L_{2,3}$ edge XRS spectrum does not show significant changes as the value of q increases, and the calculated B feature is in an overall good agreement (it is also true for the higher energy range spectrum) with the measured one for all core hole approximations tested. In contrast, we have seen that the accuracy of the reproduction of the A feature is very dependent on the chosen core hole approximation, in addition to its evolution with increasing q values being of paramount importance to accurately reproduce the measured data. Fig. 4.17 shows similar results as the ones obtained when studying the origin of the A feature of the calculated XRS

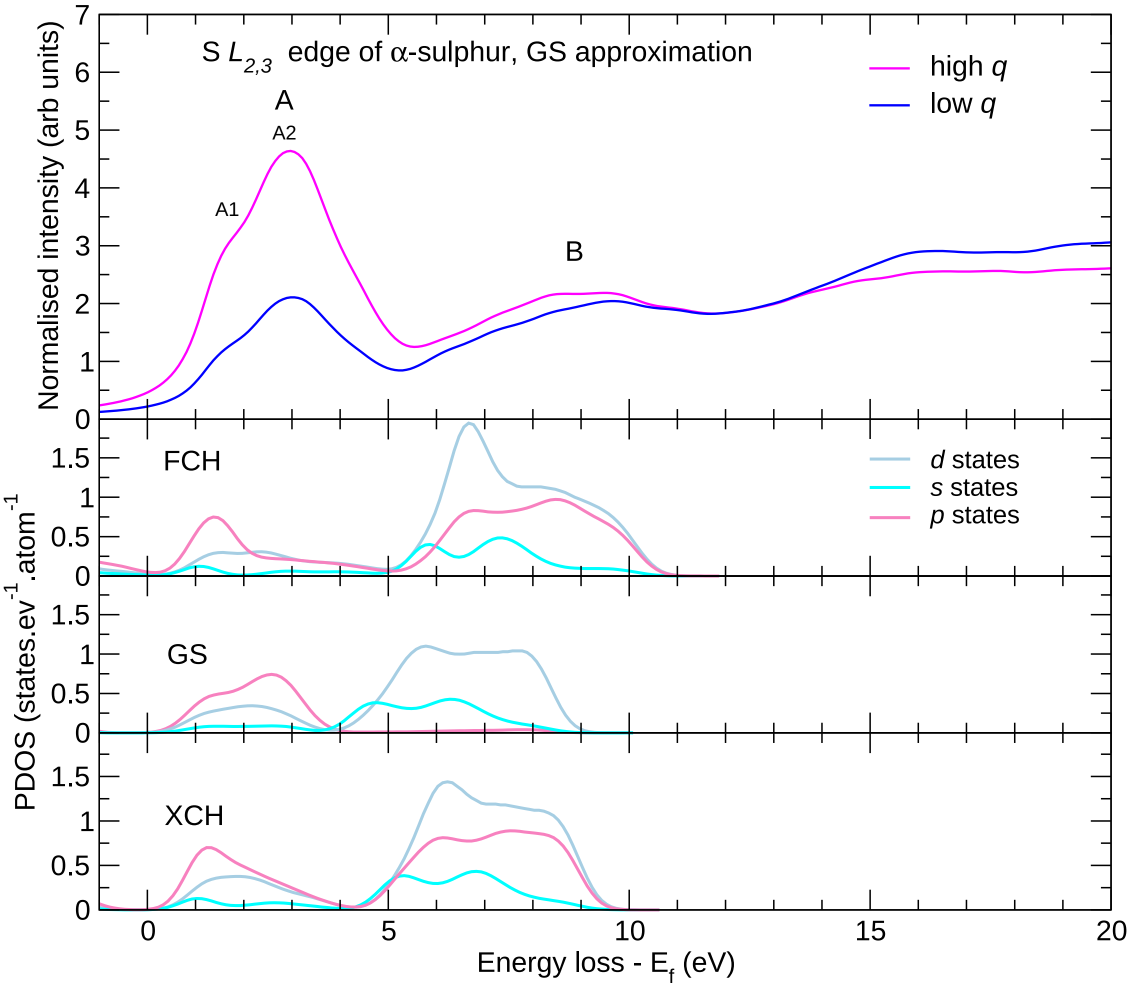

Figure 4.17: Calculations of partial density of states, projected on the excited S atom. On the top panel, the calculated S $L_{2,3}$ edge XRS spectrum of α-sulphur for the 'low' and 'high' q values used to discuss the core hole approximation effects (q values of 4.0 and 12.0 Å^{-1}) is shown as a reference for the energy placement of the A feature. Then from top to bottom, the PDOS calculated using the FCH, GS and XCH approximations, respectively, are shown. The chosen energy range is smaller than the specta shown before, as we focus on the A feature.

S $L_{2,3}$ spectrum of Li_2SO_4. More precisely, empty s, p and d states of the excited S atom are all present in the energy range of the A feature, though empty p states seem to dominate the A feature energy range. This is consistent with the A feature quickly becoming dominated by the monopole transition as the value of q increases. In the energy range of the A feature, the FCH and XCH core hole approximations lead to very similar empty states energy distributions, with sharp s and p density of states located on the A1 peak of the A feature, with the s states located at slightly lower energies than the empty p states. In contrast, in the energy range of the A feature, the GS approximation leads to broader energy distribution of empty p and d states, located on both peaks of the A feature. Moreover, the empty s states are not placed at slightly lower energies than the p states, and occupy roughly the same energies as the p states, unlike what is observed in the FCH and XCH approximations. The sharper energy distributions of the empty states when a core hole is present on the excited atom are attributed to the attractive effect of the core hole, which also localises the empty states on smaller energy ranges. This effect of the core hole was already discussed in the previous chapter, and is consistent with the results of PDOS calculations in the case of the S $L_{2,3}$ edge XRS spectrum of Li_2SO_4. For all core hole approximations, the energy distribution of the empty d states in the A feature energy range is similar, and thus does not explain the drastic change of the shape of the A features when using different core hole approximations.

The study of PDOS allows to understand that the clear separation, for the spectra calculated in the FCH and XCH approximations, of the A feature into the A1 and A2 peaks, stemming respectively from the L_3 and L_2 edges. Indeed, it is the presence of a core hole on the excited atom which localises the empty s and p states on a smaller energy range, which causes sharper dipole and monopole contributions to the A feature for both the L_2 and L_3 edges. This ultimately ends up creating, for all values of q, two L_3 and L_2 edge contributions to the A feature of the S $L_{2,3}$ edge, sharp enough for the energy difference between the S L_2 and L_3 edge (1.1 eV) to separate the two contributions into two distinct peaks, A1 and A2. In contrast, the GS approximation leads to a broader energy distribution of the empty s and p states, which lead to broader monopole and dipole contributions to L_2 and L_3 edges, which in turns lead to broader L_2 and L_3 edge contributions to the S $L_{2,3}$ edge, at all values of q. The energy difference between S L_2 and L_3 is thus too small to separate those broad contributions into independent contributions to the A1 and A2 peaks of the A feature of the S $L_{2,3}$ edge.

4.3.3.6 Conclusion

To summarise the results obtained on the XRS S $L_{2,3}$ edges spectra of α-sulphur, we saw that the main difference between the spectra calculated using different core hole approximations was the A feature and the relative intensities of its two peaks, A1 and A2. The rest of the spectrum, i.e the B feature and the spectrum at higher energies, is relatively unaffected by the chosen core hole approximation and in good agreement with the measured data. We also discussed how, in the case of the S $L_{2,3}$ edge spectrum of α-sulphur, the FCH and XCH approximations produce a better agreement between theory (calculations) and experiment, at low q values only, regarding the shape of the A feature. At higher values of q however, the FCH and XCH approximations failed to reproduce the correct A feature. In comparison, GS calculations provided an overall better agreement with experiment, and especially at high values of q, where the agreement between calculation and experiment is very good. However, the GS approximation does not allow to accurately reproduce the shape of the A feature for the lower q values.

Study of PDOS, as well as all those previous elements, suggest that at low q, the A feature of the XRS S $L_{2,3}$ edge spectrum of α-sulphur, just like its XAS counterpart, is best explained as the sum of two separate A1 and A2 peaks, only slightly overlapping, each a respective signature of the individual L_3 and L_2 edges contributions. The relative intensity of the A1 and A2 peaks not being 2:1 as expected stems from this slight overlapping. As the value of q increases however, the relative intensity of the A1 and A2 peaks gets reversed and the previous description does not explain the shape of the A feature anymore. Indeed, the theoretical branching ratio of 2:1 between the calculated L_3 and L_2 edge makes it impossible for the A2 peak to be more intense than the A1 peak. This makes the interpretation, which is done for the low q spectra, of the A1 and A2 peaks as signature peaks of the L_3 and L_2 edges, respectively, invalid at high q values. Instead, GS calculations showed that the A feature at high values of q is best explained as two broader contributions from the L_3 and L_2 edges, with the A1 and A2 peaks no longer being signature peaks of the L_3 and L_2 edges, respectively. Instead, the L_3 edge contributes to both the A1 and A2 peaks and the L_2 edge contributes mainly to the A2 peak. In this new description, the broad L_3 and L_2 edge contributions at low and high q values stem from a broader energy distribution of the empty s and p empty states in the conduction band than the energy distribution of the empty s and p states obtained in the presence of a core hole on the excited atom (FCH and XCH).

Thus, the A feature of the calculated XRS S $L_{2,3}$ edge spectrum of α-sulphur was identified as the most sensitive feature to the core hole approximation. Since this feature is the most glaring difference between accurate or inaccurate reproductions of the experimental data, understanding this sensitivity is of paramount importance to accurately reproduce the measured XRS S $L_{2,3}$ edge spectrum of α-sulphur at all values of q. The sensitivity of the A feature shape to the chosen core hole approximation was directly explained by the effect of the core hole, in particular, on the density of empty p states in the A feature energy range. This is consistent with conclusions drawn in the previous section in the case of the XRS S $L_{2,3}$ edge of Li_2SO_4, where the effect of the core hole on the energy distribution of the s and p states, and thus on the monopole and dipole contribution (but more specifically on the monopole contribution), had a clear effect on the shape of the A feature of the spectrum.

Finally, the fact that the FCH and XCH approximations yield the better agreement at low q values where the dipole contribution dominates while the GS approximation yields better agreement at high q values where the monopole contribution dominates might indicate that the core hole presence might have too much effect on the p states in the FCH and XCH approximations available to DFT. Indeed, since at high q values, the delocalised empty p states in the A feature energy range yields better agreement with experiment, the core hole presence in the FCH and XCH approximations might localise the empty p states too much in the A feature energy range. The FCH and XCH yielding good agreement between the calculated and measured A features for low q values on the other hand suggest that the effect of the presence of the core hole has the correct effect on the empty s states in the A feature energy range.

To continue exploring this question, as well as the capacity of the modified XSpectra module to reproduced measured XRS $L_{2,3}$ edge spectra, preliminary calculations were performed on other sulphur compounds, and it was intended to obtain XRS S $L_{2,3}$ edge spectra measured for different values of q at the ID20 beamline of ESRF for comparison. These calculations are briefly shown in the next section.

4.3.4 Calculations at the S $L_{2,3}$ edge of several other sulphur compounds

This section is dedicated to preliminary calculations performed at the XRS S $L_{2,3}$ edge of diverse sulphur compounds, namely realgar (chemical formula As_4S_4), pyrite (FeS_2), arsenopyrite (FeAsS) and orpiment (As_2S_3). These calculations were motivated because the $L_{2,3}$ edges are more rarely studied in the literature (except of course in the specific case of transition metals, since these edges then allows to easily have access to the empty $3d$ states of those elements) than K edges. Our primary goal was therefore to evaluate to which extent edges could bring information complimentary to K edges in the broad context of environmental mineralogy. However, a problem pertaining to dilution during the samples preparation caused the obtained signal to be too weak to properly acquire the XRS spectra, as the XRS signal is far weaker and thus harder to measure than the XAS signal. Nevertheless, these preliminary calculations are still shown as they can be compared to some data found in the literature (XAS S $L_{2,3}$ edge of pyrite, (79)) and discussed in light of the results from the previous sections.

4.3.4.1 Computational details

The calculation process followed to obtain the XRS S $L_{2,3}$ edge spectra of the mentioned compounds is similar to the process followed for both α-sulphur as well as Li_2SO_4.

First, the charge density in the material was calculated by SCF calculations, for each supercell of the material. The supercells used to described each compound were fully relaxed beforehand. As we consider four different materials here, it is more convenient to summarise the calculation and structure parameters in a table (see Table 4.1). Fig. 4.18 shows illustrations of the supercells of the different compounds. The calculations were performed using the FCH approximation, with a core hole on the excited S atom. The supercell of realgar and orpiment contain respectively four and three inequivalent S sites. Thus, for these compounds, a charge density calculation was performed for each inequivalent site. The pseudopotentials used to describe the different atoms (S, As, Fe) were taken from the PS Library, and generated following the RRKJ formalism mentioned earlier. In the case of the excited S atom, a core hole was generated by reducing the occupancy of the $2p$ shell by one. These calculations were then used to perform the XRS S L_2 edge calculations.

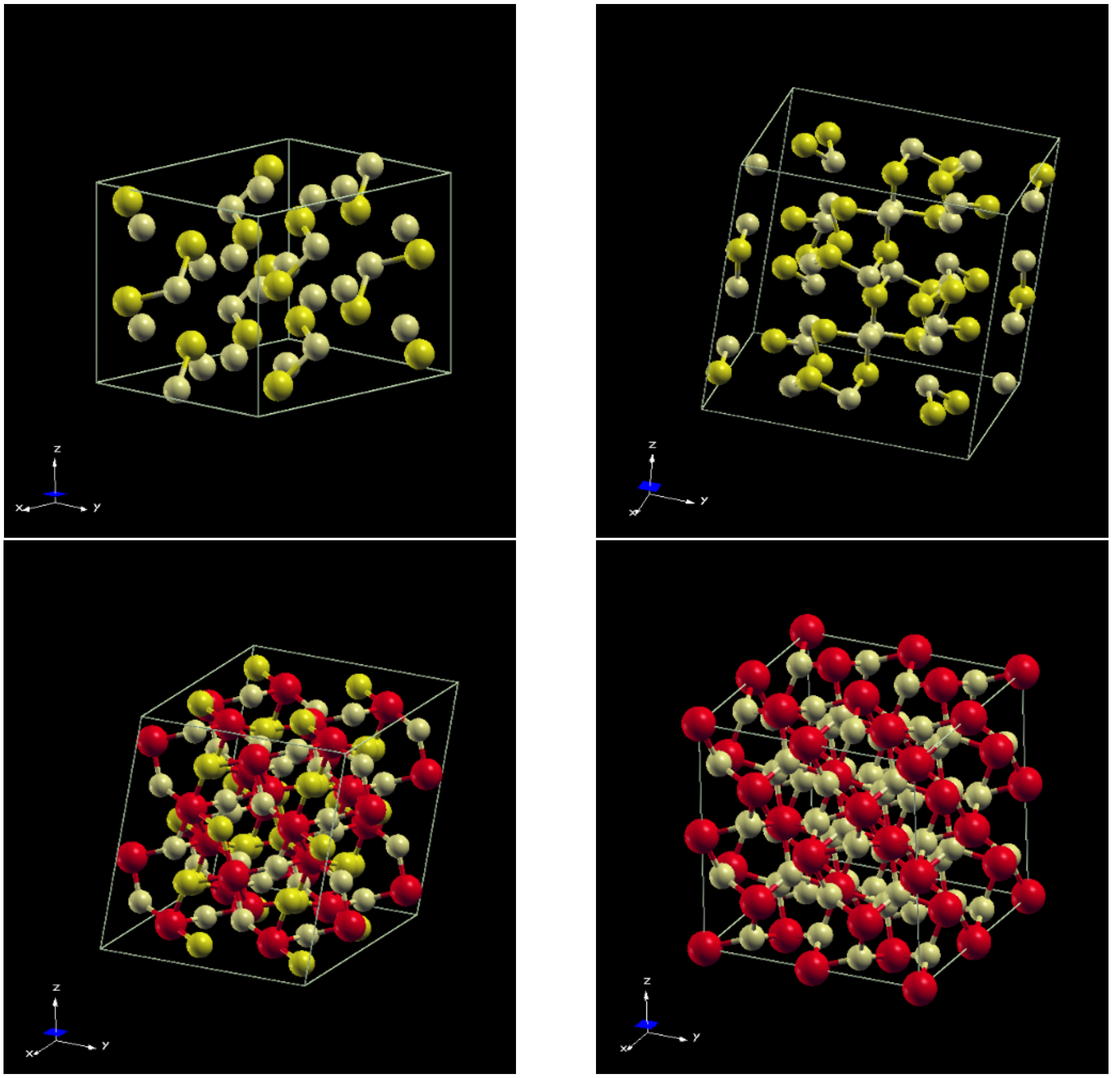

Figure 4.18: Images produced from the XCrysden program of the supercells used to calculate the XRS $L_{2,3}$ edges spectra presented in this section. On top, supercells of orpiment (left) and realgar (right). Below, supercells of arsenopyrite (left) and pyrite (rigth). Sulphur atoms are in pale yellow, iron atoms in red and arsenic atoms in yellow.

Compound	Crystal system, Space group	SCF super cell, number of atoms, Inequivalent S sites	unit cell parameters	k-points grid, Ecutwfc Ecutrho
Orpiment (As_2S_3)	Monoclinic $P2_1/n$	$1 \times 1 \times 2$ 40 atoms 3	$a = 11.61$ Å, $b = 9.64$ Å, $c = 8.48$ Å $\beta = 90.4$ °	$2 \times 2 \times 2$ 60 Ry 480 Ry
Realgar (As_4S_4)	Monoclinic $P2_1/n$	$1 \times 1 \times 2$ 64 atoms 4	$a = 9.35$ Å, $b = 13.66$ Å, $c = 13.15$ Å $\beta = 106.1$ °	$3 \times 2 \times 2$ 60 Ry 480 Ry
Arsenopyrite (FeAsS)	Monoclinic $P2_1/c$	$2 \times 2 \times 2$ 96 atoms none	$a = 9.35$ Å, $b = 13.66$ Å, $c = 13.15$ Å $\beta = 112$ °	$1 \times 1 \times 2$ 80 Ry 640 Ry
Pyrite (FeS_2)	Cubic $Pa\bar{3}$	$2 \times 2 \times 2$ 96 atoms none	$a = 10.81$ Å,	$4 \times 4 \times 4$ 60 Ry 480 Ry

Table 4.1: Table presenting the different structure and calculation parameters used for SCF charge density calculations. Ecutwfc and Ecutrho are the energy cut-offs for wave functions and charge density, respectively

The L_2 edge calculation parameters were similar for all compounds. A $4 \times 4 \times 4$ k-point grid was used to sample the Brillouin zone, and the broadening parameter was set of 0.5 eV, as this value was found adequate for the previous sulphur compounds. For all compounds, the monopole and dipole contribution were calculated separately, and for two different values of q, representing a 'low' and 'high' value of q, chosen as 2.0 and 9.0 Å^{-1}. The isotropic dipole contribution was obtained as the sum of dipole spectra calculated for the scattering vector $\boldsymbol{q}$ oriented along the x, y and z axes. The monopole contribution, insensitive to the orientation of $\boldsymbol{q}$, was obtained by arbitrarily orienting $\boldsymbol{q}$ along the x axis. The total L_2 edge was obtained by summing the monopole and dipole contributions. For realgar and orpiment supercells, four and three spectra were respectively calculated were calculated for each norm value and orientation of $\boldsymbol{q}$, for each multipole contributions, because of inequivalent sites of S in these materials. The total spectra was in these cases obtained as an average of the total spectra obtained for each inequivalent site, after shifting each individual site spectrum in energy following the ΔSCF procedure in the case of multiple inequivalent sites, and already described in section 3.3.2.2.

The obtained L_2 spectra were then used to obtain the L_3 edge spectra by multiplying their intensity by two and shifting their energy by -1.1 eV. The $L_{2,3}$ spectrum is then calculated as the sum of the L_2 and L_3 edge spectra.

To compare the XRS S $L_{2,3}$ edge spectra calculated for the four different compounds, each of them had to be shifted in energy, with respect to a chosen spectrum (chosen as the spectrum calculated for arsenopyrite), following the ΔSCF procedure described precisely in section 3.2.2.2. Each spectrum was normalised using its on its energy range up to 30 eV, with respect to a reference spectrum (chosen as the XRS S $L_{2,3}$ edge spectrum of arsenopyrite calculated at $q = 9.0$ Å^{-1}).

Finally, to help understand the results, PDOS calculations were performed, on the supercells describing each compounds, using 4×4×4 k-points grid to sample the brillouin zone and a broadening parameter of 0.5 eV. Partial density of states projected on the s p and d states of the excited S atom can thus later be shown.

4.3.4.2 Comparison of the calculated spectrum

Fig. 4.19 shows the comparison between the XRS S $L_{2,3}$ edge spectra of orpiment, realgar, arsenopyrite and pyrite calculated at $q = 2.0$ Å^{-1} and $q = 9.0$ Å^{-1}. The general shape of the spectra is similar to the S $L_{2,3}$ (calculated or measured) edge spectra of Li_2SO_4 and α-sulphur shown in the two different sections, with at the lower energies an A feature which is closely followed by an intensity increase and, at higher energies, a relatively flat spectrum. Unlike the spectra shown in the previous sections, no feature (at the time noted B) is discernible in the spectra at around 7-8 eV after the A feature. The main change in the spectra as the value of q increases is the large increase of the A feature intensity. The spectrum at high energies only changes slightly as q increases, in comparison. The XRS S $L_{2,3}$ edge spectra of orpiment and realgar are very similar to each other, but very different from the XRS S $L_{2,3}$ edge spectra of arsenopyrite and pyrite, who are also similar to each other. This is true for both values of q for which the spectra were calculated. Indeed, the A feature of the $L_{2,3}$ edges of orpiment and realgar are split in two peaks noted once again A1 and A2, though this is more easily seen for the spectra calculated at the higher value of q. In comparison, the A feature of the $L_{2,3}$ edges of arsenopyrite and pyrite more closely resemble a single peak. The red arrow on the figure shows that the splitting of the A1 and A2 peaks is of approximately 1.1 eV, indicating that each peak,

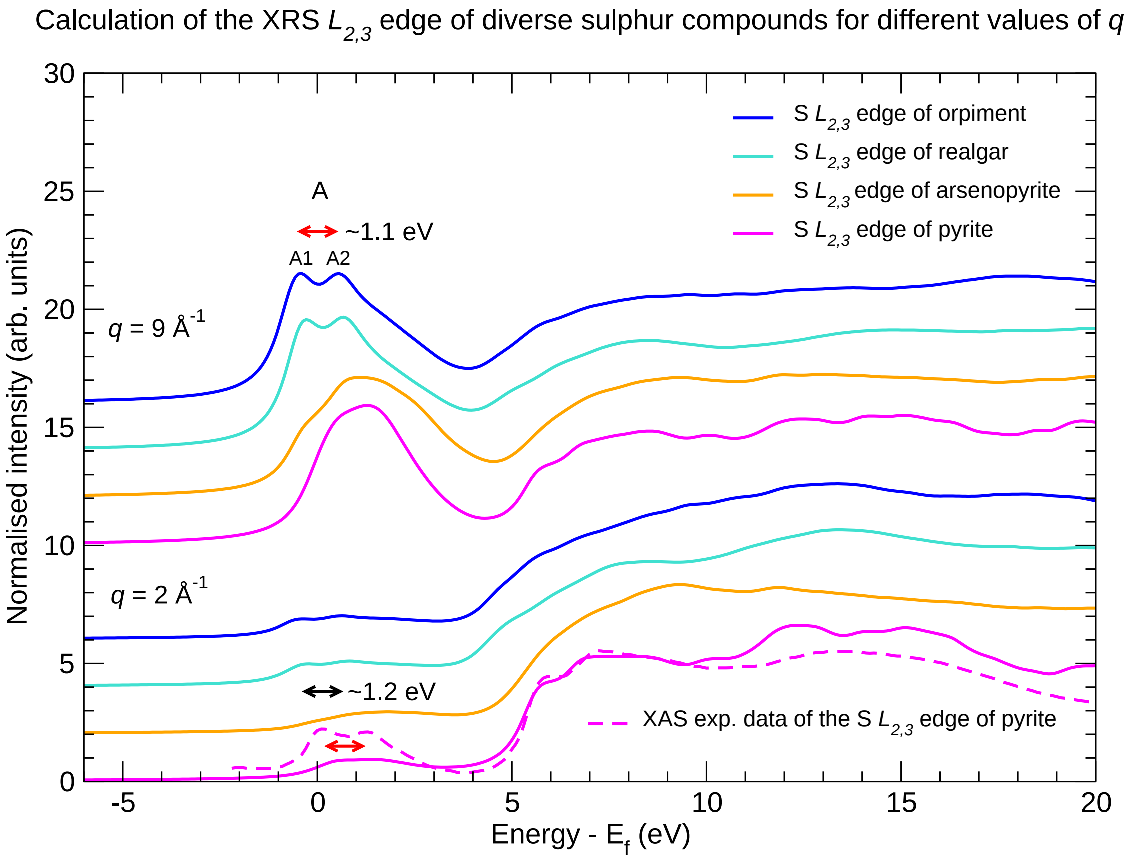

Figure 4.19: Comparison of the XRS spectra, calculated at the S $L_{2,3}$ edge, of orpiment (blue), realgar (cyan), arsenopyrite (orange) and pyrite (magenta). Spectra calculated for the two different values of q were first shifted vertically by 10 a.u., and each compound is shifted from each other by 2 a.u. The XAS S $L_{2,3}$ edge of pyrite, found in the literature (79), is also shown (magenta, dotted line), and was shifted in energy, and scaled, to best match the XRS S $L_{2,3}$ edge of pyrite calculated at $q = 2.0$ Å^{-1}.

when visible, is probably a signature of the individual L_3 and L_2 edges respectively. Moreover, the A features of the calculated spectra of orpiment and realgar are shifted by about 1.2 eV (for both values of q) from the A features of the calculated spectra of arsenopyrite and pyrite, shown by the black arrow on the figure. In refs. (80; 79), the XAS S $L_{2,3}$ and K edge spectra of diverse sulphur compounds are showcased and the shift of the absorption edge in energy is directly related to the oxidation state of the sulphur absorbing atom, with the absorption edge shifting to higher energies as the oxidation state increases. Though DFT technically cannot calculate absolute energies, this shift is reproduced by calculation, and coherent given the expected oxidation states of sulphur in the different compounds (-2 for realgar and orpiment and -1 for arsenopyrite and pyrite).

We know (see section 4.1.3) that the XAS $L_{2,3}$ and the XRS $L_{2,3}$ edge spectra are equivalent for low q values. Thus, the XAS S $L_{2,3}$ edge spectrum of pyrite can be compared to the XRS S $L_{2,3}$ edge spectrum of pyrite calculated for a low q values. Fig. 4.19 shows that calculation and measured data are in relatively good agreement when looking at the global spectrum. However, the A feature is not very accurately reproduced when compared to the A feature of the experimental XAS data. The calculated A feature more closely resemble a single peak when the measured A feature is clearly separated in the A1 and A2 peaks, and the calculated A feature is reproduced at sightly higher energies than the measured A feature. Moreover, the intensity of the calculated A feature is almost half that of the measured feature. Interestingly, the same problem was observed in the case of the calculation of the XRS S $L_{2,3}$ edge of α-sulphur (see section 4.3.3.3. Indeed, for the lower q value, calculations performed in the XCH and FCH approximation (the FCH approximation is used here) lead to reproducing an A feature too low in intensity compared to the measured A feature from the XRS data.

The separation of the calculated spectra into the monopole and dipole contribution, as well as the individual L_2 and L_3 edge spectra, are shown in the next section, and the result compared with the previous results.

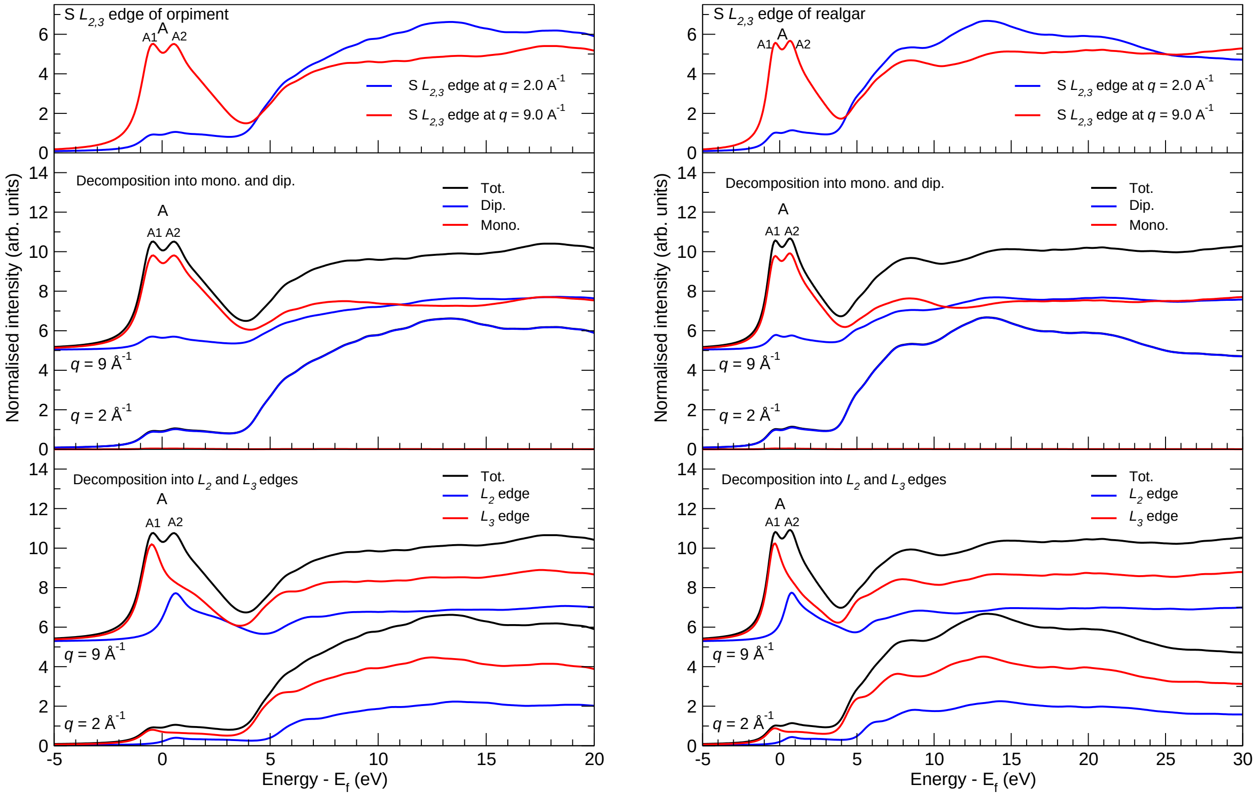

Figure 4.20: Decomposition of the XRS S $L_{2,3}$ edge spectrum of orpiment (left) and realgar (right). The decomposition figures are composed by three panels. Top panel shows the comparison between the calculated S $L_{2,3}$ at $q = 2.0$ Å^{-1} (blue) and $q = 9.0$ Å^{-1} (red) edge. Middle panel shows the decomposition of the calculated S $L_{2,3}$ edge spectrum into the monopole (red) and dipole (blue) contributions. Bottom panel shows the decomposition of the calculated S $L_{2,3}$ edge into the individual L_2 (blue) and L_3 (red) edges. In the middle and bottom panels, spectra calculated for different values of q were shifted vertically for clarity.

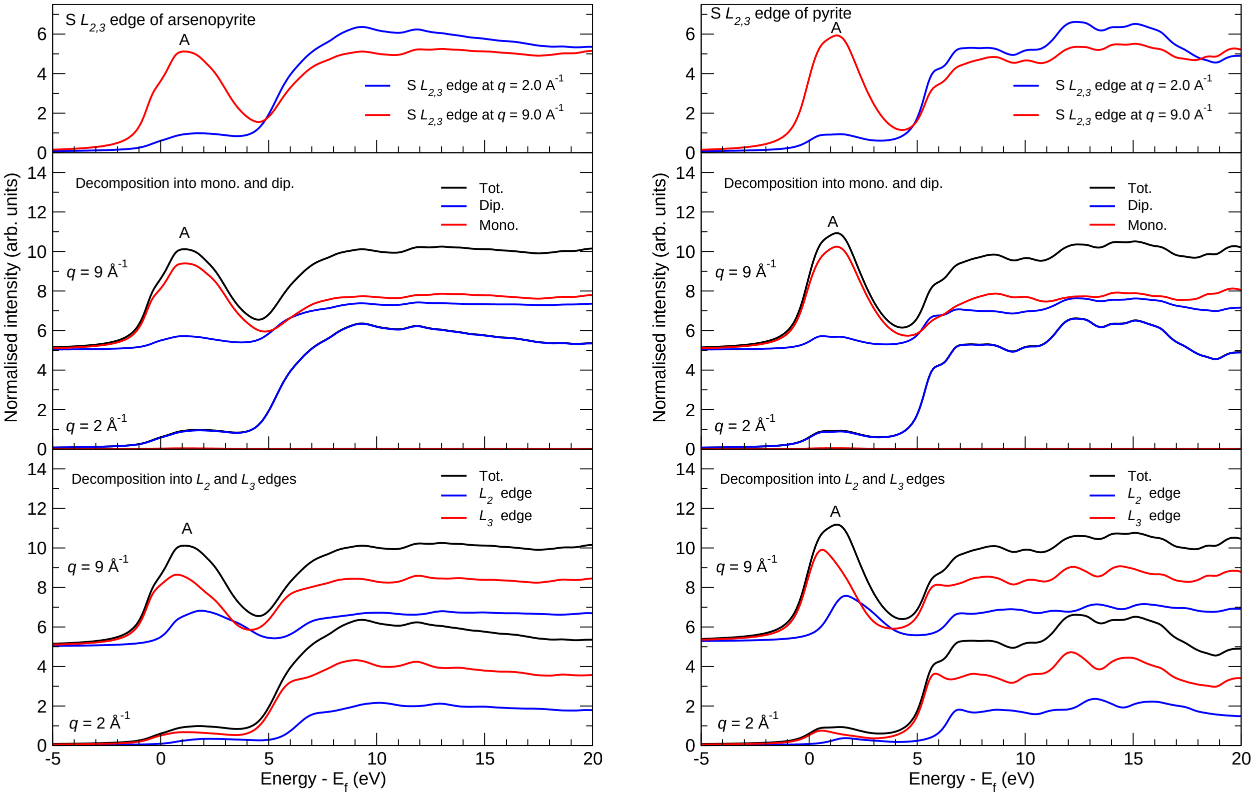

Figure 4.21: Same figure as Fig. 4.20, but this time featuring the calculated $L_{2,3}$ edge of arsenopyrite (left) and pyrite (right).

4.3.4.3 Decomposition of the calculated spectra

Figs.4.20 and 4.21 show the decomposition of the calculated XRS $L_{2,3}$ edge of orpiment and realgar, and arsenopyrite and pyrite, respectively. On the top panels of each figure, the calculated spectrum is shown for $q = 2.0\text{Å}^{-1}$ (blue) and $q = 9.0\text{Å}^{-1}$ (red). The middle panel of each figures shows the corresponding calculated XRS S $L_{2,3}$ edge spectrum (black line), decomposed into the monopole (red) and dipole (blue) contributions, for both values of q. The bottom panel of each figure finally shows the decomposition of the calculated XRS S $L_{2,3}$ edge spectrum (black line) into the individual L_2 and L_3 edges.

The top panels of each figure shows the global variations of the calculated XRS S $L_{2,3}$ edge spectra of orpiment, realgar, arsenopyrite and pyrite as the value of q increases. More precisely, they show, for all compounds (more easily than Fig. 4.19), how the A feature, located at the lower energies of the spectra, is the part of the spectra that is the most affected by the increase of the value of q, seeing its intensity multiplied by a factor of five (or more) as the value of q goes from 2.0 Å^{-1} to 9.0 Å^{-1}. In contrast, they also show how the spectra at higher energies are either almost unaffected by the increase of the value of q, or see their intensity slightly decrease (at most by a factor of 1/6) as q increases. These global variations are very similar to those observed for the XRS S $L_{2,3}$ edge spectra of Li_2SO_4 and α-sulphur shown in the previous sections (sections 4.3.2 and 4.3.3, respectively).

The middle panels of the figures show the change of the relative weights of the monopole and dipole contributions for the different values of q. They show how while at the low q value, the spectra are largely dominated by the dipole contribution, with the monopole contribution barely visible on the figures, the spectra at the higher q value are in contrast dominated by the monopole contribution. They confirm how, just like the case of the XRS S $L_{2,3}$ edge spectra of Li_2SO_4 and α-sulphur shown in previous sections (sections 4.3.2 and 4.3.3, respectively), the variations of the calculated spectra as the value of q increases mainly stems from the drastic change of relative intensity between the monopole and dipole contributions. The A feature in particular, is the most changing part of the spectrum as the value of q increases because the monopole contribution, as the value of q increases, goes from not contributing to the A feature at low q to being the major contribution to the A feature at higher q values. The spectra at higher energies in contrast, goes from stemming mainly from the dipole contribution to becoming a mix of more or less equal weights, of the dipole and monopole contributions. The monopole contribution becoming a more dominant part of the A feature than of the spectrum at higher energies explains why these two parts of the spectrum behave in an opposite way, albeit in a less pronounced way for the spectrum at higher energies than the A feature, as the value of q increases.

Finally, the bottom panels of the figures showing the decomposition of the calculated XRS S $L_{2,3}$ edge spectra into the individual L_2 and L_3 edges are also very interesting. Indeed, the figures show different types of contributions from the L_3 and L_2 edges to the A feature of the calculated XRS S $L_{2,3}$ edge spectra, for the different sulphur compounds, which lead to it clearly separating into the A1 and A2 peaks or not. For orpiment and realgar, the compounds for which the calculated XRS spectra A feature clearly splits into two peaks, the figure clearly shows a sharp and well defined peak located at the A1 and A2 peaks of the A feature, in the contribution from the L_3 and L_2 edges, respectively. In contrast, for arsenopyrite and pyrite, the for which the A feature in the calculated spectra does not clearly split into two peaks and more closely resemble a single, broader peak, the contributions from the individual L_3 and L_2 edges to the A feature are broader, defined by a clearly larger FWHM (Full Width at Half Maximum) than the individual contributions from the L_2 and L_3 edges in the case of orpiment and realgar (approximately 1.5 and 2.0 eV for orpiment and realgar, against approximately 4.0 and 3.0 eV for arsenopyrite and pyrite). It is interesting and surprising to see that in the case of arsenopyrite and pyrite, calculations performed in the FCH approximation lead to a seemingly non split A feature. Indeed, in comparison, in the previous cases of Li_2SO_4 and α-sulphur, calculations performed in the FCH approximation, consistently with the observed results for orpiment and realgar, systematically lead to a split A feature into the A1 and A2 peaks, which could then be interpreted as signature of the individual L_3 and L_2 edges, respectively. Moreover, the A feature of the experimental data of the XAS S $L_{2,3}$ spectrum of pyrite shown in Fig 4.19 is also clearly split in the A1 and A2 peaks. The sensitivity of the shape of the A feature, and more precisely its splitting into the A1 and A2 peaks, was already shown to stem from the sharpness of the contribution from the individual L_2 and L_3 contributions to the A feature in the case of L_2SO_4 and α-sulphur. This sensitivity was ultimately shown to stem, in these cases, from the

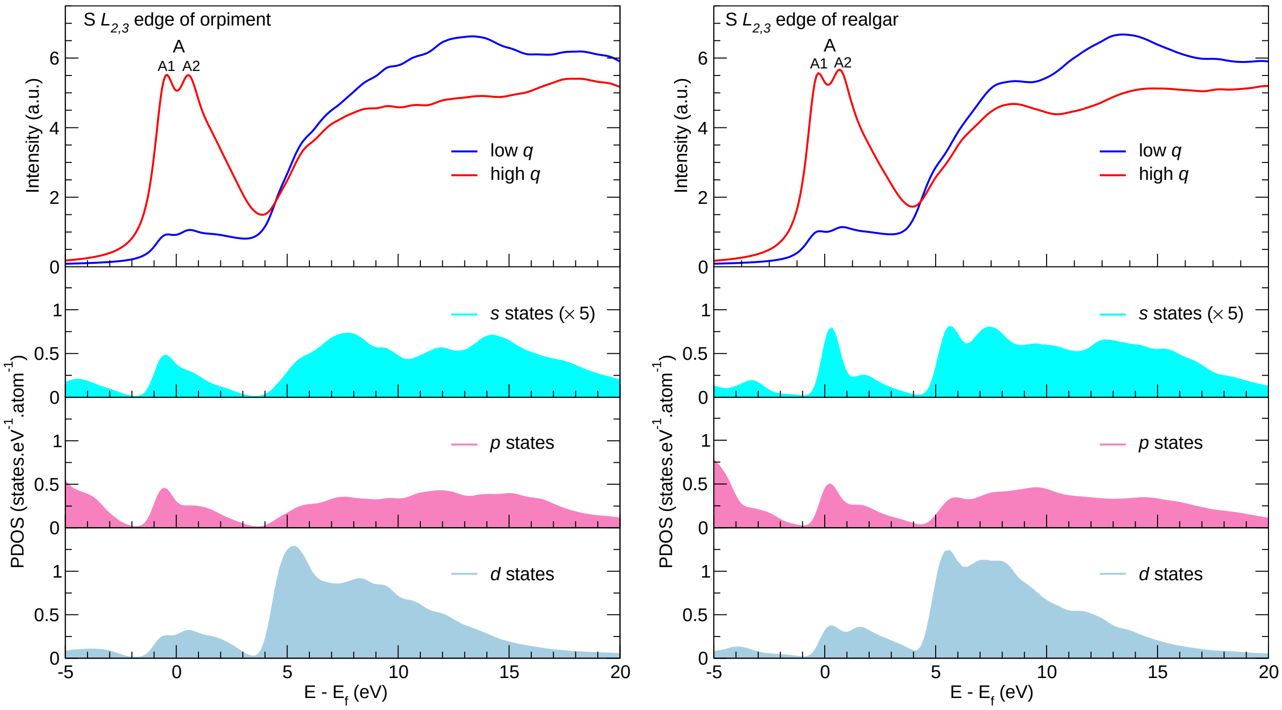

Figure 4.22: Calculation of the Projected Density of States performed on the supercell describing orpiment (left) and realgar (right). For reference, the calculated XRS S $L_{2,3}$ edge spectrum is shown for both q values of 2.0 (blue) and 9.0 Å^{-1} (red) on the top panel. Then, from top to bottom, the partial density of s, p and d states, projected on the excited S atom are shown. The density of s states was multiplied by 5 to be able to compare all densities of states on the same intensity scale.

reproduced energy distribution of the empty p states energy distribution in the A feature energy range, i.e of the monopole contribution to the A feature. PDOS calculations, performed for all this compounds, confirm this result.

4.3.4.4 Projected density of states calculations

Figures 4.22 and 4.23 show the partial density of s, p and d states projected on excited S atom respectively on the top, middle and bottom last three panels of the figures, respectively for orpiment and realgar, and arsenopyrite and pyrite. On the first panel, the calculated XRS S $L_{2,3}$ edge spectrum of the corresponding compound is shown, for both values of q (2.0 Å^{-1} in blue

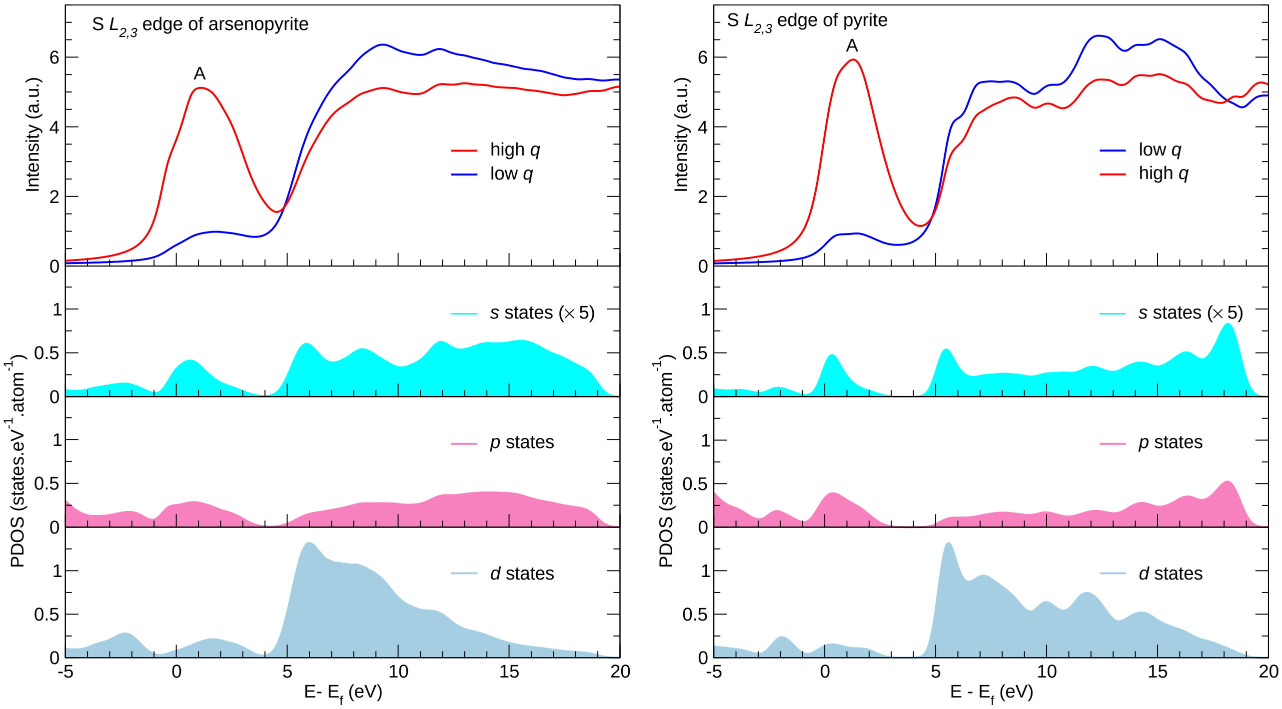

Figure 4.23: Same figure as Fig. 4.22, but this time featuring calculations performed on the arsenopyrite (left) and pyrite (right) supercells.

and 9.0 Å^{-1} in red). The density of states were shifted by the energy shift of the difference between the L_2 and L_3 edges, which explains why the empty states seem to occupy only half the energy range of the A feature. PDOS calculations allow to highlight how the sensitivity of the A feature, for the calculated spectrum of the different compounds, is related to the empty p states energy distribution. This was also already observed when studying the sensitivity of the XRS S $L_{2,3}$ edges spectra of α-sulphur and $\mathrm{Li_2SO_4}$, whose A feature was very sensitive to the chosen core hole approximation, which was related to the effect of the presence of the core hole on the excited atom on the energy distribution of its empty p states. Indeed, Fig. 4.22 show how for orpiment and realgar, whose A feature split into the A1 and A2 peaks, the empty p (and s) states in the A feature energy range are far more localised on the A1 peak. In comparison, Fig. 4.23 shows how the empty p (and s) states are delocalised more evenly on almost the whole A feature energy range. This is why the monopole (and dipole) contributions to the A feature are sharp and lead to a clearly split A feature, in the case of orpiment and realgar, and why in the case of arsenopyrite and pyrite, the $L_{2,3}$ edges spectra show an A feature in the shape of a single, broader peak, stemming from broader monopole and dipole contributions. Similarly to results observed for the previous compounds ($\mathrm{Li_2SO_4}$ and α-sulphur), the density of d states has little effect on the sensitivity of the A feature shape to the different tested compounds. Indeed, though the intensity of the density of d states is slightly higher in the case of orpiment and realgar in the A feature energy range, than in the case of arsenopyrite and pyrite, the energy placement of the d states in this energy range is very similar for all the compounds. To summarise, the failure to clearly split the A feature of the XRS S $L_{2,3}$ edge spectrum of pyrite into the A1 and A2 peaks, for the low q value, compared to the experimental XAS $L_{2,3}$ edge data, likely stems from bad reproduction of the empty s state energy distribution by DFT. Unfortunately, given the lack of experimental data, we can not know if the evolution of the A feature, as q increases, is properly reproduced, and for which compounds. It could also be interesting to study the effects of the core hole on the calculated spectra, and see what approximation leads to the better agreement, and in which case. Nevertheless, the sensitivity of the calculated A feature in the spectrum of the different compounds, which is the part of the spectrum that varies the most with the increase of the value of q, by comparing the decomposition of spectrum calculated for each compound as well as PDOS calculations performed for each compounds, was shown to stem from the energy placement of the s and p states.

4.3.4.5 Conclusion

The results observed and discussed in this section, dedicated to the presentation and analysis of the preliminary calculation of the XRS S $L_{2,3}$ edge spectrum of orpiment, realgar, arsenopyrite and pyrite, performed in the FCH approximation, are mostly consistent with results that were found in the sections dedicated to calculations at the S $L_{2,3}$ edge of $\mathrm{Li_2SO_4}$ and α-sulphur. More precisely, calculations once again showed that the most important factor in the change of the spectrum shape, as the value of q increases, is the rapid change of the relative weights of the monopole (stemming from $2p \to p$ electronic transitions) and dipole (stemming from $2p \to s$ and $2p \to d$ electronic transitions) contributions, with the dipole contribution dominating at low q values and the monopole contribution dominating at high q values, especially in the early region (A feature) of the spectrum. The shape of the A feature was shown to be very sensitive to the studied compound, going from a feature clearly split into two peaks for orpiment and realgar to being a seemingly unsplit feature, consisting in a seemingly broader single peak. This sensitivity was shown to stem from different energy placement of the empty p and s states, which are more localised in the A energy range for orpiment and realgar than for arsenopyrite and pyrite. This leads to sharper monopole and dipole contributions to the A feature of the individual L_3 and L_2 edges, which in turn creates sharper contributions from those edges to the A feature of $L_{2,3}$ edge, ultimately leading to a split A feature for orpiment and realgar and not for arsenopyrite and pyrite. This is consistent to results observed for the individual cases of $\mathrm{Li_2SO_4}$ and α-sulphur where the placement of the empty p states had a tremendous effect on the shape of the A feature of these spectra. On a side note, it should be noted that calculations reproduce an energy shift towards high energy of the arsenopyrite and pyrite spectra, compared to the orpiment and realgar spectra. Literature (80; 79) has shown the oxidation state of sulphur in diverse compounds to be responsible for an energy shift towards higher energies of the S $L_{2,3}$ and K absorption edges (The higher the oxidation level of the absorbing sulphur, the larger the shift of the absorption edge). Though DFT technically cannot calculate absolute energies, once shifted using the ΔSCF procedure, the calculated spectra of the different compounds exhibit the same shift, for the spectra calculated for both the lower q (and equivalent to the measured

XAS S $L_{2,3}$ shown to exhibit this shift in litterature) and higher q values. Due to the lack of experimental data, however, the shift for high q values, as well as the global evolution of the calculated spectra as the value of q increases, cannot yet be verified.

4.4 Summary and conclusion

This chapter was dedicated to the implementation of XRS $L_{2,3}$ edge calculation in a modified XSpectra module of quantum ESPRESSO, and inspired by both the implementation of XRS K edge calculation, already implemented in the modified XSpectra module (47), and of XAS $L_{2,3}$ edge calculation in XSpectra.

After reminding or introducing theoretical elements relevant to the implementation in the modified XSpectra module, the description of the implementation was made. The theoretical elements presented included the expression of the XRS dynamic structure factor and the expansion of the XRS transition operator. The description of the implementation included developing the expression of the pseudo wave function $|\tilde{\phi}_0\rangle$ in the pseudopotential framework and PAW formalism, and needed to calculate the initial vector allowing the Lanczos algorithm to calculate the spectrum as a continued fraction. The importance of the norm and orientation of $\boldsymbol{q}$ was highlighted. This description also included more technical details more relative to the code itself, and relevant to understand which parts of the spectrum can be calculated separately, or when they are calculated and how. The final spectrum is calculated as a continued fraction, to avoid explicit calculations of all the possible final states involved in the electronic transition. The modified XSpectra module calculates separately, and one by one, the monopole and dipole contribution calculation, stemming respectively from $2p \rightarrow p$, and $2p \rightarrow s$ and $2p \rightarrow d$ electronic transitions. Because of spin-orbit coupling, the $2p$ states split into the $2p_{1/2}$ and $2p_{3/2}$ states, giving rise, respectively, to the L_2 and L_3 edges, whose sum is the $L_{2,3}$ edge. The modified XSpectra module currently calculates the two edges, but separately and one by one.

Then, the modified XSpectra module was tested, to verify it was operational and gave the expected results in specific cases, on a simple test case included in Quantum ESPRESSO. It allowed to verify that the XRS $L_{2,3}$ edge spectrum calculated by the modified XSpectra module, for low q values, was equivalent to the XAS $L_{2,3}$ spectrum calculated by the regular version of

XSpectra, as this is theoretically expected. Moreover, though the L_3 and L_2 edge calculations are possible using the modified XSpectra module, in DFT which is a single electron scheme, the calculated L_2 and L_3 edge spectra are expected to be equivalent, save for an intensity factor of 2, stemming for the the multiplicity of the $2p_{1/2}$ states being half the multiplicity of the $2p_{3/2}$ states. Moreover, the L_2 and L_3 edges are calculated at the same energy in DFT. This first test case thus serves as an efficient first validation test of the implementation.

After using the test case presented in section 4.3.1 to verify that the calculation of the XRS L_2 and L_3 edge spectra were yielding the expected results, the modified XSpectra module was further tested by calculating the XRS S $L_{2,3}$ edge of $\mathrm{Li_2SO_4}$ and of α-sulphur, and comparing the results to available experimental data, measured for similar values of the norm q of the scattering factor $\boldsymbol{q}$ at the ID20 beamline of the ESRF thanks to a collaboration with E. de Clermont Gallerande and C. Sahle. The effect of the presence, or lack thereof, of a core hole on the excited shell was also studied by comparing the spectra obtained using the different cole hole approximations available in DFT, and used during the SCF charge density calculation preceding the spectrum calculation between themselves. In the case of $\mathrm{Li_2SO_4}$, a good agreement between theory and experiment was obtained at low q values, especially for calculation performed in the presence of a core hole on the excited shell of the excited S atom (FCH and XCH approximations). The GS calculation did not lead to a good agreement between theory and experiment at low q values, as the shape of the different calculated spectral features were found too broad to properly match the measured ones. In contrast, though the global evolution of the spectrum with the increasing values q is satisfyingly reproduced overall, for higher q values, no core hole approximations allowed to accurately reproduce the A feature. In comparison, in the case of α-sulphur, a better overall agreement was obtained by using the GS approximation, especially for high q values, for which the agreement was impressive. This was surprising, considering the calculation was done without taking into account the core hole, even though XRS is a spectroscopy based on core level excitations. However, by comparing the calculation to both XAS (found in the literature) and XRS (measured at ID20) data at low q values, the shape of the calculated A feature is once again not accurately reproduced, and is closer to the measured A shape when including a core hole on the excited atom (FCH and XCH approximations), though the intensity of the reproduced A shape is lower than the intensity of the measured on in that case. Thus, the A shape of the XRS $L_{2,3}$ edge spectrum of both $\mathrm{Li_2SO_4}$ and α-sulphur was found to be very sensitive to the adopted core hole approximation, and the main factor to good or bad agreement between calculation and experiment, as the A feature is subjected to the most changes when changing the core hole approximation. Decomposition of the calculated spectra into the monopole and dipole contributions as well as into the separate L_3 and L_2 edge spectra allowed to highlight interesting key results. First, the major factor behind the evolution of the spectrum as the value of q increased was identified as the relative weights of the monopole and dipole contributions to the spectrum, with the dipole contribution dominating the whole spectrum at low q values, and the monopole dominating the early energy range of the calculated spectra (A feature), and contributing in roughly equal parts with the dipole contribution to the spectrum at higher energies (B feature and after). Secondly, at low q values, the two peaks A1 and A2 of the A feature in the S $L_{2,3}$ edges of both $\mathrm{Li_2SO_4}$ and α-sulphur can be interpreted as signature contributions from the L_3 and L_2 edges, respectively, which is consistent with the attribution of those peaks in the A feature of the XAS S $L_{2,3}$ edge of α-sulphur in the literature (79). At higher q values however, this interpretation is no longer valid, and the decomposition of the XRS S $L_{2,3}$ edge spectrum of α-sulphur calculated for high q values and using the GS approximation, as well as the impressive agreement between this calculation and the XRS spectrum measured at low q values, support instead another interpretation. In this other interpretation, for high values of q where the L_3 and L_2 edge contributions to the A feature are broader than at low q values, the A1 and A2 peaks are no longer only a signature of the L_3 and L_2 edges, respectively. Finally PDOS calculations allowed to make a link between the sensitivity of the shape of the A feature of the calculated XRS S $L_{2,3}$ edge spectrum of α-sulphur to the chosen core hole approximation, and the energy distribution of the empty s and p states of the excited atom. Indeed, in the presence of a $2p$ core hole on the excited atom (FCH and XCH approximations), the empty p and s states in the A feature energy range are more localised, leading to sharp monopole and dipole contributions to the A feature of the individual L_3 and L_2 edges. This in turn leads to sharp L_3 and L_2 contributions to the A1 and A2 peak of the A feature of the $L_{2,3}$ edge, respectively, which are thus signatures of these two respective edge. This ultimately leads to better agreement between calculation and experiment at low q values. In contrast, with no core hole on the excited atom (GS approximation), the empty p and s state in the A feature energy range are more delocalised, spread evenly in the whole A feature. This leads to broader monopole and dipole contributions to the A feature of the L_2 and L_2 edges, and then to broader L_2 and L_3 edge contributions to the A feature of the $L_{2,3}$ edges, ultimately leading to the correct shape of the A feature at higher values of q. The failure to reproduce the correct shape of the A feature by calculations performed with a core hole at high q values can thus be a consequence of DFT not being able to properly model the core hole. Indeed, a correct shape is obtained for the spectrum calculated using the GS approximation, at high q values, with delocalised p states spread on the whole energy range of the A feature. It is thus possible that the core hole creates a stronger attraction and localisation of the empty p to low energies, which prevents accurate reproduction of the spectrum at high q values.

Finally, the preliminary calculations of the XRS S $L_{2,3}$ edge spectra of orpiment, realgar, arsenopyrite, performed using the FCH approximation, were discussed. As no measured data was available for these compounds, because of a dilution problem during sample preparation leading to a too small signal for proper measurement, it was not possible to further assess the capacity of the modified XSpectra module to reproduce measured spectra for various values of q. However, the obtained results could still be discussed in light of the previous ones. The global shape of the calculated spectra, as well as its evolution with an increase of the value of q, were similar to what was observed for the calculated XRS S $L_{2,3}$ edge spectra of Li_2SO_4 and α-sulphur. Interestingly, the modified XSpectra module was able to produce a shift towards lower energies, of about 1.2 eV, of the XRS S $L_{2,3}$ edges of orpiment and realgar compared to that of the arsenopyrite and pyrite. In the literature, (80; 79) the shift of the absorption edge of S K and $L_{2,3}$ edge spectra towards higher energies was shown to stem from the increasing oxidation state of the absorbing S atom. In our case, given the expected oxidation states of S in the different studied compounds (-2 for realgar and orpiment and -1 for arsenopyrite and pyrite), the produced shift is thus expected for the low q spectra. Calculations also produced this same shift for the high q spectra. Additionally, most of the previous results were confirmed by these new calculations. The major factor behind the variation in the XRS S $L_{2,3}$ edge spectra of these four compounds was once again shown to be the change of the relative weights of the monopole and dipole contributions, with the dipole contribution dominating the low q spectra and the monopole dominating the early energy range of the spectra, and contributing, in roughly equal parts, to the spectra at higher energies. The shape of the A feature of these calculated spectra of different compounds was once again very sensitive, this time to the studied compounds rather than the chosen core hole approximation. The calculated A feature either appeared split into A1 and A2 peaks in the case of realgar and orpiment, or appear as a broader single peak in the case of arsenopyrite and pyrite. The sensitivity of the A feature of the different XRS S $L_{2,3}$ edge spectra was shown to once again be linked to the reproduced energy distribution of the empty p and s states of the excited S atom. In the A feature energy range, for realgar and orpiment, more localised p and s states lead to a split A feature, while for arsenopyrite and pyrite, more delocalised p and s states lead to a broader A feature, appearing as a single peak. The comparison of the experiment XAS data of the S $L_{2,3}$ (found in (79)) edge spectrum with the XRS S $L_{2,3}$ edge spectrum calculated at a low q value however, suggests that at least for low q values, the pyrite A feature should be more clearly split, and follow the interpretation of the A1 and A2 peak being signatures of the L_3 and L_2 edges, respectively, indicating that once again the presence of the core hole is possible not well modelled, this time not attracting and localising the p states enough, leading to a non split A feature in the calculated pyrite $L_{2,3}$ low q edge spectrum instead of a split one, as featured in the XAS data.

5 General conclusion

5.1 Conclusion

This thesis work was focused on two core level spectroscopy techniques, X-Ray Absorption Spectroscopy (XAS) and X-ray Raman Scattering (XRS), which rely on the excitation of a core level electron to study the electronic or structural properties of materials. More specifically, it was focused on their computational modelling using the Quantum ESPRESSO suite of codes, based on Density Functional Theory (DFT) and the use of periodic boundary conditions, pseudopotentials and plane wave basis sets to expand the wave functions, to reproduce data that can be measured using these two spectroscopy techniques. More specifically, this thesis work was divided in two distinct objectives.

The first objective was to assess the effects of the quantum thermal vibrations of nuclei on the multipole contributions, stemming from different channels of electronic transitions of the excited core level electron to the available states, to XRS and XAS spectra. To take these thermal effects into account, the spectrum cannot be calculated using the Quantum ESPRESSO suit of codes in a standard way, i.e with only the equilibrium structure of the material as input. The thermal vibrations were taken into account according to the work developed during a previous thesis work and summarised in two articles (41; 42). The method elaborated during the thesis work of R. Nemausat and allowing to take vibrations into account, referred to as the QHA model, consists in calculating the spectrum as an average of individual spectra calculated for different atomic configurations of the supercell of the studied material. In these atomic configurations, atoms are moved from their equilibrium positions according to both vibrational properties (phonon) of the material, as well as finite temperature. This study was completed using two well known reference materials for which experimental data at different temperatures were available. For XRS, the Al K edge spectrum of α-Al_2O_3 was measured on a powder sample, at room temperature. For XAS, the Ti K edge spectrum of rutile TiO_2 was measured, for temperatures ranging from 6 to 698 K, on a single crystal sample and a specific experimental set-up allowing to also study the temperature dependence of the empty $3d$ states of Ti. While the method had already been used to study thermal effects on XAS spectra of light element oxides, it was never applied to XRS spectra, for which the monopole transition channel, forbidden in XAS, is available. The study concluded that taking into account thermal vibrations of the nuclei systematically improved agreement between theory and experiment. Moreover, save for a slight shift towards lower energies of the whole spectra, temperature was shown to affect the different multipole contributions very differently. While the monopole (in XRS) and quadrupole (XAS) contributions were left mainly unchanged save from a slight broadening of the feature in the case of the monopole contribution, the dipole contribution was greatly affected, in the form of both modified intensity for some already present spectral features as well as completely new features, adding intensity to spectral features otherwise signature of d or s empty states, and thus expected to only contribute to the quadrupole (XAS or XRS, though in this study the quadrupole contribution was only probed in XAS) and monopole (XRS only) contributions in the equilibrium symmetry. This was especially pronounced in the case of the pre-edge region of the Ti K edge of TiO_2. These effects were shown to essentially stem from on-site hybridisation between empty p and s or d states of the excited atom. It should be noted that thermal expansion effects, in principle included in the QHA model, were not taken into account in the case of rutile TiO_2 because phonon calculations, if not performed on the fully relaxed supercell of rutile TiO_2 at 0 K, lead to imaginary phonon modes, which has already been documented in the literature. Nevertheless, temperature is still taken into account in the modified QHA model used for calculation of XAS Ti K edge spectra of rutile TiO_2, when the different configurations of the fully relaxed supercell of rutile TiO_2 are generated. The modified QHA model thus could lead to the accurate reproduction of the variations of the measured in-plane mean signal of the XAS Ti K edge spectrum of rutile TiO_2, as temperature increased. In the case of TiO_2, the study nevertheless highlighted a problem never before encountered when using the modified QHA model. Indeed, the subtle signal related to the angular dependence of the quadrupole (E2) signal of the spectra was not properly reproduced. While the E2 signal was properly reproduced, the modified QHA model lead to adding a spurious and theoretically unexpected (according to the symmetry of TiO_2) dipole (E1) contribution to the calculated signal. Using the QHA model, while granting better understanding of the temperature variations of the XAS Ti K edge of TiO_2, also led to lose the symmetry properties of the spectrum expected according to the symmetry of the rutile TiO_2 crystal. A method based on group theory, and justified using theoretical arguments, was then developed to recover the symmetry property of the average spectra, thus recovering the correct angular dependence of the calculated spectrum. It should be noted that this method, used to recover the symmetry properties can be used for any calculation methods that includes the use of atomic configurations, and is not limited to calculations performed using Quantum ESPRESSO only.

The second objective of the thesis was to implement, in Quantum ESPRESSO (and more precisely in XSpectra, the module used to calculated XRS and XAS spectra), XRS spectrum calculations at the $L_{2,3}$ edge. This objective followed the recent thesis work of E. De Clermont Gallerande, who implemented XRS calculations at the K edge (47). XRS provides similar information to XAS when measured at low values of the norm q of the scattering vector $\boldsymbol{q}$, but relies on highly energetic incident x-rays and thus, in some cases when XAS has to rely on 'soft' (less energetic) x-rays, can provide an alternative to XAS. Indeed, this allows XRS measurements in less demanding experimental set-up, making even *in situ* measurement of light element edges possible. Compared to XAS, the specificity of XRS is that as the value of q increases, the relative weights of the different multipole contributions also change. The implementation was inspired on the implementation of K edge in XSpectra by E. de Clermont Gallerande as well as the implementation of the XAS $L_{2,3}$ edge in XSpectra. XRS $L_{2,3}$ edge calculations were implemented is the same version of the module in which the previous implementation of XRS K edge calculations was done. Consequently, the XRS $L_{2,3}$ edge calculation was implemented so that the different multipole contributions to the spectrum are calculated separately. Moreover, the calculation of the individual L_3 and L_2 were also implemented to be calculated separately. The implementation was first tested on a test case included in the Quantum ESPRESSO suite, to verify that XRS $L_{2,3}$ edge calculations were running correctly, and to verify that the expected properties of XRS $L_{2,3}$ edges in a single particle scheme were reproduced. More precisely, the branching ratio of the L_3 and L_2 edge is expected to be 1:2 in a single particle scheme, meaning that the L_3 edge is equal to twice the L_2 edge in intensity. Moreover, the XRS $L_{2,3}$ edge spectrum, for low values of q (more precisely, in the $qr \ll 1$ limit) is expected to be equivalent (save for an intensity factor) to the XAS $L_{2,3}$ spectrum, because of the XAS and XRS transition operators being equivalent for small q values, when replacing the orientation of the polarisation vector in XAS by the orientation of the scattering vector in XRS. After it was verified the XSpectra module yielded the expected result for the test case regarding these basic properties, calculations were performed on various sulphur compounds and compared to available measured data, and for various values of q, to further validate the implementation. At low q values, we managed to accurately reproduce the XRS S $L_{2,3}$ edge spectrum of $\mathrm{Li_2SO_4}$ by including a core hole on the excited S atom. At higher q values however, no core hole approximations allowed to properly reproduce the A feature of the spectrum. The global variation of the spectrum, as q increases, is however otherwise satisfyingly reproduced. Strikingly, the XRS S $L_{2,2}$ edge spectrum of α-sulphur is reproduced with overall very good agreement by not including any core hole on the excited atom $2p$ shell. The variation of the spectrum as q increases is also well reproduced. However, for the lowest q values, though the intensity of the A feature is lower than the experiment data, the shape is more accurately reproduced by calculations performed using the FCH or XCH approximation. The shape of the A feature is nevertheless reproduced far more accurately when using the GS approximation rather than the FCH or XCH approximations for the higher values of q. Thus, in both cases, though overall a good agreement between calculation and experiment can be reproduced using various core hole approximations, the evolution of the shape of the A feature is not accurately reproduced for the whole range of variation of the value of q. The ability to separate the calculated spectra into the monopole and dipole contributions as well as into the separate L_2 and L_3 edges allowed to highlight several key points. First, the variation of the calculated S $L_{2,3}$ spectrum, as q increases, is caused by the relative weight of the monopole and dipole contributions also changing when q increases. While the spectrum is mainly dominated by the dipole contribution at low q values, the monopole contribution rapidly becomes dominant in the A feature energy range and contributes in equal part with the dipole contribution at higher energies. Secondly, at low q values, the interpretation of the A feature of the XRS S $L_{2,3}$ edge spectra is that the A1 and less intense A2 peaks are a signature of the individual L_3 and L_2 edges. At higher q values however, the interpretation is no longer valid, and the A1 and now more intense A2 peaks, are not only a signature of the L_3 and L_2 edges, respectively. Finally, this change of the shape of the A feature of the calculated XRS S $L_{2,3}$ spectra when different core hole approximations are used, and which is responsible for obtaining, or not, good agreement between calculation and experiment, is related to the energy distribution of the empty p (and s) states of the excited S atom, as shown by PDOS calculations. Indeed, calculations performed using the FCH or XCH approximation generally lead to, in the A feature range of the various calculated $L_{2,3}$ edge spectra, localised empty p (and s) states, mainly located on the first half of the A feature energy range. This leads to sharper monopole contributions, and, ultimately, sharper contributions from the individual L_3 and L_2 edge contributions to the A feature of the calculated $L_{2,3}$ spectra, which become signature contributions of the A1 and A2 peaks of the A feature. This leads to good agreement between calculated and measured XRS and XAS spectra at low q values, with the XAS data found in literature. This interpretation is also consistent with what is explained in the reference (79) in which the XAS data was found regarding the origin of the A1 and A2 peaks (noted 1 and 2, respectively, in the reference). In contrast, calculations performed using the GS approximation usually lead, in the A feature energy range of the calculated XRS $L_{2,3}$ edge spectra, to delocalised empty p (and s !) states, spread on almost the whole A feature energy range. This leads to broader monopole and dipole contribution, and, ultimately, to broad L_3 and L_2 edge contributions to the A feature of the $L_{2,3}$ edge, which is in good agreement with the measured data in the case of the XRS S $L_{2,3}$ edge spectrum of α-sulphur measured at high values of q. Finally, the preliminary calculations performed using the FCH approximation of the XRS S $L_{2,3}$ edge spectra of orpiment, realgar, arsenopyrite and pyrite were shown and discussed in light of the previous results. These calculations, though they could not be compared to measured data due to a dilution problem that occurred during sample preparation, allowed to confirm most of the previous results. The main factor behind the variation of the calculated spectra with an increasing value of q was indeed shown to be the change of the relative weights of the monopole and dipole contributions, for these calculations as well, with the monopole contribution being more dominant at high values of q, and the dipole contribution dominating the whole spectra at low q values. Moreover, though the shape of the A feature was also shown to be sensitive to the studied compound, and not just the core approximation chosen, and to produce A features appearing as a single peak in the case of arsenopyrite and pyrite, unlike all other FCH calculations, these change of shapes were once again related to the energy distribution of the empty p (and s, of course) states of the excited atom in the A feature energy range.

5.2 Perspectives

To complete this thesis work, some work still needs to be done in a more or less short time frame. This short section is dedicated to perspectives related to the completion or improvement of this work.

The short term perspectives, and that I would personally would like to pursue, after this thesis are mainly related to the technical part of the second part of this thesis work. Indeed, though the modified XSpectra module has indeed been modified to include XRS $L_{2,3}$ edge calculation, some work remains to be done in that regard. First, the code was modified using the XSpectra module of a previous version of Quantum ESPRESSO, and the format of the XSpectra module has since changed. This means that the modified XSpectra module could not be integrated, as is, into the current distribution of Quantum ESPRESSO. Thus, work should be done in that direction to make the modified XSpectra module and the regular version of the XSpectra module more compatible. A second part of this work would be to further modify the subroutines responsible for calculating the dipole part of the L_2 and L_3 edges. Indeed, as of now, when calculating one of these two edge in the dipole approximation, the modified XSpectra module does not allow selection between the 'plus' or 'minus' part of the selection rule ($\Delta l = \pm 1$) and calculates the dipole contribution as the sum of these two contributions. It would be nice to be able to choose between the minus or plus part of the selection rule. Moreover, the calculation of these two dipole transition channels ($2p \rightarrow s$ and $2p \rightarrow d$) are done separately, and the dipole contribution is then obtained as the sum of squared transition matrix element. This neglects eventual cross terms arising if between these two transition matrix elements for the dipole contribution, and now that the first implementation has been tested, it would be interesting to investigate those cross terms. The same could be said for the monopole-dipole cross terms. The term corresponding to $\lambda = 2$ in the expansion of the transition operator using Bessel functions should also be implemented next. Finally, it would be useful to add more explicit messages in the output file when some specific error occur. For example, when the pseudopotential of the absorbing atom has no d projectors, since the dipole contribution of the XRS $L_{2,3}$ spectrum is calculated as the sum of contributions stemming from the plus and minus selection rules, but the plus selection rule cannot be calculated without d projectors, the code simply crashes, but no indications as to why is present in the output file. To summarise, the code still needs some measure of optimisation.

On a longer term perspective, the assessment of the capacity of the modified XSpectra module to provide additional information to K edges by accurately reproducing experimental data is an ongoing work. First, it would be interesting to finally get experimental data for the XRS S $L_{2,3}$ edge spectrum of orpiment, realgar, arsenopyrite and pyrite, for various values of q. Indeed, the lack of those data prevents final conclusions from being drawn for the spectra calculated at high q values. For example, calculations predict a different shape of the A feature, at high q, for those different compounds, with a split A feature in the case of orpiment and realgar and a non split feature in the case of arsenopyrite and pyrite. Though this shape was shown to be accurate at low q values, by comparison with XAS data of this spectrum, and experimental data is needed to verify if this is still the case at high q values, and if it is, would help confirm or infirm the reason being related the energy placement of empty p states of the excited S atom, like it was the case for the other compounds. In short, the variations of those spectra as the value of q increases could be studied to complete the results already obtained for the other sulphur compounds (Li_2SO_4 and α-sulphur). Moreover, since the A feature of those calculated spectra was shown to be sensitive to the studied compounds, assessing the core hole effects on those spectra would also be very interesting, for different values of q. On another note, calculations were mainly performed for sulphur compounds, but it would be interesting to perform calculations and obtain data, for various values of q, for other light elements, while keeping in mind that XAS data can always be used to analyse calculations at low q values.

Bibliography

[1] O. Durmeyer, J.P. Kappler, E. Beaurepaire, J.M. Heintz and M. Drillon *J. Phys.: Condens. Matter* **2**, 6127 (1990).

[2] S.-J. Hwang, J.-H. Choy and N.H. Hur, *Phys. Rev. B* **57**, 1259 (1998).

[3] N.L. Saini, A. Lanzara, H. Oyanagi, H. Yamaguchi, K. Oka, T. Ito and A. Bianconi, *Phys. Rev. B* **55**, 12759 (1997).

[4] Y.K. Kim, W.S. Jung, G.R. Han, K.-Y. Choi, C.-C. Chen, T.P. Devereaux, A. Chainani, J. Miyawaki, Y. Takata, Y. Tanaka, M. Oura, S. Shin, A.P. Singh, H.G. Lee, J.-Y. Kim, and C. Kim, *Phys. Rev. Lett.* **111**, 217001 (2013).

[5] F. Bridges, C.H. Booth, G.H. Kwei, J.J. Neumeier and G. A. Sawatzky, *Phys. Rev. B* **61**, R9237 (2000).

[6] A.Y. Ignatov, N. Ali and S. Khalid, *Phys. Rev. B* **64**, 014413 (2001).

[7] P. Ghigna, A. Carollo, G. Flor, L. Malavasi, and G. Subias Peruga, *J. Phys. Chem. B* **109**, 4365 (2005).

[8] A. Yoshiasa, T. Nakatani, T. Hiratoko, T. Tobase, A. Nakatsuka, M. Okube, H. Arima and K. Sugiyama, *J. Phys.: Conference Series* **712**, 012121 (2016).

[9] A. Yoshiasa, G. Kitahara, T. Tobase, T. Hiratoko, H. Hongu, T. Nakatani, and K.-I. Murai, *Phys. Status Solidi B* **255**, 1800050 (2018).

[10] E. Cockayne, E.L. Shirley, B. Ravel, and J.C. Woicik, *Phys. Rev. B* **98**, 014111 (2018).

[11] I. Jonane, A. Cintins, A. Kalinko, R. Chernikov, A. Kuzmin, *Low temp. phys.* **44**, 434 (2018).

[12] I. Jonane, A. Anspoks, G. Aquilanti, A. Kuzmin, *Acta Mat.* **179**, 26 (2019).

[13] M.P. Seah and W.A. Dench, *Surf. Interface Anal.*, **1**, 2 (1979)

[14] J.A. Soininen, A.L. Ankudinov and J.J. Rehr, *Pyhs. Rev. B* **72**, 045136 (2005).

[15] K. Hämäläinen and S. Manninen *J. Phys.: Condens. Matter* **13** 7539 (2001)

[16] U. Bergmann, P. Glatzel and S.P. Cramer, *Microchemical Journal* **71**, 221 (2002).

[17] C. Sternemann and M. Wilke, *High Press. Res.* **36**, 275 (2016).

[18] S. K. Lee, P. J. Eng, H.-K. Mao, Y. Meng, M. Newville, M. Y. Hu, and J. Shu, *Nat. Mater.* **4**, 851 (2005).

[19] J.-F. Lin, H. Fukui, D. Prendergast, T. Okuchi, Y. Q. Cai, N. Hiraoka, C.-S. Yoo, A. Trave, P. Eng, M. Y. Hu, and P. Chow, *Phys. Rev. B* **75**, 012201 (2007).

[20] G. Lelong, L. Cormier, G. Ferlat, V. Giordano, G. S. Henderson, A. Shukla, and G. Calas, *Phys. Rev. B* **85**, 134202 (2012).

[21] J.S. Tse, M. Hanfland, R. Flacau, S. Desgreniers, Z. Li, K. Mende, K. Gilmore, A. Nyrow, M. Moretti Sala, and C. Sternemann, *J. Phys. Chem. C* **118**, 1161 (2014).

[22] H. Conrad, F. Lehmkühler, C. Sternemann, A. Sakko, D. Paschek, L. Simonelli, S. Huotari, O. Feroughi, M. Tolan and K. Hämäläinen, *Phys. Rev. Lett.* **103**, 218301 (2009).

[23] C.J. Sahle, C. Sternemann, C. Schmidt, S. Lehtola, S. Jahn, L. Simonelli, S. Huotari, M. Hakala, T. Pylkkänen, A. Nyrow, K. Mende, M. Tolan, K. Hämäläinen, and M. Wilke, *Proc. Natl. Acad. Sci. (U.S.A.)* **110**, 6301 (2013).

[24] C.J. Sahle, S. Kujawski, A. Remhof, Y. Yan, N.P. Stadie, A. Al-Zein, M. Tolan, S. Huotari, M. Krisch and C. Sternemann, *Phys. Chem. Chem. Phys.* **18**, 5397 (2016).

[25] W. Kohn and L. J. Sham, *Phys. Rev.* **136**, B864 (1964)

[26] W. Kohn and L. J. Sham, *Phys. Rev.* **140**, A1133 (1965)

[27] P. E. Blöchl, *Phys. Rev. B* **50**, 17953 (1994)

[28] R. Haydock, V. Heine and M. J. Kelly, *J. Phys. C: Solid State Phys.*, **5**, 2845 (1972)

[29] L. X. Benedict and E. L. Shirley, *Phys. Rev. B* **59**, 5441 (1999)

[30] D. Cabaret and C. Brouder, *J. Phys.: Conf. Ser.* **190**, 012003 (2009).

[31] C. Brouder, D. Cabaret, A. Juhin, and P. Sainctavit, *Phys. Rev. B* **81**, 115125 (2010).

[32] D. Manuel, D. Cabaret, C. Brouder, P. Sainctavit, A. Bordage, and N. Trcera, *Phys. Rev. B* **85**, 224108 (2012).

[33] A.L. Ankudinov and J.J. Rehr, *Phys. Scrip.* **T115**, 24 (2005).

[34] T. Fujikawa, *J. Phys. Soc. Jpn.* **68**, 2444 (1999).

[35] T.A. Pascal, U. Boesenberg, R. Kostecki, T.J. Richardson, T.-C. Weng, D. Sokaras, D. Nordlund, E. McDermott, A. Moewes, J. Cabana and D. Prendergast, *J. Chem. Phys.* **140**, 034107 (2014).

[36] P. Müller, K. Karhan, M. Krack, U. Gerstmann, W. Gero Schmidt, M. Bauer, and T.D. Kühne, *J. Comput. Chem.* **40**, 712 (2019).

[37] M.P. Ljungberg, J.J. Mortensen and L.G.M. Pettersson, *J. Electron Spectrosc. Relat. Phenom.* **184**, 427 (2011).

[38] C. Lamberti, S. Bordiga, F. Bonino, C. Prestipino, G. Berlier, L. Capello, F. D'Acapito, F. X. Llabrés i Xamena and A. Zecchina, *Phys. Chem. Chem. Phys.* , **5**, 4502–4509 (2003).

[39] M. Wilke, G. M. Partzsch, R. Bernhardt and D. Lattard, *Chemical Geology*, **220** 143–161 (2005)

[40] M. Wilke, P. J. Jugo, K. Klimm, J. Susini, R. Botcharnikov, S. C. Kohn and M. Janousch *American Mineralogist*, **93** 235-240 (2008)

[41] R. Nemausat, D. Cabaret, C. Gervais, C. Brouder, N. Trcera, A. Bordage, I. Errea and F. Mauri, *Phys. Rev. B* **92**, 144310 (2015).

[42] R. Nemausat, C. Gervais, C. Brouder, N. Trcera, A. Bordage, C. Coelho-Diogo, P. Florian, A. Rakhmatullin, I. Errea, L. Paulatto, M. Lazzeri and D. Cabaret, *Phys. Chem. Chem. Phys.* **19**, 6246 (2017).

[43] D. Cabaret, A. Bordage, A. Juhin, M. Arfaoui and E. Gaudry, *Phys. Chem. Chem. Phys.* **12**, 5619 (2010).

[44] F. M. F. de Groot, Z. W. Hu, M. F. Lopez, G. Kaindl, F. Guillot and M. Tronc, *J. Chem. Phys. 101* **8**, 1994

[45] F.M.F. de Groot, *X-ray Absorption Fine Structure-XAFS13*, AIP Conference Proceedings, **882**, 37 (2007).

[46] W. Schülke, *Electron Dynamics by Inelastic X-ray Scattering*, Oxford Series on Synchrotron Radiation No. 7 (Oxford University Press, Oxford, 2007)

[47] E. de Clermont Gallerande, D. Cabaret, G. Lelong, C. Brouder, M.-B. Attaiaa, L. Paulatto, K. Gilmore, Ch.J. Sahle and G. Radtke, *Phys. Rev. B* **98**, 214104 (2018).

[48] Y. Joly, C. Cavallari, S.A. Guda and C.J. Sahle, *J. Chem. Theory and Comput.* **13**, 2172 (2017).

[49] G. Beutier, S.P. Collins, G. Nisbet, E.N. Ovchinnikova and V.E. Dmitrienko, *Eur. Phys. J. Special Topics* **208**, 53 (2012).

[50] S. Huotari, C. J. Sahle, C. Henriquet, A. Al-Zein, K. Martel, L. Simonelli, R. Verbeni, H. Gonzalez, M.-C. Lagier, C. Ponchut, M. Moretti Sala, M. Krisch and G. Monaco, *J. Synchrotron Rad.* **24**, 521 (2017).

[51] M. O. Krause and J. H. Oliver, *J. Phys. Chem. Ref. Data* **8**, 329 (1979)

[52] M. Born and R. Oppenheimer, *Ann. Phys.* **389**, 457-484 (1927).

[53] C. Brouder, *J. Phys.: Condens. Matter* **2**, 701 (1990).

[54] S. Baroni, S. de Gironcoli, A. Dal Corso and P. Giannozzi, *Rev. Mod. Phys.* **73**, 515 (2001).

[55] P. Giannozzi, S. Baroni, N. Bonini, M. Calandra, R. Car, C. Cavazzoni, D. Ceresoli, G. L. Chiarotti, M. Cococcioni, I. Dabo, A. Dal Corso, S. de Gironcoli, S. Fabris, G. Fratesi, R. Gebauer, U. Gerstmann, Ch. Gougoussis, A. Kokalj, M. Lazzeri, L. Martin-Samos, N. Marzari, F. Mauri, R. Mazzarello, S. Paolini, A. Pasquarello, L. Paulatto, C. Sbraccia, S. Scandolo, G. Sclauzero, A.P. Seitsonen, A. Smogunov, P. Umari and R.M. Wentzcovitch, *J. Phy.: Condens. Mat.* **21**, 395502 (2009).

[56] P. Giannozzi, O. Andreussi, T. Brumme, O. Bunau, M. Buongiorno Nardelli, M. Calandra, R. Car, C. Cavazzoni, D. Ceresoli, M. Cococcioni, N. Colonna, I. Carnimeo, A. Dal Corso, S. de Gironcoli, P. Delugas, R.A. DiStasio, A. Ferretti, A. Floris, G. Fratesi, G. Fugallo, R. Gebauer, U. Gerstmann, F. Giustino, T. Gorni, J. Jia, M. Kawamura, H.-Y. Ko, A. Kokalj, E. Küçükbenli, M. Lazzeri, M. Marsili, N. Marzari, F. Mauri, N.L. Nguyen, H.-V. Nguyen, A. Otero-de-la-Roza, L. Paulatto, S. Poncé, D. Rocca, R. Sabatini, B. Santra, M. Schlipf, A.P. Seitsonen, A. Smogunov, I. Timrov, T. Thonhauser, P. Umari, N. Vast, X. Wu and S. Baroni, *J. Phy.: Condens. Mat.* **29**, 465901 (2017).

[57] P. Giannozzi, O. Baseggio, P. Bonfà, D. Brunato, R. Car, I. Carnimeo, C. Cavazzoni, S. de Gironcoli, P. Delugas, F. F. Ruffino, A. Ferretti, N. Marzari,I. Timrov, A. Urru, S. Baroni, *J. Chem. Phys.* **152**, 154105 (2020)

[58] M. Taillefumier, D. Cabaret, A.M. Flank and F. Mauri, *Phys. Rev. B* **66**, 195107 (2002).

[59] Ch. Gougoussis, M. Calandra, A. Seitsonen and F. Mauri, *Phys. Rev. B* **80**, 075102 (2009).

[60] O. Bunau and M. Calandra, *Phys. rev. B* **87**, 205105 (2013)

[61] J. Vinson, J. J. Rehr, J. J. Kas and E. L. Shirley, *PHYSICAL REVIEW B* **83**, 115106 (2011)

[62] P. Krüger, *J. Phys.: Conf. Ser.* **190** 012006 (2009)

[63] R. Laskowski and P. Blaha, *Phys. Rev. B* **82**, 205104 (2010)

[64] C. Sternemann, J. A. Soininen, S. Huotari, G. Vankó, M. Volmer, R. A. Secco, J. S. Tse, and M. Tolan1, *Phy. Rev. B* **72**, 035104 (2005)

[65] J. A. Bearden and A. F. Burr, *Rev. Mod. Phys.* **39**, 125 (1967).

[66] M. Cardona and L. Ley, Eds., *Photoemission in Solids I: General Principles* (Springer-Verlag, Berlin, 1978).

[67] J. C. Fuggle and N. Mårtensson, *J. Electron Spectrosc. Relat. Phenom.* **21**, 275 (1980).

[68] D. Vanderbilt, *Phys. Rev. B* **41**, 7892 (1990).

[69] A. Dal Corso, *Comput. Mater. Sci.* **95**, 337 (2014).

[70] A. M. Rappe, K. M. Rabe, E. Kaxiras, and J. D. Joannopoulos, *Phys. Rev. B* **41**, 1227 (1990).

[71] J.P. Perdew, S. Burke and M. Ernzerhof, *Phys. Rev. Lett.* **77**, 3865 (1996).

[72] B. Montanari and N.M. Harrison, *Chem. Phys. Lett.*, **364**, 528 (2002).

[73] K. Refson, B. Montanari, P.D. Mitev, K. Hermansson and N.M. Harrison, *Phys. Rev. B* **88**, 136101 (2013).

[74] J.P. Perdew and A. Zunger, *Phys. Rev. B* **23**, 5048 (1981).

[75] G. Fiquet, P. Richet and G. Montagnac *Phys. Chem. Minerals* **27**, 103 (1999).

[76] G. Lelong, G. Radtke, L. Cormier, H. Bricha, J.P. Rueff, J.M. Ablett, D. Cabaret, F. Gélébart and A. Shukla, *Inorg. Chem.* **53**, 10903 (2014).

[77] S. Rossano, F. Mauri, C. J. Pickard and I. Farnan, *J. Phys. Chem. B* **109**, 7245–7250, 2005

[78] C. Patrick, and F. Giustino, *Nat Commun* **4** , 2006 (2013)

[79] M.E. Fleet, *Canadian mineralogist*, **43** , 1811 (2005)

[80] D. Li, G. M. Bancroft, M. Kasrai, M. E. Fleet, X. Feng, K. Tan, *Canadian mineralogist*, **33** , 949 (1995)

[81] J. K. Burdett, T. Hughbanks, G. J. Miller, J. W. Richardson, and J. V. Smith *J. Am. Chem. Soc.* **109** (12), 3639-3646, 1987

[82] K. V. Krishna Rao, S. V. Nagender Naidu, and L. Iyengar *J. Am. Cer. Soc.* **53** (3), 124-126 (1970)

[83] D.W. Fischer, *Phys. Rev. B* **5**, 4219 (1972).

[84] B. Poumellec, R. Cortes, G. Tourillon and J. Berthon, *Phys. Status Solidi B* **164**, 319 (1991).

[85] T. Uozumi, K. Okada, A. Kotani, O. Durmeyer, J.P. Kappler, E. Beaurepaire and J.C. Parlebas, *Europhys. Lett.* **18**, 85 (1992).

[86] E. Beaurepaire, S. Lewonczuk, J. Ringeissen, J.C. Parlebas, T. Uozumi, K. Okada and A. Kotani, *Europhys. Lett.* **22**, 463 (1993).

[87] Y. Joly, D. Cabaret, H. Renevier and C.R. Natoli *Phys. Rev. Lett.* **82**, 2398 (1999).

[88] D. Cabaret, Y. Joly, H. Renevier and C.R. Natoli *J. Synchrotron Rad.* **6**, 258 (1999).

[89] E.L. Shirley, *J. Electron Spectrosc. Relat. Phenom.* **136**, 77 (2004).

[90] P. Le Fèvre, H. Magnan, D. Chandesris, J. Jupille, S. Bourgeois, A. Barbier, W. Drube, T. Uozumi, and A. Kotani, *Nucl. Instrum. Methods Phys. Res. A* **547**, 176 (2005).

[91] Z.Y. Wu, G. Ouvrard, P. Gressier, and C.R. Natoli, *Phys. Rev. B* **55**, 10382 (1997).

[92] R. Brydson, H. Sauer, W. Engel, J.M. Thomass, E. Zeitler, N. Kosugi and H. Kuroda, *J. Phys. : Condens. Matter* **1**, 797 (1989).

[93] T. C. Rossi, D. Grolimund, O. Cannelli, G.F. Mancini, C. Bacellar, D. Kinschel, J.R. Rouxel, N. Ohannessian, D. Pergolesic and M. Chergui *J. Synchrotron Rad.* **27**, 425 (2020).

[94] S. Nozawa, T. Iwazumi and H. Osawa, *Phys. Rev. B* **72**, 121101(R) (2005).

[95] M. Chassé, A. Juhin, D. Cabaret, S. Delhommaye, D. Vantelon and G. Calas *Phys. Chem. Chem. Phys.* **20**, 23903 (2018).

[96] A. Kokalj, *J. Mol. Graphics Modelling* **17**, 176-179 (1999).

[97] K. Momma and F. Izumi, *J. Appl. Crystallogr.* **44**, 1272-1276 (2011).

[98] We used a local orthonormal system of coordinates oriented along the two-fold rotation axes of the $\mathrm{D_{2h}}$ point group of the Ti site. We arbitrarily chose $\hat{x}$ to point along [001] and $\hat{z}$ along [110] and considered the Ti located at (0,0,0). With this choice, the $\hat{z}$ axis is oriented along the 1.98 Å Ti-O bond and $\hat{x}$ and $\hat{y}$ point toward the middle of the edges of the rectangle formed by the four equatorial O ions distant from the central Ti by 1.94 Å. Accordingly, real d orbitals $d_{x^2-y^2}$, d_{xz}, d_{yz}, d_{z^2} and d_{xy} transform as the irreducible representations $\mathrm{A_g}$, $\mathrm{B_{2g}}$, $\mathrm{B_{3g}}$, $\mathrm{A_g}$ and $\mathrm{B_{1g}}$, respectively.

[99] If the eigenvalues are degenerate, the set of degenerate states is a group representation presented by unitary matrices and the final result is the same.

[100] Similarly in XRS, the transition operator being $\mathcal{O}(\boldsymbol{r}) = e^{i\boldsymbol{q}\cdot\boldsymbol{r}}$, translations do not affect the dynamic structure factor and we have again $S(\hbar\omega, \boldsymbol{q}; D\bar{\boldsymbol{R}}) = S(\hbar\omega, \mathcal{S}^{-1}\boldsymbol{q}; \bar{\boldsymbol{R}})$.

[101] If $\chi_0^i(D\bar{\boldsymbol{R}})$ and $\chi^i(\bar{\boldsymbol{R}})$ are degenerate, the set of degenerate states is a group representation presented by unitary matrices and the final result is the same.

[102] On a side note, for the spectrum calculated using the GS approximation and for the lowest q value ($q = 2.1$Å^{-1}), which is shown in Fig. 4.13, the decomposition into the monopole and dipole contributions shows that the monopole and dipole contributions have an equal weight in the A feature. The reason the decomposition of the calculated spectra for the lowest q value is not shown is that the S $L_{2,3}$ edge spectra of α-sulphur obtained using the XCH and FCH approximations was only calculated for $q = 4.0$ Å^{-1} and $q = 12.0$ Å^{-1}, as mentioned earlier.